Euler/Euler/Lagrange model development for the numerical simulation of multiphase flows loaded with particles

Federico Baraglia

RÉPUBLIQUE FRANÇAISE
Liberté Égalité Fraternité

Université de Toulouse

Doctorat de l'Université de Toulouse

préparé à Toulouse INP

Développement d'un modèle triphasique Euler/Euler/Lagrange pour la simulation numérique des écoulements liquide-gaz chargés en particules.

Thèse présentée et soutenue, le 8 avril 2024 par

Federico BARAGLIA

École doctorale
MEGEP - Mécanique, Énergétique, Génie civil, Procédés

Spécialité
Dynamique des luides

Unité de recherche
IMFT - Institut de Mécanique des Fluides de Toulouse

Thèse dirigée par
Olivier SIMONIN

Composition du jury
M. François-Xavier DEMOULIN, Président, Université de Rouen
Mme Anne TANIÈRE, Rapporteuse, Université de Lorraine
M. Pierre RUYER, Rapporteur, IRSN
Mme Catherine COLIN, Examinatrice, Toulouse INP
M. Berend VAN WACHEM, Examinateur, Otto von Guericke Universität Magdeburg
Mme Maria Giovanna RODIO, Examinatrice, CEA Paris Saclay
M. Olivier SIMONIN, Directeur de thèse, Toulouse INP

Membres invités
M. Jérôme LAVIÉVILLE, EDF R&D

La connaissance du réel est une lumière qui projette toujours quelque part des ombres.

G. Bachelard

À ma famille, mes amis, amies et à Delphine.

Abstract

This manuscript sums up the work carried out during a thesis at the MFEE department of EDF R&D on liquid-gas flows laden with dispersed particles under the supervision of Olivier Simonin (IMFT), Jérôme Laviéville (EDF), and Nicolas Mérigoux (EDF). The thesis aims at providing a working environment for the numerical simulation of two-phase bubbly flows and free-surface flows loaded with particles that can interact with all the fluids present in their continuous or dispersed form. These flows can be found in industrial situations such as chemical reactors, power plants, or wastewater treatment plants, as well as in natural situations such as during a flood event. The developed tool allows predictions to be made about the performance of these industrial devices or the damage caused by exceptional natural events. The developments are included in the most up-to-date version of neptune_cfd, a multi-fluid solver developed by EDF, CEA, IRSN, and Framatome, based on the standard multi-fluid method that allows the simulation of multiphase flow independently of their typology.

The methods implemented are based on well-known two-phase approaches. The stochastic Lagrangian particle tracking method is adapted so that each particle can interact with all the fluids. Closures are proposed to determine the impact of each phase on the behavior of the particles. To verify certain assumptions, a new closure for the Langevin equation on the fluid velocity seen by the particle is proposed. Its behavior is compared to standard models and literature on simple verification cases of homogeneous isotropic turbulence and inhomogeneous cases. The Lagrangian equations obtained are used to close an Eulerian model based on the probability density function approach. The performance of the two developed three-phase models is established in terms of particle agitation and turbulence or gravity drivzen deposition.

A significant part of the thesis focuses on an issue that arose during preliminary checks: the phenomenon of air entrainment in plunging jets. Indeed, due to the nature of the solver, bubbles or dispersed droplets can detach from the free-surface depending on the flow conditions. The quantity of these transferred structures and their characteristic size being crucial quantities which drives their behavior, a new model had to be developed. Mass transfer between continuous structures and dispersed inclusions is ensured by the model that describes the evolution of resolved interfaces, the latter was not modified. The one regarding the size of the created bubbles/droplets is integrated into the evolution equation of the interfacial area, a quantity that allows tracking the diameter of the inclusions.

All developed models are compared to experimental measurements. The air entrainment model is first tested without the presence of particles in various cases. A hydraulic jump case is also considered to establish the generality of the model. Then, the three-phase models are tested in various configurations. First, configurations without air entrainment to isolate the behavior of the particles, then with air entrainment. The different cases highlighted the importance of certain phenomenons and the differences between stochastic Lagrangian and Eulerian methods.

Résumé

Ce manuscrit retranscris un travail effectué au cours d'une thèse au département Mécanique des Fluides Énergie et Environnement d'EDF R&D sur les écoulements liquid-gaz chargés en particules dispersées sous la direction d'Olivier Simonin (IMFT), de Jérôme Laviéville (EDF) et de Nicolas Mérigoux (EDF). Le but de la thèse est de fournir un cadre de travail pour la simulation numérique d'écoulements eau-air à bulles, à phases séparés ou en régime mixte, chargés en particules pouvant interagir avec les fluides présents sous leur forme continue ou dispersée. Ces écoulements peuvent se retrouver aussi bien dans des situations industrielles comme des réacteurs chimiques, des centrales de production d'électricité ou des usines de traîtement des eaux usées que dans des situations naturelles comme durant la crue d'un fleuve. L'outil développé permet de faire des prédictions sur les performances de ces dispositifs industriels ou sur les dégâts causés par des évènements naturels exceptionnels. Les développements sont inclus dans la version de production du code de calcul neptune_cfd, un solveur N-fluides développé par EDF, le CEA, l'IRSN et Framatome, basé sur la méthode multi-fluide qui permet la simulation d'écoulements à plusieurs phases.

Les méthodes mises en place sont basées sur des approches diphasiques bien connues. La méthode Lagrangienne stochastique de suivi de particules est adaptée pour que chaque particule puisse interagir avec tous les champs fluides présents. Des fermetures sont proposées pour déterminer l'impact de chacune de ces phases sur le comportement des particules. Afin de vérifier certaines hypothèses, une nouvelle fermeture pour l'équation de Langevin sur la vitesse de fluide vue par la particule est proposée. Son comportement est comparée aux modèles standards et de la littérature sur des cas de vérification simples de turbulence homogène isotrope et des cas inhomogènes. Les équations Lagrangiennes obtenues sont utilisées pour fermer un modèle aux moments basé sur l'approche fonction densité de probabilité. Les performances des deux modèles triphasiques développés sont établies en matière d'agitation et de déposition.

Un pan entier de la thèse se concentre sur une problématique apparue durant des vérifications préliminaires: le phénomène d'entraînement d'air dans les jets plongeants. En effet, à partir d'une structure résolue, en fonction des conditions d'écoulements, des bulles ou gouttelettes dispersées peuvent apparaître. La quantité de ces structures transférées ainsi que leur taille caractéristique étant des grandeurs primordiales, il a fallu mettre en place un nouveau modèle prédictif. Le transfert de masse entre structures continues et inclusions dispersées est assuré par le modèle qui décrit l'évolution des interfaces résolues. Nous ne l'avons pas modifié. Celui qui concerne la taille des bulles/gouttelettes créées s'intègre dans l'équation d'évolution de l'aire interfaciale, grandeur qui permet de suivre le diamètre des inclusions.

Tous les modèles développés sont comparés à des mesures expérimentales. Le modèle d'entraînement d'air est d'abord testé sans la présence des particules sur des cas divers. Un cas de ressaut hydraulique est aussi envisagé pour établir la généralité du modèle mis en place. Les modèles triphasiques sont testés sur des configurations variées, d'abord sans entraînement d'air pour isoler le comportement des particules puis avec tous les phénomènes. Les différents cas ont permis de mettre en valeur l'importance de certains phénomènes ainsi que les différences entre les méthodes Lagrangienne stochastique et Eulerienne.

Acknowledgments

I would like to express my sincere gratitude to my thesis director, Olivier S. and supervisors, Jérôme L. and Nicolas M. Your support and insight on numerical and theoretical fluid mechanics has vastly contributed to my great working experience here at EDF and as a doctorate candidate altogether. You were always implicated in my work and your high academic standards enhanced the quality of my research as well as my personal growth. I cannot stress enough how your goodwill has been important to me. If I felt as good as I did during the thesis, even in the most challenging periods, it is also thanks to you.

I extend my appreciation to the referees of the thesis, Anne T. and Pierre R., for accepting to review my manuscript and their precise and thorough feedback on the matter. I am also grateful towards the other members of the committee for their time and dedication during the defence and the weeks leading to it: Berend V. W., Maria Giovanna R. and François-Xavier D.

I would like to thank all the members of the I8A group here at EDF. Your warm welcome and continued support during the three years have been flawless and very welcomed. A special mention goes to Lianfa W., sharing an office with you and the various discussions we had has been a pleasure. I wish you the very best and I hope our paths will cross again in the future. To other members of the MFEE department who played a role in my journey, Antoine B. in particular, your input has been very valuable to me. The team of experimenters in the LNHE department deserves a special thanks for their accurate work on the experiments which led to the validation of the numerical methods. Clément B., you made it easy for me to get involved in the processes by inviting me and answering my questions. I am very grateful for your team's help. I would like to also thank the members of the IMFT laboratory as well. Your warm welcome has contributed to making my stays in the laboratory more pleasant. Thank you for including me in the groups activities despite my rare visits.

Finally, I am obviously in debt towards my family and friends. This work would definitely not have been possible without your unconditional love, support and help. I feel very fortunate to be part of such an amazing group of caring and loving people. In this manuscript lies a part of each and everyone of you.

Summary

List of Tables

List of Figures

Nomenclature

Abbreviations

GLIM Generalised Large Interface Model

IATE Interfacial Area Transport Equation

LIM Large Interface Model

PDF Probability Density Function

Constants

γ_c Constant in the collision models

λ_0, ω Constants in the deposition flux model from Simonin (2008)

ξ Constants in the agitation models

C_0 Constant in the turbulence models

C_μ Turbulence constant

k_b Boltzmann constant

Exponents

$+$ Refers to dimensionless quantities

A Mean pressure contribution

D Drag contribution

Indexes

c, b Coalescence and breakup terms

cf, df Continuous and dispersed phases

f, f' Fluid phases

fs Free-surface quantity

g, l, p Gas, liquid or solid phase

H Relative to Hinze scale

I, J Mesh cells

IJ Index for the value used to compute a variable flux through a face

m Mixture quantity

n Normal quantity

w, a Water or air phase

at Denotes the quantity of fluid f at the position of the particle p

Variables

α Mean volume fraction

β Smooth continuous function between 0 and 1

χ Phase indicator function

δ_{ij} Kronecker symbol

$\dot{F_{c,b}}$ Variation of the bubble size distribution function due to coalescence and breakup events

ϵ Turbulent kinetic energy dissipation

η Free-surface roughness coefficient

Γ Mean mass transfer between two phases

γ Function indicating the free-surface

γ_i Stochastic integral

γ_s Surface tension coefficient

κ Interface curvature

$\langle \mathbf{w} \rangle_\psi$ Mean velocity weighted by the moment ψ

$\mathbb{C}$ Collision term in the moment's equations

$\mathbf{A}$	Friction coefficient along a free surface
$\mathbf{c_f}$	Fluid velocity in the phase space
$\mathbf{c_p}$	Particle velocity in the phase space
$\mathbf{f_s}$	Surface tension forces
$\mathbf{H}$	Phase space
$\mathbf{n}$	Interface normal vector
$\mathbf{U_r}$	Relative velocity between two entities
μ_ψ	Moment ψ of a density function
ν, μ	kinematic and dynamic Viscosities
Ω	Volume
ϕ	Flux
Π	Fluid-particle fluctuation interaction terms
ψ_p	Moment of the particle density function
ρ	Density
σ	Stress tensor
τ_m	Weighted particle relaxation time
τ_p	Particle relaxation time
τ_{AB}	Time separating two collisions between entities A and B
τ_{ij}	Dissipative part of the stress tensor
$\tau_{p,c}$	Time separating two particle collisions
A_i	Drift vector
a_i	Interfacial area
B_{ij}	Diffusion vector
C	Inclusion concentration
C_A	Added mass coefficient
C_D	Drag coefficient
d	Diameter
$d_{3,2}$	Sauter diameter
E_c	Collision efficiency
e_c	Restitution coefficient
F_i	External forces
f_p	Particle probability density function
g	Gravity
J	Particle flux through a plane
k	Turbulent kinetic energy
K_{ij}	Diffusion tensor
L	Lift coefficient
m_p	Particle mass
n_p	Number of entities per unit volume
p	Pressure
P_{ij}	Dunford triangular matrix factor
q_p	Particle agitation
q_{fp}	Fluid-particle covariance
r	Diameter
$R_{f,ij}$	Fluid Reynolds tensor
$R_{fp,ij}$	Fluid-particle covariance tensor
$R_{p,ij}$	Particle variance tensor
S	Reverse coupling source terms in the fluid turbulent equations
t, τ	Time
T	Temperature
T_f^L	Lagrangian fluid time scale
u^*	Friction velocity
u_i	Velocity
u_τ	Wall shear velocity
V_d	Deposition velocity

$V_{f,i}$	Drift velocity
W_i	Wiener process
$x = \langle x \rangle + x'' = X + x''$	Reynolds decomposition
X	Reduced interfacial area
x_i	Position vector
y^+	Wall distance

Dimensionless numbers

F_r	Froude number
K	Stokes number
Re_τ	Wall Reynolds number
Sc	Schmidt turbulent number
W_e	Weber number (the index c specifies a critical Weber number)

1 | Scientific and industrial outline

Particles and multiphase flows are at the core of many modern challenges. These flows are encountered in a number of scenarios in the industry: power plants, chemical reactors, wastewater treatment plants and in natural settings: rivers, breaking waves. Their complexity and importance has driven scientists and engineers to experiment and simulate phenomenons related to liquid-gas-solid flows. The aim of the current thesis is to pursue this movement and suggest two new numerical simulation frameworks allowing the study of such configurations. This thesis took place in the research department of Électricité de France (EDF) with the collaboration of l'Institut de Mécanique des Fluides de Toulouse (IMFT), it is part of a broader project at EDF which aims at exploring new techniques in Computational Fluid Dynamics (CFD) and applying those to real-life scenarios, in the nuclear industry or in other research topics. The purpose of my work at EDF is to expand the capabilities of neptune_cfd, a solver jointly developed by EDF, CEA, IRSN and Framatome. The main goal being to develop a framework for liquid-gas-solid flows modelling where particles can deposit and interact with continuous phases and dispersed inclusions. All the developments are included in a development branch of the solver to ensure its featuring in future official releases.

In the manuscript, for the sake of simplicity, specifically in the probability density function formalism, the arguments of some functions are dropped after having been introduced. This produces a lighter, easier to read, mathematical expression without hindering its understanding. Indexes i, j and k denotes the three directions unless specified otherwise whereas f, f' and g refer to different phases name. Most frequently, indexes w and a are used to denote water and air fluids. The index $f@p$ describes an undisturbed fluid property at a particle position. Finally, the double dash denotes the fluctuation of a variable x defined along with an averaging operator $x \mapsto \langle x \rangle$ such that: $x = \langle x \rangle + x''$. In the manuscript upper case letters denote the averaged quantities whereas lower case letter their instantaneous value ($\langle x \rangle = X$).

The following chapter aims at presenting the scientific and industrial contexts for the thesis as well as providing a broad glimpse of what exists in terms of numerical simulation models for liquid-gas-solid flows.

1.1 Liquid-gas-solid flows settings

Liquid-gas-solid flows are characterised by any combination of identical or distinct elements in three different state of matter. In this work, two of the phases are fluids (either gas or liquid) and the third one is a solid phase composed of a large number of small spherical inclusions. In natural settings, rivers and oceans are regarded as the most common places to find these types of flows. They tend to transport sediments which

interact with air bubbles generated in highly turbulent flows or complex geometrical configurations. These sediments may, during extreme events such as floods, be found further away from the sea shore or river bed. In the case of human exploitation, this phenomenon can become of public safety concern (Nones, 2019; Weber et al., 2023). In industrial applications, there are a wider variety of liquid-gas-solid flows frequently encountered. Air-water-sediments are important in chemical plants where bubbles may be introduced in the reactors to amplify the reactions taking place (Kara et al., 1982; Muroyama and Fan, 1985). They are also important in water treatment power plants where air bubbles are used to catch debris and bring them to the surface. This can be an efficient way to remove particles from water in order to make it safer to drink for example. In the oil and gas industry, this topic is recurring. During hole boring or oil and gas transportation, water, oil and gas may transport sediments thus creating a three-phase flow (Cazarez et al., 2010). In this last case, the two continuous phases may be liquid which is not the subject of this work although all of the models introduced would be suitable in most cases. It can also be an important topic in mine engineering where bubbles are used to separated different minerals from each other (Shahbazi et al., 2010). Depending on the solid particle properties it can be absorbed by the bubble interface or it can be entrained. The differences in behaviour allow for species separation. Figure 1.1 shows a variety of three-phase flows encountered in natural or industrial settings.

Figure 1.1: Different scenarios with three-phase flows. From top left to bottom right, the purge of a dam with water containing sediments and entraining air bubbles due to the highly turbulent nature of the flow; river flood transporting sediments to potentially inhabited locations; laboratory scale particle loaded bubble column encountered in chemical plants; a hole boring machine used in the oil and gas industry and a dead tree stuck in a vortex generated by an air entraining waterfall in the town of Belfort.

For EDF, these types of flow may be encountered in different scenarios related to power generation facilities. In dams, the issues are similar to those faced in natural

flows. In nominal operation, sediments can be present in the water inlet to the turbine thus introducing particles in an already consistently aerated water flow. Understanding the particle behaviour, its interaction with both fluids and its turbulence is key and allows for a better prediction of turbine blades erosion (Guo et al., 2021) and the whole system efficiency. In a context where every replacement is expensive and time consuming, these types of models might help preventing damage by identifying the primary causes of failure and designing systems capable of preventing them. In power plants and specifically nuclear power plants, these flows can be encountered in water supplies like in hydroelectric dams but, most of the times, they are encountered in accidental situations (Couturier, 2004) illustrated in figure 1.2. When the primary circuit linking the nuclear core to the vapour generators leaks, a loss a coolant accident occurs. This leak can vary in size, each introducing specific challenges. In that scenario, a large quantity of high pressure water is ejected from the breach to the inside of the reactor building. During this ejection, due to the high pressure, debris are formed. These can be paint particles, glass fibers, beads insulation material or cement particles. Details about their exact composition (size, density and chemical properties) are difficult to predict. Most of the time, estimates and sensitivity studies are needed in numerical simulations and experimental setups to overcome the uncertainty related to these quantities.

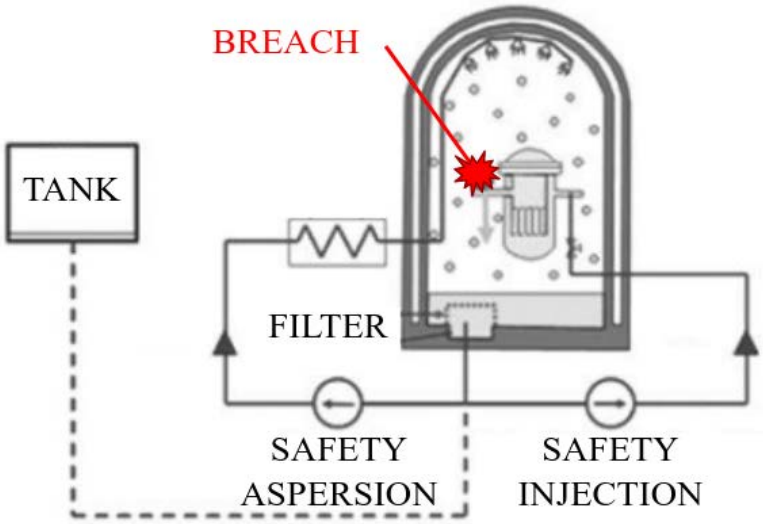

Figure 1.2: Sketch showing the reactor building, the breach in the primary circuit of the reactor, the safety devices (injection and aspersion), the water tank and the filters which may face sealing issues (Couturier, 2004). The dashed line represent a circuit which closes once the tank no longer has enough water to supply it.

In any case, these particles are transported towards the bottom of the reactor building which fills up with water. Meanwhile, since core cooling cannot be achieved by the primary circuit anymore, safety systems are turned on. They are twofold. The first one is a water injection directly inside the primary circuit and the second one is a water aspersion from the top of the reactor building. In both cases the water comes from a tank located outside the building and ends up, ultimately, towards its floor. When the water level in the tank is below a certain level, a recirculating circuit is activated.

It withdraws water from the bottom of the reactor building and inject it in the two safety systems. Before being injected, it goes through a series of filters which prevent debris and particles from damaging the pumps. However, depending on the fluid flows, particles can agglomerate on the filters and, due to chemical reactions or geometric accumulation, they might seal the filters and inhibit the safety mechanisms. The main challenge is therefore to predict the transport of particles in such configurations including water jets and overflowing nappes which generate a large amount of air bubbles below the free-surface. These can increase the particle transport by changing the flow characteristics or by capturing particles on their surface as in water treatment plants. The huge economic impact illustrated by all possible scenarios where three-phase flows take place justify the interest they have driven in academic as well as engineering communities. Understanding them requires thorough experimental and numerical investigation. Both giving different insights and both improving the other. The aim of this work is to provide an insight from the numerical simulation standpoint.

1.2 Challenges in liquid-gas-solid flows

The biggest challenge posed by liquid-gas-solid flows is the presence of various scales and domain of physics. The size of particles and bubbles can vary over several decades introducing a number of different flow phenomenons. At a local scale, the main challenge in liquid-gas-solid flows lies in understanding the behaviour of particles going through a fluid-fluid interface (Magnaudet et al., 2020). When a particle crosses an interface, many phenomenons are observed. Before impacting the surface, the particle displaces the fluid separating it from the interface. This displacement tends to decrease the solid velocity and can be noticeable depending on the fluids-particle characteristics. When it first makes contact with the free-surface, a particle faces additional forces due to surface tension effects at the triple contact point (Manga and Stone, 1995; Vella, 2015; Magnaudet et al., 2020). To precisely compute this force, physical, chemical and geometrical properties of the setup must be carefully accounted for. The sketch in figure 1.3 shows the forces acting on a partially submerged particle. After the particle crosses an interface, it is likely to carry a mass of fluid in its wake, drastically changing its hydrodynamics properties and the flow around it. Depending on the particle and fluid characteristics, this mass of fluid can be well defined (low velocity and high viscosity) or highly turbulent (high density ratio, high velocity and low viscosity) (Pierson and Magnaudet, 2018*a*,*b*). In both cases, the typical length and time scale of these perturbations can only be captured at the scale of the particle. Structures may be entrained well below the interface and contribute to changing the fluid flow near the surface and the particle. Figure 1.4 shows different scenarios for a particle crossing an interface. From a numerical point of view, capturing these effects implies resolving all the relevant scales related to these phenomenons. Because available computing capabilities are limited, this means drastically reducing the size of the studied sample.

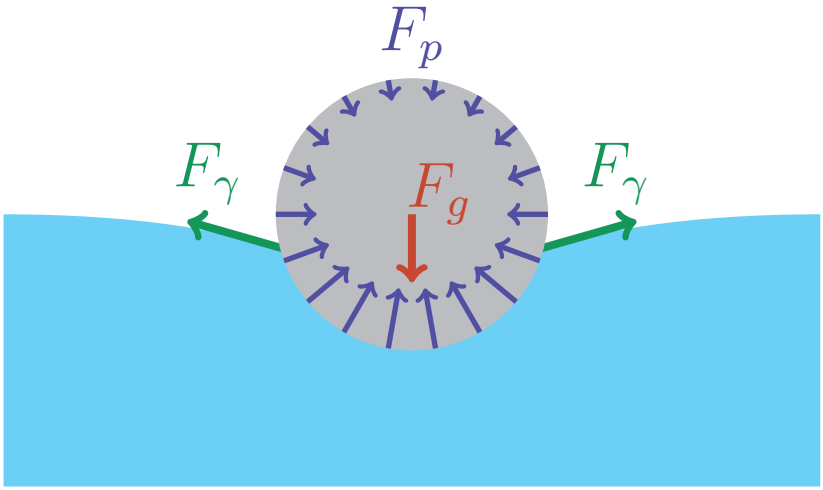

Figure 1.3: Forces acting on a partially submerged particle. F_p is the pressure force, F_g is the particle weight and F_γ is the surface tension force.

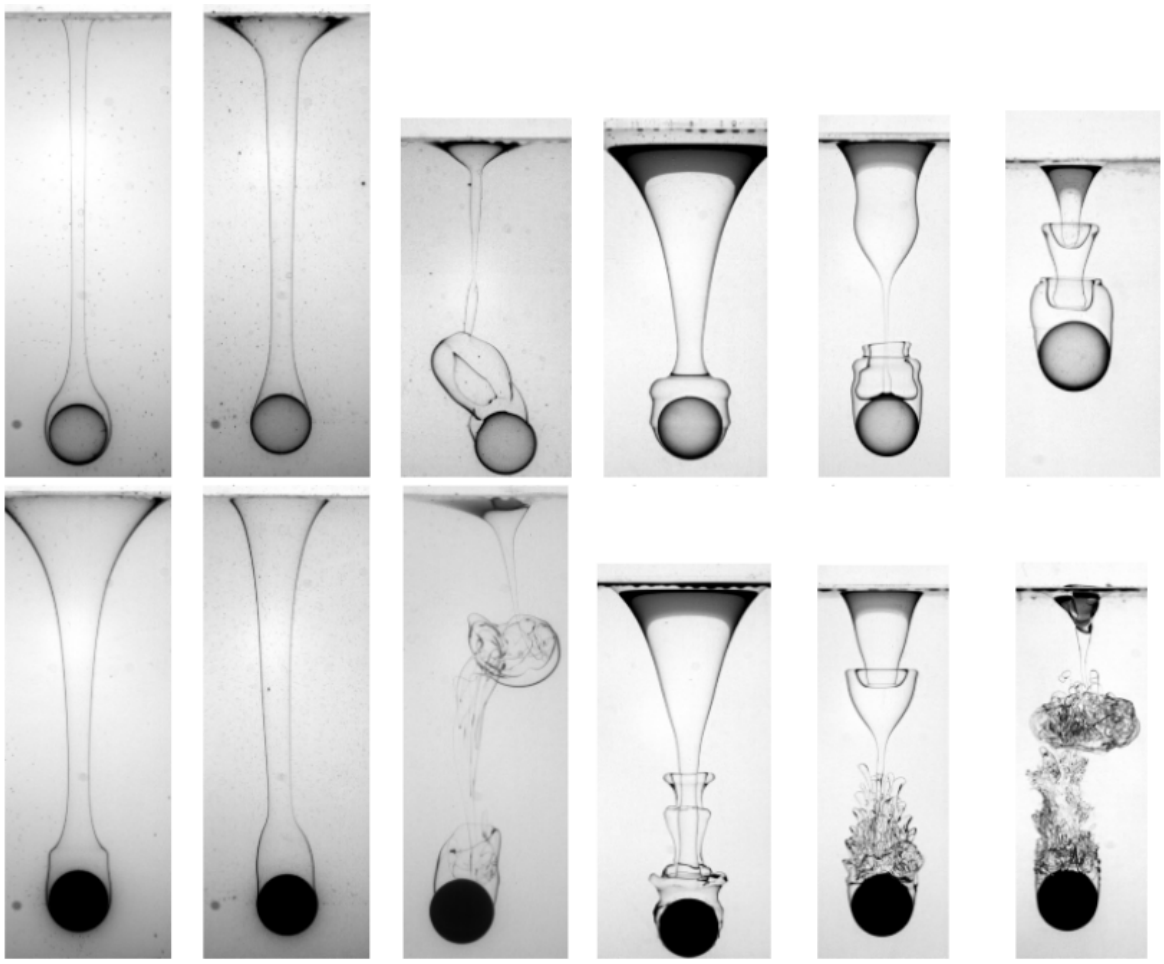

Figure 1.4: Wakes observed for solid particles crossing a fluid-fluid interface. Extracted from Magnaudet et al. (2020).

On the other hand, an ensemble of particles may have an effect on global flow

phenomenons. Usually, in two-phase flows, when particle or bubble loading increases, turbulence modulation and collisions start being noticeable and their impact cannot be neglected anymore (Gai et al., 2020; Liu et al., 2021). Table 1.1 sums up the different possible regimes for increasing inclusion volume fraction. For very dilute flows, the fluid dynamics plays the most important role in the particle transport and particles may not influence the flow. As soon as the loading increases, the behaviour is primarily driven by collisions then contacts and they have an important effect on flow phenomenons. Collisions can be accounted for following Grad's theory of gases (Grad, 1949). Additionally, Lavieville et al. (1997) showed that a similar approach can be used to tackle the correlated collision model where the behaviour of particles also depends on the ratio between particle relaxation time and eddy-particle interaction time. Illustrating the correlated movement of particles transiting in the same fluid turbulent eddy.

Very dilute flow	$\alpha_p < 0.01\%$	Transport is imposed by fluid turbulence, fluid turbulence is slightly influenced by the presence of particles and collisions can be neglected.
Kinetic regime	$0.01\% < \alpha_p < 5\%$	Transport is dominated by fluid turbulent fluctuations, particle dispersion is caused by fluid turbulent fluctuations and inter-particle collisions. Fluid turbulence is heavily impacted by the presence of particles.
Collisional regime	$5\% < \alpha_p < 50\%$	Transport is dominated by short time collisions and pseudo turbulence is generated from the particles.
Frictional regime	$50\% < \alpha_p$	Particle flow is dominated by friction, their behaviour is expressed with continuum solid mechanics.

Table 1.1: Solid particle regime depending on the volume fraction (Elghobashi, 1994; Sommerfeld, 2017).

In three-phase flows, these effects are still present but new interface phenomenons may be observed. Turbulence modulation is affected by several dispersed phases but the effect of coupled modulation has not been extensively studied yet. As for collisions, they can occur within a particular phase or between different species (Gourdel et al., 2000; Dai et al., 2000; Shahbazi et al., 2010; Chan et al., 2022), changing the overall flow properties. Dense flows and liquid-gas-solid fluidized bed systems are the classic configuration where these phenomenons take place (Muroyama and Fan, 1985; Gandhi et al., 1999; Pan et al., 2016). Depending on the particle, liquid and gas properties, the mixture can be very aerated with large gas structures or very densely packed without much movement (Johnson et al., 1953). Understanding the system state and evolution can be crucial to determine the overall performance of the reactor. Finally, bubble dynamics is also influenced by high particle loading. Coalescence and breakup are usually associated with a collision frequency between two entities causing an event (two bubbles for coalescence, a bubble and an eddy for breakup) and an event efficiency. In a liquid-gas-solid flow, it is possible that particle-bubble collision would cause a bubble breakup as well, increasing the overall breakup frequency. Due to a change in film

drainage properties, the presence of particles may also alter the efficiency of an event (Ojima et al., 2014).

These overall phenomenons may be captured only if a very large number of particles are considered. It is clear that these requirements are incompatible from a numerical point of view. We cannot simulate the surface tension effects on every particle if we need many of them to observe global phenomenons. We face a modelling choice: rely on direct numerical simulations to model exactly the physics of particles in multiphase flows, in which case we can only model a limited amount of particles; or, model the global behaviour of particles and try to capture the effects they have on the flow. Since simulation of local phenomenons such as the flow around a finite size particle crossing an interface is incompatible with the number of particles and domain sizes encountered in industrial or pilot scale setups, we chose to focus on trying to model the global behaviour of particles.

1.3 Liquid-gas-solid flows numerical simulations

Liquid-gas-solid flow models are increasingly studied and the rise in computing power makes these kinds of flows even more accessible. The purpose of this section is to present a literature review of existing frameworks allowing for their simulation. From resolved to modelled approaches, we will provide a wide point of view of what is currently available and detail any advantages or disadvantages for each method.

These three-phase flows can be classified according to their degree of resolution in turbulence, liquid-gas interface and particle representation. Turbulence is either completely resolved (Direct Numerical Simulation or DNS), resolved down to a certain length scale and then modelled with a sub grid turbulence model (Large Eddy Simulation or LES) or completely modelled (Reynolds averaged Navier Stokes or RANS). Of course, from DNS to RANS frameworks, the computing cost decreases dramatically. Turbulence not being the core aspect studied in the three-phase flows we face, we mainly focus on the liquid-gas interface and the particle representation. Several models enable the simulation of liquid-gas interfaces: the Lattice Boltzmann Method (LBM) (Kim and Pitsch, 2009), the Smooth Particle Hydrodynamics (SPH) (Monaghan and Kocharyan, 1995), the multifluid approach and the one-fluid approach. In all of them, the mesh size (or equivalent measure in mesh-less approaches) determines the smallest possible simulated free-surface. Below that scale, liquid-gas interfaces must be modelled. In the one-fluid approach, there are two classes identified. The interface tracking methods (front tracking Unverdi and Tryggvason (1992); Tryggvason et al. (2001)) and the interface capturing methods (volume of fluid (Hirt and Nichols, 1981), level-set or particle improved level-set (Enright et al., 2002)). In the first class, the mesh is updated to follow the interface. This can be costly but a higher accuracy is expected compared to the second class where the interface is constructed from the physical quantities in an otherwise static mesh. Again, depending on the configuration, simulating all the liquid-gas interfaces can greatly increase the computing time since it must decrease the mesh size (or equivalent measure in mesh-less approaches). In situations where it is not possible to simulate the interfaces, other methods can be used. The hybrid PDF-Eulerian method is one example (Simonin, 2000). It allows for the simulation of gas structures without needing the simulation of every liquid-gas interface. Another such method is the drift fluxes model (Zaichik, 1999) where one set of equations describes the mixture of liquid and gas and there is either no addi-

tional equations (homogeneous) or an additional equation for the drift velocity of the inclusion phase (inhomogeneous).

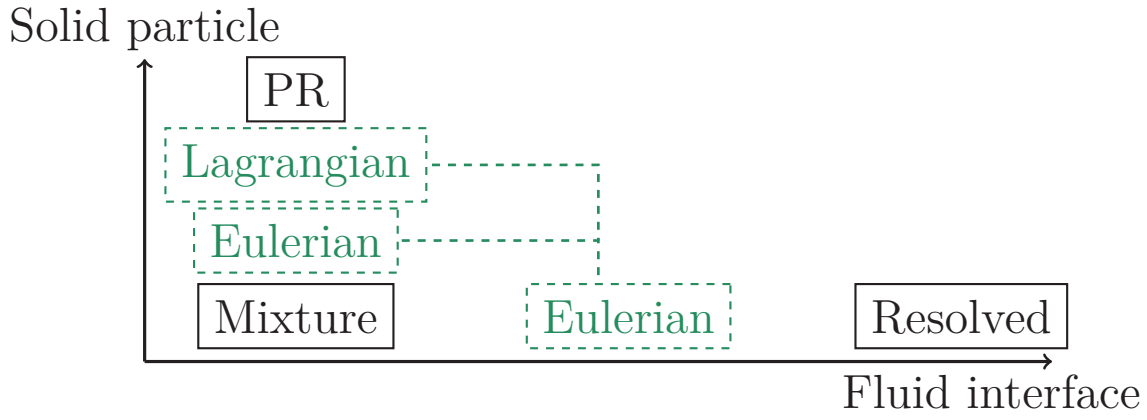

Figure 1.5: Classification of liquid-gas-solid models according to their degree of resolution. Green dashed lines represent the two new models developed during the thesis: a Lagrangian Eulerian and a multi-Eulerian hybrid model. Black arrows denotes a decrease in modelling or an increase in accuracy and computing time.

In particle resolved simulations (PR), the flow around a particle is simulated giving access to the fluid stresses around each solid. These approaches are very accurate but require large computing capabilities. They can be performed with mesh moving frameworks to track the particle surface position (ALE). Most of the time, since mesh moving methods are not very efficient for large displacements, particles are represented by an immersed boundary approach which tracks the position of the particle surface without changing the computing mesh. When particles are sufficiently small compared to fluid length scales, point particle approaches are preferred. It consists in replacing the particles by points and tracking the position and velocity of their centre of mass during time. This model is quite a lot faster than the previous one but requires a closure for the hydrodynamic forces acting on the particles. In large industrial applications, this approach can still be out of reach from today's computing facilities. In such case averaged models seem to be more suitable such as the multifluid model or the drift flux approaches. In the multifluid model, the solid phase is described with continuous fields (velocity, volume fraction...). This increases the number of achievable scenarios but requires thorough modelling to reproduce the correct particle behaviour for the solid phase, behaviour lost in the averaging process. These models usually include, hydrodynamic forces, collisions, friction and cohesion forces. In the drift flux models, the change is even more drastic. The solid phase is only accounted for through a drift velocity which characterises its behaviour relative to the carrier phase. In the latter, it is extremely difficult to take into account specific particle phenomenons. Figure 1.5 sums up all the different models ranked according to their computing requirements. The following review of existing simulation approaches follows the same classification: from the most time intensive methods to the most adapted to simulating industrial scales.

In the following paragraphs, we review existing numerical models for each class introduced above, detailing, when possible, their specificity and their purpose.

1.3.1 Direct numerical simulations

The methodology presented in Sun and Sakai (2016) consists in capturing the liquid-gas interface with a volume of fluid approach and the particles with an immersed boundary method. Because all phases are simulated on the same grid, a particle volume fraction ϕ_p identifies the position of the solid inclusions. Similarly to the VOF approach, the particle surface is identified by the contour $\phi_p = 0.5$. A specific forcing term ensures that the particles behave as rigid body solids. As for the particle dynamics, they include a particle-particle and particle-wall boundary contact forces model based on a Voigt model Sun and Sakai (2015). Particles are also subject to an additional capillary force which includes a term based on the Laplace pressure and a term based on surface tension at the contact line between three different phases. The accuracy of the model is verified on several test cases including a bubble spreading on a solid sphere and the simulation of liquid bridges between solid spheres. It gives interesting insights on academic three-phase configurations. By design, because it overcomes most of the issues encountered in reduced order models, this method is extremely powerful. However, it is still far from being computationally viable in industrial or laboratory scales motivating the current work. Figure 1.6 shows the capabilities of such method. It highlights the broad range of physical phenomenons it covers. Solid particles, surface tension effects and free-surfaces can be modelled. Turbulence not being mentioned in the paper, it is unclear as to whether it is accounted for or not. Considering the scales of the scenarios, it is assumed it is not taken into consideration.

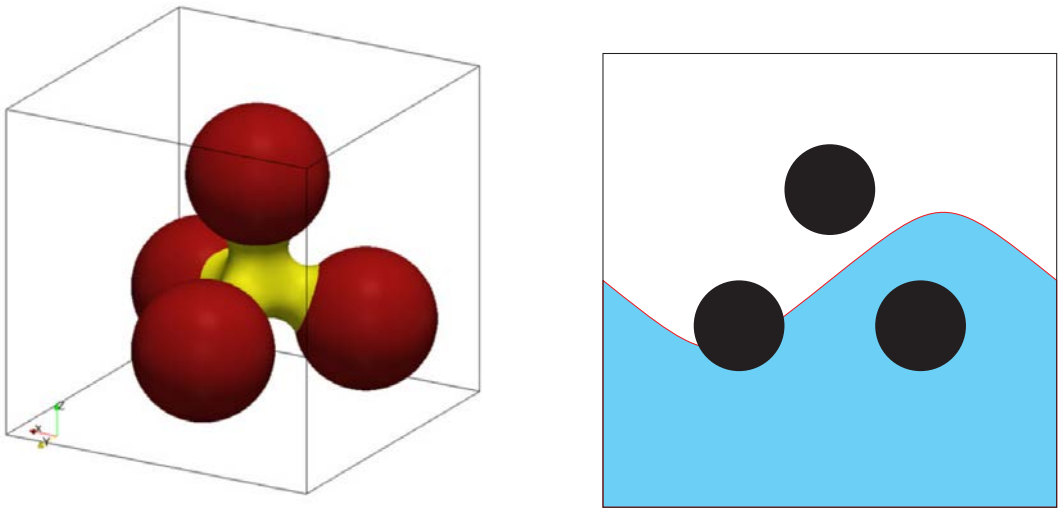

Figure 1.6: (left) Liquid bridge geometry linking three solid particles in a tetrahedral configuration. To accurately model the shape of the bridge, the surface tension effects must be accounted for. Extracted from Sun and Sakai (2016). (right) Sketch illustrating the capabilities of the PR-DNS framework. It can simulate particles with a finite volume in air, water or at the interface between the two.

Another example of particle-resolved liquid-gas-solid flow modelling approach can be found in the JADIM solver. This is a software developed at the IMFT where liquid gas structures are resolved with a volume of fluid method and solid particles are tracked with an immersed boundary approach. The hydrodynamic forces on the particles are computed through a volumetric forcing term rather than the integration of fluid stresses on the solid surface as in the previous method. Once this external

force is known, the solid position and orientation (which can be spherical or not) is tracked with a momentum balance equation. Surface tension effects are modelled at the fluid-fluid interface but no special treatment is done at the liquid-gas-solid triple contact line. This is a perspective but it has not been integrated yet. This setup is especially useful for simulating laboratory scale granular flows interacting with liquid-gas interfaces. It helps determining important closures for reduced order model and gain insights on the complex physics behind those kind of flows. They also recently explored coupling Lagrangian tracking for small bubbles and the transition occurring when these coalesce into a sufficiently large air pocket for it to be resolved with the VOF method. Thus opening the way to modelling and simulation of three-phase flows where gases can be continuous or dispersed.

1.3.2 Multi-Eulerian-Lagrangian approach

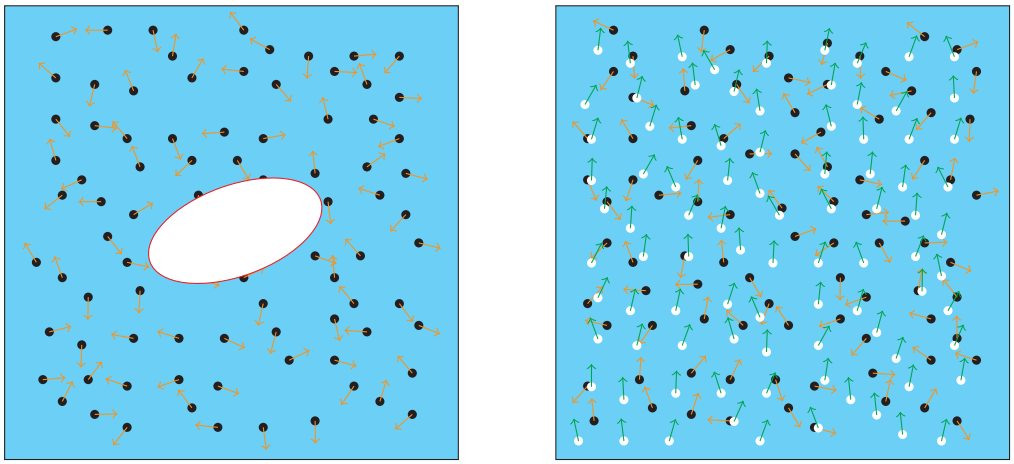

Figure 1.7: (left) Front-tracking or volume of fluid method to simulate a large air structure and Lagrangian particles for the solid inclusions. (right) Lagrangian particles for the air bubbles (white) and the solid inclusions (black). Each Lagrangian particle is defined by its position and linear velocity vector.

As exposed above, to reduce computational costs compared to particle resolved DNS, the solid inclusions can be replaced by point particles. The idea behind this simplification is illustrated in figure 1.7. These can then be included in a DNS or a modelled turbulent simulation. This approach can be used to simulate the behaviour of particles in liquid flows with resolved liquid-gas interfaces as presented in Li et al. (1999) or van Sint Annaland et al. (2005) where particles evolve in water and large bubbles are simulated with the VOF or front tracking (FT) method respectively. In the first reference, particles are assumed to be influenced by the neighbouring fluid only. Each experiences hydrodynamic forces (drag, added mass and buoyancy) as well as a surface tension contribution when they are near a resolved interface. It is a bubble induced force model. The liquid gas model in that framework completely solves the interface and adds a continuum surface force to account for surface tension effects. The gas flow inside the bubble is neglected and the particle effect on the fluids is considered inside the cell containing a particle with a specific treatment.

The approach and purpose are similar in the second framework (van Sint Annaland et al., 2005). Particles are tracked in a Lagrangian manner inside the liquid phase.

Particle experience drag, lift and added mass; collisions are accounted for with the model from Hoomans et al. (1996). The liquid-gas flow is completely resolved with a front tracking marker and cell method (Harlow and Welch, 1965) and the continuum surface force for surface tension effects. A special interpolation is set up to compute the correct fluid properties at the position of the particles and the position of the effect a particle has on the flow properties. The main difference with the first approach is the lack of effect from the interface to the particles. Otherwise, the methods are similar, they both neglect the fluid turbulence effect on the particle probably because of the low Reynolds numbers encountered. They both focus on simulating particles in liquid with a large rising bubble. By design, they can model the behaviour of many particles but only one bubble. They are not suited for bubbly flows with a lot of different scales which would make complete liquid-gas interface resolution much more difficult.

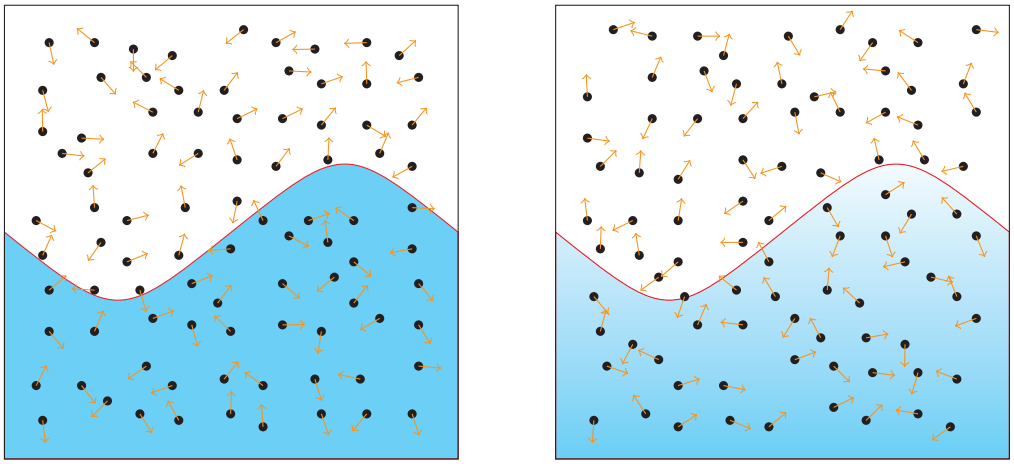

Figure 1.8: (left) Multifluid method with Lagrangian particles for the solid inclusions. The two fluids are immiscible. (right) Multifluid method with Lagrangian particles for the solid inclusions. In this setup, particles can also interact with bubbles.

Such an approach is also described in Xiao et al. (2019); Guo et al. (2021). Each particle trajectory is tracked over time by solving a momentum balance equation but this time, fluid turbulence effects are also taken into account (Gosman and loannides, 1983). The fluids are simulated using the VOF approach. which limits to large interfaces the scope of the method. Particles are assumed dilute enough not to consider two- or four-way coupling. Particle-solid surface impacts are modelled using a restitution coefficient. This method is a lot less computationally intensive compared to PR-DNS, it gives access to simulating laboratory scale experiments and simple industrial configurations. It is specifically set up to simulate the effects of water-air-sediments flows on Pelton turbines and predict the position of maximum erosion on a turbine blade. Even if there are some limitations, this approach still provides valuable insights on laboratory or industrial scales situations.

To simulate the behaviour of particles as well as a large amount of bubbles, another setup must be developed. Instead of solving air-water interfaces, bubbles can be tracked in the same way as particles are. such frameworks are illustrated in figure 1.8. This is the idea behind the method presented in Zhang and Ahmadi (2005). The liquid is solved with a volume-averaged approach. Bubbles and particles are tracked in a Lagrangian framework, bubble/bubble and particle/particle collisions are taken into account with a hard sphere model (Hoomans et al., 1996) and bubble/particle collisions

are also accounted for. When a particle hits a bubble, it always flows through it and surrounding fluid properties are changed accordingly. It is unclear if this has any effect on the bubble behaviour or if the particle is experiencing a specific force when it crosses the interface. The effect bubbles and particles have on the fluid is taken into account and, again, a special interpolation routine is setup to overcome the bias between Lagrangian particle positions and the Eulerian grid points. Unfortunately, no details are given on the turbulence effect for the particles or the bubbles.

Another Eulerian-Lagrangian method for particle loaded bubbly flows is described in Jianping Wen and Huang (2005). This time, bubbles are accounted for in a two-fluid model with interpenetration and a discrete particle method tracks the position of a set of particles. In this setup, the fluid-fluid interface may not be simulated completely thus introducing dispersed bubbles or droplets in the simulation. The effect of solid inclusion is accounted for in the fluid equations but no details are given as to the kind of interpolation setup. They also alter the k-ϵ models chosen for the continuous structures with an additional source term on the turbulent kinetic energy conservation equation. The particle experience drag from the two phases described by the multifluid model (air and water). The interaction with bubbles also includes a special term related to the velocity gradient induced by the bubble which is not accounted for in other models. Finally, particles also experience buoyancy effects and contact forces due to collisions. This framework is mostly used for simulating fluidized beds, it is close to what we are aiming at developing during the thesis.

The main advantage of the previous methods is their ability to simulate rather complex scenarios with a large amount of particles and bubbles as well as large resolved interfaces. To this day, they still generate interest in the scientific community as the model described in Zhang et al. (2023) attests. The latter introduces an approach with a population balance framework to account for bubble diameter polydispersion. This approach enables the simulation of polydisperse bubbly flows carrying particles. Again, it is mostly used to simulate turbulent bubble columns loaded with solid particles. This class of models is commonly used in medium sized configurations. It struggles when the case is too big or when too many particles are required but can still give interesting insights on cases approaching pilot or industrial scales.

1.3.3 Multi-Eulerian approach

When the number of particles becomes a limiting factor to achieve laboratory or industrial scale simulations, another step in the reduced order modelling has to be taken. The main idea is to replace the set of particles where each individual element is tracked by a continuous field description. By doing so, the number of particles becomes irrelevant in the computing time. A drawing illustrates this switch in modelling approach in figure 1.9.

The model described in Tomiyama and Shimada (2001); Tomiyama et al. (2006) allows for the simulation of liquid-gas-solid flows with large interfaces, bubbles and solid particles of various diameter. It is called the $N+2$ model and it is a combination of the multifluid method for the dispersed phases and an interface capturing method for the free-surface. Continuous liquids and gases are solved with a one-fluid formulation Tryggvason et al. (2011), they are represented by one velocity field and two volume fraction fields. Dispersed bubbles and particles are accounted for with a population balance method: each population is represented by different velocities and volume

fraction fields. The set of all the evolution equations is coupled through interfacial transfer terms arising from mass and momentum exchange between dispersed classes or between dispersed classes and continuous fields. The mass transfer terms are driven by coalescence and breakup, modelled with classic approaches described in Prince and Blanch (1990); Luo and Svendsen (1996). Collisions and dense models for particles are accounted for. These may be modified in the case of dense solid flows, see Ojima et al. (2014) for more details. This framework is powerful and allows for a wide variety of complex configurations to be studied numerically even though it is not clear how the transition between dispersed air bubbles and continuous air takes place. The main advantage of the method is its ability to simulate bubbly flows with the addition of particles and large interfaces while being a lot faster than tracking method described. However, it is still computationally intensive to simulate a wide range of length scales with the population balance method. The wider the range, the more classes are required to approximate the density function. Since each requires a set of balance equation to be solved, it is easy to set up configurations which would be too long to simulate with this method.

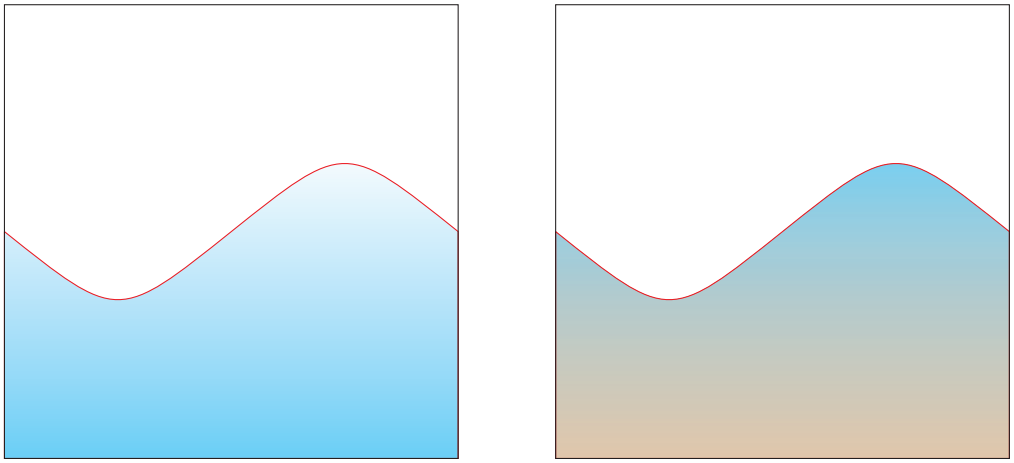

Figure 1.9: (left) Air volume fraction and (right) solid volume fraction in a triple Eulerian framework. The solid particles and bubbles appear as continuous fields. The resolved interface in red can be simulated with a dedicated VOF approach as in Tomiyama and Shimada (2001); Tomiyama et al. (2006) or a general multifluid approach as in Panneerselvam et al. (2009); Li and Zhong (2015)

Another multifluid model is described in Panneerselvam et al. (2009). This time, population balance models are not included, the dispersed inclusions are mono-dispersed. It is based on the same principles of previous Eulerian multifluid methods. A single pressure is considered and its impact on all the phases is weighted by the phase volume fraction, turbulence is computed with a k-ϵ model with turbulence modulation from the particle and bubble phases (Sato et al., 1981). Solid pressure is accounted for with the model from Gidaspow (1994) and classic closures are selected for interfacial momentum transfer terms. This model allows for the simulation of liquid-gas-solid flows with free-surfaces as well as bubbles and particles although it is unclear how the transition between bubbles and free-surface is enforced.

A liquid-gas-solid model based on a multifluid approach is also presented in Li and Zhong (2015). Mass and momentum balance equations are solved for each phase. These are coupled through interfacial transfer terms which represent the exchange of

momentum between the three phases. In the solid equation, kinetic granular theory and the works of Gidaspow et al. (1991) give a closure for unresolved terms. A k-ϵ model allows for the simulation of turbulence for continuous phases but no turbulence model is included for the solid dispersed phase. This model is adapted for dense flows where particle motion is not affected by turbulence. Thus restricting the possibilities of the approach.

A similar approach to the $N+2$ method can be found in Kihara and Okada (2023). This model relies on a VOF approach for the continuous structures and a granular approach for the dispersed solid inclusions. Particles interact with surrounding fluids through drag and fluid pressure and their turbulent energy is based on kinetic theory (Gidaspow et al., 1991). The particle shear stress and pressure are closed with expressions found in Lee et al. (2015). Compared to the $N+2$ model, it cannot simulate the presence of bubbles or the interaction between bubbles and particles. However, it can predict the behaviour of particles crossing liquid-gas interfaces and - most importantly - the behaviour of densely packed particles.

Compared to Lagrangian approaches, the dense regime is easier to model with multifluid techniques because they are not restricted by the number of particles. This illustrates one of the most important advantage of such a method. On the other hand, the gain in computing time is usually balanced by a loss in accuracy and an increase in modelling requirements. Additionally, the models are very sensitive and require extreme care to give consistent results. Figure 1.10 shows the differences between discrete particle and continuous methods. In Eulerian methods the solid phase is represented as a continuous field whereas in discrete particle models, each particle must be represented and tracked during the simulation. The models described above are similar to the second type of model developed during my work at EDF.

Figure 1.10: Differences in modelling between multifluid (left) and multifluid-Lagrangian tracking (right) methods for liquid-gas-solid flows. Cases presented in chapter 5.

1.3.4 Mixture models

A mixture model is described in Kuang et al. (2012) where a conservation equation of momentum is solved for a mixture field m representing the entire liquid-gas-solid flow.

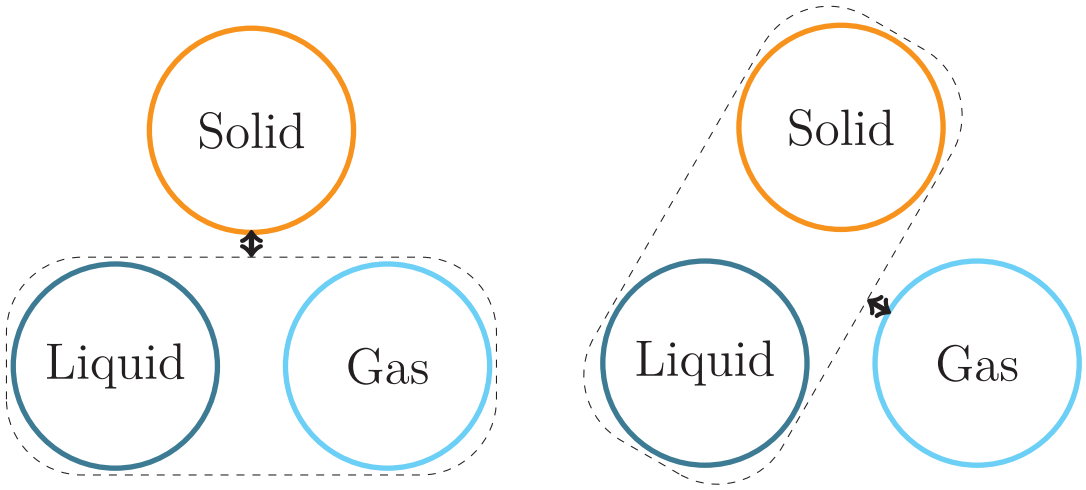

Figure 1.11: (left) liquid-gas mixture interacting with a solid phase. (right) liquid-solid mixture interacting with a gas phase. The arrows represent interface transfers. These typically include mass, momentum and energy.

A continuity equation is solved for each phase and an additional set of equation is solved for determining the drift velocities between the dispersed phase and water Zaichik (1999). Turbulence is accounted for with a Reynolds stress model and solid closures take into account collisions and kinetic viscosity. This model is applied to the simulation of flows in cyclones and specifically the determining of the effect of particles on the device efficiency. The advantage of this method is its low computational cost compared to multifluid models, DEM approaches or particle resolved simulations, its accuracy is lower but it remains a tool of choice for industrial settings or real-time simulations. Similarly to multifluid models, they require extensive modelling to accurately represent reality. Naturally, it is also possible to consider such a mixture for two out of the three phases present and use well-known two-phase flow modelling approach for the mixture and the remaining phase. Figure 1.11 illustrates the mixing process for two different cases. The diagram on the left shows a liquid gas mixture interacting with the solid phase and the right one shows a liquid-solid mixture interacting with a gas phase. Depending on the situation, these two simplifications can be more than enough.

1.3.5 Simplified interaction models

For simple cases with extensive experimental data validating such hypothesis, some inter-phase interactions can be neglected and two-phase flow models used without any addition accounting for the third phase. For example, for free-surface flows without aeration, with particles transported by the liquid phase only, two independent two-phase flow models without further modelling can be used instead of a complex three-phase flow model. In figure 1.12, all the possible interactions are illustrated on the left diagram; while, in the right one, the interaction between solid and gas is neglected.

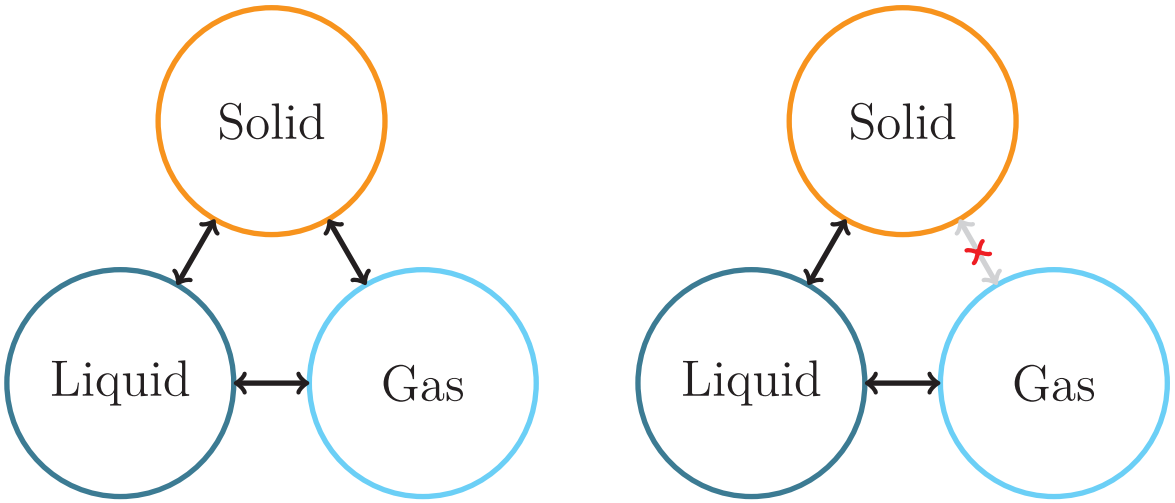

Figure 1.12: (left) Diagram illustrating all the possible momentum transfers. (right) The gas-solid interaction is neglected. The arrows represent interface transfers. These typically include mass, momentum and energy.

1.4 Structure of the manuscript

The main goal of the manuscript is to present two new modelling frameworks for liquid-gas-solid flows and to apply them to academic as well as industrial scenarios in order to show their potential in tackling real-life configurations. The work starts with the description of current two-phase flow models on which we base our developments in chapter 2. The Lagrangian stochastic and the Eulerian velocity moments method are presented along with a thorough discussion on the validity of certain stochastic models. The numerical framework of neptune_cfd is presented at the end of this chapter. Chapter 3 focuses mainly on presenting the two three-phase flow models developed during the thesis: the Lagrangian stochastic and hybrid Eulerian with multiple carrier fields. This chapter is also an opportunity to present all ad-hoc modifications carried out in neptune_cfd to make the new models compatible with several other modules of the software. Finally, a particle deposition model is introduced and compared with experimental data for the Lagrangian stochastic and hybrid Eulerian models. In chapter 4, we present the air entrainment process, an important phenomenon in the experimental cases explored during the thesis. The mechanisms of air entrainment are presented before introducing a new model to take it into account in neptune_cfd. The chapter also includes a comparison to experimental data from selected air entrainment models and experimental setups. The final chapter 5 is a compilation of all the experimental setups used to test the accuracy of our models. Several bubble columns loaded with particles are explored before tackling the LNHE experiments of impacting and submerged particle loaded jets. The final section of the final chapter is devoted to the study of the integral case motivating the thesis: the particle loaded jets in the scaled down reactor building during a loss of coolant scenario. Conclusion and outlook bring the manuscript to an end.

2 | General two-phase flow models

In this chapter, we introduce the two-phase flow modelling approaches from which the liquid-gas-solid models will be developed in chapter 3. This bedrock will clarify the choices and highlight the challenges encountered when adapting them to the more complex multi-phase case. The first two-phase method is the Lagrangian stochastic approach. A framework where point particles are introduced in the domain and their trajectory is computed through a set a stochastic and ordinary differential equations (Haworth and Pope, 1986; Thomson, 1987; Reynolds and Cohen, 2002; Sommerfeld, 2017). The second method - the Eulerian multifluid model - consists in deriving the set of conservation equations of mean quantities for a fluid from the local instantaneous equilibrium (Delhaye, 1974; Kataoka, 1985; Ishii and Hibiki, 2011) and the evolution equations for dispersed inclusions in fluids (bubbles, droplets or solid particles) from the velocity moment method and the Lagrangian closures. The conservation equations for moments of the probability density function describing the set of particles can be obtained in a general manner (Simonin, 2000). Then, Lagrangian equations are used to close the moments equations. Solving these leads to modelling the behaviour of particles evolving in a fluid as a continuous phase. At the end of the chapter, some details about the numerical solver neptune_cfd and its modelling approaches are presented.

2.1 Lagrangian modelling of solid particles in fluid flows

2.1.1 General Lagrangian framework

A Lagrangian framework is used when dealing with systems of discrete particles. It consists in considering every solid inclusion individually and following their trajectory with a momentum balance equation. There are two main classes of methods, the first is the particle resolved simulations, usually coupled with a direct numerical simulation for the continuous phase (PR-DNS), with either a body-conforming mesh (Hu et al., 2001) or an immersed boundary method (Uhlmann, 2005). These approaches are very accurate since the fluid stresses are simulated around the particles but require a lot of computing time. As of today, there has been simulations with around at most 1×10^4 particles (Picano et al., 2015; Horne and Mahesh, 2019). When more particles need to be simulated, PR-DNS methods become too expensive and Euler-Lagrange (EL) methods are used instead. They rely on the point particle hypothesis, models for the interaction forces between the particles and the surrounding fluid and tracking each individual particle by solving balance equations 2.1. This requires the particles to be sufficiently small compared to the fluid Taylor scale and requires the use of a drag

model which may be challenging depending on the configurations. Since they do not require the mesh to be as fine as in particle resolved simulations, more particles can be introduced in the system. In Capecelatro and Desjardins (2013), simulations with around 1×10^7 particles are performed.

If $\mathbf{F}$ is the total force acting on a particle per unit mass, $\mathrm{d}/\mathrm{d}t$ is an increment along the particle trajectory and $(\mathbf{x_p}, \mathbf{u_p})$ are the particle position and velocity, the evolution equation for one particle reads in a standard reference frame:

$$\begin{aligned} \frac{\mathrm{d}x_{p,i}}{\mathrm{d}t} &= u_{p,i}(t) \\ \frac{\mathrm{d}u_{p,i}}{\mathrm{d}t} &= F_i(t) \end{aligned} \tag{2.1}$$

The external force term may include hydrodynamic forces such as drag, lift, added mass or Basset forces expressed as in Maxey and Riley (1983); Gatignol (1983) but it can also include external forces such as gravity or electromagnetic forces (Boutsikakis et al., 2022). Models for $\mathbf{F}$ rely on the underlying fluid resolution. From DNS to RANS simulations, the modelling required increases. In Yeung and Pope (1988); Zahtila et al. (2023), a DNS is performed and no model is needed to compute the particle trajectory. In LES, a filtered velocity which contains some information about velocity fluctuations is available. In cases where the particle inertia is large, the subgrid scale turbulence seems to have little to no effect on the particle trajectory (Kuerten, 2016). Justifying the use of the filtered velocity only in the particle behaviour in Wang and Squires (1996*a*); Kasper et al. (2019). In the case where subgrid scale becomes important, either a stochastic model is added (Kuczaj and Geurts, 2006), modelling from scratch the subgrid scale fluctuation, or a new component is added to the fluid velocity effectively retrieving the unfiltered quantity (Shotorban and Mashayek, 2005). When coupled to a RANS simulation, most of the velocity fluctuation information is lost and it cannot be accessed directly in the particle equations. This requires a modelling of the turbulence at the position of the particle, usually named stochastic modelling due to its random character.

Lagrangian point particle modelling also enables the tracking of other particle characteristics. In some more advanced models where combustion is important, particle diameter, density or temperature can be included in the particle evolution equations. As long as closure equations are defined for each new variable, their evolution equations on particle trajectory can be determined. When their behaviour requires the modelling of a random fluctuating part, stochastic equations may be considered for these variables as well.

2.1.2 Overview of stochastic models

Initially, stochastic models were used in atmospheric science to predict the dispersion of fluid elements in single phase flow (Obukhov, 1959; Haworth and Pope, 1986). Their goal was to reconstruct the fluid velocity from the underlying fluid simulation quantities and use it in the particle momentum equation in the case of low inertia solid particles. There are many approaches, the most basic one consists in using the mean fluid velocity only in the particle equation, effectively neglecting the impact of turbulence on the particle. It can be appropriate for large dense particles not influenced by turbulent flows. However, in most scenarios, this assumption is not verified.

In the following paragraphs, for brevity, drag is the only force acting on the particles. For more details on this hypothesis, see Thomson (1987). A more advanced model consists in adding a random fluctuation to the fluid velocity increment along a particle trajectory $\mathbf{u_{f@p}}$ (Simonin et al., 1993; Minier and Peirano, 2001; Iliopoulos et al., 2003; Arcen and Tanière, 2009).

$$\delta u_{f@p,i} = A_i \delta t + B_{ij} \delta W_j \tag{2.2}$$

$$\delta u_{p,i} = \frac{u_{f@p,i} - u_{p,i}}{\tau_p} \delta t \tag{2.3}$$

Where τ_p is the particle relaxation time in the fluid, A_i and B_{ij} are parameters of the model and δW_j is a random fluctuating term. This method includes turbulent information on the fluid velocity at the position of the particle through $\mathbf{u_{f@p}}$, used in the particle momentum equation 2.1. It is widely spread and there are many different expressions for A_i and B_{ij}. These may include specific terms to tackle the crossing trajectory effect Simonin et al. (1993); Minier and Peirano (2001) or the effects of boundary layers Bocksell and Loth (2006); Dehbi (2008). In some cases, it is also possible to express the stochastic equations in terms of normalized quantities Sikovsky (2015, 2016). The normalization process allows for the correct particle behaviour to be predicted when turbulence is no longer homogeneous. Thus improving the deposition prediction for low stokes numbers.

Another modelling option would be to consider the fluid acceleration at the position of the particle $\mathbf{a_{f@p}}$ and to add a fluctuating term in its increment along the particle trajectory (Reynolds, 1999).

$$\delta a_{f@p,i} = A'_i \delta t + B'_{ij} \delta W_j \tag{2.4}$$

$$\delta u_{f@p,i} = a_{f@p,i} \delta t \tag{2.5}$$

This formulation reproduces the exact fluid auto-correlation function even for low Stokes number particles. This addition has an impact mainly when considering two-way coupled simulations. In fact, the reverse coupling is mainly the difference between the fluid-particle covariance and the fluid variance terms which are very sensitive at low Stokes number. However, this model is strictly limited to homogeneous.

Finally, it is also possible to include the random fluctuating term directly in the particle equation of motion as it is done in Reeks (1991). There is no need to model the fluid velocity at the position of the particle which helps avoiding problems related to crossing trajectory effects but the fluctuating part in the particle equation is harder to model.

Two-way coupling (particle effect on the fluid) and four-way coupling (particle-particle interaction) are also routinely included in Lagrangian stochastic models (Eaton, 2009; Zeren et al., 2010; Vreman, 2016). Since they will not be studied in the new Lagrangian model suggested, we are not detailing them further. However, for future works where these phenomenons are considered, these references may provide valuable information.

2.1.3 Langevin stochastic equation for the fluid velocity seen by the particle

The main goal of the current and following sections is to introduce the Langevin stochastic models for the fluid velocity seen by particles in a single phase in order to introduce the work carried out during the thesis for particles evolving in a multi-phase flow. To clarify those sections, let us start by defining some preliminary notations and conventions. A fluid element represents an infinitely low inertia particle. The fluid velocity at the position of the element is defined as $u_{f@p,i}(t) = u_{f,i}(x_p(t), t)$. This notion introduces the following notations:

$$\begin{array}{lll} u''_{f,i}(\mathbf{x},t) = u_{f,i}(\mathbf{x},t) - U_{f,i}(\mathbf{x},t) & & \langle u''_{f,i}\rangle = 0 \\ u_{f@p,i}(t)'' = u_{f@p,i}(t) - U_{f@p,i}(t) & \Longrightarrow & \langle u''_{f@p,i}\rangle = 0 \\ u_{f@p,i}(t)' = u_{f@p,i}(t) - U_{f,i}(\mathbf{x_p}(\mathbf{t}),t) = u'_{f,i}(\mathbf{x_p}(\mathbf{t}),t) & & \langle u'_{f@p}\rangle = V_{f,i}(\mathbf{x},t) \\ u''_{p,i}(t) = u_{p,i}(t) - U_{p,i}(t) & & \langle u''_{p,i}\rangle = 0 \end{array} \tag{2.6}$$

Where $\mathbf{V_f}$ is the drift velocity and the second order velocity variance and covariance tensors are defined below.

$$\begin{array}{l} R_{f,ij}(\mathbf{x},t) = \langle u''_{f,i}u''_{f,i}\rangle(\mathbf{x},t) \\ R_{f@p,ij}(\mathbf{x},t) = \langle u''_{f@p,i}u''_{f@p,j}\rangle(\mathbf{x},t) \\ \langle u'_{f@p,i}u'_{f@p,j}\rangle(\mathbf{x},t) = R_{f@p,ij}(\mathbf{x},t) + V_{f,i}(\mathbf{x},t)V_{f,j}(\mathbf{x},t) \\ R_{fp,ij}(\mathbf{x},t) = \langle u''_{f@p,i}u''_{p,j}\rangle(\mathbf{x},t) = \langle u'_{f@p,i}u''_{p,j}\rangle(\mathbf{x},t) \\ R_{p,ij}(\mathbf{x},t) = \langle u''_{p,i}u''_{p,j}\rangle(\mathbf{x},t) \end{array} \tag{2.7}$$

The Langevin equation used to predict the fluid velocity at the position of the particle is presented in equation 2.8 and is inspired from the work of Tanière et al. (2010). It takes the following form:

$$\delta u_{f@p,i} = A_{f@p,i}\delta t + B_{f@p,ij}\delta W_{f,j} \tag{2.8}$$

Where $A_{f@p}$ and $B_{f@p,ij}$ are the drift and diffusion tensors - they are function of time and the particle state vector. The choice for these parameters defines the stochastic model. δW_f is the increment of a vector-valued Wiener process with independent components which satisfies:

$$\begin{array}{ll} \forall \tau > 0, & \langle \delta W_{f,i}(t) W_{f,j}(t+\tau)\rangle = 0 \\ & \langle \delta W_{f,i}(t)\delta W_{f,j}(t)\rangle = \delta t \delta_{ij} \end{array} \tag{2.9}$$

According to Thomson (1987); Minier et al. (2014); Tanière and Arcen (2016), the choice of the two parameters is restricted. Some properties have to be verified in order to ensure consistency. However, since the listed properties vary depending on the authors, it is unclear which to choose for our models. Let us first review the guidelines here, we will continuously come back to them when defining a new model to make sure they verify them.

1. The drift and diffusion tensors should be written in correct tensor notation and their expression should verify the usual invariance principles - Galilean and extended Galilean.

2. The expressions given for A and B should be functions of known variables.

3. Low inertia limit: In the limit of infinitely low inertia particles, the behaviour should reflect the one of the fluid. According to Thomson (1987); Minier et al. (2014), this is equivalent to the conservation of fluid elements concentration distribution.

4. Large inertia limit: In the limit of infinitely large inertia - particles stand still or have no interaction with the turbulence - the statistics seen by the particle should match those of the carrier fluid.

5. The predicted turbulent kinetic energy with the fluid velocity seen equation should give appropriate results in analytical situations. In homogeneous isotropic turbulence and decaying turbulence the behaviour of particles should match known results (Batchelor, 2000).

6. Resulting models for drift velocity should match existing models or be justified with an appropriate model (Wallis, 2020).

7. The model introduced should be consistent with Equilibrium Eulerian approaches (Balachandar and Eaton, 2010).

We stress the presence of item 4 in the previous list. This criteria is not present in the guidelines from Thomson (1987) or Minier et al. (2014) but it seems to be the justification for the addition to the stochastic model made in Arcen and Tanière (2009). We decide to include this requirement as well when developing a new stochastic model. It seems a natural addition since infinitely inertial particles do not interact with the fluid turbulence. Therefore, because their impact on the fluid is neglected, the statistics seen by the particle set should match the Eulerian statistics. The particles see exactly what a set of cell centres would in an Eulerian framework.

It is possible to use the fluid conservation of momentum equation to re-write the Langevin equation on the fluid velocity seen by the particle in terms of fluctuations. This is not recommended when dealing with two-way coupling (Minier et al., 2014) since it tends to make things more complicated. However, since we are only focused on one-way coupling, it can be helpful to write equation 2.8 in terms of fluctuating fluid velocity seen by the particle $u''_{f@p,i}$. It will also turn out to be extremely useful when several fluids interact with the particles (see section 3.1).

The fluid momentum conservation equations for incompressible flows reads:

$$\frac{\partial U_{f,i}}{\partial t} + U_{f,j}\frac{\partial U_{f,i}}{\partial x_j} = -\frac{1}{\rho_f}\frac{\partial P_f}{\partial x_i} + \frac{\partial}{\partial x_j}\left(\frac{1}{\rho_f}T_{f,ij} - R_{f,ij}\right) \tag{2.10}$$

Where $U_{f,i}$ is the fluid mean velocity, P_f is its pressure, ρ_f its density and $T_{f,ij}$ and $R_{f,ij}$ are the mean dissipative part of the fluid stress tensor and the Reynolds tensor. The increment of fluid velocity seen by the particle along its trajectory can be written, by definition of the fluctuations (equation 2.6), as:

$$\begin{aligned}\delta u'_{f@p,i} &= A_{f@p,i}\delta t + B_{f@p,ij}\delta W_{f,j} - \delta U_{f,i} \\ &= A_{f@p,i}\delta t + B_{f@p,ij}\delta W_{f,j} - \frac{\partial U_{f,i}}{\partial t}\delta t - u_{p,j}\frac{\partial U_{f,i}}{\partial x_j}\delta t \\ &= \left(A_{f@p,i} - \frac{\partial U_{f,i}}{\partial t} - U_{f,j}\frac{\partial U_{f,i}}{\partial x_j} + (U_{f,j} - u_{p,j})\frac{\partial U_{f,i}}{\partial x_j}\right)\delta t + B_{f@p,ij}\delta W_{f,j}\end{aligned} \tag{2.11}$$

There exist many models for $A_{f@p,i}$ in the literature which can be written in terms of fluctuating fluid velocity seen by the particle (Simonin et al., 1993; Minier and Peirano, 2001; Arcen and Tanière, 2009). We write down a general Langevin equation which reduces down to known model depending on the parameter H_i (equation 2.13). Since the model in Minier and Peirano (2001) cannot be written from the general form, we write it down as well (equation 2.12).

$$\delta u'_{f@p,i} = \left[(\langle u_{p,j}\rangle - u_{p,j})\frac{\partial U_{f,i}}{\partial x_j} + G_{f@p,ij}u'_{f@p,j} + \frac{\partial\langle u''_{f,i}u''_{f,j}\rangle}{\partial x_j}\right]\delta t + B_{f@p,ij}\delta W_{f,j} \tag{2.12}$$

$$\delta u'_{f@p,i} = \left[(G_{f@p,ij} - \frac{\partial U_{f,i}}{\partial x_j})u'_{f@p,j} + H_i\right]\delta t + B_{f@p,ij}\delta W_{f,j} \tag{2.13}$$

Where, if $H_i = \frac{\partial R_{fp,ij}}{\partial x_j}$, we get the model from Arcen and Tanière (2009) and if $H_i = \frac{\partial R_{f,ij}}{\partial x_j}$, we get the model from Simonin et al. (1993). These three models, assuming the expression for $G_{f@p,ij}$, H_i and $B_{f@p,ij}$ are appropriate, verify the guidelines expressed in Thomson (1987) and Minier et al. (2014). However, only the model described by equation 2.13 with $H_i = \frac{\partial R_{fp,ij}}{\partial x_j}$ verifies the fourth criteria in the guidelines presented above. The three parameters are function of the Eulerian fields output from the N-Euler framework. In the most simple case, the fields value are taken at the centre of the cell the particle is in. For a sufficiently refined mesh, this method introduces a small interpolation error. However, for coarse grids, this kind of interpolation may introduce large errors in the computation. By using a P1 interpolation instead, it is possible to improve the behaviour of the model. However, the effect of such interpolation on the particle behaviour must be evaluated with care. Let us now detail the expressions for the two unclosed terms in these models. The expression for $G_{f@p,ij}$ can be found in the work from Csanady (1963).

$$G_{f@p,ij} = -\frac{1}{T^{L,*}_{f@p,j}}\delta_{ij} \tag{2.14}$$

Where $T^{L,*}_{f@p,i}$ is a modified time-scale which corresponds to the integral time scale of the velocity of the fluid seen. According to Csanady's theory, this integral time scale is related to the classic Lagrangian time scale through the following expressions:

$$T^{L,*}_{f@p,1} = \frac{T^L_f}{\sqrt{1 + \beta^2\frac{3|\mathbf{U_r}|^2}{2k}}} \tag{2.15}$$

$$T^{L,*}_{f@p,2} = T^{L,*}_{f@p,3} = \frac{T^L_f}{\sqrt{1 + 4\beta^2\frac{2|\mathbf{U_r}|^2}{3k}}} \tag{2.16}$$

Where $\beta = T_f^L/\tau_{p,f}$ is the ratio of the Lagrangian time scale to the Eulerian time scale, k is the fluid turbulent kinetic energy and $\mathbf{U_r}$ is the relative difference between the particle velocity and the surrounding fluid element velocity. For further computations, we also define $G_{fp,ij}$:

$$G_{fp,ij} = G_{f@p,ij} - \frac{\partial U_{f,i}}{\partial x_j} \tag{2.17}$$

The expression for the diffusion matrix $B_{f@p,ij}$, which closes the stochastic model, is obtained from considering subsequent simple cases and assuming that the behaviour of particles in decaying isotropic turbulence and homogeneous isotropic turbulence are coherent with results from Batchelor (2000).

$$B_{f@p,ij} = \sqrt{\langle \epsilon_f \rangle \left(C_0 b_i \frac{\tilde{k_f}}{k_f} + \frac{2}{3}(b_i \frac{\tilde{k_f}}{k_f} - 1) \right) \delta_{ij}} \tag{2.18}$$

Where ϵ_f is the fluid turbulent kinetic energy dissipation term, $b_i = \frac{T_f^L}{T_{f@p}^{L,*}}$ is the ratio between the Lagrangian time scale and the fluid seen velocity integral time scale and $\tilde{k_f}$ is the fluid turbulent kinetic energy weighted by Csanady's coefficients. This allows for the compensation of the anisotropy in the fluid velocity seen time scale.

$$\tilde{k_f} = \frac{\sum_i b_i \langle u_{f,i}'^2 \rangle}{\sum_i b_i} \tag{2.19}$$

The stochastic models are closed with the expressions of the drift and diffusion terms. To complete the model, an expression must be provided for the particle relaxation time τ_p. It can be obtained from the external forces acting on the particle. If drag is the only interaction force, it reads:

$$\tau_p = \frac{\rho_p}{\rho_f} \frac{4 d_p}{3 C_D \| \mathbf{u_{f@p}} - \mathbf{u_p} \|} \tag{2.20}$$

Where ρ_p and ρ_f are the particle and fluid densities, d_p is the particle diameter, C_D is the drag coefficient and $\mathbf{u_{f@p}}$ and $\mathbf{u_p}$ are the particle and fluid seen velocity vectors. The drag coefficient C_D depends on the type of particles and fluids considered. A detailed expression is given in section 3.2.4. The equations for the increment of particle velocity and fluid velocity seen by the particle represent a possible closure for the probability density function describing the ensemble of particles. In the following section, we derive the evolution equation for the PDF and demonstrate how to get Eulerian moment equations from it. The latter can help showing the coherence of the Lagrangian models but also enables the introduction of a new Eulerian model.

2.1.4 The probability density function formalism

The state of an ensemble of particles is described by a vector in the phase space $\mathbf{H}$. The one-particle probability density function (PDF) is a function f_p defined on the phase

space for which $f(\mathbf{c_p}, \mathbf{c_f}; \mathbf{x}, t)\delta\mathbf{c_p}\delta\mathbf{c_f}\delta\mathbf{x}$ is the mean number of particles with a centre of mass $\mathbf{x_p}$ in the volume $\Omega = \{\mathbf{x}, \mathbf{x} + \delta\mathbf{x}\}$ and with a velocity $\mathbf{u_p} \in \{\mathbf{c_p}, \mathbf{c_p} + \delta\mathbf{c_p}\}$ and a fluid velocity seen $\mathbf{u_{f@p}} \in \{\mathbf{c_f}, \mathbf{c_f} + \delta\mathbf{c_f}\}$ at time t. Along with the PDF, the number density function $n_p(\mathbf{x}, t)$ defines the probable number of particles at time t in the volume $\Omega = \{\mathbf{x}, \mathbf{x}+\delta\mathbf{x}\}$. By definition, the number density function can be written in terms of the probability density function.

$$n_p(\mathbf{x}, t) = \int f_p \mathrm{d}\mathbf{c_p}\mathrm{d}\mathbf{c_f} \tag{2.21}$$

According to common practice, f_p is solution of the following Liouville evolution equation (Simonin, 1996, 2000).

$$\begin{aligned}\frac{\partial f_p}{\partial t} + \frac{\partial}{\partial x_j}\left(c_{p,j} f_p\right) + \frac{\partial}{\partial c_{p,j}}\left[\left\langle \frac{\mathrm{d}u_{p,j}}{\mathrm{d}t} | \mathbf{u_p}(t) = \mathbf{c_p}, \mathbf{u_{f@p}}(t) = \mathbf{c_f}, \mathbf{x_p}(t) = \mathbf{x} \right\rangle f_p\right] \\ + \frac{\partial}{\partial c_{f,j}}\left[\left\langle \frac{\mathrm{d}u_{f@p,j}}{\mathrm{d}t} | \mathbf{u_p}(t) = \mathbf{c_p}, \mathbf{u_{f@p}}(t) = \mathbf{c_f}, \mathbf{x_p}(t) = \mathbf{x} \right\rangle f_p\right] \\ = \left(\frac{\partial f_p}{\partial t}\right)_{\text{coll}}\end{aligned} \tag{2.22}$$

Where $a \mapsto \langle a | \mathbf{u_p}(t) = \mathbf{c_p}, \mathbf{u_{f@p}}(t) = \mathbf{c_f}, \mathbf{x_p}(t) = \mathbf{x}\rangle$ is the conditional average of a knowing $\mathbf{u_p}(t) = \mathbf{c_p}$, $\mathbf{u_{f@p}}(t) = \mathbf{c_f}$ and $\mathbf{x_p}(t) = \mathbf{x}$; and $\left(\frac{\partial f_p}{\partial t}\right)_{\text{coll}}$ is the variation in time of the PDF due to collisions between particles. In the following derivations, the equalities as well as some arguments will be neglected in the name of clarity. The arguments of the probability density function are dropped for similar reasons. From equation 2.22, it is possible to obtain the evolution equation for moments of f_p by multiplying by ψ_p, a function of the phase space variables, and integrating over the phase space variables. By also assuming the mass of particles is constant, this leads to equation 2.23 (Swailes et al., 1998).

$$\begin{aligned}\frac{\partial}{\partial t}(n_p m_p \langle\psi_p\rangle) + \frac{\partial}{\partial x_j}(n_p m_p \langle u_{p,j}\psi_p\rangle) = n_p m_p \langle\langle \frac{\mathrm{d}u_{p,i}}{\mathrm{d}t} | \mathbf{c_p}, \mathbf{c_f}\rangle \frac{\partial \psi_p}{\partial c_{p,j}}\rangle \\ + n_p m_p \left\langle \langle \frac{\mathrm{d}u_{f@p,i}}{\mathrm{d}t} | \mathbf{c_p}, \mathbf{c_f}\rangle \frac{\partial \psi_p}{\partial c_{f,j}} \right\rangle + n_p \mathbb{C}(m_p u_{p,i})\end{aligned} \tag{2.23}$$

Where m_p is the constant mass of a particle and $\mathbb{C}$ includes the effects of particle-particle interactions.

$$\mathbb{C}(m_p u_{p,i}) = \int \psi_p \left(\frac{\partial f_p}{\partial t}\right)_{\text{coll}} \mathrm{d}\mathbf{c_p}\mathrm{d}\mathbf{c_f} \tag{2.24}$$

By replacing ψ_p with the appropriate function of the fluid velocity seen by the particle, it is possible to obtain evolution equations for the drift velocity $\mathbf{V_f}$ defined in equation 2.6 and the fluid velocity variance $R_{f@p,ij}$ seen by the particle. Then, in the limit cases identified above (low and large inertia particles), these equations are simplified and show the consistencies or the issues of the stochastic model. The

evolution equation for the drift velocity can be obtained by replacing ψ_p by $c_{f,i}$ and then subtracting the evolution equation for the mean fluid velocity $U_{f@p,i}$ seen by the particles.

$$n_p \frac{\partial V_{f,i}}{\partial t} + n_p U_{p,j} \frac{\partial V_{f,i}}{\partial x_j} = -\frac{\partial}{\partial x_j}(n_p R_{fp,ij}) + n_p H_i + n_p \left(G_{f@p,ij} - \frac{\partial U_{f,i}}{\partial x_j} \right) V_{f,j} \quad (2.25)$$

The evolution equation for the fluid velocity variance $R_{f@p,ij}$ seen by the particle is obtained by replacing ψ_p by $c_{f,i}c_{f,j}$ and then subtracting the evolution equation for the mean fluid kinetic energy $U_{f@p,i}U_{f@p,j}$ seen by the particles. The latter can be expressed in terms of the evolution equation for the mean fluid velocity seen by the particles.

$$\begin{aligned} \frac{\partial}{\partial t}(n_p R_{f@p,ij}) + \frac{\partial}{\partial x_k}(n_p U_{p,k} R_{f@p,ij}) = & -\frac{\partial}{\partial x_k}(n_p \langle u''_{f@p,i} u''_{f@p,j} u''_{p,k} \rangle) \\ & - n_p R_{fp,ik} \frac{\partial V_{f,j}}{\partial x_k} - n_p R_{fp,jk} \frac{\partial V_{f,i}}{\partial x_k} \\ & + n_p G_{fp,ik} R_{f@p,jk} + n_p G_{fp,jk} R_{f@p,ik} \\ & + n_p B_{f@p,ik} B_{f@p,jk} \end{aligned} \quad (2.26)$$

In equation 2.26, the model for H_i appears implicitly in the terms with the drift velocity $\mathbf{V_f}$. The terms on the right-hand side represent variance transport by fluctuation of the fluid seen, turbulent production due to mean drift velocity gradients, coupling terms and a pressure-velocity contribution.

2.1.5 Standard analytic cases

The main goals of this section are, on the first hand, to introduce verification cases to show the correct behaviour of the stochastic models and, on the other hand, to suggest a new stochastic model, compatible with all the guidelines described above. These cases have also been used to verify the good behaviour of subsequent new liquid-gas-solid models developed during the thesis.

Fluid elements dispersion in homogeneous isotropic turbulence

The first analytic case consists in a set of fluid elements (*ie* particles of infinitely small inertia), initially located at the centre of a periodic, cubic domain, dispersing in homogeneous, isotropic turbulence initialised with $u_f = 0\,\mathrm{m\,s^{-1}}$, $k_f = 0.1\,\mathrm{m^2\,s^{-2}}$ and $\epsilon_f = 1\,\mathrm{m^2\,s^{-3}}$. The speed at which the particles disperse should match the analytical results found in Batchelor (2000).

$$\begin{aligned} t \to 0 \quad &\Longrightarrow \langle y_p(t) y_p(t) \rangle = \langle u_p^2 \rangle t^2 \\ t \to \infty \quad &\Longrightarrow \langle y_p(t) y_p(t) \rangle = 2 \langle u_p^2 \rangle \tau_{p,f} t \end{aligned} \quad (2.27)$$

Figure 2.1 shows the results obtained with three degrees of mesh refinement with the original model. The model gives satisfactory results with a sufficiently fine mesh. Those obtained with a coarser mesh are still reasonable but it is more difficult to

define the initial position of the particle set. Hence the differences in results between the meshes.

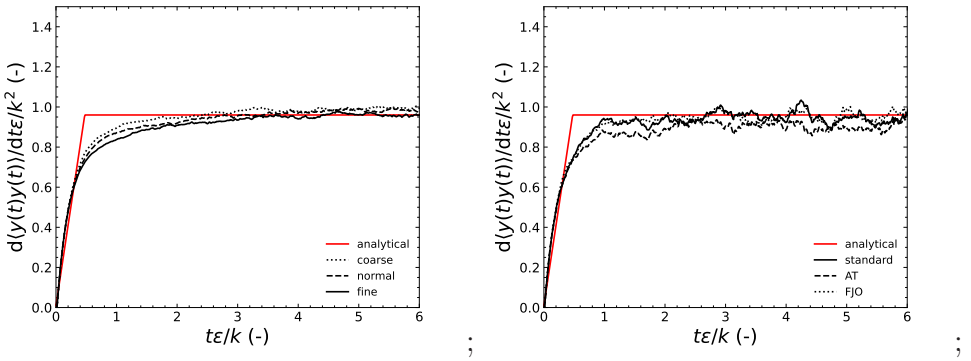

Figure 2.1: (left) Mesh sensitivity with the standard stochastic model. (right) Comparison between the standard model Simonin et al. (1993), the model from Arcen and Tanière (2009) (AT) and a new model with $H_i = \frac{\partial}{\partial x_j}(R_{f,ij} + R_{fp,ij} - R_{f@p,ij})$ (FJO).

Figure 2.1 also shows the results obtained with the fine mesh with different stochastic models. Results are still satisfactory with the other stochastic equations.

Fluid elements in a mixing layer

This second case consists in the simulation of a set of fluid elements in a mixing layer formed between two uniform parallel streams of different flow velocities. The goal of the case is to verify the *well-mixed condition* and check that Lagrangian statistics (the mean particle velocity and mean particle velocity variance) match the Eulerian quantities in the low inertia limit. This case has been used for verification purposes before, for more details on it, see Bahlali et al. (2020).

Numerical simulations of the fluid flow are carried out in a rectangular domain of dimensions $10\,\mathrm{m} \times 0.8\,\mathrm{m} \times 0.004\,\mathrm{m}$. The left hand side boundary face is an inlet, the right hand side boundary face is an outlet and all the other boundary faces are symmetries. In the inlet, if $y < 0.4\,\mathrm{m}$, the fluid velocity is $U_m = 2\,\mathrm{m\,s^{-1}}$; if $y > 0.4\,\mathrm{m}$, the fluid velocity is $U_M = 3\,\mathrm{m\,s^{-1}}$. It is common practice for this case (Champagne et al., 1976; Pope, 2000) to define the following quantities to highlight the self-similar character of the flow:

$$\delta = y_{0.9} - y_{0.1} \tag{2.28}$$

$$\xi = \frac{y}{\delta} \tag{2.29}$$

$$f(\xi) = \frac{U - U_c}{U_s} \tag{2.30}$$

Where $U_c = \frac{1}{2}(U_m + U_M)$, $U_s = U_M - U_m$ and δ is the characteristic length of the flow. Figure 2.2 sums up the different quantities defined above.

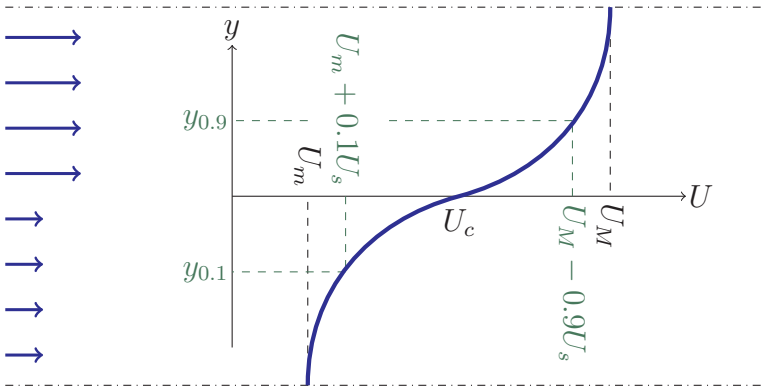

Figure 2.2: Sketch describing the considered mixing layer case. U represents the flow velocity.

When the simulation reaches a steady-state, fluid elements respecting the fluid mass flow are injected in the domain. Then, a second steady-state is reached. From that point on, Lagrangian quantities are averaged to achieve statistical convergence. These quantities include the particles average velocity, their velocity variance and their concentration. Initially, the results are shown with the stochastic model $H_i = \frac{\partial R_{fp,ij}}{\partial x_j}$. The results obtained with $H_i = \frac{\partial}{\partial x_j}(R_{f,ij} + R_{fp,ij} - R_{f@p,ij})$ are shown to give better results in figure 2.5. The introduction of this new model was driven by the lack of consistency between the Eulerian quantities and Lagrangian statistics in the second-order moments in the large inertia limit with the standard model. In figure 2.3, we ensure that the stationary fluid flow reached is coherent with experimental results from Champagne et al. (1976) and that it is self-similar.

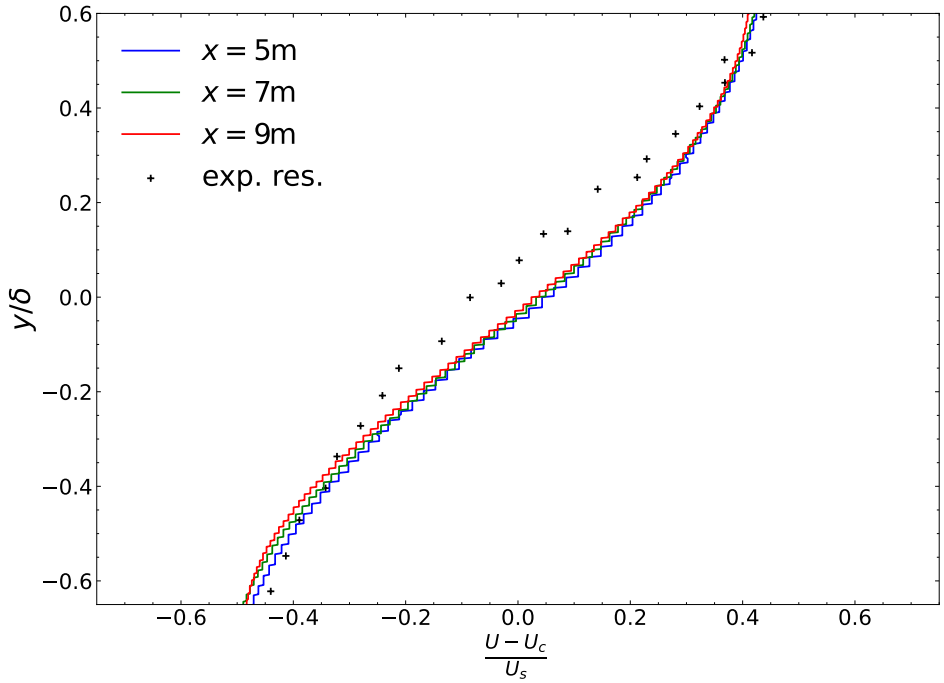

Figure 2.3: Fluid axial velocity for $x = 5\,\text{m}$, $7\,\text{m}$ and $9\,\text{m}$. Experimental results can be found in Champagne et al. (1976)

The *well-mixed condition* is verified if the particle concentration is constant in the

domain when the steady state is reached. Figure 2.4 shows that this condition is verified. Near the inlet we can see a slight increase of particle concentration due to the boundary condition. Once the particles are sufficiently well mixed together, they are uniformly distributed inside the domain.

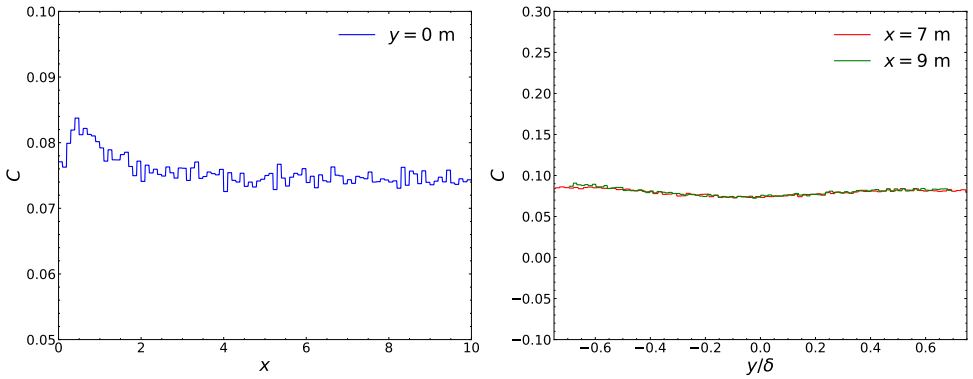

Figure 2.4: Particle concentration on an horizontal profile and two vertical profiles.

Eventually, we check the consistency between the Lagrangian and Eulerian turbulent quantities. The averaged particle velocity variance should match the Reynolds tensor components computed with the RSM turbulence model (R_{ij}-ϵ SSG model). Figure 2.5 shows that the Lagrangian stochastic model gives satisfactory results. However, there are still some discrepancies between the two approaches. In the Eulerian computations, the two components R_{YY} and R_{ZZ} are different (as they are in experimental results). However, with the standard stochastic model and the model found in Arcen and Tanière (2009), these two components are equal even though they are not with the new stochastic model introduced. The new model correctly predicts the difference between the two components mentioned above and it gives a better prediction for all the components altogether.

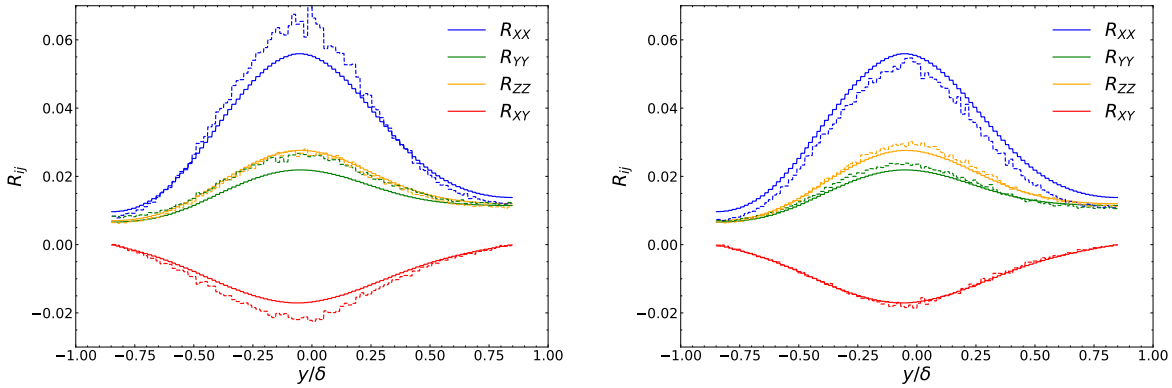

Figure 2.5: Reynolds components computed with the Lagrangian model (dashed lines) and with the Eulerian model (solid lines). (left) Stochastic model described by $H_i = \frac{\partial R_{fp,ij}}{\partial x_j}$ and new stochastic model (right).

By writing down the evolution equation for the drift velocity $V_{f,i}$ and the fluctuating

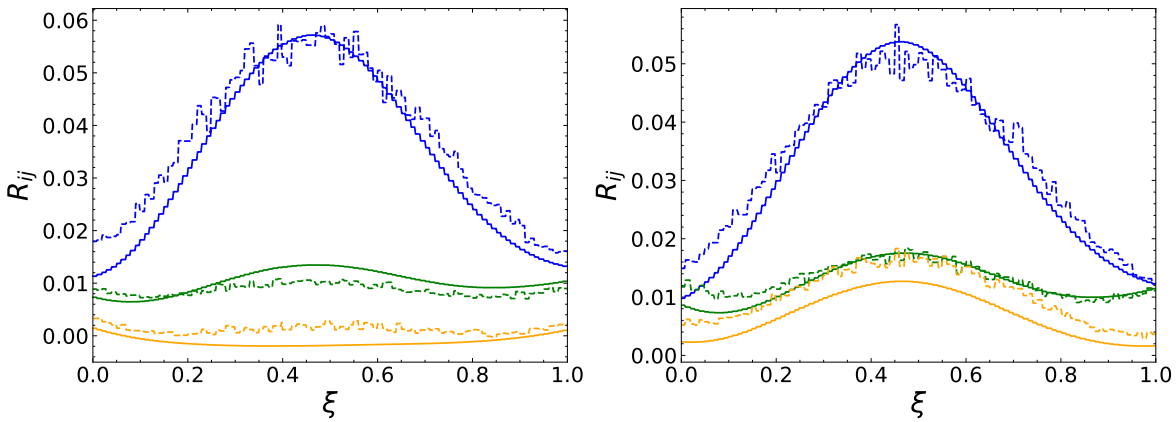

Figure 2.6: Comparison of $R_{f,ij}$ (solid lines) and $R_{f@p,ij}$ (dashed lines) in a rotated mesh. On the left $\theta_r = 20°$ and on the right $\theta_r = 40°$.

fluid velocity seen by the particle variance $R_{f@p,ij}$, it is possible to understand why these two models give different results. In a stationary state, these equations reduce down to:

$$n_p U_{p,j} \frac{\partial V_{f,i}}{\partial x_j} = -\frac{\partial}{\partial x_j}(n_p R_{fp,ij}) + n_p H_i + n_p G_{fp,ij} V_{f,j} \tag{2.31}$$

and,

$$\begin{aligned}\frac{\partial}{\partial j}(n_p U_{p,j} R_{f@p,ij}) = &-\frac{\partial}{\partial x_k}(n_p \langle u''_{f@p,i} u''_{f@p,j} u''_{p,k} \rangle) - n_p R_{fp,ik} \frac{\partial V_{f,j}}{\partial x_k} - n_p R_{fp,jk} \frac{\partial V_{f,i}}{\partial x_k} \\ &+ n_p G_{fp,ik} R_{f@p,jk} + n_p G_{fp,jk} R_{f@p,ik} + n_p B_{f@p,ik} B_{f@p,jk}\end{aligned} \tag{2.32}$$

The governing equations vary depending on the expression for H_i. In the model from Arcen and Tanière (2009), $H_i = \frac{\partial R_{f@p,ij}}{\partial x_j}$ where in the new model developed $H_i = \frac{\partial}{\partial x_j}(R_{f,ij} + R_{fp,ij} - R_{f@p,ij})$. Since the set of equations are different depending on the model, it seems reasonable to assume there must also be a difference in the components of the fluctuating velocity seen variance tensor. Unfortunately, we have not identified this difference in the equations.

To check the stochastic system is properly solved, the mesh can be rotated by an angle θ_r and the same quantities compared. Figure 2.6 demonstrates the correct behaviour of the models when the mesh is rotated. The simulation protocol is exactly the same as before. A fluid simulation is performed on the rotated mesh until a steady state is reach. Then particles are injected and once a steady state is achieved Lagrangian statistics are computed on a sufficiently high number of time steps.

It seems that results are a little bit less precise, especially in the most extreme case $\theta_r = 40°$. However, results are still satisfactory.

Low and large inertia particles in a channel flow

This verification case consists in an infinite wall bounded channel flow at $Re_\tau = u_\tau \frac{\delta}{\nu} = 450$. Where u_τ is the fluid wall shear velocity, δ is the channel half width and ν is

the fluid viscosity. Single phase flow simulations are carried out on a $1\,\mathrm{m} \times 1\,\mathrm{m} \times 1\,\mathrm{m}$ domain with one cell in the direction of the flow, one cell in the off plane direction and a geometric progression in the wall normal direction in order to ensure simulation of the turbulent sub-layers. The simulations are performed with a second-order model with wall resolved turbulence (R_{ij}-ϵ EBRSM model (Manceau and Hanjalic, 2002)) with y^+ values below 1. The lower boundary is a wall, the upper boundary is a symmetry and the boundaries on the left and right hand side are periodic (the boundary conditions are shown in figure 2.7).

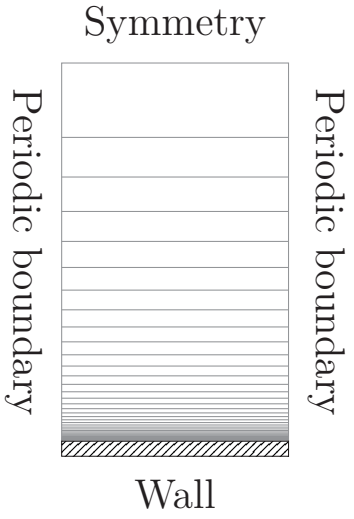

Figure 2.7: Sketch representing the domain and the boundary conditions.

When the steady state is achieved, low inertia particles (fluid elements) are inserted from the left hand side boundary of the domain. They move through the domain and exit it at the right hand side boundary. Large inertia particles on the other hand are initially uniformly distributed inside the domain. Due to their inertia, they tend not to move at all. After a sufficient number of time steps, Lagrangian statistics are significant and should match the Eulerian quantities. Similarly to the previous case, writing down the evolution equations for the drift velocity ($V_{f,x}$ and $V_{f,y}$), the particle velocity variance $R_{p,ij}$ and the fluid velocity seen variance $R_{f@p,ij}$ helps understand the results obtained with the different models. In the low inertia case the equations reduce to:

$$n_p U_{p,j} \frac{\partial V_{f,x}}{\partial y} = -\frac{\partial}{\partial y}(n_p R_{fp,xy}) + n_p H_x + n_p G_{fp,xj} V_{f,j} \tag{2.33}$$

$$n_p U_{p,j} \frac{\partial V_{f,y}}{\partial y} = -\frac{\partial}{\partial y}(n_p R_{fp,yy}) + n_p H_y + n_p G_{fp,yj} V_{f,j} \tag{2.34}$$

and,

$$\begin{aligned} \frac{\partial}{\partial y}(n_p U_{p,y} R_{f@p,ij}) = &-\frac{\partial}{\partial y}(n_p \langle u''_{f@p,i} u''_{f@p,j} u''_{p,y} \rangle) - n_p R_{fp,iy} \frac{\partial V_{f,j}}{\partial y} - n_p R_{fp,jy} \frac{\partial V_{f,i}}{\partial y} \\ &+ n_p G_{fp,ik} R_{f@p,jk} + n_p G_{fp,jk} R_{f@p,ik} + n_p B_{f@p,ik} B_{f@p,jk} \end{aligned} \tag{2.35}$$

The stochastic model verifies the guidelines stated in Minier et al. (2014) if $n_p H_i = \frac{\partial n_p R_{fp,ij}}{\partial x_j}$. As shown in figure 2.8, this is the case for all the models that have been written earlier. In the large inertia case the equations reduce to:

$$\begin{pmatrix} V_{f,x} \\ V_{f,y} \end{pmatrix} = -G^{-1}_{fp,ij} \begin{pmatrix} H_x \\ H_y \end{pmatrix} \tag{2.36}$$

and,

$$R_{f@p,xx} = \frac{R_{f@p,xy}}{G_{fp,xx}} \frac{\partial U_{f,x}}{\partial y} - \frac{1}{2} \frac{B^2_{f@p,yy}}{G_{fp,yy}} \tag{2.37}$$

$$R_{f@p,yy} = -\frac{1}{2} \frac{B^2_{f@p,yy}}{G_{fp,yy}} \tag{2.38}$$

$$R_{f@p,xy} = \frac{\partial U_{f,x}}{\partial y} \frac{R_{f@p,yy}}{G_{fp,xx} + G_{fp,yy}} \tag{2.39}$$

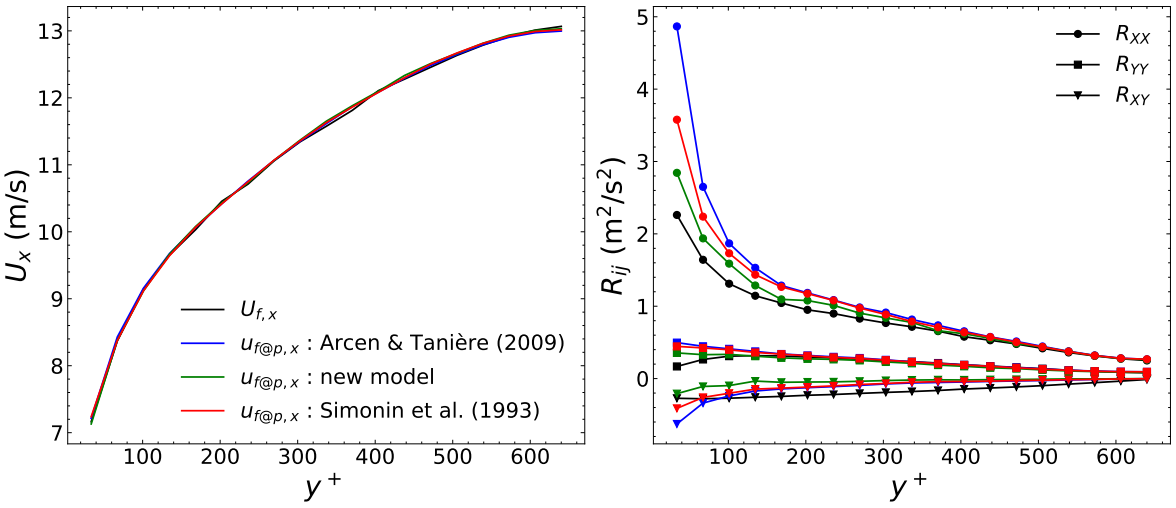

Figure 2.8: Velocity and second order statistics in the channel for the small inertia limit. Black lines represent results from the Eulerian computation whereas coloured lines come from Lagrangian statistics.

The stochastic models consistency is ensured as long as $H_i = 0$. The original model from Simonin et al. (1993) and the model from Minier and Peirano (2001) do not verify this equation and mean velocity plots shown in figure 2.9 highlight the lack of consistency of the former model in the large inertia limit: it is unable to reproduce the Eulerian quantities (the mean velocity seen by the particles does not equal the mean fluid velocity or the off diagonal component of the fluid velocity seen variance does not match the off diagonal component of the fluid velocity variance). The model from Minier and Peirano (2001) is not shown in figure 2.9 but the lack of consistency can be seen when plotting R_{XY}. Since the production terms are 0 for this model in the large inertia case, the model misses this component. However, due to another inconsistency in the model, this bias does not appear in the mean velocity plots as it does for the standard model of Simonin et al. (1993). Thus, justifying the introduction of new

models such as the one described in Arcen and Tanière (2009) or the one introduced in the previous section, developed during the thesis. Figures 2.8 and 2.9 also show that, for particles which centre of gravity is located at $y_p^+ < 100$ (near the wall boundary), $R_{f@p,ij}$ is further away from its Eulerian counterpart $R_{f,ij}$. This is natural since, in that region, viscous effects dominate the flow and they are not taken into account in the stochastic equation for the fluid velocity seen. This class of models are not designed to simulate the behaviour of particles at very small Reynolds number. A similar issue is pointed out in section 3.3 with several ways to deal with it when it impacts the behaviour of inertial particles.

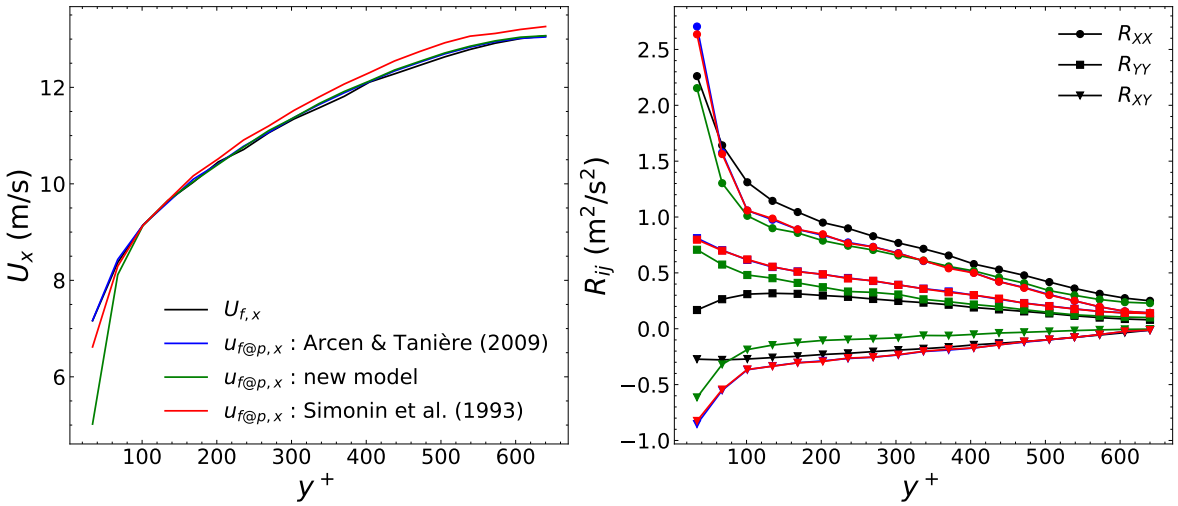

Figure 2.9: Velocity and second order statistics in the channel for the large inertia limit. Black lines represent results from the Eulerian computation whereas coloured lines come from Lagrangian statistics.

As in the previous case, this verification also gives the opportunity to check whether the *well-mixed criteria* is verified or not. Figure 2.10 shows the normalized particle concentration along the wall normal direction for three different stochastic models. It clearly shows that no spurious drift is introduced in the particle behaviour: the criteria is verified. It is easy to check that the criteria is no longer verified if the term H_i is neglected in the stochastic equations. This is illustrated with the red curve in figure 2.10. To check there are no spurious drifts, it is also possible to start with a non uniform particle distribution. If the stochastic models are consistent, the model should predict a uniform distribution equilibrium condition for the fluid elements. Figure 2.11 shows the particle normalised concentration along the wall normal direction at different time steps for an initial non uniform distribution. On both figures showing solid concentration, the black dotted line highlights the uniform theoretical distribution the models need to match.

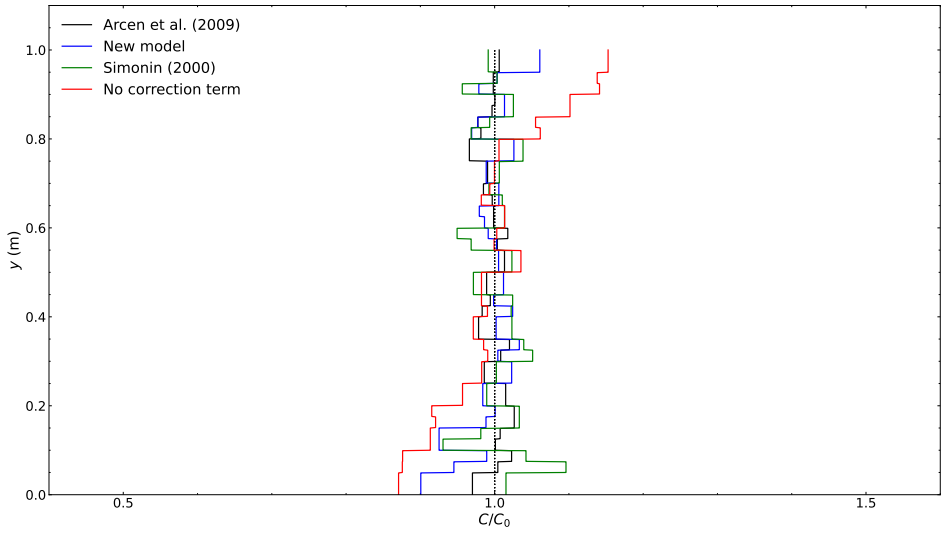

Figure 2.10: Normalised particle concentration C/C_0 along the wall normal direction. The normalizing coefficient C_0 is the average particle concentration in the channel.

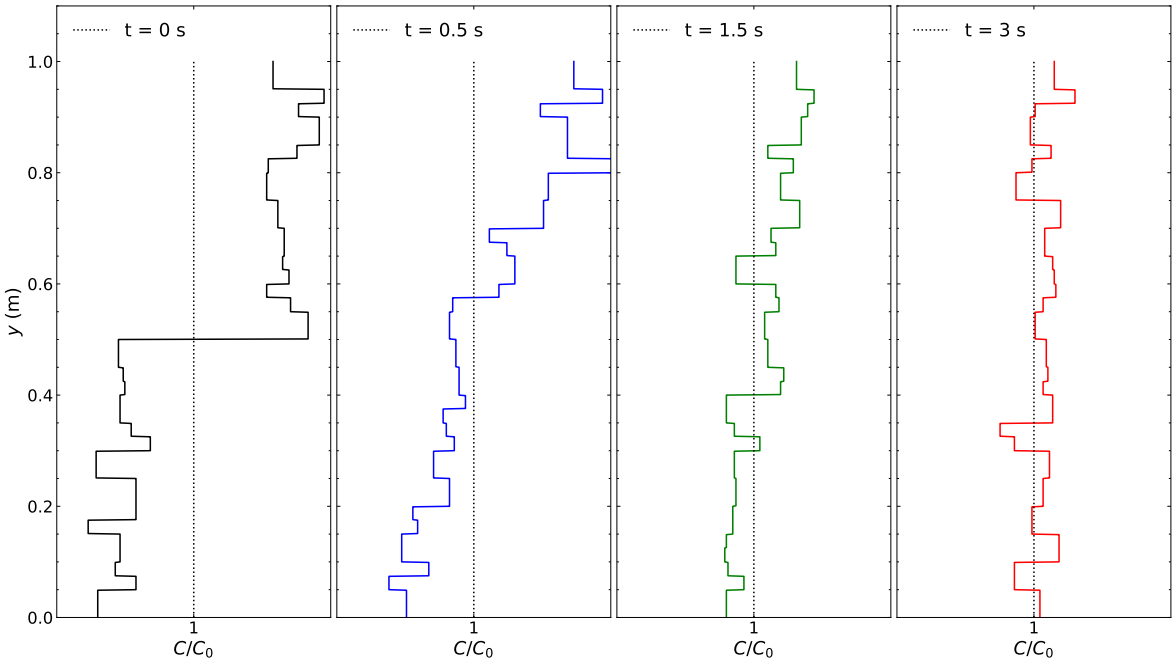

Figure 2.11: Normalised particle concentration C/C_0 along the wall normal direction at different time steps with the model from Arcen and Tanière (2009). The normalizing coefficient C_0 is the average particle concentration in the channel. The same scale is used on all the plots.

Initially, in neptune_cfd, only the stochastic model from Minier and Peirano (2001) was included. During the thesis, we implemented the literature models from Simonin et al. (1993), Arcen and Tanière (2009) and the new model introduced.

2.2 Multiphase flow modelling for immiscible fluids

This section is devoted to the introduction of multifluid models for continuous multiphase flows. The hybrid method for two-phase flows is introduced and will provide a starting point for the presentation of the new method developed during the thesis for liquid-gas-solid flows. The latter being described in section 3.2. Eventually, some details about the solver in particular and how the equations are implemented are introduced.

2.2.1 Equations for separated continuous phases

In this subsection, we focus on a system of continuous immiscible fluids - no dispersed inclusions are introduced in the system.

Let us consider a geometrical domain containing different fluids f. If they are inviscid, the domain can be divided into sub-domains where only one of the two fluid is present. Thus, for every geometric point M strictly within one of these regions, there exist a control volume Ω containing only fluid from phase f. In Ω, the fluid physical quantities necessary to describe the flow can be defined and local instantaneous single-phase balance equations can be obtained. They reflect the conservation of mass, momentum and energy of a mechanical continuum Delhaye (1974); Ishii and Hibiki (2011).

$$\begin{aligned} &\frac{\partial}{\partial t}(\rho) + \frac{\partial}{\partial x_j}(\rho u_j) = 0 \\ &\frac{\partial}{\partial t}(\rho u_i) + \frac{\partial}{\partial x_j}(\rho u_i u_j) = \frac{\partial}{\partial x_j}(\sigma_{ij}) + \rho g_i \end{aligned} \tag{2.40}$$

Where $\mathbf{u}$ is the fluid velocity, ρ is the mass per unit volume, $\sigma_{ij} = -p\delta_{ij} + \tau_{ij}$ is the stress tensor, p is the pressure field, τ_{ij} is the dissipative part of the stress tensor and g is the gravity. In an inviscid multiphase flow, it is possible to define the indicator function of each phase: χ_f. This function equals 1 inside phase f and 0 everywhere else. Since the interfaces are infinitely thin (they are of zero measure in the sense of distributions (Schwartz and Huet, 1961)), system 2.40 can be extended to the entire domain by including the indicator functions and jump conditions (Delhaye, 1974; Kataoka, 1985; Ishii and Hibiki, 2011).

$$\begin{aligned} &\frac{\partial}{\partial t}(\rho\chi_f) + \frac{\partial}{\partial x_j}(\rho u_j \chi_f) = -\rho(u_j - w_j)n_{f,j}\delta_f \\ &\frac{\partial}{\partial t}(\rho u_i \chi_f) + \frac{\partial}{\partial x_j}(\rho u_i u_j \chi_f) = \frac{\partial}{\partial x_j}(\sigma_{ij}\chi_f) + \rho g_i \chi_f + [\sigma_{ij} - \rho u_i(u_j - w_j)]n_{f,j}\delta_f \end{aligned} \tag{2.41}$$

Where $\mathbf{w}$ is the velocity of the interface, $\mathbf{n_f}$ is the normal to the interface pointed towards the region not occupied by fluid f and δ_f is the Dirac delta function associated with the interface surrounding phase f. The interface has no mass - it has no inertia, but it is subject to surface tension forces, the jump conditions in the system of equations 2.41 must verify:

$$\sum_f \rho(u_j - w_j) n_{f,j} \delta_f = 0 \tag{2.42}$$

$$\sum_f [\sigma_{ij} - \rho u_i (u_j - w_j)] n_{f,j} \delta_f = f_{s,i} \delta_s \tag{2.43}$$

Where δ_s is the Dirac delta function associated with all the interfaces and $\mathbf{f_s}$ is the surface tension force per unit interfacial area. Since there is only one pressure for both fluids $p_f = P$ (Ishii and Hibiki, 2011), there is no pressure jump across an interface. Therefore, the surface tension force $\mathbf{f_s} = 0$. Then, in order to obtain equations on mean quantities, it is necessary to define an averaging operator $x \mapsto \langle x \rangle$. This operator must verify Reynolds axioms Monin and Yaglom (1971); it must be linear, idempotent and must commute with differential operators. An Eulerian mean value G_f associated with the variable g for phase f is therefore defined as:

$$\alpha_f \rho_f G_f = \langle \rho g \chi_f \rangle \tag{2.44}$$

Where $\alpha_f = \langle \chi_f \rangle$ is the mean volume fraction occupied by phase f and ρ_f is its mean density. It is easy to verify this phase averaging operator verifies Reynolds axioms. Applying this operator to system 2.41 leads to the conservation equations of the mean quantities describing the fluids.

$$\frac{\partial}{\partial t}(\alpha_f \rho_f) + \frac{\partial}{\partial x_i}(\alpha_f \rho_f U_{f,i}) = \sum_{f' \neq f} \Gamma_{f' \to f} \tag{2.45}$$

$$\begin{aligned} \frac{\partial}{\partial t}(\alpha_f \rho_f U_{f,i}) + \frac{\partial}{\partial x_j}(\alpha_f \rho_f U_{f,i} U_{f,j}) = \alpha_f \rho_f g_i - \frac{\partial}{\partial x_j}\langle \rho u''_{f,i} u''_{f,j} \chi_f \rangle + \frac{\partial}{\partial x_j}(\alpha_f \Sigma_{f,ij}) \\ + \sum_{f' \neq f} (I_{f' \to f,i} + \Gamma_{f' \to f} U_{f,i}) \end{aligned} \tag{2.46}$$

Where $\Gamma_{f' \to f}$ and $I_{f' \to f}$ are the mean transfer terms obtained from averaging the jump conditions in the local instantaneous equations. $\Gamma_{f' \to f}$ is the mean mass transfer across an interface between fluids f and f', $I_{f' \to f}$ is the mean transfer of momentum across the same interface, $u''_{f,i} = u_i - U_{f,i}$ is the velocity fluctuation for phase f and $\alpha_f \rho_f \Sigma_{f,ij} = \langle \rho \sigma_{f,ij} \chi_f \rangle$ is the mean stress tensor. When considering a Newtonian fluid, the stress tensor can be written as an affine function of the linearised strain tensor (Batchelor, 2000).

$$\Sigma_{f,ij} = -P_f \delta_{ij} + T_{f,ij} = -P \delta_{ij} + T_{f,ij} \tag{2.47}$$

Where P_f is the mean pressure inside fluid f and $T_{f,ij}$ is the mean dissipative part of the stress tensor - the viscous stress tensor. The mean momentum conservation equation can therefore be written as in equation 2.48. In that equation, the interfacial transfer term from all the phases but f to phase f appears reduced by the mean pressure contribution, $\sum_{f' \neq f} I'_{f' \to f,i} = \sum_{f' \neq f} I_{f' \to f,i} - P \frac{\partial \alpha_f}{\partial x_i}$.

$$\frac{\partial}{\partial t}(\alpha_f \rho_f U_{f,i}) + \frac{\partial}{\partial x_j}(\alpha_f \rho_f U_{f,i} U_{f,j}) = \alpha_f \rho_f g_i - \frac{\partial}{\partial x_j}\langle \rho u''_{f,i} u''_{f,j} \chi_f \rangle + \frac{\partial}{\partial x_j}(\alpha_f T_{f,ij}) - \alpha_f \frac{\partial P}{\partial x_i} + \sum_{f' \neq f} \left(I'_{f' \to f,i} + U_{f,i} \Gamma_{f' \to f} \right) \tag{2.48}$$

In the subsequent work, no phase change are considered, thus, $\Gamma_{g \to f} = 0$ in the mass and momentum conservation equations 2.45 and 2.48. Additionally, no surface tension effects are taken into account, thus $f_s = 0$.

In equation 2.48 appears the Reynolds stress tensor for fluid f: $R_{f,ij} = \langle \rho u''_{f,i} u''_{f,j} \chi_f \rangle$. This accounts for velocity fluctuation effects on the fluid mean momentum. It is the second term - with the interfacial transfer term - that requires closure. Different approaches are commonly used, in this manuscript we will describe the 2-equations models (k-ϵ) or R_{ij}-ϵ models - with k the turbulent kinetic energy and R_{ij} the Reynolds stress tensor. By manipulating the mean momentum equation 2.48, one can get the evolution equation for the Reynolds stress components $R_{f,ij}$.

$$\rho_f \frac{\partial R_{f,ij}}{\partial t} + \frac{\partial}{\partial x_k}(\rho_f u_{f,k} R_{f,ij}) - \frac{\partial}{\partial x_k}\left(\mu_f \frac{\partial}{\partial x_k} R_{f,ij} \right) = \frac{\partial}{\partial x_k}(S_{f,ijk}) + P_{f,ij} + g_{f,ij} + \Phi_{f,ij} - \rho_f \epsilon_{f,ij} \tag{2.49}$$

Where μ_f is the dynamic viscosity, $\Phi_{f,ij}$ is the pressure-velocity correlation term, $g_{f,ij}$ and $P_{f,ij}$ are the production terms due to gravity and mean flow strain rate, the first term on the right-hand side is the diffusive term and $\epsilon_f = \frac{3}{2}\epsilon_{f,ii}$ is the turbulent energy dissipation rate which satisfies equation 2.50.

$$\rho_f \frac{\partial \epsilon_f}{\partial t} + \frac{\partial}{\partial x_k}(\rho_f u_{f,k} \epsilon_f) - \frac{\partial}{\partial x_k}\left(\mu_f \frac{\partial \epsilon_f}{\partial x_k} \right) = \frac{\partial}{\partial x_k}(S_k) + C_{\epsilon,1} \frac{\epsilon_f}{k_f}(P + G_\epsilon) - \rho_f C_{\epsilon,2} \frac{\epsilon_f^2}{k} \tag{2.50}$$

Where $C_{\epsilon,1}$ and $C_{\epsilon,2}$ are two constants of the model, the first term on the right-hand side is the diffusion term, $k_f = \frac{1}{2}R_{f,ii}$ is the turbulent kinetic energy, $P = \frac{1}{2}P_{f,ii}$ and $G_\epsilon = \frac{1}{2}g_{f,ii}$. For more details and information about the way these equations are derived or about the different possible closures, see for example Speziale et al. (1991). These equations represent the second order model. By taking the trace of equation 2.49, it is possible to get the equations for a first order model (Launder and Spalding, 1974). It is quite faster since it only solves 1 equation instead of 6 for the turbulent kinetic energy terms but it is also less accurate. It tends to diffuse the mean velocity a lot more.

2.2.2 Dispersed inclusions inside a continuous phase

In this section, we focus on dispersed inclusions in one continuous fluids - be it gas or liquid. We start by deriving the mean quantities conservation equation with the ensemble averaging approach. Then, we describe the additional hypothesis needed to couple the interfacial transfer terms with those obtained from the phase averaging and, finally, we introduce how the turbulence is taken into account.

Mass and momentum conservation equations

The starting point for this section is the conservation equation for the moments of the PDF f_p (equation 2.23). In the previous section, we derived the conservation equation for the turbulent quantities related to the fluid seen by the solid phase. In this section, we derive the conservation equation for the particle phase as well as the associated turbulent quantities. By replacing ψ_p with the appropriate function of the phase space variables, it is possible to obtain the conservation equations needed to describe the particle phase. When $\psi_p = 1$, equation 2.23 becomes the particle mass conservation equation. In the derivation of this equation, it is supposed that there are no mass transfer with the fluid phase or between the particles.

$$\frac{\partial}{\partial t}(n_p m_p) + \frac{\partial}{\partial x_i}(n_p m_p U_{p,i}) = 0 \tag{2.51}$$

When $\psi_p = c_{p,i}$, equation 2.23 becomes the particle mean momentum conservation equation.

$$\begin{aligned}\frac{\partial}{\partial t}(n_p m_p U_{p,i}) + \frac{\partial}{\partial x_j}(n_p m_p U_{p,i} U_{p,j}) = &- \frac{\partial}{\partial x_j}\left(n_p m_p \langle u'_{p,i} u'_{p,j}\rangle\right) \\ &+ n_p m_p \langle \frac{\mathrm{d}u_{p,i}}{\mathrm{d}t}\rangle + n_p \mathbb{C}(m_p u_{p,i})\end{aligned} \tag{2.52}$$

When deriving this equation, the mean change rate in particle momentum appears: $m_p\langle\frac{\mathrm{d}u_{p,i}}{\mathrm{d}t}\rangle$. It is the mean particle acceleration between two instantaneous collisions. This term can include, among other contributions, the fluid to particle momentum transfer such as drag or Archimedes force $F_{f\to p,i}$, the long-distance particle-particle interaction terms such as electrostatic forces $\sum_{p'} F_{p'\to p,i}$ and external body forces such as gravity or magnetic fields $F_{B\to p,i}$.

$$m_p \frac{\mathrm{d}u_{p,i}}{\mathrm{d}t} = m_p \left(F_{f\to p,i} + \sum_{p'} F_{p'\to p,i} + F_{B\to p,i} \right) \tag{2.53}$$

Coupling the interfacial transfer terms

To highlight the consistency between the PDF approach and the phase averaging, the momentum transfer terms have to be reorganised. In the PDF framework, the mean momentum transfer at the interface $I_{f\to p,i} = n_p\langle F_{f\to p,i}\rangle$ is the mean force acting on particles which centre of gravity is located in the control volume.

$$F_{f\to p,i} = \int_{S_p} (\sigma_{f@p,ij} + \delta\sigma_{f,ij}) n_{p,j} \mathrm{d}S = -v_p \frac{\partial P_{f@p}}{\partial x_i} + F^D_{f\to p,i} \tag{2.54}$$

Where S_p is the surface of particles which centre of gravity is located in the volume average, $\sigma_{f@p,ij}$ is the fluid stress tensor undisturbed by the presence of the particle. We assume, it only includes the pressure effect. $\delta\sigma_{f,ij}$ is the fluid stress tensor associated with the particle presence, $\mathbf{n_p}$ is the normal of the surface S, v_p is the volume of a particle, $P_{f@p}$ is the undisturbed pressure at the position of the particle and $F^D_{f\to p,i}$

represents the fluid force on the particle without the contribution of the undisturbed flow which we limit to drag. It is further assumed that the gradient of the fluid pressure seen by the particle is equal to the mean pressure gradient.

In contrast, in the phase averaging framework, the mean momentum transfer at the interface $I_{p\to f,i} = -\langle \sigma_{f,ij} n_{p,j} \delta_{fp} \rangle$ represents the total force acting from the fluid on the particle surfaces included in the control volume.

$$F_{p\to f,i} = \int_{\Sigma_p} \sigma_{f,ij} n_{p,j} \mathrm{d}S \tag{2.55}$$

Where δ_{fp} is the Dirac delta function associated with the fluid-particle interface and Σ_p is the particle surface included in the volume average. From equations 2.54 and 2.55, for partially included particles in the volume, the two mean transfer terms are not equal. According to Zhang and Prosperetti (1994), the bias introduced in the system can be written as the divergence of a flux $\theta_{fp,ij}$. In homogeneous flows, this bias is 0 but it is not the case in general. For a volume sufficiently close to a wall boundary for instance, there can be no particles (distance to the wall smaller than the particle radius), despite the presence of a particle surface. Figure 2.12 shows the differences between the two frameworks.

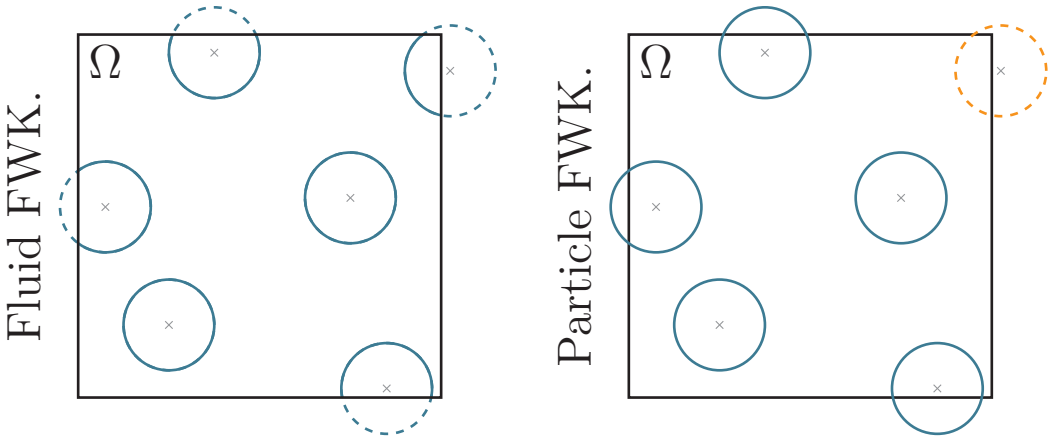

Figure 2.12: (left) Fluid point of view, all the interfaces included in Ω are used to compute the interfacial transfer terms. (right) Particle point of view, only the surface of particles which center of gravity is in Ω is used to compute the same term.

This bias can be seen as a flux of partially included particles on the boundary of Ω:

$$I_{p\to f,i} + I_{f\to p,i} = \frac{\partial \theta_{fp,ij}}{\partial x_j} \tag{2.56}$$

As a first approximation, the bias is only accounted for in the mean pressure contribution term of the interfacial momentum transfer terms. If v_p is the volume occupied by a particle, the bias reads:

$$I^A_{p\to f,i} = -I^A_{f\to p,i} + \frac{\partial \theta_{fp,ij}}{\partial x_j} = -I^A_{f\to p,i} - n_p v_p \frac{\partial P}{\partial x_i} + P \frac{\partial \alpha_f}{\partial x_i} \tag{2.57}$$

With $\theta_{fp,ij} \approx -(1-\alpha_f)P\delta_{ij}$, the sum of the mean pressure contribution in the interfacial transfer term and the pressure term in the stress tensor in equation 2.48 can be written as:

$$I^A_{p\to f,i} - \frac{\partial \alpha_f P}{\partial x_i} = -\alpha_f \frac{\partial P}{\partial x_i} \tag{2.58}$$

Therefore, the contribution not related to mean pressure in the interfacial transfer terms verifies:

$$I^D_{p\to f,i} = -I^D_{f\to p,i} \tag{2.59}$$

Thus, even if the transfer term differs in the two approaches, by organising them correctly, it is possible to demonstrate the consistency between both and it is possible to close the unknown term in the fluid equations. This justifies the use of the same framework for the two equations, despite them being obtained from two different methods. This illustrates the simplest form of bias leading to a consistent system of equations. It is possible to assume the bias is accounted for in the viscous term as well. This would end up in a more complex expression more suitable in high viscosity fluids. For more details on those expressions, see Jackson (2000).

Turbulence modelling for solid inclusions

Different models exist in neptune_cfd to account for particle dispersion. The first one is the model developed in Mou (1947) and Hinze (1959) later examined by Desjonqueres et al. (1986). It consists in constitutive relations for the particle velocity variance and covariance tensors when particle experience drag only. These relations are consistent if, first of all, the particle Reynolds number is sufficiently small to neglect the non-linearity in the drag coefficient. Then, the fluid turbulence must be homogeneous, isotropic and stationary. And, finally, the Lagrangian fluid statistics must match those computed along a particle trajectory. Following these assumptions, by writing down the momentum balance for a particle, using the Fourier transform and assuming the expression of the fluid velocity Lagrangian auto-correlation function, it is possible to obtain the relations below.

$$\langle u''_{p,i} u''_{p,j} \rangle = \langle u''_{f,i} u''_{p,j} \rangle \tag{2.60}$$

$$\langle u''_{f,i} u''_{p,j} \rangle = \langle u''_{f,i} u''_{f,j} \rangle \frac{T^L_{f@p}}{T^L_{f@p} + \tau_{p,f}} \tag{2.61}$$

When the flow is not isotropic, an equivalent kinetic stress model for the particles can be obtained. It consists in deriving, from the moments equation 2.23, the evolution equations for the fluid velocity variance $R_{p,ij}$ and fluid-particle velocity $R_{fp,ij}$ covariance tensors and taking the trace of the system obtained. More details on these equations can be found in appendix A.

$$\begin{aligned}
&\frac{\partial}{\partial t}(n_p m_p R_{p,ij}) + \frac{\partial}{\partial x_k}(n_p m_p R_{p,ij} U_{p,k}) = -\frac{\partial}{\partial x_k}(n_p m_p \langle u''_{p,i} u''_{p,j} u''_{p,k} \rangle) \\
&- n_p m_p R_{p,jk} \frac{\partial U_{p,i}}{\partial x_k} - n_p m_p R_{p,ik} \frac{\partial U_{p,j}}{\partial x_k} \\
&+ n_p m_p \frac{1}{\tau_{p,f}} \left[R_{fp,ij} + R_{fp,ji} - 2R_{p,ij} \right] + \mathbb{C}(m_p u''_{p,i} u''_{p,j})
\end{aligned} \tag{2.62}$$

$$\begin{aligned}
&\frac{\partial}{\partial t}(n_p m_p R_{fp,ij}) + \frac{\partial}{\partial x_k}(n_p m_p R_{fp,ij} U_{p,k}) = -\frac{\partial}{\partial x_k}(n_p m_p \langle u''_{f@p,i} u''_{p,j} u''_{p,k} \rangle) \\
&- n_p m_p R_{p,jk} \frac{\partial V_{f,i}}{\partial x_k} - n_p m_p R_{fp,ik} \frac{\partial U_{p,j}}{\partial x_k} \\
&+ n_p m_p G_{fp,jk} R_{f@p,ki} + n_p m_p \frac{1}{\tau_{p,f}} \left[R_{f@p,ij} - R_{fp,ij} \right]
\end{aligned} \tag{2.63}$$

In the particle kinetic stress equations, the terms on the right hand side represent variance (covariance) transport by particle velocity fluctuations, modelled with a Boussinesq-type approximation, the turbulence production due to mean particle or drift velocity and the interaction between the fluctuating motions of particles and the fluid. The collision term above can be expressed using Grad's theory of rarefied gases (Grad, 1949) by approximately expanding the distribution function with Hermite polynomials. The collisional term ends up being written like a return-to-isotropy contribution analogous to the Rotta term in the fluid Reynolds stress models and an inelastic collision contribution.

$$\mathbb{C}(m_p u''_{p,i} u''_{p,j}) = -n_p m_p \Big[\underbrace{\frac{\gamma_c}{\tau_{p,c}} \left(R_{p,ij} - \frac{2}{3} q_p \delta_{ij} \right)}_{\text{return-to-isotropy}} + \underbrace{\frac{1 - e_c^2}{3\tau_{p,c}} \frac{2}{3} q_p \delta_{ij}}_{\text{Inelastic collisions}} \Big] \tag{2.64}$$

Where $q_p = \frac{1}{2} R_{p,ij}$, $\tau_{p,c}$ is the time separating two inter-particle collisions, e_c is the restitution coefficient and γ_c is a constant. With particle diameter d_p:

$$\tau_{p,c} = \frac{d_p}{6\alpha_p \pi \sqrt{\frac{16}{\pi} \frac{2}{3} q_p}} \tag{2.65}$$

$$\gamma_c = \frac{(1 + e_c)(3 - e_c)}{5} \tag{2.66}$$

$$\xi_c = \frac{(1 + e_c)(49 - 33 e_c)}{100} \tag{2.67}$$

By writing the evolution equation for $S_{p,ijk} = \langle u''_{p,i} u''_{p,j} u''_{p,k} \rangle$ and using a Boussinesq-type approximation, following the work in Hanjalić and Launder (1972), the following relation can be obtained:

$$S_{p,ijk} = -K_{p,il} \frac{\partial R_{p,jk}}{\partial x_l} - K_{p,jl} \frac{\partial R_{p,ki}}{\partial x_m} - K_{p,kl} \frac{\partial R_{p,ij}}{\partial x_l} \tag{2.68}$$

Where, with constants ξ_{fp}^F and ξ_{fp}^t, the diffusivity tensor reads:

$$K_{p,mn} = \left[\frac{\tau_{p,f}}{\xi_{fp}^F} R_{p,mn} + \frac{T_f^L}{\xi_{fp}^t} R_{fp,mn}\right] \left[1 + \frac{5}{9}\tau_{p,f}\frac{\xi_c}{\tau_{p,c}}\right]^{-1} \tag{2.69}$$

In order to simplify the model, Simonin (1996) proposed another formulation, still compatible with Daly and Harlow (1970) and with the same expression for the diffusion tensor $K_{p,mn}$:

$$\frac{\partial S_{p,ijk}}{\partial x_k} = -\frac{\partial}{\partial x_k}\left[K_{p,kl}\frac{\partial R_{p,ij}}{\partial x_l}\right] \tag{2.70}$$

In neptune_cfd, an even simpler version is implemented for the triple correlation terms. The latter neglects the anisotropy effects in the diffusion tensor:

$$-\frac{\partial}{\partial x_k}(n_p m_p \langle u''_{p,i} u''_{p,j} u''_{p,k}\rangle) = -\frac{\partial}{\partial x_k}\left(n_p m_p K_p \frac{\partial R_{p,ij}}{\partial x_l}\right) \tag{2.71}$$

Where the diffusivity and viscosities read:

$$K_p = \left[\nu_{fp} + \frac{5}{9} q_p \frac{2}{3}\frac{\tau_{p,f}}{2}\right]\left[1 + \frac{5}{9}\tau_{p,f}\frac{\xi_c}{\tau_{p,c}}\right]^{-1} \tag{2.72}$$

$$\nu_{fp} = \frac{1}{3} q_{fp} T^L_{f@p} \tag{2.73}$$

$$\tag{2.74}$$

If collisions are strong or if the turbulence is mostly isotropic, a 2-equations model may be sufficient to describe particle dispersion accurately. To obtain it, the two previous equations are used to get the evolution equation of the traces $q_p = \frac{1}{2}R_{p,ii}$ and $q_{fp} = \frac{1}{2}R_{fp,ii}$.

$$\begin{aligned}&\frac{\partial}{\partial t}(n_p m_p q_p) + \frac{\partial}{\partial x_k}(n_p m_p q_p U_{p,k}) = -\frac{\partial}{\partial x_k}(n_p m_p \langle u''_{p,i} u''_{p,j} u''_{p,k}\rangle) \\ &- n_p m_p R_{p,ik}\frac{\partial U_{p,i}}{\partial x_k} + \Pi_{q_p} + \mathbb{C}(m_p q_p)\end{aligned} \tag{2.75}$$

$$\begin{aligned}&\frac{\partial}{\partial t}(n_p m_p q_{fp}) + \frac{\partial}{\partial x_k}(n_p m_p q_{fp} U_{p,k}) = -\frac{\partial}{\partial x_k}(n_p m_p \langle u''_{f@p,i} u''_{p,j} u''_{p,k}\rangle) \\ &- n_p m_p R_{p,ik}\frac{\partial V_{f,i}}{\partial x_k} - n_p m_p R_{fp,ik}\frac{\partial U_{p,i}}{\partial x_k} \\ &+ \frac{1}{2} n_p m_p G_{fp,ik} R_{f@p,ki} + \Pi_{q_{fp}}\end{aligned} \tag{2.76}$$

In the 2-equations model, the terms on the right hand side correspond to transport of the variance (covariance) by the particle velocity fluctuations, the next term is the turbulence production by mean particle or drift velocity, the following term corresponds

to fluid-particle fluctuating motion interaction (Π_{q_p} and $\Pi_{q_{fp}}$) and the last one in the equation for q_p accounts for collisions. In a dilute flow, the coupling terms can be written:

$$\Pi_{q_p} = n_p m_p \frac{1}{\tau_{p,f}} \left(q_{fp} - 2q_p\right) \tag{2.77}$$

$$\Pi_{q_{fp}} = n_p m_p \frac{1}{\tau_{p,f}} \left(2R_{f@p,ii} - q_{fp}\right) \tag{2.78}$$

Again, an eddy-viscosity type assumption allows the closure of the unknown term in the previous equations. In the event of high particle loading, the effect of particles on the fluid must not be neglected. In that case, an additional term might be included in the evolution equation for the fluid-particle covariance q_{fp}. According to Sun et al. (2022), in the event of uncorrelated motion, the coupling term between fluid and particle fluctuations in equation 2.76 $\Pi_{q_{fp}}$ might contain a destruction term proportional to the fluid-particle covariance:

$$\Pi_{q_{fp}} = n_p m_p \frac{1}{\tau_{p,f}} \left[2R_{f@p,ii} - q_{fp} + \frac{n_p m_p}{\alpha_f \rho_f} q_{fp}\right] \tag{2.79}$$

Where ρ_f and α_f are the fluid density and volume fraction. Adapting the previous models and equations in the case of liquid-gas-solid flow is the purpose of section 3.2.

2.2.3 neptune_cfd: general concepts and models

neptune_cfd is a multiphase solver based on the architecture of the open source software code_saturne, developed in EDF. All models presented in future chapters are included in the development version of the software and will be supported in future versions. It is a 3-dimensional (3D) N-fluid Reynolds averaged Navier-Stokes (RANS) solver developped by EDF, CEA, IRSN and Framatome initially for nuclear applications. The 3D full-unstructured finite volume discretisation with colocated variables is based on the multi-fluid single pressure formulation proposed by Delhaye (1974); Kataoka (1985); Ishii and Hibiki (2011). The convection scheme for all the variables but the pressure is Second Order Linear Upwind (SOLU) or Upwind. In general, the solver is built around a pressure correction fractional step approach and gradients are computed mostly to the second order accuracy (for regular cells). By design, when obtaining the governing equations, some information about the interfacial transfer terms is lost, the averaged system thus requires the introduction of closures. This procedure also requires the introduction of turbulence modelling which is readily available in neptune_cfd with 1$^{\text{st}}$ order models such as the k-ϵ model Launder and Spalding (1974) or the k-ϵ model with linear production Guimet and Laurence (2002), and 2$^{\text{nd}}$ order model such as the R_{ij}-ϵ SSG model Speziale et al. (1991) and its wall-resolved equivalent, the R_{ij}-ϵ SSG-EBRSM model Manceau and Hanjalic (2002). In all our studies, the flows are adiabatic and there are no phase changes. This causes some simplifications in the governing system which is shown in equations 2.45 and 2.46 for a fluid f. The mean mass transfer term $\Gamma_{g\to f}$ is neglected in all the manuscript. An additional important assumption is the fact that all the phases constitute all of the material present in the domain.

$$\sum_f \alpha_f = 1 \tag{2.80}$$

In the following paragraphs, in order to describe multiple regimes, we define four new indexes: cg, dg, cl, dl. They represent continuous gas, dispersed gas, continuous liquid and dispersed liquid. When not specified, the index refers to the phase in general without accounting for its morphology. They do not reflect a real segmentation in the framework but allow for a clearer presentation of the different models.

Interfacial transfer terms in dispersed flows

The main advantage of this method is its natural ability to tackle different flow regimes. It can simulate separate phases configurations where two continuous phases are separated by a free surface and it can simulate dispersed flows where bubbles or droplets are present inside a continuous phase. This approach also allows any combination of the two previous cases: two continuous phases separated by a free-surface and containing dispersed inclusions. The kind of regime the flow is in determines the expression for the interfacial momentum transfer terms. In the dispersed case, the interfacial transfer term is divided in a laminar ($\mathbf{I}^L$) and a turbulent ($\mathbf{I}^T$) contribution. Let's assume cl is a continuous phase and dg is a dispersed phase carried by the continuous field (it could represent bubbles, droplets or solid particles).

$$I'_{cl\to dg,i} = I^L_{cl\to dg,i} + I^T_{cl\to dg,i} \tag{2.81}$$

In neptune_cfd, the laminar contribution includes the usual interaction forces (drag, lift and added mass) for bubbles or droplets. For solid dispersed inclusions, drag is usually the only interfacial momentum transfer term.

$$\begin{aligned}\mathbf{I}^L_{cl\to dg} = &- \alpha_{dg}\rho_{cl}F_D^{cl\to dg}\mathbf{V}_r^{cl\text{-}dg} - \alpha_{dg}\rho_{cl}C_A^{cl\text{-}dg}\frac{\mathrm{d}\mathbf{V}_r^{cl\text{-}dg}}{\mathrm{d}t} \\ &- \alpha_{dg}\rho_{cl}L^{cl\to dg}(\mathbf{U}_{dg}-\mathbf{U}_{cl})\wedge(\nabla\times\mathbf{U}_{cl})\end{aligned} \tag{2.82}$$

Where $F_D^{cl\to dg}$ is the drag coefficient between phase cl and dg, $\mathbf{V}_r^{cl\text{-}dg} = \mathbf{U}_{dg} - \mathbf{U}_{cl}$ is the average relative velocity, $C_A^{cl\text{-}dg}$ is the added-mass coefficient and $L^{cl\to dg}$ is the lift coefficient. There has been - and still is - extensive work regarding the possible closure for those terms; in neptune_cfd, the closures used for these terms can be found in Ishii and Zuber (1979); Zuber (1964), Mimouni et al. (2011) and Tomiyama et al. (1998).

The expression for the turbulent term in equation 2.81, which includes the turbulent contributions in drag, lift and added mass; can be found in Laviéville et al. (2017). Moreover, terms in the turbulent quantities evolution equations are modified or included to account for modulation due to dispersed inclusions.

Inclusion diameter - interfacial area transport equation method

In the interfacial momentum transfer terms, one of the most important variable is the equivalent diameter of the inclusions. This value drives all of the coefficients and plays a key role, as we should see in the following chapters, in the accuracy of

the models. In neptune_cfd, this diameter can be constant, a value is picked at the beginning of the simulation and is used throughout the simulation. This approach is definitely useful when experimental data supports the hypothesis of bubbles all being the same size. However, in general, there is either no experimental data on the sizes of the inclusions or it cannot support the hypothesis of a single diameter. In which case, the polydispersed representation of the diameter is more suitable. The set of dispersed inclusions is considered through a phase space as is presented in section 2.2.2. This space contains the position of an inclusion $\mathbf{x}$, its size d_b and the velocity of its centre of mass $\mathbf{w}$. F is the density function associated to this phase space such that $F(d_b, \mathbf{w}; \mathbf{x}, t)\delta d_b \delta \mathbf{w} \delta \mathbf{x}$ is the probable number of inclusions with size and velocity $(d_b, \mathbf{w}) \in \{d_b, d_b + \delta d_b\} \times \{\mathbf{w}, \mathbf{w} + \delta \mathbf{w}\}$ in the volume $\delta \mathbf{x}$ centered around $\mathbf{x}$ at time t. The size distribution f is defined as follows:

$$f(d_b; \mathbf{x}, t) = \int F(d_b, \mathbf{w}; \mathbf{x}, t) \mathrm{d}\mathbf{w} \tag{2.83}$$

The number density function n and the probability density function P per unit size of an inclusion are classically defined.

$$n(\mathbf{x}, t) = \int f \mathrm{d}d_b \tag{2.84}$$

$$f(d_b; \mathbf{x}, t) = n(\mathbf{x}, t) P(d_b; \mathbf{x}, t) \tag{2.85}$$

As was done in section 2.2.2, it is possible to obtain an evolution equation for F - a Liouville equation. It is also straightforward to obtain an Enskog's type equation for the evolution of moments of the density function μ_ψ. These moments are defined through the definition of an ensemble average.

$$\mu_\psi(\mathbf{x}, t) = n(\mathbf{x}, t) \langle \psi \rangle_1 = \int F \psi \mathrm{d}d_b \mathrm{d}\mathbf{w} \tag{2.86}$$

Where,

$$\langle \psi \rangle_Y = \frac{\int F \psi Y \mathrm{d}d_b \mathrm{d}\mathbf{w}}{\int F Y \mathrm{d}d_b \mathrm{d}\mathbf{w}} \tag{2.87}$$

Thus resulting in the following equation:

$$\frac{\partial \mu_\psi}{\partial t} + \nabla . (\mu_\psi \langle \mathbf{w} \rangle_\psi) = n \left\langle \frac{\partial \psi}{\partial d_b} \frac{\mathrm{d}d_b}{\mathrm{d}t} \right\rangle + \underbrace{\int \dot{F}_{c,b} \psi \mathrm{d}d_b \mathrm{d}\mathbf{w}}_{\dot{\mu_\psi}} \tag{2.88}$$

Where $\dot{\mu_\psi}$ reflects the change of the moment due to specific phenomenon (coalescence, fragmentation, phase change, growth...) and $\langle \mathbf{w} \rangle_\psi$ is not - by default - the velocity of the fluid carrying the inclusions. Since in our cases there are no phase change and air is incompressible the first term on the right hand side of equation 2.88 is 0. From this point on, many options exist for the description of the polydispersion. The very popular population balance method Carrica et al. (1999) consists in subdividing the inclusions in classes of similar sizes. A velocity and volume fraction is

associated to each fraction. Then the evolution equations are solved for all these fields. It is an accurate way of dealing with the polydispersion. However, it can be costly if the range of diameters spans several decades. The change in size due to coalescence or fragmentation are taken into account through source and sink terms in the evolution equations for all the classes. In order to conserve the mass in the system, these terms must be introduced carefully (Montoya et al., 2014), their expressions represent a sizeable challenge.

In neptune_cfd, a moment with an assumption on the shape of the density function f has been pursued. It consists in reducing the complexity of the problem by solving equation 2.88 for specific moments only with known relations output from the assumed density function. Mainly, the moments treated in neptune_cfd are the dispersed phase volume fraction α_{dg} (the total inclusion volume per unit volume of fluids) and the interfacial area a_i (the total fluid-inclusion surface area per unit volume). We are rapidly detailing this method but more information about it can be found in the original work from Ruyer (2007).

$$\frac{\partial a_i}{\partial t} + \nabla.(a_i \langle \mathbf{w} \rangle_{d_b^2}) = \int_{d_b} \int_{\mathrm{w}} \dot{F}_{c,b} \pi d_b^2 \mathrm{d_b} \mathrm{d}\mathbf{w} \tag{2.89}$$

There are more sophisticated models Kim et al. (2021) where second order moments may be used: see the references for more details on these. The assumed expression for the probability density function should be simple enough to enable a simple relation between the moments and a simple expression for the source and sink terms due to coalescence, fragmentation and phase change. Finding this expression cannot be easy and some intuitive guesses may not be appropriate. A Dirac delta distribution would signify a constant diameter which is not very informative. The choice of a log-normal distribution for example poses some difficulties since it gives an infinite value for the source term related to a binary fragmentation of bubbles Riou (2002). The main objective of this assumed PDF is to be statistically accurate rather than to reproduce accurately the details of the population. Thus, the expression selected for neptune_cfd for which more details can be found in Ruyer (2007), is the following:

$$f(\mathbf{x}, t) = \begin{cases} \dfrac{3n(\mathbf{x}, t) d_b}{4 \langle d_b \rangle_1^3} \left(2 \langle d_b \rangle_1 - d_b\right), & \text{if } d_b < 2 \langle d_b \rangle_1 \\ 0, & \text{otherwise} \end{cases} \tag{2.90}$$

From equation 2.90, it is possible to derive the relationships between the moments a_i, α_{dg} and $d_{3,2}$.

$$a_i = \frac{6 \alpha_{dg}}{d_{3,2}} \tag{2.91}$$

Where $d_{3,2} = \frac{4}{3} \langle d_b \rangle_1$ is Sauter mean diameter - the diameter of a sphere having the same volume over surface ratio as the bubble it represents (Morel et al., 2010).

$$d_{3,2} = \frac{\int d_b^3 f \mathrm{d}d_b \mathrm{d}\mathbf{w}}{\int d_b^2 f \mathrm{d}d_b \mathrm{d}\mathbf{w}} \tag{2.92}$$

Thus, if the term on the right hand side of the equation 2.89 is closed, solving the equation determines a diameter which can be used in the interfacial transfer terms. A mechanistic approach leads to the fragmentation and coalescence terms closure (Luo and Svendsen, 1996; Yao and Morel, 2004; Ruyer, 2007; Morel et al., 2010). The main idea is to identify the mechanisms driving coalescence and fragmentation and then to separate their probability of occurrences with their efficiencies. Coalescence can occur only when two bubbles collide. Therefore the probability of coalescence is the product of the probability of collision between two bubbles and the ratio between the number of coalesced bubbles to the number of collisions. The coalescence efficiency is determined from modelling the contact time and the drainage time of the film separating two bubbles (Prince and Blanch, 1990; Yao and Morel, 2004).

Fragmentation occurs when a bubble collides with a similarly sized turbulent eddy (Luo and Svendsen, 1996). Therefore, the probability of fragmentation is the product of the number of collisions between a bubble and a similarly sized eddy and the ratio between the number of fragmented bubbles to the number of such collisions. The fragmentation efficiency is determined from a critical Weber number and a Weber number built from the turbulent quantities associated with the bubble diameter Yao and Morel (2004). This leads to the final expression:

$$\int \dot{F}_{c,b}\pi d_b^2 \mathrm{d}d_b \mathrm{d}\mathbf{w} = a_i^{5/3}\epsilon_{dg}^{1/3}\alpha_{dg}^{1/3}\xi(N_c) \tag{2.93}$$

Where $N_c = 8.06 a_i^{-5/6}\alpha_{dg}^{5/6}\epsilon^{1/3}\sqrt{\rho_{cl}/\gamma_s}$, ϵ_{dg} is the fluid turbulent kinetic energy dissipation, ξ is a function of N_c only and γ_s is the surface tension. It contains a contribution for coalescence $\xi_c(N_c)$ and another for breakup $\xi_b(N_c)$. Again, for more details on these expressions and their derivation, I highly recommend looking at the original work from Ruyer (2007).

Interfacial transfer term in separated flows (LIM)

In order to apply interfacial models to a simulated interface, it is mandatory to detect it. The method, transcribed here, can be found in Coste (2013). In neptune_cfd, depending on the gradient of volume fraction, some cells are flagged as interfacial cells. In order to prevent issues related to residual phases, nearby cells are also flagged as interfacial cells (one on each side of the interface). This set of cells matching the fluid-fluid interface is named the three-cell stencil. A cell contains a large interface (LI) if the liquid volume fraction gradient $\nabla\alpha_{cl}$ exceeds a threshold value. The two adjacent cells are found by moving away from the LI cell in the normal direction to the interface $\mathbf{n} = \nabla\alpha_{cl}\|\nabla\alpha_{cl}\|^{-1}$. After locating the interface, the shear stresses on either side can be estimated with a similar method to those used in boundary layer theory. Eventually, by also taking into account the surface roughness (Brocchini and Peregrine, 2001*a*,*b*), it is possible to obtain the friction velocities u_{cg}^* and u_{cl}^* used to compute momentum transfer across a large interface. In all the cells but the three-cell stencil, the interfacial transfer term $\mathbf{I}_{g\to l}^D$ is defined according to usual models (see equation 2.82). In the three-cell stencil, a normal contribution is kept solely for numerical purposes. It helps enforce the relation $(\mathbf{U}_{cl} - \mathbf{U}_{cg}).\mathbf{n} = 0$ which would not be verified otherwise. To that, an anisotropic contribution which depends on the friction velocities and the sub-grid scale roughness is added to take into account surface friction.

$$\mathbf{I}^{D}_{cg\to cl,i} = \alpha_{cl}\alpha_{cg}F_D\left[(\mathbf{u}_{cg}-\mathbf{u}_{cl}).\mathbf{n}\right].\mathbf{n} - \mathbf{A}_{cg\to cl} \tag{2.94}$$

Where F_D is the standard drag coefficient used in dispersed flows and $\mathbf{A}_{cg\to cl}$ is the friction coefficient along the free surface. The expression for this friction term can be found in Coste (2013).

$$\mathbf{A}_{cg\to cl} = \rho_l u^*_{cl} a_i \frac{\mathbf{u}_{cg}-\mathbf{u}_{cl}}{\|\mathbf{u}_{cg}-\mathbf{u}_{cl}\|} \tag{2.95}$$

The turbulent quantities transport equations, specifically the production and dissipation terms, are also modified in the free-surface region in order to account for its presence (Coste and Laviéville, 2015). Since these have not been explored in this work, they are not discussed here.

Interfacial transfer terms in multi-regime flows (GLIM)

In the LIM model, cells that are not flagged as containing an interface may still contain both phases. In those, the momentum transfer term may not represent the real drag sustained by the dispersed phase. The main idea behind the GLIM model is to avoid this issue by integrating the models from previous sections in the LIM model. This process starts by identifying the three-cell stencil in all the domain and by applying the appropriate interfacial transfer terms in those cells. In other cells containing liquid and gas that are not flagged as interface cells, the disperse models are applied. Figure 2.13 shows regions which contains continuous and dispersed structures. The continuous-continuous interfaces are treated with the LIM approach and the small inclusions with the dispersed model. To maintain consistency, the transition between both models is continuously made with a weighting coefficient γ (Mérigoux, 2022). The total interfacial momentum transfer term can be decomposed as:

$$\mathbf{I}'_{cl\to g} = \gamma\mathbf{I}'_{cl\to dg} + (1-\gamma)\mathbf{I}'_{cl\to cg} \tag{2.96}$$

With,

$$\gamma = \beta(1-\min(f_c,1)) \tag{2.97}$$

Where β is a continuous function which equals 0 where $\alpha_l = 0$ and 1 where $\alpha_l = 1$:

$$\beta = \frac{1}{2}\left[\tanh\left(20\left(\alpha_l - \frac{1}{2}\right)\right)+1\right] \tag{2.98}$$

f_c is proportional to the ratio on the local volume fraction gradient and the maximum possible surface contained in a cell S_M.

$$f_c = \min\left(4\frac{\|\nabla\alpha_g\|}{S_M}, 1\right) \tag{2.99}$$

This weighting method, giving encouraging results, is also tested in a similar manner in other CFD softwares such as OpenFOAM. For examples see Mathur et al. (2019); De Santis, Colombo, Hanson and Fairweather (2021); De Santis, Hanson and Fairweather (2021). Like in the dispersed case and the LIM, turbulent quantities evolution equations are adapted to account for modulation effects. More detail on those can be seen in appendix B.

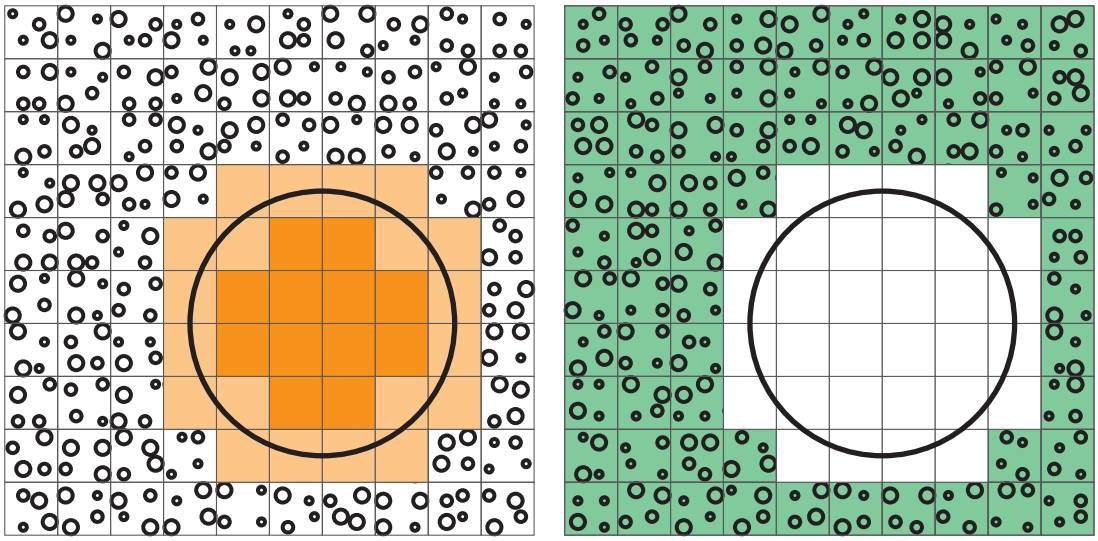

Figure 2.13: Sketch showing the different models applied in different regions of the domain depending on the flow characteristics. The orange zone is a continuous structures, the green region includes dispersed inclusions and the interface between the two is treated with the large interface model. The two point of view combined constitute the generalized large interface model from neptune_cfd.

The main objective during the thesis has been to develop a particle model in which large interfaces as well as dispersed phases can be simulated. The idea is to make the Lagrangian stochastic and Eulerian velocity moments models compatible with the large interface formulation. Thus introducing the idea that several continuous fields may interact with the same solid phase. Be it Lagrangian particles in the Lagrangian stochastic framework or a dispersed field in the Eulerian velocity moments formulation.

3 | Liquid-gas-solid flows models

In this chapter, we introduce the two models developed during the thesis. Both allow for modelling and simulation of particles evolving in multiphase flows. Both are also enhancements of existing two-phase models presented in the previous chapter. The Euler-Lagrange model is an evolution of the standard Lagrangian stochastic model for particles in single phase flows. The multi-Eulerian is the Eulerian counterpart of the Euler-Lagrange model, obtained from the Lagrangian increments and the velocity moments equations. In practice, the work carried out during the thesis consists in merging the existing Lagrangian stochastic models and the Eulerian velocity moments method with the standard multifluid model.

We start by introducing the two new models before considering updates on gravity and turbulence driven deposition.

3.1 Euler-Lagrange model

In this section, a new Euler-Lagrange stochastic model is introduced. The main goal is to combine existing Lagrangian stochastic models with a multifluid solver in order to simulate the behaviour of particles in liquid-gas flows. In practice, if no assumption is made on the behaviour of particles, they must be able to interact with every field present in the N-Eulerian framework independently from the underlying flow morphology. As a matter of fact, due to the design of the multifluid framework, one particle is never exclusively in one continuous phase or the other, it is moving inside a cell in a domain containing some volume fraction for every phase present in the computation. Therefore, the new method is not straightforward. Moreover, interfacial momentum transfer term closures are well documented for two-phase systems; for three or more phases, there is little to no experimental work on the topic. Some details about them can be found in Baltussen et al. (2017); Loudet et al. (2020).

The current way Lagrangian stochastic models are used in neptune_cfd is presented before introducing the limitations and issues arising from the formulation. Then, a new approach is presented and thoroughly analytically studied before presenting its behaviour when applied on an academic case.

3.1.1 Combining the existing model with neptune_cfd

Before the work carried out in this thesis, the Lagrangian stochastic model could be used in two different ways for particles moving in a two-phase flow. The first one consisted in eliminating the interaction between one continuous phase and the dispersed solid phase. Doing as if one of the two continuous phases did not exist and as if the particles were exclusively carried by the other phase. This strong hypothesis can

be verified but it would require extensive experimental investigation to be confirmed which can be, in the best case scenario, very expensive. Additionally, the basic case of particles falling through air and impacting a water free-surface would be impossible to model with such a model. The second method consists in creating a new mixture field from the two continuous phases and using this mixture field in the Lagrangian stochastic model. This is modelling the interaction between the particle phase and all the continuous phases but the way the mixture fields are defined is unclear. For example, for a variable X of n continuous fields, the mixture variable X_m could be defined as the following average:

$$X_m = \frac{\sum_{i=1}^{n} \alpha_i \rho_i X_i}{\sum_{i=1}^{n} \alpha_i \rho_i} \tag{3.1}$$

This would work well for the velocity because it would accurately average the overall drag sustained by the particle but it would make no sense to do the same for the turbulent fields. Therefore making it difficult to mathematically justify. The second method is able to predict the behaviour of particles impacting a water free-surface when turbulence for both fluids is weak. In a test case carried out at the beginning of the thesis, where particles were flowing inside a rectangular aerated free-surface jet (Carrillo, Castillo, Marco and García, 2020), particles were seen being ejected from the free surface due to turbulent values being abnormal in the region near water surface. Thus highlighting the need for a more suitable model to predict the behaviour of solid particles crossing a free-surface.

These two methods being unsatisfactory, a new approach had to be thought of. The main goal being to ensure interaction of particles with more than one fluid independently of its nature and topology. As seen in section 2.1, a stochastic Lagrangian approach for a solid phase p evolving in a fluid f can be described with the following system of equations.

$$\begin{aligned}
\delta x_{p,i} &= u_{p,i}\delta t \\
\delta u_{p,i} &= \frac{u_{f@p,i} - u_{p,i}}{\tau_{p,f}}\delta t \\
\delta u_{f@p,i} &= A_{f@p,i}\delta t + B_{f@p,ij}\delta W_{f,j}
\end{aligned} \tag{3.2}$$

The way we want to modify this approach is by assuming the particles exchange momentum with all the phases that could have a non zero volume fraction at the position they are in. λ_f is the weight each fluid f has on the overall momentum transfer experienced by the particle. Then for each fluid f, a Langevin type stochastic equation has to be solved in order to appropriately model their turbulence in the particle momentum balance equation. Figure 3.1 shows a schematic of a particle evolving in a liquid-gas flow for different kind of flow morphologies. Depending on the expression of the weight coefficient, this segmentation can have different physical meaning. For more details about the different models, refer to section 3.1.3.

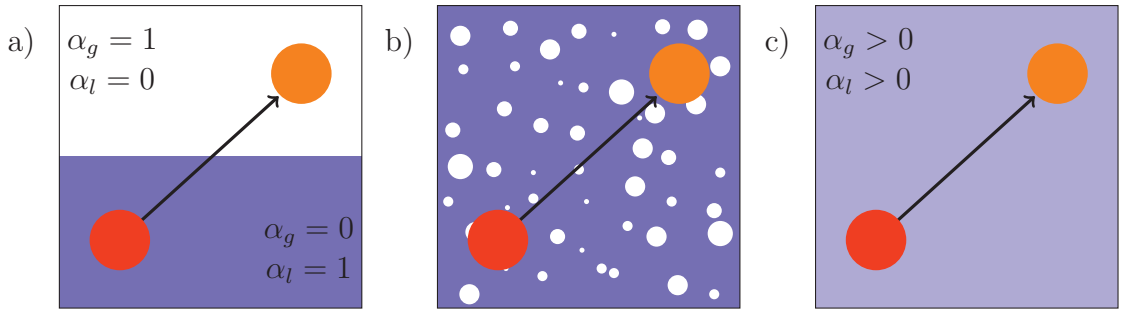

Figure 3.1: Different drawings showing a particle evolving in a liquid-gas mixture. The arrow represents the movement of a particle in time. Figure a) shows a particle moving through a resolved interface, figure b) shows a particle moving through a fully resolved bubbly flow and figure c) shows a particle moving through a statistically simulated liquid-gas flow.

For now, let's rewrite the Lagrangian stochastic system with the new formulation. Bearing in mind that there are as many Langevin equations on the fluid velocity seen by the particles as there are continuous phases they can interact with. Here, there are n continuous phases. Similarly to the introductory chapter, we decide to write the stochastic model in terms of the fluctuating fluid velocity seen rather than the total velocity seen by the particle.

$$
\begin{aligned}
&\delta x_{p,i} = u_{p,i}(t)\delta t \\
&\delta u_{p,i} = \left[\sum_{f=1}^{n} \frac{\lambda_f}{\tau_{p,f}} (u_{f@p,i} - u_{p,i}) + m_p g_i - m_p v_p \frac{\partial P}{\partial x_i} \right] \delta t \\
&\forall f \in [1, n]\,, \\
&\quad u_{f@p,i} = U_{f,i} + u'_{f@p,i} \\
&\quad \delta u'_{f@p,i} = \left[(G_{f@p,ij} - \frac{\partial U_{f,i}}{\partial x_j}) u'_{f@p,j} + H_i \right] \delta t + B_{f@p,ij} \delta W_{f,j}
\end{aligned}
\tag{3.3}
$$

In this case, it is easier to work with the fluctuating velocity seen by the particle $u'_{f@p,i}$ instead of the total velocity seen by the particle $u_{f@p,i}$. Indeed, the Langevin equations must be consistent with the mean fluid momentum conservation equations. Therefore, the interfacial transfer term should be included in the Langevin model. If it is not included, the pressure gradient faces no counterpart and the particle quickly behaves abnormally. By assuming there are no turbulent contributions to the interfacial transfer terms, we can simplify the Langevin model by expressing them in terms of fluctuating velocity seen (as it is done in equations 2.13). Working that way requires a special attention when it comes to fluctuation manipulation. Also, it seems to make the models more complex when two-way coupling is taken into account (Minier et al., 2014). However, since this phenomenon is not included in our new stochastic model, we prefer to work with the fluctuating component rather than the total velocity. Especially since, as will be noted in section 3.1.4, it also provides a noticeable improvement in the model accuracy. For details about the expressions for parameters of the model ($G_{f@p,ij}$, H_i and $B_{f@p,ij}$) see the previous chapter.

The way we solve this set of equations is inspired by how it is done in the standard model of code_saturne. Since the methodology has not been presented in the previous

chapter and that there are still some important variations that need to be addressed, we provide a detailed explanation here.

3.1.2 Stochastic system integration

Fully-implicit resolution of the stochastic equation

To solve the entire system, the fluctuation of fluid velocity seen by the particle must be integrated first. With the original stochastic model (Minier and Peirano, 2001), the fluid velocity seen components could be integrated independently with the constant variation method. Since, in the new general case, the velocity seen components are no longer independent, this method cannot be applied directly. However, for one fluid f, the equation for each components constitute a linear stochastic differential system.

$$\delta \mathbf{u'_{f@p}} + \mathrm{A}\mathbf{u'_{f@p}}\delta t = \mathbf{B}\delta t + \mathrm{C}\delta \mathbf{W_f} \tag{3.4}$$

By considering the system without right-hand side terms and by applying the constant variation method, it is possible to obtain a general form for the vector $\mathbf{u'_{f@p}}$.

$$\mathbf{u_{f@p}}' = e^{t\mathrm{A}}\mathbf{H} = \sum_{k=0}^{+\infty} \frac{(t\mathrm{A})^k}{k!}\mathbf{H} \tag{3.5}$$

Where the power series definition of the exponential function is used for computing matrices exponential and $\mathbf{H}$ is determined from the linear stochastic system (system 3.4). It is possible to obtain a general solution to this system, however, this method is impractical. In order to easily compute the exponential term, A must either be nilpotent, diagonal or diagonalisable. If that is not the case, the exponential can still be computed in practice with the Dunford decomposition (Lang, 2002). Unfortunately, in most cases, computing such a decomposition is time consuming. Since there are potentially many particles and time steps, investigating these possibilities further seemed inappropriate.

Semi-implicit resolution of the stochastic equation

A faster approach consists in isolating the diagonal terms in A, considering them implicitly and considering the rest of the matrix explicitly. This reduces the accuracy of the method and increases its dependency to the numerical time step but makes it a lot faster since it allows us to solve each component independently. We look for a solution to the stochastic equation written as an exponential term multiplied by a function C_i to be determined.

$$u'_{f@p,i} = C_i(t)e^{-\frac{t}{T^{L,*}_{f@p,i}}} \tag{3.6}$$

By assuming $u'_{f@p,i}$ is a solution to the stochastic equation, C_i must verify:

$$\delta C_i = e^{\frac{t}{T^{L,*}_{f@p,i}}}\left[\left(-\frac{\partial U_{f,i}}{\partial x_j}u_{f@p,j} + H_i\right)\delta t + B_{f@p,ij}\delta W_{f,j}\right] \tag{3.7}$$

Finally, by integrating between t_0 and t, with $\Delta t = t - t_0$, the expression for the fluctuating fluid velocity seen by a particle reads:

$$\begin{aligned} u'_{f@p,i}(t) = u'_{f@p,i}(t_0) e^{-\frac{\Delta t}{T^{L,*}_{f@p,i}}} + T^{L,*}_{f@p,i} \left(1 - e^{-\frac{\Delta t}{T^{L,*}_{f@p,i}}}\right) \left(H_i - \frac{\partial U_{f,i}}{\partial x_j} u'_{f@p,j}\right) \\ + B_{f@p,ij} e^{-\frac{\Delta t}{T^{L,*}_{f@p,i}}} \underbrace{\int_{t_0}^{t} e^{\frac{s}{T^{L,*}_{f@p,i}}} \mathrm{d}W_{f,j}(s)}_{\gamma_{f,i}(t)} \end{aligned} \tag{3.8}$$

Where $B_{f@p,ij}$ is proportional to δ_{ij} so that all the components are independent (see equation 2.18). The expression for the stochastic integral $\gamma_{f,i}$ will be detailed later. From equation 3.8, by carefully adding the mean velocity seen by the particle, it is possible to write an expression for the particle velocity and the particle position.

$$\begin{aligned} u_{p,i}(t) = u_{p,i}(t_0)\ e^{-\frac{\Delta t}{\tau_m}} + \left(\sum_{f=1}^{n} \frac{\lambda_f}{\tau_{p,f}} \int_{t_0}^{t} e^{\frac{s}{\tau_m}} U_{f@p,i}(s) \mathrm{d}s\right) e^{-\frac{t}{\tau_m}} \\ + \sum_{f=1}^{n} \frac{\lambda_f}{\tau_{p,f}} u'_{f@p,i}(t_0) \frac{\tau_m T^{L,*}_{f@p,i}}{T^{L,*}_{f@p,i} - \tau_m} \left(e^{-\frac{\Delta t}{T^{L,*}_{f@p,i}}} - e^{-\frac{\Delta t}{\tau_m}}\right) \\ + \sum_{f=1}^{n} \frac{\lambda_f}{\tau_{p,f}} C_{f,i} T^{L,*}_{f@p,i} \tau_m \left[\left(1 - e^{-\frac{\Delta t}{\tau_m}}\right) - \frac{T^{L,*}_{f@p,i}}{T^{L,*}_{f@p,i} - \tau_m} \left(e^{-\frac{\Delta t}{T^{L,*}_{f@p,i}}} - e^{-\frac{\Delta t}{\tau_m}}\right)\right] \\ + \underbrace{\sum_{f=1}^{n} e^{-\frac{t}{\tau_m}} \frac{\lambda_f}{\tau_{p,f}} \int_{t_0}^{t} e^{\frac{s}{\tau_m}} \gamma_{f,i}(s) \mathrm{d}s}_{\Gamma_i(t)} \end{aligned} \tag{3.9}$$

and,

$$\begin{aligned} x_{p,i}(t) = x_{p,i}(t_0) + u_{p,i}(t_0) \tau_m \left(1 - e^{-\frac{\Delta t}{\tau_m}}\right) \\ + \sum_{f=1}^{n} \frac{\lambda_f}{\tau_{p,f}} \frac{1}{2} \left(\frac{\Delta t^2}{2} U_{f,i}(x_p(t), t) + \tau_m \left(\Delta t\ e^{-\frac{\Delta t}{\tau_m}} - (1 - e^{-\frac{\Delta t}{\tau_m}})\right) U_{f,i}(x_p(t_0), t_0)\right) \\ + \sum_{f=1}^{n} \frac{\lambda_f}{\tau_{p,f}} \tau_m \frac{T^{L,*}_{f@p,i}}{T^{L,*}_{f@p,i} - \tau_m} u_{f@p,i}(t_0) \left[T^{L,*}_{f@p,i} \left(1 - e^{-\frac{\Delta t}{T^{L,*}_{f@p,i}}}\right) - \tau_m \left(1 - e^{-\frac{\Delta t}{\tau_m}}\right)\right] \\ + \sum_{f=1}^{n} \frac{\lambda_f}{\tau_{p,f}} \tau_m T^{L,*}_{f@p,i} C_{f,i} \left[\Delta t - \tau_m \left(1 - e^{-\frac{\Delta t}{\tau_m}}\right)\right. \\ \left. - \frac{T^{L,*}_{f@p,i}}{T^{L,*}_{f@p,i} - \tau_m} \left(T^{L,*}_{f@p,i} \left(1 - e^{-\frac{\Delta t}{T^{L,*}_{f@p,i}}}\right) - \tau_m \left(1 - e^{-\frac{\Delta t}{\tau_m}}\right)\right)\right] \\ + \underbrace{\int_{t_0}^{t} \sum_{f=1}^{n} e^{-\frac{s}{\tau_m}} \frac{\lambda_f}{\tau_{p,f}} \int_{t_0}^{s} e^{\frac{s'}{\tau_m}} \gamma_{f,i}(s') \mathrm{d}s' \mathrm{d}s}_{\Omega_i(t)} \end{aligned} \tag{3.10}$$

Where τ_m is a time-scale related to the particle relaxation time in each fluid and $C_{f,i} = H_i - \frac{\partial U_{f,i}}{\partial x_j} u'_{f@p,j}$.

$$\tau_m = \frac{1}{\sum_{f=1}^{n} \frac{\lambda_f}{\tau_{p,f}}} \tag{3.11}$$

The three expressions for the particle position, velocity and the fluid velocity at the position of the particle are of the same form as the original expressions. Their implementations can coexist. Now the expressions for the stochastic integrals ($\gamma_{f,i}$, Γ_i and Ω_i) need to be computed.

Computing the stochastic integrals

For the numerical scheme detailed in equations 3.8, 3.9 and 3.10 to be complete, it needs the evaluation of the stochastic integral terms $\mathbf{X} = \{\gamma_{1,i}, \ldots, \gamma_{n,i}, \Gamma_i, \Omega_i\}$. The covariance matrix C of $\mathbf{X}$ can be written as follows:

$$\mathrm{C} = \begin{pmatrix} \langle\gamma_{1,i}^2\rangle & \ldots & 0 & \langle\gamma_{f_1,i}\Gamma_i\rangle & \langle\gamma_{f_1,i}\Omega_i\rangle \\ \vdots & \ddots & \vdots & \vdots & \vdots \\ 0 & \ldots & \langle\gamma_{n,i}^2\rangle & \langle\gamma_{f_n,i}\Gamma_i\rangle & \langle\gamma_{f_n,i}\Omega_i\rangle \\ \langle\gamma_{f_1,i}\Gamma_i\rangle & \ldots & \langle\gamma_{f_n,i}\Gamma_i\rangle & \langle\Gamma_i\Gamma_i\rangle & \langle\Gamma_i\Omega_i\rangle \\ \langle\gamma_{f_1,i}\Omega_i\rangle & \ldots & \langle\gamma_{f_n,i}\Omega_i\rangle & \langle\Gamma_i\Omega_i\rangle & \langle\Omega_i\Omega_i\rangle \end{pmatrix} \tag{3.12}$$

In order to practically compute the stochastic integral terms, it is sufficient to evaluate $\mathrm{C}\mathbf{G_f}$, where $\mathbf{G_f}$ is a Gaussian vector of dimension $n+2$. The components of $\mathbf{G_f}$ follow a zero mean normal distribution and are all independent. However, this computation can be accelerated by considering the Choleski decomposition of the covariance matrix C. Since C is symmetric, positive and definite, it can be decomposed as $\mathrm{C} = \mathrm{P}\mathrm{P}^T$ where the exponent T denotes the transposition operation and P is a triangular matrix. The vector $\mathbf{Y}$ obtained by multiplying the Gaussian vector G_f by P is of zero mean and has a covariance matrix equal to C. It can therefore be used instead of $\mathbf{X}$ to drastically reduce the number of operations needed to solve the stochastic system. The components of the triangular matrix P are related to the components of the covariance matrix C in the following manner (Lang, 2002).

$$\forall (i,j) \in [1, n+2] \times [1, n+2], i \neq j,$$

$$P_{ii} = \sqrt{C_{ii} - \sum_{k=1}^{i-1} P_{ik}^2} \tag{3.13}$$

$$P_{ij} = \frac{C_{ij} - \sum_{k=1}^{j-1} P_{ik} P_{jk}}{P_{jj}} \tag{3.14}$$

On the other hand, to express the components of the covariance matrix C, we first need to rewrite $\mathbf{X}$ in terms of a simple stochastic integral. This can be done via the use of the integration by part theorem.

$$\gamma_{f,i}(t) = B_{f@p,ij} e^{-\frac{t}{T^{L,*}_{f@p,i}}} \int_{t_0}^{t} e^{\frac{s}{T^{L,*}_{f@p,i}}} \mathrm{d}W_{f,j}(s) \tag{3.15}$$

$$\Gamma_i(t) = \sum_{f=1}^{n} \frac{\lambda_f}{\tau_{p,f}} B_{f@p,ij} \theta_{fm,i} \tau_m \left[e^{-\frac{t}{T^{L,*}_{f@p,i}}} \int_{t_0}^{t} e^{\frac{s}{T^{L,*}_{f@p,i}}} \mathrm{d}W_{f,j}(s) - e^{-\frac{t}{\tau_m}} \int_{t_0}^{t} e^{\frac{s}{\tau_m}} \mathrm{d}W_{f,j}(s) \right] \tag{3.16}$$

$$\begin{aligned} \Omega_i(t) = \sum_{f=1}^{n} \frac{\lambda_f}{\tau_{p,f}} B_{f@p,ij} \theta_{fm,i} \tau_m \Bigg[& -T^{L,*}_{f@p,i} e^{-\frac{t}{T^{L,*}_{f@p,i}}} \int_{t_0}^{t} e^{\frac{s}{T^{L,*}_{f@p,i}}} \mathrm{d}W_{f,j}(s) \\ & + T^{L,*}_{f@p,i} \int_{t_0}^{t} \mathrm{d}W_{f,j}(s) + \tau_{m,i} e^{-\frac{t}{\tau_m}} \int_{t_0}^{t} e^{\frac{s}{\tau_m}} \mathrm{d}W_{f,j}(s) - \tau_m \int_{t_0}^{t} \mathrm{d}W_{f,j}(s) \Bigg] \end{aligned} \tag{3.17}$$

Where,

$$\theta_{fm,i} = \frac{T^{L,*}_{f@p,i}}{T^{L,*}_{f@p,i} - \tau_m} \tag{3.18}$$

Then, after tedious calculations, with the assumption that fluid fluctuations seen by the particle are independent, the covariance matrix terms read:

$$\langle \gamma^2_{f,i} \rangle = B^2_{@pf,ij} \frac{T^{L,*}_{f@p,i}}{2} (1 - e^{-2\Delta t / T^{L,*}_{f@p,i}}) \tag{3.19}$$

$$\begin{aligned} \langle \gamma_{f,i} \Gamma_i \rangle = \frac{\lambda_f}{\tau_{p,f}} \theta_{fm,i} \tau_m B^2_{f@p,ij} T^{L,*}_{f@p,i} \Bigg[& \frac{1}{2} (1 - e^{-2\Delta t / T^{L,*}_{f@p,i}}) \\ & - \frac{\tau_m}{T^{L,*}_{f@p,i} + \tau_m} (1 - e^{-\Delta t (1/T^{L,*}_{f@p,i} + 1/\tau_m)}) \Bigg] \end{aligned} \tag{3.20}$$

$$\begin{aligned} \langle \Gamma^2_i \rangle = \sum_f \frac{\lambda^2_f}{\tau^2_{p,f}} B^2_{f@p,ij} \theta^2_{fm,i} \tau^2_m \Bigg[& \frac{T^{L,*}_{f@p,i}}{2} (1 - e^{-2\Delta t / T^{L,*}_{f@p,i}}) \\ & - 2 \frac{T^{L,*}_{f@p,i} \tau_m}{T^{L,*}_{f@p,i} + \tau_m} (1 - e^{-\Delta t (1/T^{L,*}_{f@p,i} + 1/\tau_m)}) + \frac{\tau_m}{2} (1 - e^{-2\Delta t / \tau_m}) \Bigg] \end{aligned} \tag{3.21}$$

$$\begin{aligned} \langle \gamma_{f,i} \Omega_i \rangle = \frac{\lambda_f}{\tau_{p,f}} B^2_{f@p,ij} \theta_{fm,i} \tau_m T^{L,*}_{f@p,i} \Bigg[& - \frac{T^{L,*}_{f@p,i}}{2} (1 - e^{-2\Delta t / T^{L,*}_{f@p,i}}) \\ & + T^{L,*}_{f@p,i} (1 - e^{-\Delta t / T^{L,*}_{f@p,i}}) \\ & + \frac{\tau^2_m}{T^{L,*}_{f@p,i} + \tau_m} (1 - e^{-\Delta t (1/T^{L,*}_{f@p,i} + 1/\tau_m)}) - \tau_m (1 - e^{-\Delta t / T^{L,*}_{f@p,i}}) \Bigg] \end{aligned} \tag{3.22}$$

$$\begin{aligned} \langle \Gamma_i \Omega_i \rangle = \sum_f \left(\frac{\lambda_f}{\tau_{p,f}} B_{f@p,ij} \theta_{fm,i} \tau_m \right)^2 \Bigg[& (T^{L,*}_{f@p,i} - \tau_m) \left(T^{L,*}_{f@p,i} (1 - e^{-\Delta t / T^{L,*}_{f@p,i}}) - \tau_m (1 - e^{-\Delta t / \tau_m}) \right) \\ & - \frac{1}{2} \left({T^{L,*}_{f@p,i}}^2 (1 - e^{-2\Delta t / T^{L,*}_{f@p,i}}) + \tau^2_m (1 - e^{-2\Delta t / \tau_m}) \right) + \tau_m T^{L,*}_{f@p,i} (1 - e^{-\Delta t (1/T^{L,*}_{f@p,i} + 1/\tau_m)}) \Bigg] \end{aligned}$$

(3.23)

$$\begin{aligned}\langle\Omega_i^2\rangle = \sum_f \left(\frac{\lambda_f}{\tau_{p,f}} B_{f@p,ij}\theta_{fm,i}\tau_m\right)^2 \Bigg[& (T_{f@p,i}^{L,*} - \tau_m)\Bigg((T_{f@p,i}^{L,*} - \tau_m)\Delta t \\ & - 2\left({T_{f@p,i}^{L,*}}^2(1 - e^{-2\Delta t/T_{f@p,i}^{L,*}}) + \tau_m^2(1 - e^{-2\Delta t/\tau_m})\right)\Bigg) \\ & + \frac{1}{2}\left({T_{f@p,i}^{L,*}}^3(1 - e^{-\Delta t/T_{f@p,i}^{L,*}})(1 + e^{-\Delta t/T_{f@p,i}^{L,*}}) + \tau_m^3(1 - e^{-\Delta t/\tau_m})(1 + e^{-\Delta t/\tau_m})\right) \\ & - 2\frac{{T_{f@p,i}^{L,*}}^2\tau_m^2}{T_{f@p,i}^{L,*} + \tau_m}(1 - e^{-\Delta t(1/T_{f@p,i}^{L,*} + 1/\tau_m)})\Bigg]\end{aligned}$$

(3.24)

With the expression of the components of C and the relation between C and its decomposition P, it is possible to express the stochastic terms in the general expression of the particle position, velocity and the fluid velocity seen by the particle. A significant comment has to be made on the hypothesis of fluids fluctuation independence which was made to compute the components of the covariance matrix. This assumption cannot be made in the case of a turbulent coupling between the carrier phases. Additionally, all the developments have been carried out for an arbitrary number of continuous phases; the model is, in practice, not limited to liquid-gas-solid flows. The scope of the thesis on the other hand is limited to these types of flows.

3.1.3 Models for the weight coefficients

As seen in the previous sections, the weight coefficient model represents the main challenge for the developed method. Fortunately, some related work can be found in the literature and will help in the determination of this coefficient. The main challenge is still the fact that the liquid-gas flow is not entirely resolved. Thus, choosing an indicator function for λ_f is not suitable. A model needs to be developed in order to take into account the presence of statistically treated dispersed inclusions and continuous regions. This model should include various variables from all the phases present at the position of the particle including - but not limited to - the volume fraction, the velocity, the mean inclusion diameter if applicable and the physical properties of the particles and the fluids.

Initially, a natural model for the weight coefficient consists in thinking as if the particle is still in a liquid-gas mixture and to count the amount of mass from each phase interacting with it. This is equivalent to $\lambda_f = \frac{\alpha_f}{\sum_{f'}\alpha_{f'}}$. However, this is also equivalent to render the particle velocity not correlated to the phase it evolves in - which is not ideal for moving particles. Another possibility is to weight the drag contribution with the fluid density $\lambda_f = \frac{\alpha_f\rho_f}{\sum_{f'}\alpha_{f'}\rho_{f'}}$. This correlates the velocity of the particle to the fluid it evolves in but we struggle to find a mathematical justification to the expression. Another way of obtaining an expression for the weight coefficient is to consider a particle moving in a straight line through a randomly generated liquid-gas flow. Then, λ_f becomes an output of the numerically computed particle trajectory.

We set up this case for a particle of diameter d_p and mass per unit volume ρ_p moving in a random mixture of liquid and gas of mass per unit volume ρ_l and ρ_g, kinematic viscosity ν_l and ν_g, volume fraction α_l and $\alpha_g = 1 - \alpha_l$, the liquid velocity is u_l and the relative velocity between the two phases is $u_r = u_l - u_g$. The position and velocity of the particle are $t \mapsto x_p(t)$ and $t \mapsto u_p(t)$. The volume fraction of the particle is negligible. At $t = 0$, the particle is at $x_p(0) = 0$, has a velocity $u_p(0) = u_0$ and is found in the dominant phase (the one with the highest volume fraction). The only force acting on the particle is drag, written following standard practices Wen and Yu (1966) - more details on those are given in section 3.2.4. The indicator functions $\mathbb{1}$ are used to determined whether the particle is in the gas or the liquid phase: they indicate the presence of each phase. In this scenario, the particle trajectory is defined by the system of equations 3.25 in a fixed reference frame.

$$\begin{aligned} \delta x_p &= u_p(t)\delta t \\ \delta u_p &= \left(\mathbb{1}_l \frac{u_p(t) - u_l}{\tau_{p,l}} + \mathbb{1}_g \frac{u_p(t) - u_g}{\tau_{p,g}} \right) \delta t \end{aligned} \tag{3.25}$$

During the simulation, the particle starts in the predominant phase. Then, depending on the volume fraction, a probability r of collision between the particle and the dispersed inclusions is computed. This probability can be obtained from a collision efficiency E_c, the ratio between the number of particles colliding with a bubble per unit time and the number of particles flowing nearby it (Schulze, 1989). Thus limiting the time spent by particles in the bubble. Many models exist, depending on the case, it can be wiser to pick one or the other. The simplest collision efficiency model has been developed in Langmuir and Blodgett (1946). It predicts the collision efficiency as follows:

$$E_c = \left(\frac{K}{K + 0.2} \right)^2 \tag{3.26}$$

Where K is the Stokes number for the particles.

$$K = \frac{\rho_p v_b d_p^2}{9 \eta d_b} \tag{3.27}$$

This model is valid for inertial deposition of particles; limiting its use where collisions are predominantly due to geometric crossing of the trajectories or Brownian diffusion (Yang et al., 1995). In the model from Sutherland (1948), where bubbles are inside a potential flow and particles have no inertia, the collision efficiency is expressed as follows:

$$E_c = \frac{3 d_p}{d_b} \tag{3.28}$$

According to the review from Dai et al. (2000), the most promising model with regards to experimental comparison is the GSE model (Dukhin et al., 1995). However, since it includes variables which are not easily accessible in the multifluid solver, we

choose not to consider it and consider the one from Gourdel et al. (2000) instead. In that work, the mean time separating two collisions between two different inclusions A and B is:

$$\tau_{AB} = \frac{d_B^3}{6d_{AB}^2 \alpha_B \|\mathbf{U_A} - \mathbf{U_B}\|} \tag{3.29}$$

Where d_{AB} is the mean between the two inclusions diameter, $\mathbf{U_A}$ and $\mathbf{U_B}$ are the mean velocities for inclusions A and B and α_B is the volume fraction of inclusions of type B. From this expression, the mean number of collisions during a time step δt can be obtained.

$$r = \max\left(\frac{\delta t}{\tau_{AB}}, 1\right) = \max\left(\frac{6d_{AB}^2}{d_B^3}\|\mathbf{U_A} - \mathbf{U_B}\|\delta t, 1\right) \tag{3.30}$$

At each time step, a random number ω is drawn following a uniform law between 0 and 1. If $\omega < r$ then the particle enters a dispersed inclusion and stays in it until it crosses the other side of the inclusion. When it comes out of it, the same random process begins again. If $\omega > r$, the particle continues to evolve in the dominant fluid. This methodology is summed up in algorithm 1.

Algorithm 1: Weight coefficients computation routine. In this scenario the liquid phase is predominant and the gaseous phase is dispersed.

$x_p = 0$, $x_0 = 0$, $u_p = u_0$, $t = 0$, $c = 0$;
Choose α_l and α_g (in this case $\alpha_l > \alpha_g$)
Choose bubble diameter d_b, time step δt and maximum time $t_{\max}$
while $t < t_{max}$ **do**
  if $\mathbb{1}_g = 1$ **then**
    criteria $= \|x_0 - x_p\| < d_b$
  end
  else
    Choose $\omega \in [0, 1]$ randomly
    Compute probability of collision $r = \max\left(\frac{\delta t}{\tau_{AB}}, 1\right)$
    $c \leftarrow \omega < r$
  end
  if c **then**
    if $\mathbb{1}_l = 1$ **then**
      $x_0 \leftarrow x_p$
    end
    $\mathbb{1}_l = 0$, $\mathbb{1}_g = 1$
  end
  else
    $\mathbb{1}_l = 1$, $\mathbb{1}_g = 0$
  end
  $u_p \leftarrow u_p + -g - \left(\mathbb{1}_l \frac{u_p - u_l}{\tau_{p,l}} + \mathbb{1}_g \frac{u_p - u_g}{\tau_{p,g}}\right)\delta t$
  $x_p \leftarrow x_p + u_p \delta t$
end

Evidently, assuming the particle moves in a straight line is a strong assumption. In reality, a tiny particle with a small relaxation time arriving in the vicinity of a larger

bubble might never collide with it. The particle would simply follow the streamlines of the liquid flow around the bubbles and go past it. Even though this is partially taken into account in the collision probability, its accuracy is still lower than in the case where the exact particle trajectory is computed. Also, the hydrophobic properties of the particles or the state of the bubble surface can alter the collision rate between bubbles and particles (Malgarinos et al., 2016; Vilela and de Souza, 2020). All of this could, in theory, be included in the model for the collision probability in our framework. The results obtained for the weight coefficients are shown in figure 3.2 for different bubble and particle diameters.

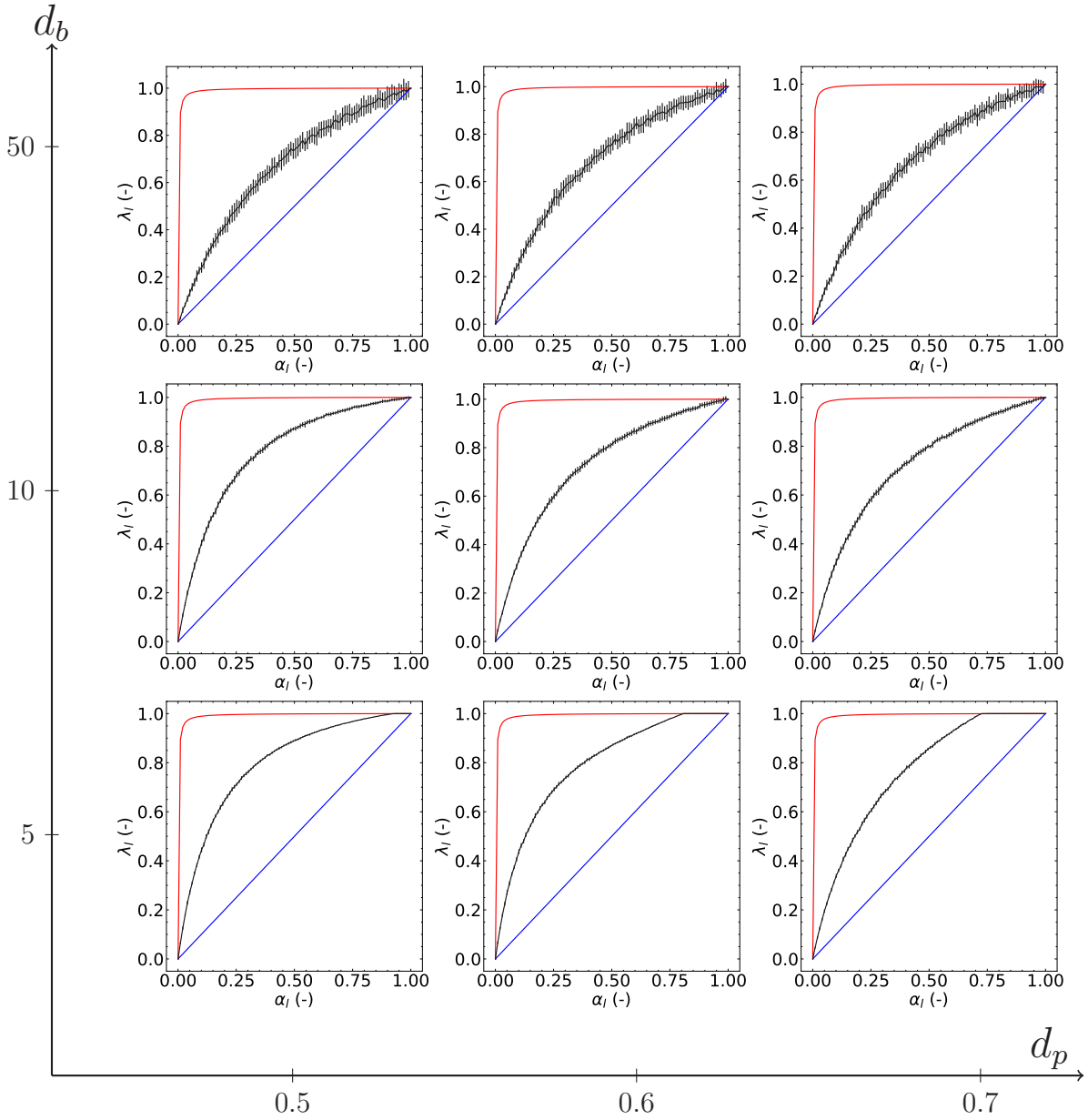

Figure 3.2: λ_l values computed with the standard models (red and blue) and with the routine presented above (black). Bubble and particle diameters are shown in mm.

The figure illustrates in general how the real time spent by a particle inside one or the other phase is not well described by the initial naive model. Finally, it should

be noted that this representation is not always applicable. In the case of surfactants trapped on a liquid-gas interface, a case widely occurring in industrial applications, the particles no longer experience drag as we defined it in the framework. They start moving along the interface which is itself moving at a certain speed. To enable the simulation of this scenario, the particle momentum balance equation should be reworked.

3.1.4 Verification case: particles falling through a density interface

In this section, we test the model on a simple verification test case: a particle falling through a density interface. At first, the model is tested on a standard simulation before comparing its prediction with an experimental setup. The standard simulation gives arguments for the use of the fluctuating fluid velocity seen rather than the total velocity seen in the Lagrangian stochastic model whereas the experimental comparison gives a more quantitative evaluation of the performance of the model. Figure 3.3 shows the concept of the test case as well as the pressure field seen by the particle.

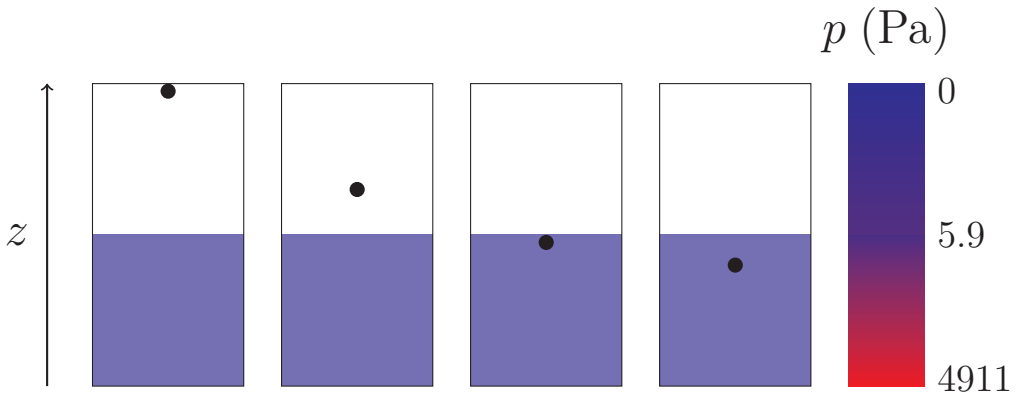

Figure 3.3: Drawings showing the particle falling. The particle slows down when it encounters a denser liquid. On the right is the pressure in Pa in the two-phase flow. Its gradient is proportional to the fluid density.

In the first test case, different particles of diameter d_p and mass per unit volume ρ_p, fall vertically through air ($\rho_a = 1.2\,\mathrm{kg\,m^{-3}}$, $\nu_a = 1.5 \times 10^{-5}\,\mathrm{m^2\,s^{-1}}$) and hit an air-water free-surface ($\rho_w = 1 \times 10^3\,\mathrm{kg\,m^{-3}}$, $\nu_w = 1 \times 10^{-6}\,\mathrm{m^2\,s^{-1}}$). The total height of the domain is 1 m and the free-surface is located at I. Two 1D Cartesian meshes are used in this case. The coarse one has 10 elements in the vertical direction and the fine one has 100. The first step consists in showing the good agreement between the simulation and expected results. Simulations with particles heavier or lighter than water and with different diameters are performed and the results are shown in figure 3.4. When applicable, the terminal velocity of particles in water is compared to analytical values. Also, particles heavier than water are expected to fall to the lower boundary whereas particles lighter than water - but still heavier than air - are expected to oscillate near the free surface. The lighter the particle, the closer to the interface it oscillates.

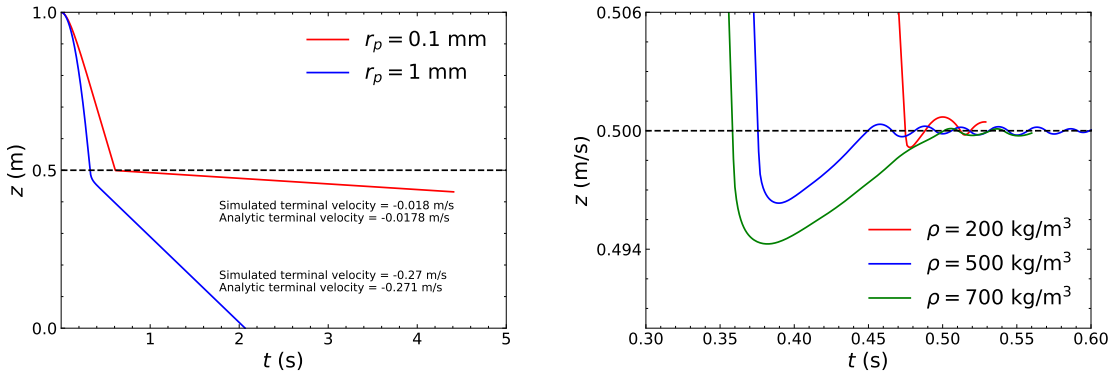

Figure 3.4: Simulated particle position as a function of time. The dashed line represents the position of the interface ($I = 0.5\,\mathrm{m}$ in this case). (left) Particles are heavier than water. (right) Particles are lighter than water.

Since the Eulerian fields are not interpolated at the position of a particle, the field value at the centre of the cell the particle is in is selected. Thus, a different behaviour between the two meshes is expected when the interface is not located on a cell boundary face. When the mesh is sufficiently fine, the position of the interface does not matter, the interpolation errors are small. For an interface located at the centre of a large cell, a particle falling through air interacts with the interface before physically reaching it. This can be quantified by comparing the simulation results in the fine and coarse meshes with a particle of diameter $r_p = 1\,\mathrm{mm}$ and mass per unit volume $\rho_p = 5 \times 10^3\,\mathrm{kg\,m^{-3}}$.

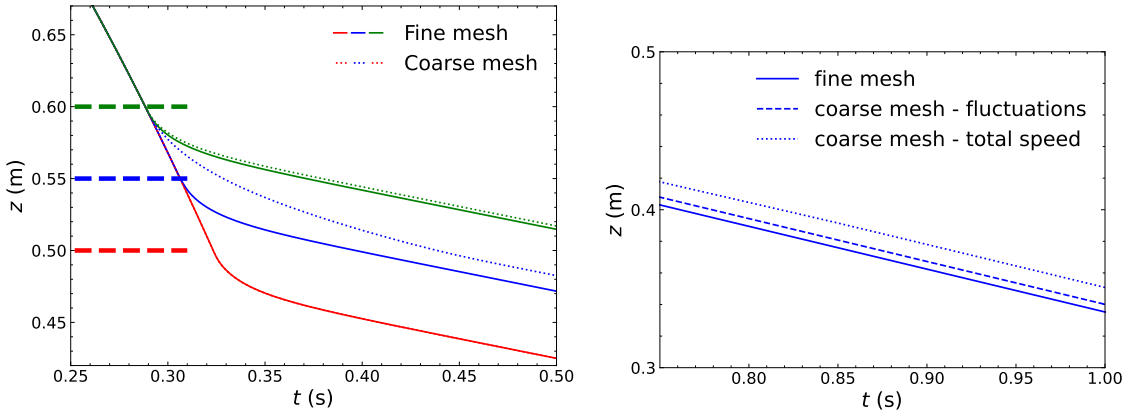

Figure 3.5: (left) Simulated particle position as a function of time. The thick dashed lines on the left denotes the position of the interface $I = 0.5\,\mathrm{m}$, $0.55\,\mathrm{m}$ and $0.6\,\mathrm{m}$. (right) Simulated results when using the total velocity seen rather than its fluctuation are shown to give worst results.

With the fine grid, the behaviour of a particle is not related to the position of the interface - except for the time at which it hits it. On the contrary, as figure 3.5 shows, with the coarse grid, when the interface is located at a cell centre ($I = 0.55\,\mathrm{m}$), the results are substantially worst than the results obtained with the fine grid compared to the difference when the interface is located at a cell boundary. The particle entering the cell which contains the interface is slowed down even though it hasn't reached the free-surface because the pressure gradient is not interpolated at the position of the particle. However, using a stochastic model on the fluctuating velocity seen instead of

the total velocity seen seems to give better results. This is probably due to the lower amount of calls to Eulerian fields in the second case. Each call introducing an interpolation error (linear interpolation), having less of them naturally improves the results.

The experimental setup of Verso et al. (2019) studies the behaviour of solid particles falling through a non-finite density interface. The measurements performed through these experiments constitute a suitable liquid-gas-solid flow dataset to judge the accuracy and performance of the new multiphase Lagrangian stochastic model. The fluids used in the experiments are stacked one on top of the other. 3 different types of particles are used (P1-P3). The top fluid is indexed by 1 and the bottom one by 2. The characteristics of the particles and the two fluids are summed up in table 3.1. As in the previous test case, a 1D Cartesian mesh is used with 100 elements in the vertical direction to reduce the interpolation errors. In the simulation, the interface is supposed to be infinitely thin. These will allow us to check the correct behaviour of the particles far away from the surface. Eventually, simulations are carried out with a density interface of thickness $h = 0.013\,\mathrm{m}$, matching the one in the experiment.

particles	ρ_p	d_p	**fluids**	ρ_1	ρ_2	ν_1	ν_2
P1	$1033 - 1100$	$850 - 1000$		976	1025	1.43×10^{-6}	1.01×10^{-6}
P2	$1150 - 1250$	$425 - 500$		-	-	-	-
P3	$2450 - 2550$	$710 - 850$		-	-	-	-

Table 3.1: Characteristics for the particles and fluids used in the experiments of Verso et al. (2019). Mass per unit volumes are in $\mathrm{kg\,m^{-3}}$, diameters in µm and viscosities in $\mathrm{m^2\,s^{-1}}$.

The simulation results are plotted against experimental data from Verso et al. (2019) in figure 3.6. z is the position of the particle along the vertical axis, $z = 0$ represents the top position of the interface in the experiment, v is the particle vertical velocity and V_1 is the terminal velocity of the particle in fluid 1. As can be seen in the figure, the particle velocity near the free-surface does not match the measurements. However, the behaviour away from the interface and the position of the particle are satisfactory. It is thought that differences in velocities near the fluid-fluid interface is due to the assumption of it being infinitely thin in the simulations compared to finite in size in the experiments. Even though results are noticeably better when the surface matches the experimental setup, there still are some discrepancies which are probably due to the low amount of physics modelled at the interface. In reality, surface tension or the interface deformation have an impact on the particle behaviour which is neglected in our case. All in all, we are happy the model gives accurate results for particles crossing a density interface.

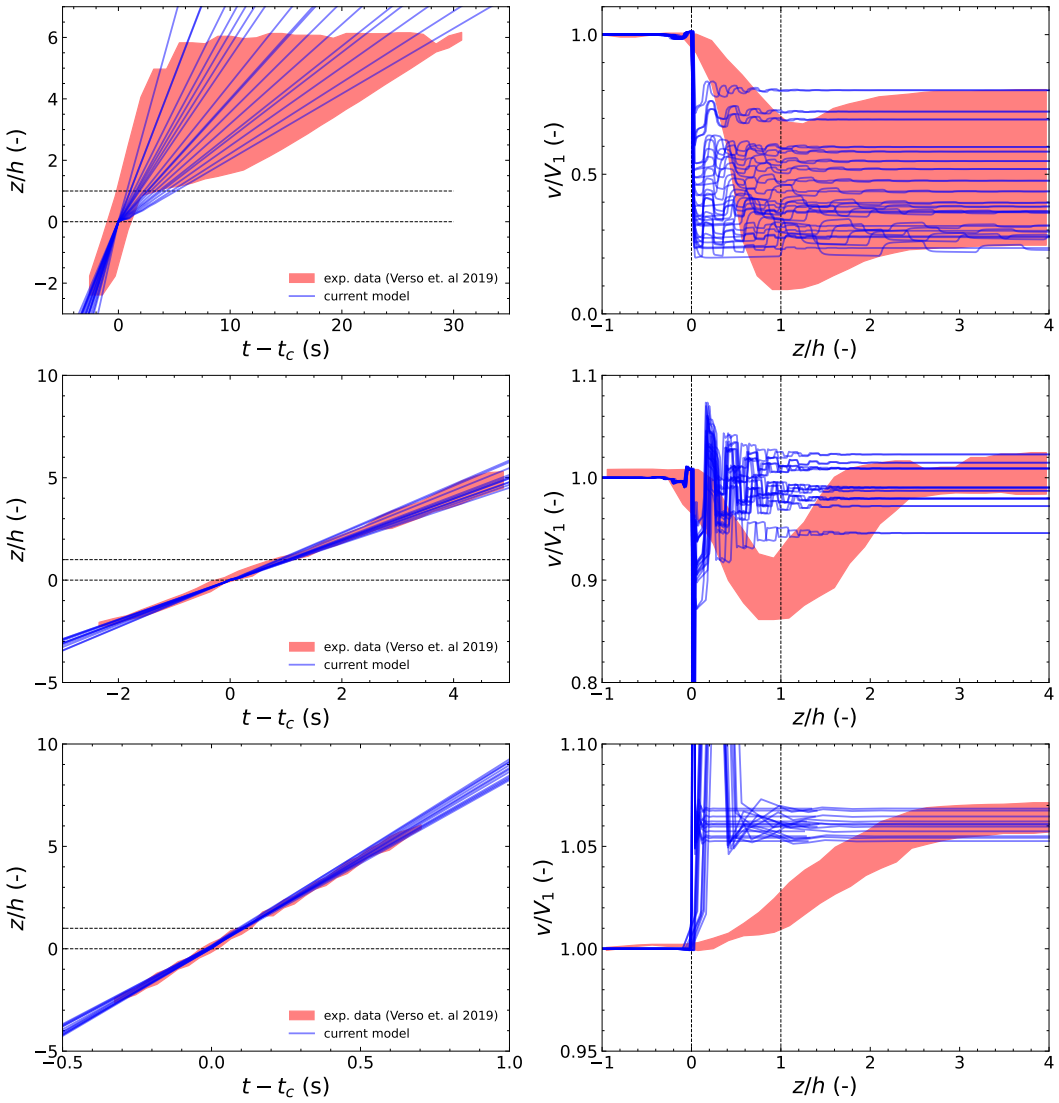

Figure 3.6: Simulation results compared with the experimental results from Verso et al. (2019). The dashed line represent the extent of the density interface in the experiments. In the simulation the interface is infinitely thin and located at $z/h = 0$

3.2 Eulerian velocity moments modelling

This section is devoted to the introduction of Eulerian modelling for a solid dispersed phase in multiphase flows. As is usually done in two-phase flows (liquid-solid or gas-solid), and as was done in section 2.2.2; it is possible, from the Lagrangian stochastic model, to get the evolution equation for the solid phase in an Eulerian framework. In this section, we introduce the new liquid-gas-solid Eulerian model based on the Lagrangian approach developed in section 3.1. Like the Lagrangian model, it originated during the thesis. We first present the fluid equations and the velocity moments method used to derive the particle phase conservation equations. Then, we show the principles behind the "hybrid" method which enables us to consider the particles and fluids phase within the same framework. This verification is similar to the one carried out in the two-phase flow case in section 2.2.2. However, since it is not trivial, it is still important to demonstrate how the arguments need to be adapted for them to stand even in this

scenario. Finally, we present the turbulence models and the closures that were obtained from this formulation.

3.2.1 Hybrid methodology: phase and ensemble average in a three-phase flows

Let us consider a liquid-gas-solid flow. Each fluid phase can be labelled with the letter f or g and the solid phase is labelled with the letter p. From the fluids point of view (see section 2.2), it is possible to obtain the conservation equation for mass and momentum from the local instantaneous equations and the jump conditions (Delhaye, 1974; Kataoka, 1985; Ishii and Hibiki, 2011). Since particles are also present and have a different impact on the fluid phases then other fluid phases do, we decided to isolate their interfacial momentum transfer contribution ($I_{p\to f,i}$) in the momentum balance equation. We immediately neglect phase change for the sake of clarity.

$$\frac{\partial}{\partial t}(\alpha_f \rho_f) + \frac{\partial}{\partial x_i}(\alpha_f \rho_f U_{f,i}) = 0 \tag{3.31}$$

$$\begin{aligned}\frac{\partial}{\partial t}(\alpha_f \rho_f U_{f,i}) + \frac{\partial}{\partial x_j}(\alpha_f \rho_f U_{f,i} U_{f,j}) = \alpha_f \rho_f g_i - \frac{\partial}{\partial x_j}\langle \rho u''_{f,i} u''_{f,j} \chi_f \rangle + \frac{\partial}{\partial x_j}(\alpha_f T_{f,ij}) \\ - \frac{\partial}{\partial x_i}(\alpha_f P) + \sum_{f' \neq f} I_{f'\to f,i} + I_{p\to f,i}\end{aligned} \tag{3.32}$$

With the same jump conditions as in the two-phase case (equation 2.42) and the same hypothesis (no mass transfer across an interface and a single pressure in all the fluids).

From the particle point of view, the phase space associated with the ensemble of particles is more detailed than in the two-phase case. Let us consider an ensemble of particles evolving in a multifluid flow. The associated phase space $\mathbf{H}$ includes time t, the probable particle position $\mathbf{x}$, velocity $\mathbf{c_p}$ and the probable fluid velocities seen by the particle $\mathbf{c_{f_1}}, \ldots, \mathbf{c_{f_n}}$. The fluid-particle joint probability density function f_p is defined on the phase space such that $f_p(\mathbf{c_p}, \mathbf{c_{f_1}}, ..., \mathbf{c_{f_n}}; \mathbf{x}, t)\delta\mathbf{c_p}\delta\mathbf{x}\prod_{g=f_1}^{f_n}\delta\mathbf{c_g}$ is the number of particles with a centre of mass at time t in the volume $\Omega = \{\mathbf{x}, \mathbf{x}+\delta\mathbf{x}\}$, with a velocity $\mathbf{u_p} \in \{\mathbf{c_p}, \mathbf{c_p}+\delta\mathbf{c_p}\}$ and the velocity of fluid f seen by the particle $\mathbf{u_{f@p}} \in \{\mathbf{c_f}, \mathbf{c_f}+\delta\mathbf{c_f}\}$. According to common derivation (Simonin, 2000), f_p satisfies the following Liouville transport equation.

$$\begin{aligned}\frac{\partial f_p}{\partial t} + \frac{\partial}{\partial x_j}(c_{p,j} f_p) + \frac{\partial}{\partial c_{p,j}}\left[\left\langle \frac{\mathrm{d}u_{p,j}}{\mathrm{d}t} | \mathbf{c_p}, \mathbf{c_{f_1}}, \ldots, \mathbf{c_{f_n}} \right\rangle f_p\right] \\ + \sum_{f=f_1}^{f_n} \frac{\partial}{\partial c_{f,j}}\left[\langle \frac{\mathrm{d}u_{f@p,j}}{\mathrm{d}t} | \mathbf{c_p}, \mathbf{c_{f_1}}, \ldots, \mathbf{c_{f_n}} \rangle f_p\right] = \left(\frac{\partial f_p}{\partial t}\right)_{\text{coll}}\end{aligned} \tag{3.33}$$

Where the arguments in the conditional averages have been neglected for brevity. For a detailed definition, see section 2.2.2. An additional hypothesis is necessary to

match those of the Lagrangian framework. To ensure $\langle u''_{f_1@p,i} u''_{f_2@p,j} \rangle = 0$ for $f_1 \neq f_2$, the PDF must verify:

$$\begin{aligned} & n_p \langle u''_{f1@p,i} u''_{f2@p,j} \rangle \\ & \quad = \int [c_{f1,i} - U_{f1@p,i}][c_{f2,j} - U_{f2@p,j}] f_p(\mathbf{c_p}, \mathbf{c_{f1}}, \ldots, \mathbf{c_{fn}}) \mathrm{d}\mathbf{c_p} \prod_{f=f1}^{fn} \mathrm{d}\mathbf{c_f} \\ & \quad = \int_{c_{f1}} \int_{c_{f2}} [c_{f1,i} - U_{f1@p,i}][c_{f2,j} - U_{f2@p,j}] f_{f1-f2}(\mathbf{c_{f1}}, \mathbf{c_{f2}}) \mathrm{d}\mathbf{c_{f1}} \mathrm{d}\mathbf{c_{f2}} \\ & \quad = 0 \end{aligned} \tag{3.34}$$

Where the arguments $\mathbf{x}$ and t are dropped in f_p and $f_{f_1-f_2}$ is the joint PDF of the set of fluids f_1 and f_2 respectively. This relation is verified when $f_{f_1-f_2} = f_{f_1} f_{f_2}$. The main idea behind this new model is to include all of the fluid phases in the statistical description since one particle can interact with all of the fluid phases. Then, as in the two-phase case, it is possible to obtain the moment equations by multiplying the PDF transport equation by ψ_p, a function of the phase space variables, and by integrating over all the possible outcomes for the ensemble of particles. Again, the mass of one particle is supposed to be constant.

$$\begin{aligned} & \frac{\partial}{\partial t}(n_p m_p \langle \psi_p \rangle) + \frac{\partial}{\partial x_j}(n_p m_p \langle u_{p,j} \psi_p \rangle) + n_p m_p \left\langle \langle \frac{\mathrm{d}u_{p,i}}{\mathrm{d}t} | \mathbf{c_p}, \mathbf{c_f} \rangle \frac{\partial \psi_p}{\partial c_{p,j}} \right\rangle \\ & \qquad + \sum_f n_p m_p \left\langle \langle \frac{\mathrm{d}u_{f@p,i}}{\mathrm{d}t} | \mathbf{c_p}, \mathbf{c_f} \rangle \frac{\partial \psi_p}{\partial c_{f,j}} \right\rangle + n_p \mathbb{C}(m_p u_{p,i}) = 0 \end{aligned} \tag{3.35}$$

Finally, by replacing ψ_p by the appropriate function, we can get the needed conservation equations for the particle phase. Since, by replacing ψ_p by 1 or $c_{p,i}$, equation 3.35 becomes equation 2.23 (the same equation as in the two-phase case), we do not detail their derivation here.

$$\frac{\partial}{\partial t}(n_p m_p) + \frac{\partial}{\partial x_i}(n_p m_p U_{p,i}) = 0 \tag{3.36}$$

$$\begin{aligned} \frac{\partial}{\partial t}(n_p m_p U_{p,i}) + \frac{\partial}{\partial x_j}(n_p m_p U_{p,i} U_{p,j}) = & - \frac{\partial}{\partial x_j}\left(n_p m_p \langle u''_{p,i} u''_{p,j} \rangle\right) \\ & + n_p m_p \langle \frac{\mathrm{d}u_{p,i}}{\mathrm{d}t} \rangle + n_p \mathbb{C}(m_p u_{p,i}) \end{aligned} \tag{3.37}$$

The expression of the particle change rate of momentum is the same as in the two-phase case except for the fact that more fluids can transfer momentum to the particle. It is the mean particle acceleration between two instantaneous collisions. Like in the two-phase case, there is a discrepancy between the way interfacial transfer terms are computed in both approaches (from the fluids or the particle phase point of view see equations 2.54 and 2.55 in section 2.2.2). However, by joining all the transfer terms together and assume the discrepancy is accounted for in the mean pressure contribution term, it is possible to show that the equations obtained from the two frameworks are consistent.

$$\begin{aligned} I^A_{p\to f,i} + \sum_{f'\neq f,p} I^A_{f'\to f,i} &= -P\langle n_{f,i}\delta_{fp}\rangle - \sum_{f'\neq f,p} P\langle n_{f,i}\delta_{ff'}\rangle \\ &= -P\langle n_{f,i}\delta_f\rangle \\ &= P\frac{\partial \alpha_f}{\partial x_i} \end{aligned} \tag{3.38}$$

Additionally, it is possible to close the unknown interfacial transfer term in the fluids equations.

$$I^D_{p\to f,i} = -I^D_{f\to p,i} \tag{3.39}$$

Because, for a mixture of strictly more than two components, the phase average of the normal vector between two phases cannot be written in terms of the gradient of a volume fraction, it is impossible to get the relation between two distinct phases. We only get the global relation.

3.2.2 Time increment closures for the particle velocity and fluid velocity seen

The closure for particle momentum and fluid velocity seen time increments is described in equation 3.3. The weight coefficient λ_f has the same meaning and definition as it does in the Lagrangian framework. We recall them hereafter with the complete set of forces accounted for in the model:

$$\begin{aligned} &\delta u_{p,i} = \left[\sum_{f=1}^{n} \frac{\lambda_f}{\tau_{p,f}}(u_{f@p,i} - u_{p,i}) + m_p g_i - m_p v_p \frac{\partial P}{\partial x_i}\right]\delta t \\ &\forall f \in [1,n]\,, \\ &\quad u_{f@p,i} = U_{f,i} + u'_{f@p,i} \\ &\quad \delta u'_{f@p,i} = \left[(G_{f@p,ij} - \frac{\partial U_{f,i}}{\partial x_j})u'_{f@p,j} + H_i\right]\delta t + B_{f@p,ij}\delta W_{f,j} \end{aligned} \tag{3.40}$$

Where m_p is the mass of a particle, v_p is its volume and P is the pressure at the position of the particle.

3.2.3 Turbulence modelling and closures

Adaptation of Tchen's turbulence theory to the liquid-gas-solid case

The first approach explored for describing the turbulence of the particle phase in a mutliphase flow was adapted from Tchen's turbulence theory (Mou, 1947). It now takes into account the influence of multiple fluids in the particle turbulence. We start by describing the particle phase with a simplified stochastic model.

$$\delta u_{p,i} = \sum_f \frac{\lambda_f}{\tau_{p,f}} u_{f@p,i}\delta t - u_{p,i}\sum_f \frac{\lambda_f}{\tau_{p,f}}\delta t \tag{3.41}$$

$$\delta u_{f@p,i} = -\frac{u_{f@p,i}}{T^L_{f@p}}\delta t + B_{f@p,ij}\delta W_{f,j} \tag{3.42}$$

Where $T^L_{f@p}$ is the fluid Lagrangian integral time scale of velocity fluctuations measured along a particle trajectory. Since, for some well chosen function g, $\mathrm{d}\langle g(\mathbf{Z})\rangle = 0$:

$$\mathrm{d}\langle u''_{f,i}u''_{f,j}\rangle = 0 \quad \Longrightarrow \; B_{f@p,ij} = 2\frac{\langle u''_{f@p,i}u''_{f@p,j}\rangle}{T^L_{f@p}} \tag{3.43}$$

$$\mathrm{d}\langle u''_{p,i}u''_{p,j}\rangle = 0 \quad \Longrightarrow \; \langle u'_{p,i}u'_{p,j}\rangle = \frac{1}{\sum_f \frac{\lambda_f}{\tau_{p,f}}}\sum_f \frac{\lambda_f}{\tau_{p,f}}\langle u'_{p,i}u'_{f@p,j}\rangle \tag{3.44}$$

$$\mathrm{d}\langle u''_{p,i}u''_{f@p,j}\rangle = 0 \quad \Longrightarrow \; \langle u''_{p,i}u''_{f@p,j}\rangle = \frac{\sum_{f'} \frac{\lambda_{f'}}{\tau_{p,f'}}\langle u''_{f'@p,i}u''_{f@p,j}\rangle}{\sum_{f'} \frac{\lambda_{f'}}{\tau_{p,f'}} + \frac{1}{T^L_{f@p}}} \tag{3.45}$$

Then, since there is no covariance between two different velocity seen by the particle, the expression for the particle velocity correlation and the fluid-particle velocity covariance follow:

$$\langle u''_{p,i}u''_{f@p,j}\rangle = \frac{\lambda_f}{\tau_{p,f}}\frac{\langle u''_{f@p,i}u'_{f@p,j}\rangle}{\sum_{f'} \frac{\lambda_{f'}}{\tau_{p,f'}} + \frac{1}{T^L_{f@p}}} \tag{3.46}$$

$$\begin{aligned}\langle u''_{p,i}u''_{p,j}\rangle &= \frac{1}{\sum_f \frac{\lambda_f}{\tau_{p,f}}}\sum_f \frac{\lambda_f}{\tau_{p,f}}\langle u''_{p,i}u''_{f@p,j}\rangle \\ &= \frac{1}{\sum_f \frac{\lambda_f}{\tau_{p,f}}}\sum_f \left(\frac{\lambda_f}{\tau_{p,f}}\right)^2 \frac{\langle u''_{f@p,i}u''_{f@p,j}\rangle}{\sum_{f'} \frac{\lambda'_f}{\tau_{p,f'}} + \frac{1}{T^L_{f@p}}}\end{aligned} \tag{3.47}$$

From the Eulerian quantities, the flow characteristics and the equations above, it is possible to take into account the particle phase turbulence with an updated Tchen theory of particle agitation. This new formulation takes into account all the fluids in the particle turbulence.

Kinetic stress model for the particle phase turbulence

During the thesis we also opted for the development of a kinetic stress model to describe the particle agitation. This choice is motivated by the existence of such a model for two-phase flows. We wanted to adapt it in order to take into account the impact of more than one fluid in the particle turbulent terms. The quantities solved in the equations are the particle Reynolds stress tensor $R_{p,ij}$ and all the fluid-particle covariance tensors $R_{fp,ij}$. For more information on the demonstration of such equations, the reader can look into appendix A.

To get the evolution equations for the components of the particle Reynolds stress tensor, ψ_p in equation 3.35 must be replaced by $c_{p,i}c_{p,j}$. Then, the transport equation of the mean quantity $U_{p,i}U_{p,j}$ must be subtracted. The latter can be expressed in terms of the evolution equations of the mean particle velocity and the mean number of particles.

$$\frac{\partial}{\partial t}(n_p R_{p,ij}) = \int c_{p,i}c_{p,j}\frac{\partial f_p}{\partial t}\mathrm{d}\mathbf{c_p}\mathrm{d}\mathbf{c_f} - \frac{\partial}{\partial t}(n_p U_{p,i}U_{p,j}) \tag{3.48}$$

This leads to the following equation which is independent of the model for H_i:

$$\begin{aligned}
&\frac{\partial}{\partial t}(n_p m_p R_{p,ij}) + \frac{\partial}{\partial x_k}(n_p m_p R_{p,ij} U_{p,k}) \\
&= -\frac{\partial}{\partial x_k}(n_p m_p \langle u''_{p,i} u''_{p,j} u''_{p,k} \rangle) - n_p m_p R_{p,jk} \frac{\partial U_{p,i}}{\partial x_k} - n_p m_p R_{p,ik} \frac{\partial U_{p,j}}{\partial x_k} \\
&+ n_p m_p \left[\left(\sum_f \frac{\lambda_f}{\tau_{p,f}} (R_{fp,ij} + R_{fp,ji}) \right) - 2 \left(\sum_f \frac{\lambda_f}{\tau_{p,f}} \right) R_{p,ij} \right] + \mathbb{C}(m_p u''_{p,i} u''_{p,j})
\end{aligned} \tag{3.49}$$

Where the last term on the right hand side, the collision term, is expressed like in the two-phase case (equation 2.64).

To get the evolution equations for the components of the fluid-particle velocity covariance tensors, ψ_p in equation 3.35 must be replaced by $c_{f,i} c_{p,j}$. Then, the transport equation of the mean quantity $U_{f@p,i} U_{p,j}$ must be subtracted. The latter can be expressed in terms of the evolution equations of the mean particle velocity, the mean fluid velocity seen by the particle and the mean number of particles.

$$\frac{\partial}{\partial t}(n_p \langle u'_{f@p,i} u'_{p,j} \rangle) = \int c_{f,i} c_{p,j} \frac{\partial f_p}{\partial t} \mathrm{d}\mathbf{c_p} \mathrm{d}\mathbf{c_f} - \frac{\partial}{\partial t}(n_p U_{f@p,i} U_{p,j}) \tag{3.50}$$

This leads to the following equation which is also independent from the model for H_i:

$$\begin{aligned}
&\frac{\partial}{\partial t}(n_p m_p R_{fp,ij}) + \frac{\partial}{\partial x_k}(n_p m_p R_{fp,ij} U_{p,k}) \\
&= -\frac{\partial}{\partial x_k}(n_p m_p \langle u''_{f@p,i} u''_{p,j} u''_{p,k} \rangle) - n_p m_p R_{p,jk} \frac{\partial V_{f,i}}{\partial x_k} - n_p m_p R_{fp,ik} \frac{\partial U_{p,j}}{\partial x_k} \\
&+ n_p m_p G_{fp,jk} R_{f@p,ki} + n_p m_p \left[\frac{\lambda_f}{\tau_{p,f}} R_{f@p,ij} - \left(\sum_{f'} \frac{\lambda_{f'}}{\tau_{p,f'}} \right) R_{fp,ij} \right]
\end{aligned} \tag{3.51}$$

When obtaining the last equation, it is assumed that there is no statistical bias in the fourth term on the right hand side, it can be written:

$$\langle u''_{f@p,i} u''_{f@p,j} \rangle = \langle u'_{f@p,i} u'_{f@p,j} \rangle \tag{3.52}$$

This assumption has been validated in large eddy simulations of gas-particle turbulent flows (Simonin, 1996; Wang and Squires, 1996*b*). For both equations, it is also assumed that the fluid-fluid velocity covariance tensor is also zero. For two different fluids f_1 and f_2, $\langle u''_{f_1,i} u''_{f_2,j} \rangle = 0$. The triple correlation terms in the transport equation for the turbulent quantities are unknown, we have to provide a model for them. One way of doing so (Simonin, 2000) is by using a Boussinesq type approximation to express them in terms of known quantities, turbulent viscosities ν_p and ν_{fp} and a diffusivity constant K_p. These are obtained by writing the equation for the deviatoric part of $R_{p,ij}$ ($a_{p,ij} = R_{p,ij} - \frac{2}{3} q_p \delta_{ij}$) and $R_{fp,ij}$ ($a_{fp,ij} = R_{fp,ij} - \frac{2}{3} q_{fp} \delta_{ij}$). Then, deviatoric parts are supposed to be homogeneous, at equilibrium and correlation tensors are supposed to be slightly anisotropic. Thus obtaining the following relations:

$$
\begin{aligned}
a_{p,ij}\sum_f \frac{\lambda_f}{\tau_{p,f}} &= \sum_f \frac{\lambda_f}{\tau_{p,f}} a_{fp,ij} - \left[\frac{R_{p,ki}}{2}\frac{\partial U_{p,j}}{\partial x_k} + \frac{R_{p,kj}}{2}\frac{\partial U_{p,i}}{\partial x_k} - \frac{1}{3}\delta_{ij}R_{p,kl}\frac{\partial U_{p,l}}{\partial x_k}\right] \\
&= \sum_f \frac{\lambda_f}{\tau_{p,f}} a_{fp,ij} - \frac{1}{3}q_p\left[\frac{\partial U_{p,j}}{\partial x_k} + \frac{\partial U_{p,i}}{\partial x_k} - \frac{2}{3}\delta_{ij}\frac{\partial U_{p,k}}{\partial x_k}\right]
\end{aligned}
\tag{3.53}
$$

Eventually, these manipulations lead to:

$$
-\frac{\partial}{\partial x_k}(n_p m_p \langle u''_{p,i}u''_{p,j}u''_{p,k}\rangle) = -\frac{\partial}{\partial x_k}\left(n_p m_p K_p \frac{\partial R_{p,ij}}{\partial x_l}\right) \tag{3.54}
$$

Where:

$$
K_p = \left[\frac{\sum_f \frac{\lambda_f}{\tau_{p,f}}\nu_{fp}}{\sum_f \frac{\lambda_f}{\tau_{p,f}}} + \frac{5}{9}q_p\frac{2}{3}\frac{1}{2\sum_f \frac{\lambda_f}{\tau_{p,f}}}\right]\left[1 + \frac{5}{9}\tilde{\tau}_p\frac{\xi_c}{\tau_{p,c}}\right]^{-1} \tag{3.55}
$$

$$
= \left[\tilde{\nu}_{fp} + \frac{5}{9}q_p\frac{2}{3}\frac{\tilde{\tau}_p}{2}\right]\left[1 + \frac{5}{9}\tilde{\tau}_p\frac{\xi_c}{\tau_{p,c}}\right]^{-1} \tag{3.56}
$$

$$
\tilde{\nu}_p = \frac{\sum_f \frac{\lambda_f}{\tau_{p,f}}\nu_{fp}}{\sum_f \frac{\lambda_f}{\tau_{p,f}}} + \frac{2}{3}q_p\frac{1}{2\sum_f \frac{\lambda_f}{\tau_{p,f}}} = \tilde{\nu}_{fp} + \frac{2}{3}q_p\frac{\tilde{\tau}_p}{2} \tag{3.57}
$$

$$
\nu_{fp} = \frac{1}{3}q_{fp}T^L_{f@p} \tag{3.58}
$$

Where $T^L_{f@p}$ is the fluid Lagrangian integral time scale of velocity fluctuations measured along a particle trajectory.

$n+1$ equations model for the particle phase turbulence

Exactly as in the two-phase case, it is possible to obtain $n+1$ evolution equations for the turbulent quantities $q_p = \frac{1}{2}R_{p,ii}$ and $q_{fp} = \frac{1}{2}R_{fp,ii}$ by taking the trace of equations 3.49 and 3.51.

$$
\begin{aligned}
&\frac{\partial}{\partial t}(n_p m_p q_p) + \frac{\partial}{\partial x_k}(n_p m_p q_p U_{p,k}) \\
&= -\frac{\partial}{\partial x_k}(n_p m_p \langle u''_{p,i}u''_{p,j}u''_{p,k}\rangle) - n_p m_p R_{p,ik}\frac{\partial U_{p,i}}{\partial x_k} \\
&+ n_p m_p\left[\left(\sum_f \frac{\lambda_f}{\tau_{p,f}}q_{fp}\right) - 2\left(\sum_{f'}\frac{\lambda_{f'}}{\tau_{p,f'}}\right)q_p\right]
\end{aligned}
\tag{3.59}
$$

$$
\begin{aligned}
&\frac{\partial}{\partial t}(n_p m_p q_{fp}) + \frac{\partial}{\partial x_k}(n_p m_p q_{fp} U_{p,k}) \\
&= -\frac{\partial}{\partial x_k}(n_p m_p \langle u''_{f@p,i}u''_{p,j}u''_{p,k}\rangle) - n_p m_p R_{p,ik}\frac{\partial V_{f,i}}{\partial x_k} - n_p m_p R_{fp,ik}\frac{\partial U_{p,i}}{\partial x_k} \\
&+ \frac{1}{2}n_p m_p G_{fp,ik}R_{f@p,ki} + n_p m_p\left[\frac{\lambda_f}{\tau_{p,f}}\frac{R_{f@p,ii}}{2} - \left(\sum_{f'}\frac{\lambda_{f'}}{\tau_{p,f'}}\right)q_{fp}\right]
\end{aligned}
\tag{3.60}
$$

In equations 3.59 and 3.60, the first term on the right hand side, the one representing variance (covariance) transport by the particle velocity fluctuation, is modelled using an eddy-viscosity approach similar to those obtained in the two-phase case and expressed in equations 3.55.

3.2.4 Additional modelling modifications

Here are some ad-hoc modifications which makes the multiphase framework in neptune_cfd more consistent with the new approach. This makes the new approach compatible and more consistent with the drag model and the turbulence two-way coupling.

Drag coefficients for particles in a multiphase flow

Drag constitutive equations have been around since the pioneering work from Ergun (1952); Wen and Yu (1966). Although there has been a lot of recent updates on what these should read (Tenneti et al., 2011; Tang et al., 2015; Hardy et al., 2022), the model implemented in neptune_cfd is based on the very first correlations (Ergun (1952) for dense particle flows and Wen and Yu (1966) for dilute particle flows). In this work, we focus primarily on the dilute case. We recall the expression of the drag force introduced in the previous chapter from a continuous phase f to a dispersed phase s.

$$\mathbf{I}_{f\to s}^{D} = -\alpha_f \rho_f F_D^{f\to s} \mathbf{V}_r^{f\text{-}s} \tag{3.61}$$

With the following expression for the drag coefficient:

$$C_D = \begin{cases} \frac{24}{R_e}\left(1 + 0.15 R_e^{0.697}\right) \alpha_s^{-2.7} & \text{if } R_e < 1000 \\ 0.44 \alpha_s^{-2.7} & \text{if } R_e \geq 1000 \end{cases} \tag{3.62}$$

Where R_e is the Reynolds number associated to the solid inclusion. It is commonly defined with the inclusion diameter d_s, the fluid mass per unit volume ρ_f and kinematic viscosity ν_f as well as the particle to fluid relative velocity $\mathbf{V_r^{f\text{-}s}}$:

$$R_e = \frac{d_s \rho_f \mathbf{V_r^{f\text{-}s}}}{\nu_f} \tag{3.63}$$

The main issue with the definition in equation 3.62 is the presence of the solid volume fraction. Since we are working with possibly many continuous phases interacting with the solid particles, it seems that this expression might not be consistent with our global approach. Since we tried some re-normalization without any significant changes to the simulation results, we do not detail them. This remains an open challenge to the model.

Two-way coupling in the continuous phase turbulence model

The particle phase naturally has an effect on the mean fluid quantities. However, the fluid turbulence model in their standard form do not include any inclusion effect. In neptune_cfd, the small inclusion model (Vermorel et al., 2003) has been implemented.

If the solid inclusions are small compared to Taylor's length scale, the impact of particles on continuous phase turbulence is taken into account as a source term S_k and S_ϵ in the evolution equations of k and ϵ.

$$S_k = \left(q_{fp} - 2q_p + \mathbf{V_d}.\mathbf{V_r^{f\text{-}s}}\right) C_D \alpha_p \Omega \tag{3.64}$$

$$S_\epsilon = C_\epsilon \left(q_{fp} - 2q_p + \mathbf{V_d}.\mathbf{V_r^{f\text{-}s}}\right) \frac{\epsilon}{k} C_D \alpha_p \Omega \tag{3.65}$$

Where q_{fp} and q_p are the traces of fluid-particle velocity covariance and particle velocity variance tensors, $\mathbf{V_f}$ is the drift velocity between the particle phase and a continuous phase f, $\mathbf{V_r^{f\text{-}p}}$ is the relative velocity between the two, α_p is the particle phase volume fraction C_D is the drag coefficient, Ω is the cell volume and C_ϵ is a constant. The modifications consist in including a new constant to match the treatment carried out in fluid-particle drag. The particle effect on continuous turbulence is weighted by the coefficient λ_f to account for the presence of more than one carrier phase. In the cases explored during the thesis, the new model of reverse coupling gave better results. However, the requirement for particle size and relaxation time were not verified.

3.3 Turbulence and gravity driven particle deposition

In the studied cases, particle deposition is an important feature measured experimentally. In order to accurately compare simulations with experimental results, this phenomenon should be taken into account in the models. In this section we present how it is implemented in the Eulerian and Lagrangian frameworks. Particle deposition can occur when its trajectory crosses the wall. At that moment, if the energy transferred to the particle is sufficiently small, the particle adheres to the wall and does not move anymore. In the present work we do not focus on re-entrainment of particles in the flow.

Let's start by introducing general concepts which will be used throughout the description of the deposition models. As defined previously, the particle relaxation time is written τ_p and its diameter is d_p. These can be combined with the fluid shear velocity $u^* = \sqrt{\tau_w/\rho_l}$ and kinematic viscosity ν_f to make dimensionless particle attributes. The deposition rate $y \mapsto V_d(y)$ represents the particle flux through a plane A parallel to the wall at a distance y from it Nerisson (2009). It can also be written in a dimensionless way using the fluid shear velocity.

$$y^+ = \frac{y u^*}{\nu_f} \tag{3.66}$$

$$d_p^+ = \frac{d_p u^*}{\nu_f} \tag{3.67}$$

$$\tau_p^+ = \frac{\tau_p u^{*2}}{\nu_f} \tag{3.68}$$

$$V_d^+(y) = \frac{V_d(y)}{u^*} = \frac{J}{C(y)} \frac{1}{u^*} \tag{3.69}$$

Where J is the particle flux through plane A per unit surface area and $y \mapsto C(y)$ is the particle concentration at a distance y from the wall. According to literature Young and Leeming (1997); Nerisson (2009), for turbulence driven deposition, there are three deposition regimes depending on the particle relaxation time. Low-inertia particles are in the diffusion deposition regime where particle deposition slightly decreases with increasing particle inertia; large-inertia particles are in the inertia-moderated regime where deposition slightly decreases with particle inertia; and other particles are in the diffusion-impaction regime where particle deposition increases sharply with the particle inertia. These regimes are shown in figure 3.7.

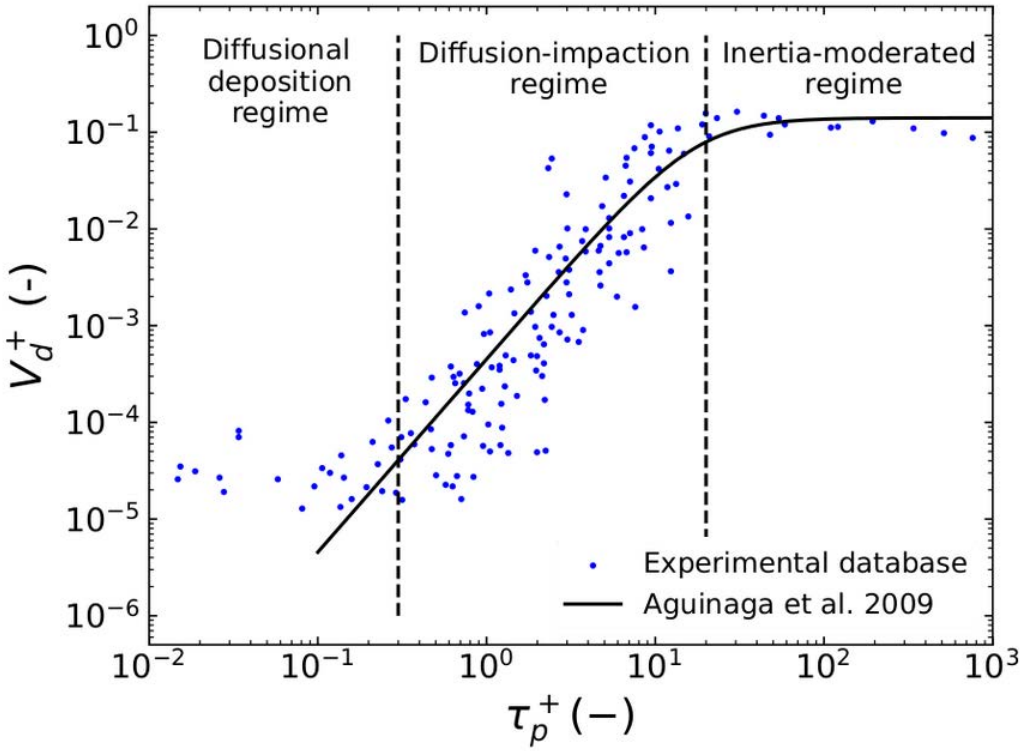

Figure 3.7: Experimental results for particle deposition in a vertical channel Young and Leeming (1997). The solid line represents the possible model for V_d^+ described by equation 3.70 for $y^+ = 30$.

Based on the work of Simonin (2008); Nerisson (2009), it is possible to obtain a formula $y \mapsto V_d^+(y)$ for the two regimes ($\tau_p^+ > 10^{-1}$) for particles subjected to gravity or not. This model is summed up in equation 3.70. It predicts the deposition rate when looking at the flow at a certain distance y from the wall. This model proved itself useful to enhance the performance of the Lagrangian method with regards to sedimentation and to introduce the notion of deposition in Eulerian frameworks.

$$V_d^+(y) = \left[\frac{Sc_f^t}{\kappa} ln(y^+) + \lambda(Sc_B, \tau_p^+, d_p^+) \right]^{-1} \tag{3.70}$$

Where $0.7 < Sc_f^t < 1$ is the fluid turbulent Schmidt number and $\kappa \approx 0.41$ is Von Karmann's constant. λ is a function of the Brownian Schmidt number and the particle relaxation time.

$$Sc_B = \frac{3\pi d_p \nu_f^2 \rho_f}{\rho_p k_b T} \; ; \qquad \lambda(Sc_B, \tau_p^+) = \left[\frac{\tau_p^{+2}}{\omega} + \frac{Sc_B^{-2/3}}{\lambda_0} \right]^{-1} \tag{3.71}$$

Where k_b is Boltzmann constant, T is the temperature of the system, $\omega \approx 2.2 \times 10^3$ and $\lambda_0 = 13.7$.

3.3.1 Particle deposition in a canal: Lagrangian description of the solid phase

In the Lagrangian framework, particle deposition is supposed to be driven by gravity and turbulent effects. In this section, we present how this phenomenon is taken into account in code_saturne, we show how it can be problematic in some cases and provide a modification for it to be more effective by using equation 3.70 similarly to what is done in Aguinaga et al. (2009). In the experimental setups studied, the issues highlighted here should not have any impact since the deposition is mostly driven by gravity. However, studying the effects of deposition has been a possible solution to a challenge faced in industrial simulations.

In code_saturne, standard deposition is taken into account at the wall faces. When a particle crosses one, it is flagged as deposited. One well known fact about the standard deposition model is that it overestimates particle deposition velocity for low relaxation time particles (Guingo and Minier, 2008). One possible way to solve this issue is to introduce more phenomenons in the behaviour of particles moving close to the wall. A successful attempt to enhance the Lagrangian stochastic deposition model, built from the DNS results obtained in Marchioli and Soldati (2002), has been proposed in Guingo and Minier (2008). This model takes into consideration coherent turbulent structures near the wall in the stochastic methodology. This complexity in the behaviour of particles near the wall has given satisfactory results, however, we have not explored it further. At first, it seemed that this problem originated from the fact that the mesh was too coarse. Indeed, for low relaxation time particles, the deposition is the consequence of their interaction with the viscous sub-layer. Since it is not simulated or modelled in the Lagrangian framework, deposition is not simulated accurately. A possible way to tackle this issue can be divided into two areas. We could try running simulations on a mesh which enables simulating the flow to the wall or we could try implementing wall-law interpolations in the Lagrangian stochastic model so that low-inertia particles can *see* and interact with the viscous layer. However, as highlighted in the following results, none of these methods give satisfying results. Therefore, a new enhancement is proposed where equation 3.70 is used to determine the probability a particle crossing a plane parallel to the wall has to deposit. This is equivalent to the Stochastic model developed in Aguinaga et al. (2009). The last model enables us to get accurate results for the deposition in a vertical channel mainly by avoiding the simulation of the interaction between a particle and the viscous layer.

The wall-laws we decided to implement are inspired from Van Driest (1956); Chieng and Launder (1980). They describe the profiles of the fluid velocity in the direction of the flow u, the fluid turbulent kinetic energy k and the fluid turbulent kinetic energy dissipation ϵ as a function of wall distance y in two layers (corresponding respectively to the linear sub-layer and the logarithmic sub-layer). They are used to interpolate

the Eulerian fields between the wall face and the first cell centre. Above the first cell centre, the Eulerian fields are P1-interpolated. The way Eulerian fields are globally interpolated is described in equations 3.72. For the sake of consistency, we made the variables of interest dimensionless by using the fluid kinematic viscosity ν_f and the fluid shear velocity u^*.

$$u^+ = \frac{u}{u^*} \tag{3.72}$$

$$k^+ = \frac{k}{u^{*2}} \tag{3.73}$$

$$\epsilon^+ = \frac{\epsilon \nu_f}{u^{*4}} \tag{3.74}$$

The P1 interpolation is computed with the gradient of the Eulerian variables. These gradients are computed at the cell centre with the neighbouring cell variable values. The wall laws are determined by first assuming the wall distance y_v at which we transition from logarithmic to laminar sub-layer. Then, we assume the profiles in the two regions Launder and Spalding (1974); Chieng and Launder (1980) and define continuous connections between the two. For the velocity, we assume a profile consistent with Van Driest theory Van Driest (1956).

$$u^+ = \int_0^{y^+} \frac{2}{1 + \sqrt{1 + 4\kappa^2(1 - e^{-\xi/A})^2 \xi^2}} \mathrm{d}\xi \tag{3.75}$$

$$k = \begin{cases} k_v \left(\frac{y}{y_v}\right)^2 & y \leq y_v \\ k_v + y \frac{k_n - k_v}{y_n - y_v} & y_v \leq y \end{cases} \tag{3.76}$$

$$\epsilon = \begin{cases} 2\frac{\nu k_v}{y_v^2} & y \leq y_v \\ 2.83 \frac{C_\mu k_p^{3/2}}{\kappa y} & y_v \leq y \end{cases} \tag{3.77}$$

Where k_v and k_n are the turbulent kinetic energy at the distance y_v from the wall and at the face opposite that of the wall in the wall cell. $C_\mu = 0.09$ is a well known turbulence constant Launder and Spalding (1974) and $A = 26$ is a constant in Van Driest theory Van Driest (1956).

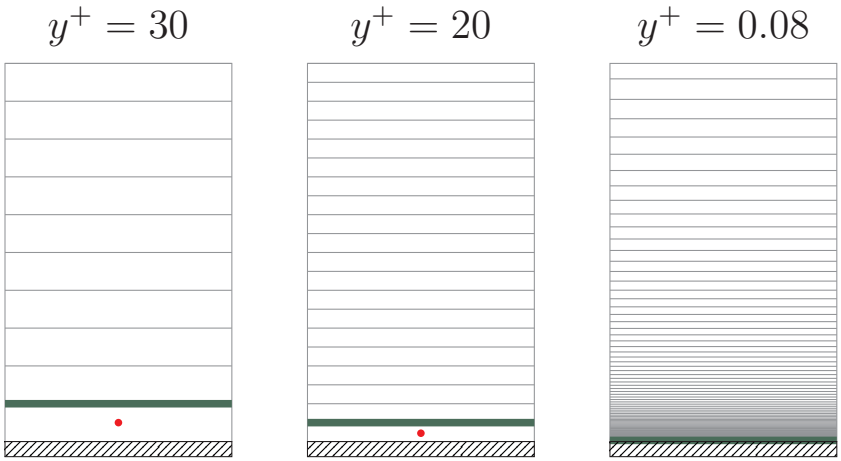

Figure 3.8: Meshes used for the deposition model verification. Red dots denote the centre of the wall cell and green line the face opposite to the wall face in the wall cell. The wall is highlighted at the bottom.

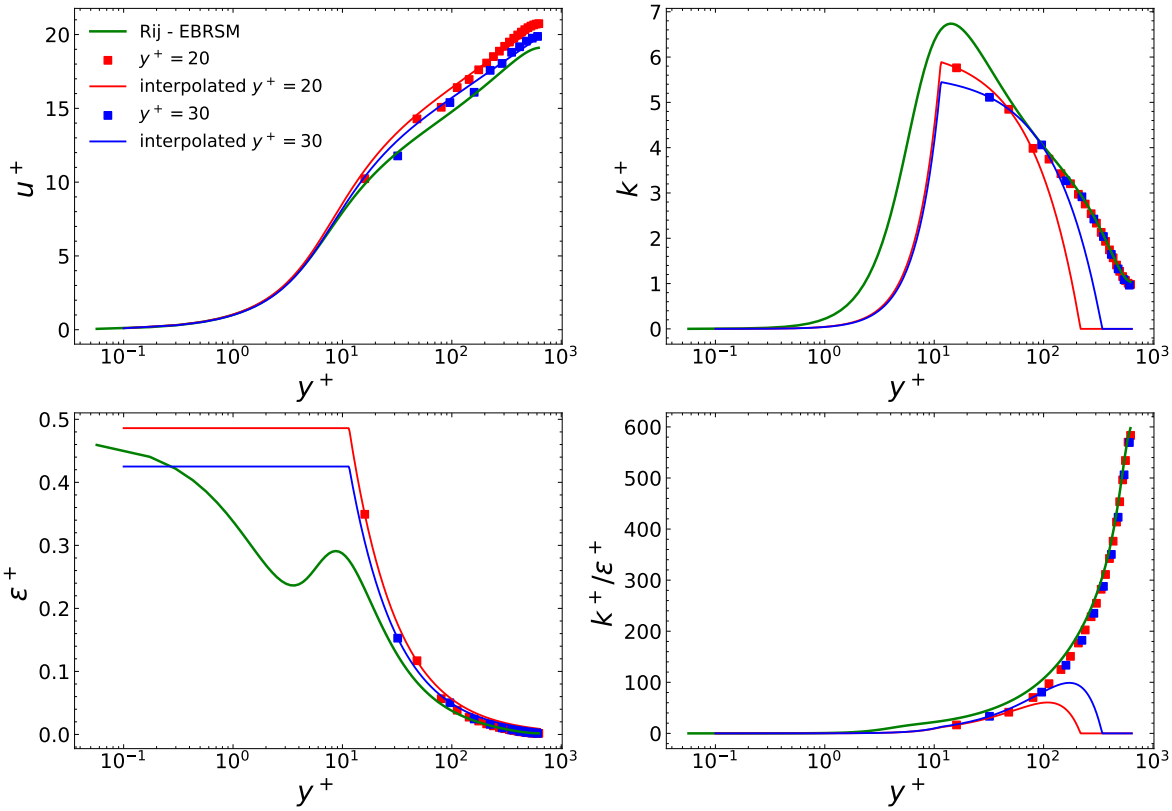

Figure 3.9: *Theoretical* profiles obtained with a wall-resolved simulation of the channel flow and the interpolated values of Eulerian quantities at the position of motionless particles. The markers represent the values at the centre of the cells. Two coarse simulations have been carried out to show the consistency of the interpolation method.

In order to check the correct implementation of the interpolation, we set up a channel flow simulation at $Re_\tau = 450$. In the test case, we make a very fine simulation with a resolved profile near the wall (with the R_{ij}-ϵ EBRSM turbulence model). This will give us the *theoretical* profiles we are looking for. The verification simulation

consists of the same channel flow, very roughly meshed and with modelled turbulence at the wall (R_{ij}-ϵ SSG turbulence model). In this simulation we distribute particles with very large inertia inside the domain. Their inertia is sufficiently large for them to be motionless. If we introduce a sufficiently large amount of particles, by activating the interpolation with equations from equations 3.76 to 3.77, it is possible to recreate a fine grained profile of the Eulerian variables, even if the mesh is quite coarse. The main goal is to compare this fine grained profile with the *theoretical* profile obtained in the wall resolved simulation. Figure 3.9 shows the results obtained for this verification case. In solid lines is the interpolation using the wall-laws (the P1-interpolation is not shown). The difference further away from the wall is corrected with the P1-interpolation.

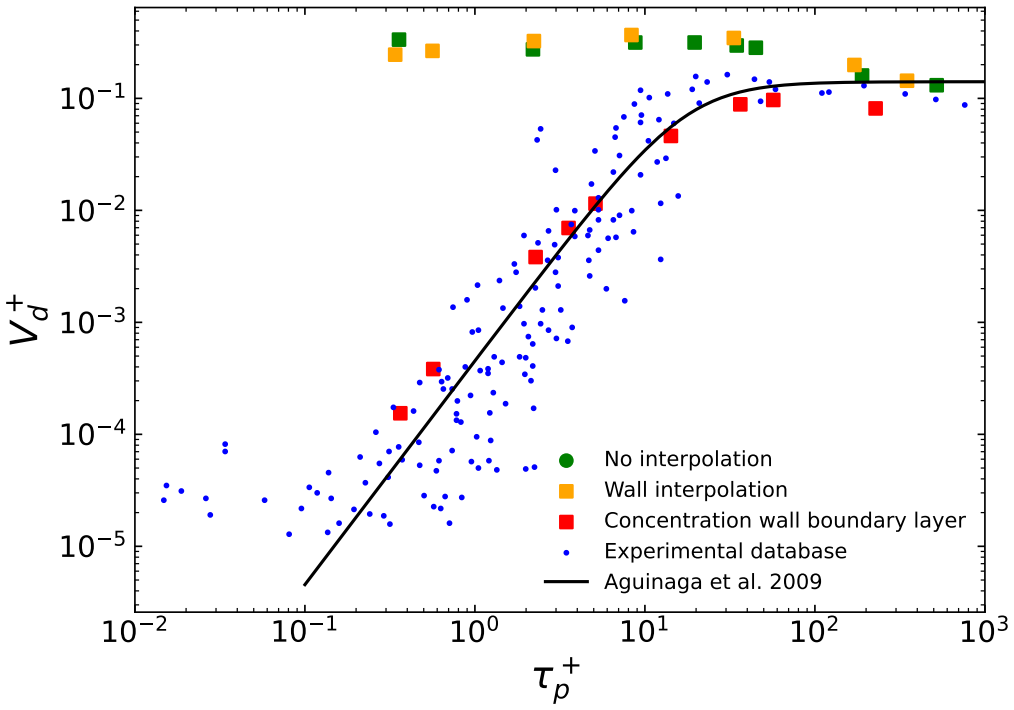

Figure 3.10: Simulation results for particle depositing in a vertical channel. Classical simulations with and without interpolation fail to capture the decrease in deposition rate which comes with decreasing particle relaxation time. Simulations with equation 3.70 give satisfactory results. The black curve is normalised by the concentration at $y^+ = 30$.

Then, in order to compare turbulence induced deposition in the Lagrangian framework with experimental results, we set up a fully developed turbulent flow in a vertical channel. These are well documented experiments Young and Leeming (1997) and simulating the case is accessible with code_saturne. Since, the lower the inertia of the particle, the closer the particle gets to the wall before depositing, we expect the interpolation of the Eulerian fields to enhance deposition results. The results for particles depositing in a vertical channel with and without interpolation of the Eulerian fields is shown in figure 3.10. It can be seen that wall law interpolation has little to no effect on the deposition rates of particles. A possible explanation would be that the Langevin stochastic model of the velocity seen by the particle we used in this study is not suited for the simulation of particles in boundary layers as was already mentioned earlier.

Since the deposition of particles with low inertia is the result of their interaction with it, not managing to simulate this interaction could be a major drawback.

This has driven us to introduce another deposition model based on the work of Aguinaga et al. (2009). This model, based on equation 3.70 presented above, avoids the simulation of particles inside the boundary layer. Instead, at a certain distance y_H from the wall, the probability of deposition of a single particle is computed. This probability can be obtained by assuming the expression of the particle velocity probability density function and assuming the inclusion agitation is in equilibrium with the fluid turbulence. With that probability, a particle either deposits or bounces off the virtual plane $y = y_H$. This model shows great results in the prediction of deposition rates in a vertical channel for a large range of particle relaxation times as exhibited in figure 3.10. More details on it can be found in the original published material.

3.3.2 Particle deposition in a canal: Eulerian description of the solid phase

In the Eulerian framework, particle deposition is assumed to be exclusively driven by gravity because our cases allow it. In order to introduce turbulence driven deposition, equation 3.70 could be used. It has not been carried out during the thesis since gravity seems to be the main driver for deposition in the studied experimental cases. In this section we start by introducing several ways gravity driven deposition could be introduced in our Eulerian simulations, we show the results they give in a standard case before concluding upon which model to keep for the validation cases.

The main idea for introducing particle deposition in our simulations consists in removing solid mass on the cells which contain one wall boundary face. This mass can either be removed from the cell itself by introducing a mass sink in it or through the specific face by implementing an outlet boundary condition for the particle phase. The cells which have a wall boundary face will, in this section, be called wall cells. We assume gravity is the only phenomenon responsible for particle deposition. It is oriented towards - and perpendicular to - the wall. The mass flux ϕ_d is defined according to the settling velocity of particles in equation 3.78.

$$\phi_d = \alpha_p \rho_p \frac{\tau_p g}{h} \tag{3.78}$$

Where α_p is the particle volume fraction in the cell, ρ_p its mass per unit volume, τ_p is the particle relaxation time, g is gravity (perpendicular to - and oriented towards - the wall) and h is the distance between the wall face and the opposite face of the wall cell. Should the gravity not be oriented towards the wall, the g must be replaced by its projection along the normal to the wall face.

The second way of defining the deposition condition is by assuming the wall face is an outlet for the particles. In neptune_cfd, this is equivalent to impose the following Neumann condition for the particle phase in the wall cell:

$$\frac{\partial u_{p,n}}{\partial n} = 0 \tag{3.79}$$

Where n represents the normal to the wall face and $u_{p,n}$ is the projection along this normal of the particle velocity. This condition is equivalent to impose a well flux

condition on the wall cell but instead of using $\tau_p g$ for the settling velocity, we use the velocity at the wall cell centre to compute $u_{p,n}$. Turbulence induced deposition can be taken into account by using equation 3.70 to determine the exiting flux of particles and adding it to the flux related to gravity. The two models defined above are tested on a very simple sedimentation test case. It consists of solid particles falling in a liquid at rest. The main goal of this case is to make sure particles are exiting the domain at a similar rate. Table 3.2 shows total deposition after 30 s. For consistency, we also test the case where we impose a flux based on the particle velocity normal to the wall. This third condition should match the outlet condition. For future studies, we keep the imposed mass flux condition. It makes it easier to control the deposited particle mass and enables new modelling to be taken into account if needed.

Imposed mass flux ($\tau_p g$)	Outlet condition	Imposed mass flux ($u_{p,n}$)
$6.194\,\mathrm{g\,m^{-2}}$	$6.318\,\mathrm{g\,m^{-2}}$	$6.155\,\mathrm{g\,m^{-2}}$

Table 3.2: Total mass deposited at the bottom of the domain after 30 s depending on the deposition model.

4 | Air entrainment modelling

Initially, the thesis was exclusively focused on liquid-gas-solid flows with an emphasis on particle modelling. However, due to unexpected circumstances, the topic of air entrainment in air-water flows has come to the forefront. The aimed industrial scale experiments encountered during the thesis included water jet features and preliminary air-water studies of this phenomenon proved to be extremely sensitive to the accuracy of simulated air entrainment.

The goal of this chapter is to review the physics of air entrainment and the existing models, to provide minor details on small corrections made to the two-phase flow framework, to suggest a new model for the entrained bubbles diameter and to show its performance when compared to experimental setups representative of the phenomenon.

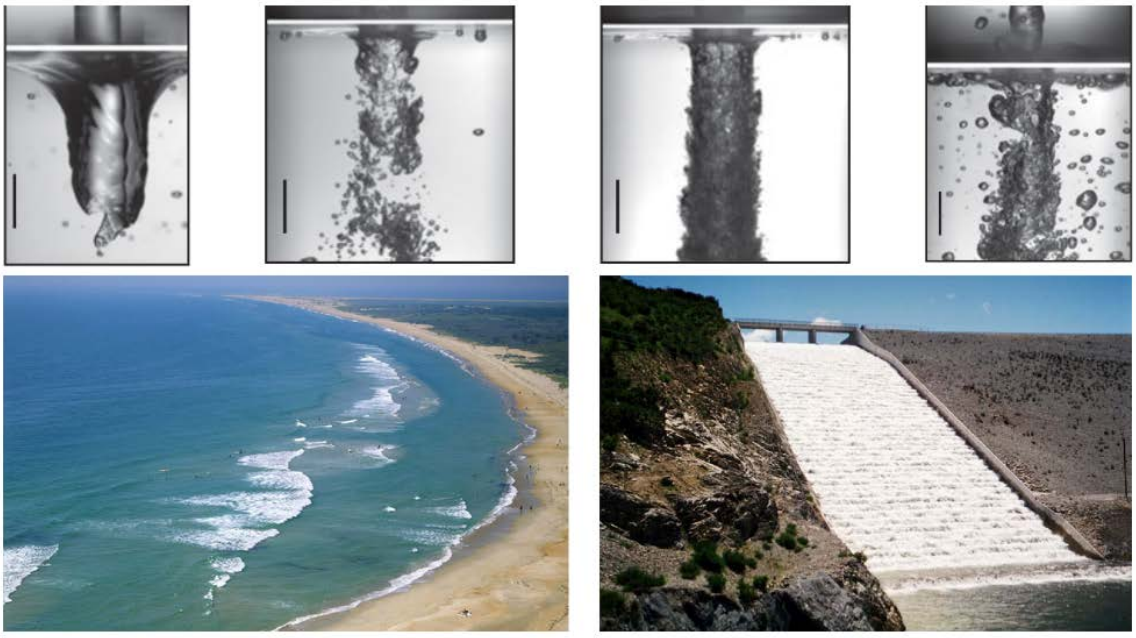

Figure 4.1: Scenarios illustrating air entrainment at three different length scales. From top left to bottom right: laminar and turbulent water jets (Kiger and Duncan, 2011), breaking waves (from National Park Service website) and stepped chute (Gonzalez and Chanson, 2007).

4.1 Air entrainment from a free surface

Air entrainment or air aeration in air-water flows is defined as the transition occurring when continuous air is transported, as bubbles or air pockets, below the free-surface. This phenomenon is widely present in natural flows: breaking waves (Sene, 1988; Kiger and Duncan, 2011), hydraulic jumps (Chanson, 2009; Viti et al., 2018; Valero et al., 2018) or highly turbulent water flows (Brocchini and Peregrine, 2001*a*,*b*). It can also appear in industrial configurations. Figure 4.1 shows different scenarios where it occurs. The experimental setup encountered during the thesis is one example representative of the most widely occurring air entraining mechanism: water jets (Donk, 1981; Bin, 1993; Ohl et al., 2000; Kiger and Duncan, 2011). In natural flows, aeration can change the physico-chemical properties of the mass of water near the free-surface disrupting wildlife (Chanson and Cummings, 1992). Understanding how it takes place helps preventing damages to ecosystems and measuring the extent of their impact when it cannot be avoided. In industrial processes, air aeration can enhance and speed up chemical reactions (Li et al., 2014; Li and Zhong, 2015; Ojima et al., 2014) or help transporting and separating particles from different species (Shahbazi et al., 2010). This mechanism, highly sought after or avoided depending on the applications, needs to be modelled accurately to provide valuable information on its characteristics.

The scope of the thesis only concerns air-water flows but, obviously, this study can be transposed to other operating immiscible fluids. Also, a similar field of study exists for the opposite process: continuous water transforming into dispersed inclusions. Since it is negligible in the experimental setups we explored, it is not considered. More details on the latter can be found in Baumgarten (2006); Ashgriz (2011). Finally, we focus on the transition happening when a continuous structure generates dispersed inclusions. Hypothetically, for very fine meshes, direct numerical simulations should be able to simulate air entrainment without the need for any modelling at all. However, due to the large range of scales present in this phenomenon, industrial applications are still out of reach from this kind of approach. Therefore, there is a serious need for models describing the transition between resolved and unresolved interfaces.

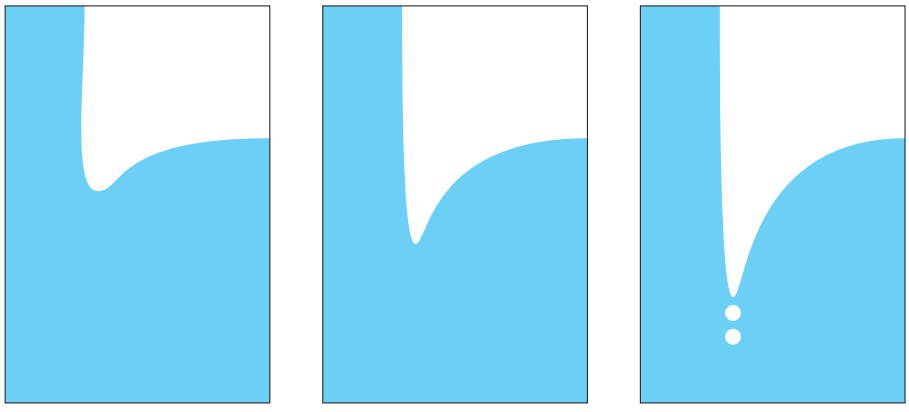

Figure 4.2: 3 steps describing air entrainment in the low intensity turbulence, small jet scenario. Inspired from Kiger and Duncan (2011) and Miwa et al. (2018)

Aeration - or air entrainment - can occur in different scenarios but the main mechanism causing it is the interaction between a turbulent water eddy and a free-surface. Depending on the configuration, the turbulent eddies responsible for air entrainment

are of different sizes: each generates its own particular bubble spectrum. For small structures with low intensity turbulence, typically, small water jets, the mechanism responsible for air entrainment is decomposed into several steps. The water impacting a free-surface creates a dimple or a cusp. If the water mass has sufficient momentum, the dimple deepens. Then, surface instabilities appear on the water surface in the cusp. When the momentum grows, these grow as well until, finally, the cusp is thin enough and the instabilities large enough that singular bubbles are detached and transported below the free-surface. Figure 4.2 illustrates these steps.

For large structures, the mechanism is different. It is also decomposed into steps. First, in a turbulent flow, the surface roughen due to the presence of eddies. When this rough surface impacts a flat liquid interface, it tends to move water away from it like when a rock impacts a free-surface. When this mass of water comes back to its equilibrium state, the surface roughness has geometrically entrapped air under the surface. These air bubbles or pockets are transported well below the free surface by the water momentum and may be subsequently broken down by turbulent eddies. Figure 4.3 illustrates these steps. This scenario occurs in large jets with high turbulent intensity but it can also be observed in breaking waves.

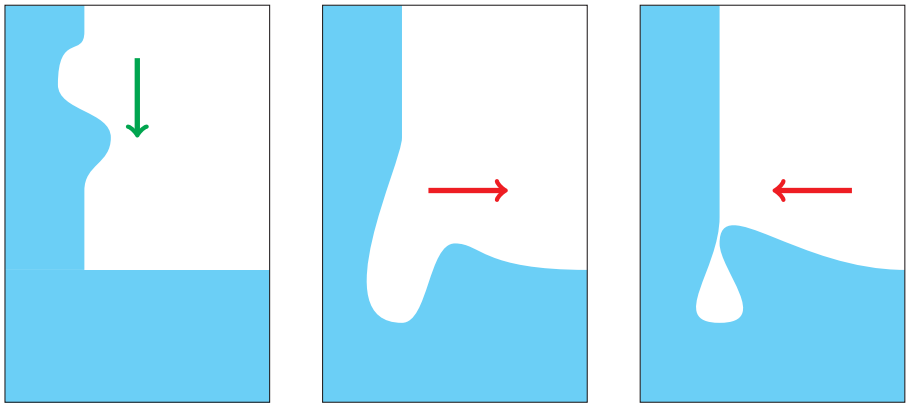

Figure 4.3: Drawing of 3 steps describing air entrainment with high intensity turbulence.

Finally, observations have shown that air can also be pre-entrained or re-entrained (Bertola et al., 2018). The first scenario can be caused by atomisation and the second one seems of little interest. Since, we study the transition between continuous and dispersed structures we do not focus on the two last mechanisms. If the simulation framework is set up correctly, at least the re-entrainment should be simulated correctly.

To characterise the phenomenon, many experimental studies have recreated the conditions for air entrainment to happen (References related to water jets: Lahey (1991); Evans et al. (1992); Clanet and Lasheras (1997), hydraulic jumps Zhang et al. (2013) and breaking waves Garrett et al. (2000); Liu and Duncan (2003); Blenkinsopp and Chaplin (2007)). The idea is primarily to understand the phenomenon and secondly to feed numerical models to make them more accurate. The latter is done by providing macroscopic scale quantities easily transferable to computational fluid dynamics in order to avoid simulating the smallest scales via DNS. The following list summarises the physical quantities of interest, the way they are usually measured and how they can improve numerical simulations other than by constituting a potential verification basis.

- Air mass transfer: In steady flows, the water level can be a good indicator of the total entrained mass of water. Alternatively, from 3D imaging techniques, it is possible to reconstruct the total amount of air holdup (Roy et al., 2013).
  The total amount of entrained air is a great measure to verify if the bubble size distribution is correctly simulated. It is also useful for creating numerical entrainment model from experimental data. In fact, many models rely on such experimental correlations (Ma et al., 2010; Qu et al., 2011).

- Entrained air volume fraction: It can be measured via conductivity probes and averages of the conductivity time series. This method is easy to setup and has been consistently used throughout the fluid community. The main disadvantage is its inability to measure high air volume fractions and its effect it can have on air structures.
  Volume fraction being a simulation output as well, it makes a suitable candidate for numerical model validation.

- Air bubble sizes: Conductivity probes have been used to measure bubble size, it is a quantity accessible from the conductivity time series and the gas velocity under certain assumptions. For this quantity at least two probes are required to measure air velocity (Cartellier and Achard, 1991). The main disadvantages are the fact that assumptions are not always verified which sometimes leads to biased results. 3D imaging techniques have been used to measure bubble size distribution (Belden et al., 2012; Bertola et al., 2018). They are costly and complicated to set up but provide accurate data without interfering with the experiments.
  For numerical models, this is the most valuable data. Not only does it provide a great validation dataset but it can also be used to directly create source terms to create bubbles at the correct size in numerical simulations.

- Liquid quantities: All available techniques (PIV, LDV...) can be used to measure fluid properties below the free-surface. They provide access to mean and fluctuating quantities most of the time Kendil et al. (2012); Boualouache et al. (2017). A challenge for these techniques is being able to separate liquid from gas properties.
  This data is mostly used as a validation tool. It can sometimes highlight flaws in the modelling process.

- Bubble penetration depth: It is obtained with imaging techniques and is a good indicator of bubble size (Iguchi et al., 1998; Kramer et al., 2016). Even though it is not as precise as bubble size distribution measurements, it can still provide valuable information for validation purposes.

- Surface roughness: It can be measured with imaging techniques (Davoust et al., 2002; Guyot et al., 2020). This measure can be coupled to bubble plumes characteristics to determine some kind of correlation between the two. The first one being accessible in numerical simulations, it could be the basis of a model for created bubble size distribution.

From a numerical simulation standpoint, the main challenge lies in understanding how the transition between continuous to dispersed structures happen so that numerical

models can take it into account when trying to set up a transition between resolved and unresolved interfaces.

4.2 Existing numerical models

In this section, we review existing numerical models accounting for air entrainment phenomenons. Some are specifically designed to capture these effects while other are developed in a general manner and a focus is made on their ability to simulate air entrainment scenarios. As in the introduction to three-phase flows, these models are ranked according to the precision to which they resolve the interfaces. This review will highlight the need for new modelling approaches specifically for the size of inclusions created from a large interface.

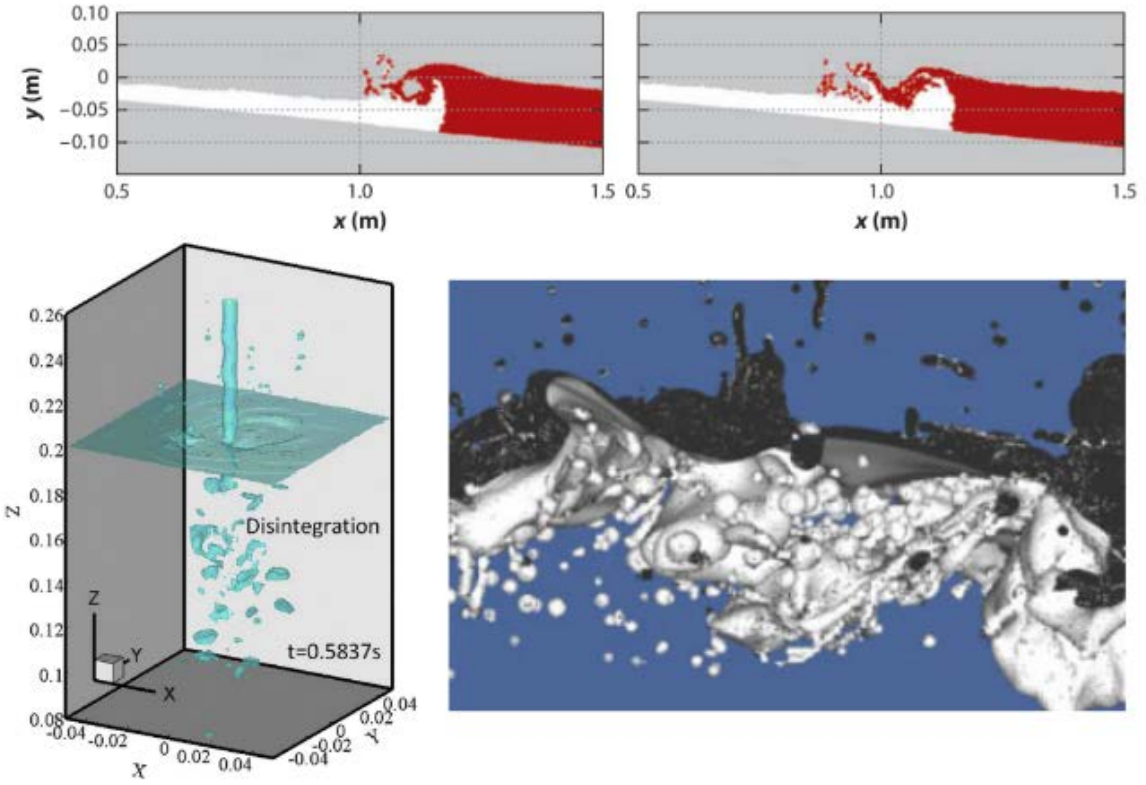

Figure 4.4: Different simulations results obtained from literature material. (top) SPH from Dalrymple and Rogers (2006), (bottom left) LES+VOF from Khezzar et al. (2015) and (bottom right) DNS from Deike et al. (2016).

Smooth particle hydrodynamics has been used to simulate air entrainment in various scenarios (Dalrymple and Rogers, 2006; De Padova et al., 2013; Fonty, 2019; King et al., 2023). The most challenging part for this method is to have sufficiently small particles in order to be able to represent correctly a small bubble generated via air entrainment. Keeping track of surface properties is also complicated due to the discretization process. This can be an issue since they are crucial to the phenomenon of air entrainment. In some cases, source terms which are also used in Eulerian simulations may be added.

Direct numerical simulations are an optimal tool to simulate the aeration phenomenon. In theory, if the mesh is fine enough, all the turbulent scales are resolved,

leading to a resolution of all the liquid-gas interfaces being resolved as well. As mentioned earlier, the biggest challenge this method faces is the computing time. Available resources grow each year but complex industrial configurations are still hard to manage. However, there have been studies showing the potential of such approach. The first one to consider it for air entrainment were Lahey Jr (2009) for impinging jets and Fuster et al. (2009) for breaking waves. More recently, there has been a serious effort to characterise the physics of breaking waves through DNS with the Basilisk software (Popinet, 2015). In the work of Deike et al. (2016), the authors carry out a comprehensive study of bubble generation through different wave breaking scenarios with DNS. From these numerical simulations and previous macroscopic entrainment models, they suggest a new turbulent bubble break-up model. In Mostert et al. (2022), the authors investigate a similar configuration. They carry out simulations of breaking waves in order to characterise bubbles and droplet generated by the phenomenon. A focus is made on identifying the laminar-turbulent transition as well as comparing the range of simulated scales with experimental data from Deane and Stokes (2002). All in all, this method seems to give satisfying results but might be too computationally expensive for the industrial applications aimed at during this thesis.

If direct numerical simulations are out of reach in practice, a second approach leads to considering the volume of fluid method along with large eddy simulation for fluid turbulence. Less costly than DNS, it solves the turbulent scales down to a certain range until a subgrid scale turbulent term is needed. However, since the smallest scales are unresolved, they should be missing in the bubble size distribution as well. If the filter used in LES is larger than the smallest scale observed in dispersed inclusions, there is no need to model it. This is done in Khezzar et al. (2015). Unfortunately, most of the time it is not the case and a specific model has to be introduced to account for subgrid scale bubbles. This is done in Derakhti and Kirby (2014) for example with an entrainment model from Ma et al. (2011).

To cut computing costs, it is possible to perform RANS simulations in the VOF approach. This combination has been used in GENTOP (Hänsch et al., 2012) with four fields and a population balance method to account for dispersed structures unresolved by the volume of fluid method. The transition between continuous and dispersed structures is enforced with general numerical expressions which are also found in multifluid approaches such as Mathur et al. (2019). The greatest challenge is to describe the transition between the continuous field and the dispersed inclusions. For the framework GENTOP, work is still being carried out to define the size distribution of continuous structures no longer resolved.

Finally, the multifluid RANS approach offers a great framework to model air entrainment (Ma et al., 2010; Mathur et al., 2019; De Santis, Colombo, Hanson and Fairweather, 2021). Their primary advantage, like the VOF+RANS method, is their low computing cost. The biggest challenge they face, compared to DNS, is the description of dispersed inclusions generated from unresolved continuous structures. The work carried out in the thesis falls into this category. There are several models widely used in CFD frameworks to account for mass transfer from continuous air to dispersed air. More details on those can be found in Moraga et al. (2008); Ma et al. (2011); Castro et al. (2016); Valero and García-Bartual (2016). They were developed with different scenarios in mind but are still reasonably effective in configurations they were not designed to be used in. They always rely on some kind of experimental calibration which embodies their greatest flaw. In the framework from neptune_cfd, the mass transfer

is an output of the simulation, thus we are not focusing on this modelling part. All we provide is a model for the transferred mass size distribution.

Another approach which is quite different from the previous one is the surface density function formalism described in Essadki et al. (2019). It gives a geometrical description of a fluid-fluid interface and links its properties to dispersed inclusions described with a statistical approach. This enables modelling of all the transitions happening near a free-surface.

4.3 Minor preliminary corrections

Before introducing the air entrainment model, a slight modification needs to be introduced to coalescence source terms. From equation 2.93, we recall the form of the source term $\dot{F}_{c,b}$ associated to coalescence and breakup. The detailed justification for its expression can be found in Prince and Blanch (1990); Ruyer (2007), here is its final expression:

$$\int \dot{F}_{c,b}\pi d^2 \partial d \partial \mathbf{w} = a_i^{5/3}\epsilon_{dg}^{1/3}\alpha_{dg}^{1/3}(\xi_c(N_c) + \xi_b(N_c)) \tag{4.1}$$

The main issue with this expression in the multi-regime model is that it is written in terms of the dispersed phase volume fraction α_{dg}. However, as explained in chapter 2, in the two-fluid formulation there is only one field per phase. Therefore, in a region where air is predominant α_g is close to 1 but talking about coalescence is nonsensical since there are no bubbles. But, by construction, the coalescence source term is not 0 which poses a significant issue. It causes the interfacial area to decrease until it reaches the minimum value allowed by the software. This is irrelevant as long as continuous air never becomes dispersed bubbles. It is clear from this short demonstration that it is a major problem in air entrainment simulations.

To overcome this issue, we decided to include a weighting factor θ in the coalescence source term effectively zeroing it when air volume fraction no longer represents dispersed bubbles. The new coalescence source term reads:

$$\int \dot{F}_{c,b}\pi d^2 \partial d \partial \mathbf{w} = a_i^{5/3}\epsilon_{dg}^{1/3}\alpha_{dg}^{1/3}(\theta\xi_c(N_c) + \xi_b(N_c)) \tag{4.2}$$

Where θ is a smooth continuous function which equals 1 when $\alpha_l = 1$ and 0 when $\alpha_l = 0$. This weighting process is consistent with the formulation of the GLIM method defined in section 2.2. Since breakup is the result of a collision between a bubble and a similarly sized water turbulent eddy, the breakup source term naturally tends to zero when air volume fraction is no longer associated with dispersed bubbles but with continuous structures. It does not require the same treatment. This modification enables us to control the interfacial area value in regions of continuous air which is important if we are to model what it becomes when such air is transformed into dispersed bubbles. Figure 4.5 shows a theoretical coalescence source term before and after the modification as a function of void fraction.

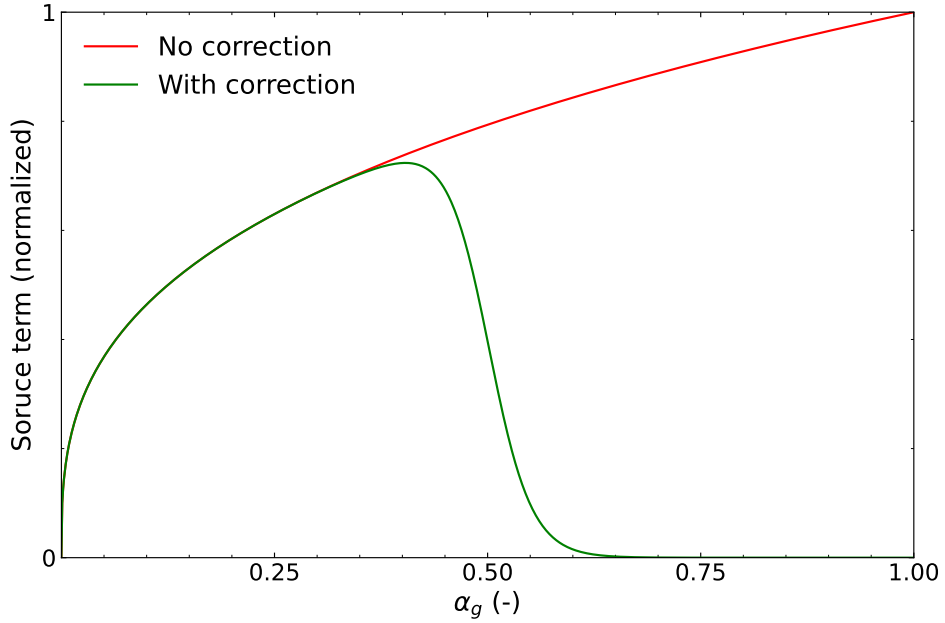

Figure 4.5: Differences between the old and new coalescence source terms as a function of air volume fraction. Water turbulent kinetic energy dissipation, interfacial area and the coefficient ξ are assumed constant.

4.4 Air entrainment inclusion diameter prediction

In this section we present the model dedicated to the prediction of air bubble diameter when they are created from air entrainment mechanisms. Here it is included in a RANS framework with an interfacial area transport equation but it could very well be adapted to VOF simulations with a population balance model since it only predicts the inclusion size when air transitions form continuous to dispersed. Before the current work, an arbitrary interfacial area value was set in the continuous air region which was transported to a region containing dispersed inclusions. The issues of this approach are obvious, first, the quantity is independent from the local flow conditions. Second, in the event of an exploratory simulation with no experimental data, choosing the interfacial area value can be tricky. Finally, its evolution in time in a region highly affected by air entrainment may not be consistent.

This work only focuses on providing a model for the interfacial area value of air transitioning between different regimes. The major impact it has on simulation results is the key motivation for this work. The development is divided into three parts, first we describe why mass transfer is not included in the process, then how the interfacial area transport equation is modified to account for new phenomenons at the interface and then different source terms are introduced with their limitations and advantages.

4.4.1 Mass transfer modelling

Before describing in details the air entrainment model, we should clarify why we decided not to model mass transfer between the continuous and dispersed air. Since a unique field is associated to every element, continuous and dispersed air are described with the same volume fraction and velocity fields. The mass transfer between both

is therefore implicitly computed during the time integration. Section 2.2 and particularly equation 2.96 illustrate the fact that on a given cell at a given time, dispersed and continuous structures both contribute to the total interaction terms. Tracking the weighting coefficient γ in equation 2.96 gives an idea of mass transfer between the two regimes. In theory, it is possible to enforce a mass transfer term through a change to this weighting coefficient. In practice, we decided to keep the weighting coefficient unchanged.

4.4.2 Interfacial area transport equation modification

As mentioned above, interfacial area is the measure of air-water surface area per unit volume of dispersed inclusion. This quantity drives the interfacial momentum transfer terms and determining it with accuracy greatly improves the global output of a simulation. In fact misrepresenting this diameter can have serious impact on total entrained air mass. Larger bubbles tend to flow back to the surface more rapidly than smaller ones thus hindering the total air holdup below the free-surface.

To predict the entrained air interfacial area, we need to change the way its evolution equation is solved. The main idea is to isolate three regions in a domain. The region containing continuous air, those containing continuous water and dispersed air and the large interfaces separating the two previous regions. Once these regions are isolated, it is possible to include different source terms in the interfacial area transport equations to model the air bubble diameter near the free-surface. The way they are identified mirrors the work already carried out in drag models with the weighting coefficient γ. The latter represents a smooth transition between the regions and allows not to associate each cell to a region. This also allows for the source term to be smoothly defined in all the computational domain, thus avoiding discontinuities in modelling. The evolution equation for a_i as it is solved in neptune_cfd without any coalescence or breakup source terms reads:

$$\alpha_g \rho_g \frac{\partial X}{\partial t} - X \frac{\partial}{\partial x_i}(\alpha_g \rho_g u_{g,i}) + \frac{\partial}{\partial x_i}(\alpha_g \rho_g u_{g,i} X) = 0 \tag{4.3}$$

Where α_g and ρ_g are air volume fraction and mass per unit volume, $u_{g,i}$ is its velocity and X is such that $\alpha_g \rho_g X = a_i$. In a cell I with neighbours in V_I between time steps n and $n+1$, equation 4.3 becomes:

$$\frac{\alpha_I \rho_I \Omega_I}{\delta t}\left(X_I^{n+1} - X_I^n\right) - X_I^{n+1} \sum_{J \in V_I} \phi_{IJ} \alpha_{IJ} + \sum_{J \in V_I} \phi_{IJ} \alpha_{IJ} X_{m,IJ}^{n+1} = 0 \tag{4.4}$$

Where $\phi_{IJ}\alpha_{IJ}$ is the mass flux between cells I and J, δt is the time step, Ω_I is the cell volume and $X_{m,IJ}$ is the value used to determine the convective flux of X through a face separating cells I and J. The last sum on the right-hand side of equation 4.4 is responsible for transporting interfacial area between regions, it is the one we are going to modify. The main idea is to write it as a linear combination of the standard flux and an imposed flux depending on local flow characteristics at the free-surface. To keep it as simple as possible, only the explicit part of the convective flux accounts for the presence of a free-surface. The implicit part is kept the same.

$$X_{m,IJ}^{n+1} = (1-\gamma)X_{fs,IJ} + \gamma X_{IJ}^{n+1} \tag{4.5}$$

Where X_{IJ}^{n+1} is the standard value of X used to compute the flux and X_{fs} is the value imposed in a free-surface region to account for air entrainment mechanisms. This approach is illustrated in figure 4.6 where, for brevity, the flux of X coming out of a free surface cell is computed completely with X_{fs}.

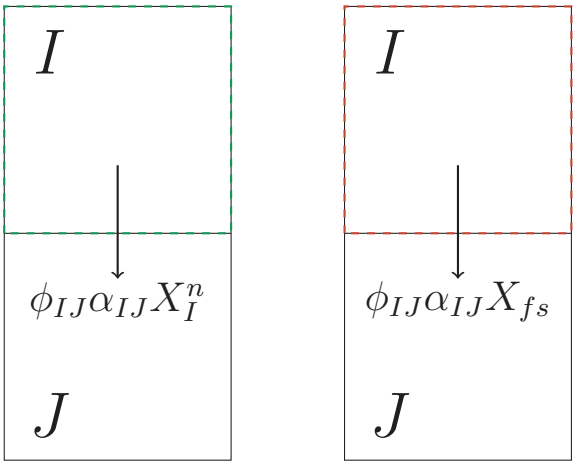

Figure 4.6: On the left, two standard cells; on the right, the cell above contains a large interface. The convective flux is supposed positive from cell I to cell J.

With an upwind approach, the discretised equation 4.4 becomes:

$$\left(\frac{\alpha_I\rho_I\Omega_I}{\delta t} - \sum_{\phi_{IJ}<0}\phi_{IJ}\alpha_{IJ}\right)X_I^{n+1} = \frac{\alpha_I\rho\Omega_I}{\delta t}X_I^n - \sum_{\phi_{IJ}>0}\phi_{IJ}\alpha_{IJ}\gamma(X_{fs,I}^n - X_I^n) - \sum_{\phi_{IJ}<0}\phi_{IJ}\alpha_{IJ}(X_{m,J}^n + \delta X_J) \tag{4.6}$$

For the equation above to be solved, an expression for X_{fs} must be provided. This expression is related to the diameter given to bubbles created from the free-surface $d_{fs} = 6/(\rho_w X_{fs})$. In practice, the resolution of the equation is unchanged compared to previous versions of the software if not for the modification of some of its terms. In order to avoid some truncation errors, a θ-scheme was explored. Since the work was inconclusive, it is not presented here. It is presented in appendix C.

4.4.3 Entrained bubble diameter modelling

This section focuses on the closure expression for X_{fs}. This term represents the value of interfacial area given to air transported from a region with a free-surface to a region with mostly dispersed air bubbles. Various options are explored, their advantages and limitations are presented before each model is compared to experimental data.

Diameter based on simulated free-surface interfacial area

The first model is based on the physical definition of the interfacial area. As mentioned above, it is the ratio between air-water surface area and air volume. For a large interface, this quantity can be computed from the simulation outputs. In fact, if α_g is the air volume fraction, and η_{fs} represents a subgrid surface roughness as defined in Brocchini and Peregrine (2001*a*,*b*), the interfacial area in a cell reads:

$$a_i = \|\nabla \alpha_g\|(1 + \eta_{fs}) \tag{4.7}$$

a_i represents the same physical quantity as the modelled interfacial area used in a bubbly region to describe the bubbles diameter. Therefore, when bubbles are created from a free-surface, their size must be related to the total surface available at the interface. Figure 4.7 shows schematically the process behind this inclusion diameter model.

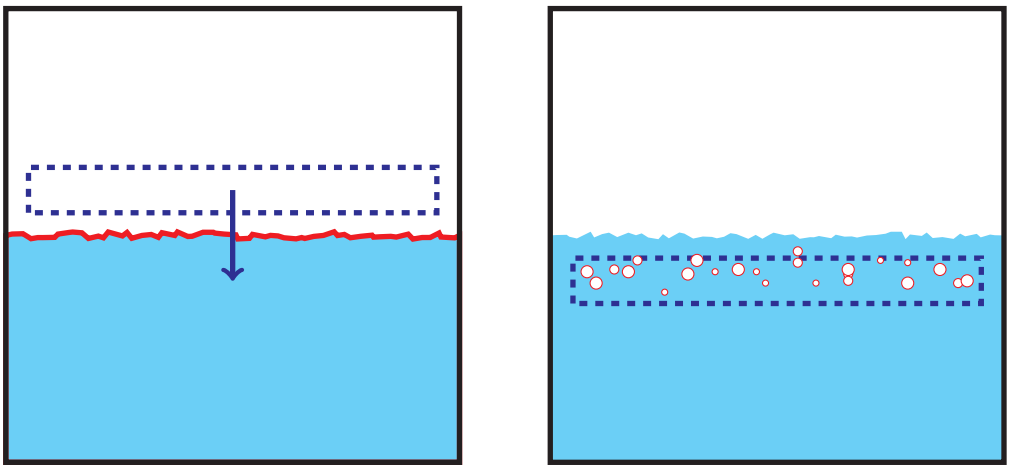

Figure 4.7: Sketch showing the idea behind the first inclusion model. Air near the free-surface is entrained below the free-surface. Its interfacial area is computed from the simulated surface area and a subgrid model accounting for interface roughness.

The rougher a free-surface, the larger the interfacial area, it acts as a surface area multiplier. An important implicit assumption of the model is the fact that this phenomenon is one-way. Bubbles are created from the interfacial area of a free-surface but their size is small compared to the size of the large interface. Creating a bubble thus does not diminish the total amount of air-water surface area. Finer models could take this into account. Specifically, when bubbles rise to the surface, they momentarily increase the amount of air-water surface area. In our study, this phenomenon is neglected due to its dissipative nature and relatively low importance compared to the entrainment mechanism.

In theory this model is consistent, however, due to the numerical aspects of the framework, some drawbacks can appear and make the model much more complex to use. The most serious inconsistency stems from the way interfacial area is computed. Its value changes depending on the mesh, making it impossible to converge spatially. A possible solution would be to consider a fixed independent mesh from which the interfacial area is computed. This is a serious issue since it requires a case by case definition, it lacks generality.

Diameter based on free-surface curvature computation

The following model is based on the simulated free-surface curvature. As in the previous example, it computes the source term from local flow characteristics which are outputs of the simulation. The main idea being that if bubbles are created from the free-surface, they tend to have the same curvature as the structures they come from (see figure 4.8 for a diagram). The advantage, compared to the previous model, is its independence with the computational mesh. Better still, the finer the mesh the more accurate the curvature prediction should be.

$$a_i = 3\alpha_g \kappa \tag{4.8}$$

Where κ is the computed curvature of the large interface issuing the bubble. The main disadvantages of this approach is the large computing time required to obtain the free-surface curvature and the challenges facing this kind of computation. In fact, in averaged methods, the interface may be smeared across several cells, making its curvature uneasily accessible. Moreover, in highly turbulent flows, this quantity requires a very fine mesh to be computed accurately. Thus limiting its use to cases where the surface is well defined. The curvature is also used in De Santis, Colombo, Hanson and Fairweather (2021) to set a transition limit between resolved and unresolved structures but its relation to physical quantities is also questioned by the authors. Thus illustrating the limit of the criteria in averaged frameworks.

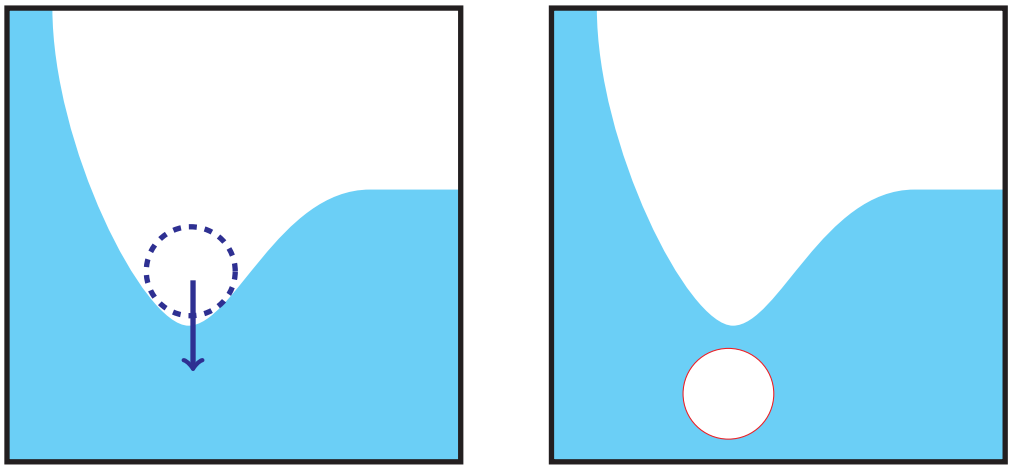

Figure 4.8: Sketch showing the idea behind the second inclusion model. Air near the free-surface is entrained below the free-surface. Its interfacial area is computed from the simulated surface curvature.

The results obtained with this model are shown in section 4.5. They highlight the deficiencies of the model in highly turbulent flows where curvature computation is not straightforward and its great performance in less turbulent cases.

Diameter based on the Hinze scale

The last model explored during the thesis is based on an approach developed in wave breaking theory (Deane and Stokes, 2002; Deike et al., 2016; Mostert et al., 2022). It

relies on several hypothesis. First, the entrained air must be created from the free-surface after its interaction with a turbulent eddy. Second, these air structures must subsequently be divided into smaller and smaller structures after their interaction with turbulent eddies of similar size. This breakup cascade, which goes on until bubbles reach the Hinze scale, must take place in a short period of time compared to flow time scales. Finally, this process must occur near the free-surface so that we can define a buffer region close to the large interface where it takes place.

The Hinze scale d_H represents the minimum size a bubble can reach after subsequently being broken down by velocity fluctuations at its scale (Kolmogorov, 1949; Hinze, 1955). By assuming the flow is unaffected by the presence of bubbles and is described by Kolmogorov's inertial subrange, it is possible to define a turbulent Weber number for each bubble of diameter d_b. A non dimensional parameter which is the ratio between fluid turbulent kinetic energy and surface tension effects.

$$W_e = \frac{\rho_w}{\gamma_s} \epsilon_w^{2/3} d_b^{5/3} \tag{4.9}$$

Where ρ_w and γ_s are the water mass per unit volume and air-water surface tension and ϵ_w is the water turbulent kinetic energy dissipation. Critical Weber numbers can be obtained from experimental studies, the typical range being $W_{e,c} \in [1, 5]$ (Risso and Fabre, 1998). Hinze's scale can be obtained from the turbulent Weber number and its critical value.

$$d_H = \left(\frac{W_{e,c}\gamma}{2\rho_w} \right)^{3/5} \epsilon_w^{-2/5} \tag{4.10}$$

In other sources (Mostert et al., 2022), Hinze's scale appears with a constant instead of the critical Weber number. This constant must be determined experimentally as well.

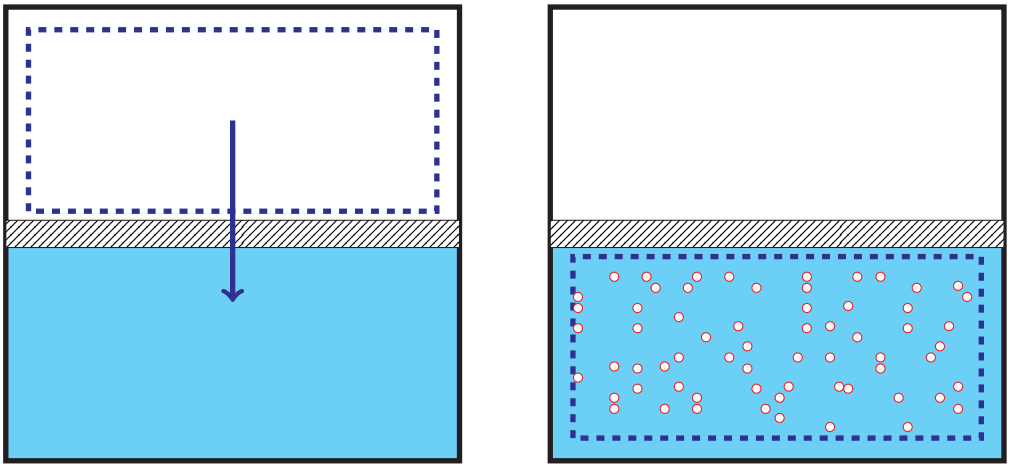

Figure 4.9: Sketch showing the idea behind the third inclusion model. A buffer region separates the continuous air from dispersed air. In that region liquid turbulent eddies breakup air structures until they reach Hinze's scale. Dispersed air exits the buffer region with that size.

By definition, the last source term is independent from the mesh as long as the water turbulent kinetic energy dissipation is more and more accurate with a mesh refinement.

Another advantage compared to the second model is the fact that it is more suitable in highly turbulent cases. On the other hand, this model also has its limitations. The most important being that it is not applicable to cases where air entrainment is mostly due to surface instabilities (Air entrainment from cusps). This will be illustrated in section 4.5 when comparing the results with experimental data. Moreover, its definition heavily relies on the framework ability to predict ϵ_w accurately.

4.5 Comparison with experimental data

This section is dedicated to the comparison of experimental measurements and simulation results obtained with the new entrainment models. The three cases are supposed to represent three different entrainment scenarios. The first one is the entrainment described by figure 4.2, the second represents the mechanism described in figure 4.3 and the last one represent the entrainment caused by highly turbulent free-surface flows.

4.5.1 Small scale water jet

The first case consists in a small size smooth water jet experiment described in Iguchi et al. (1998). Figure 4.10 shows the geometry of the experimental apparatus.

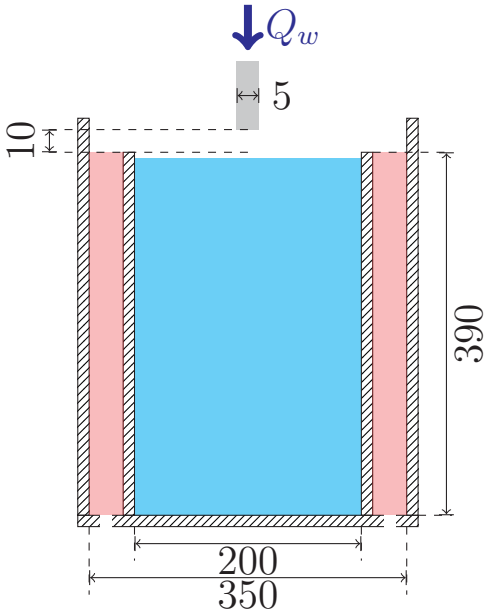

Figure 4.10: Geometry describing the small scale water jet experiment (Iguchi et al., 1998). The blue arrow represents the jet inlet. Distances are in mm.

The purpose of the experiment is to determine how the operating conditions drive the different observations in terms of bubble production and to quantitatively examine the liquid flow near the jet impact point with Laser Doppler velocimetry (LDV) imaging techniques. The circular jet has a diameter of $d_j = 5\,\text{mm}$, its mass flow rate is $Q_w = 5 \times 10^{-2}\,\text{kg}\,\text{s}^{-1}$ and the distance between its inlet point and the free-surface is $h = 10\,\text{mm}$. Its turbulent intensity at the inlet has been estimated to be between 5% and 15%. The receiving bath is circular and its dimensions are detailed in figure 4.10. When the jet is activated, the design of the experiment ensures that the

distance between the jet inception and impact points remains the same (overflowing reservoir). The water flowing inside the secondary reservoir (shaded in red in figure 4.10) is then extracted from the bottom and sent to a tank. The measurements include the depth of the bubble plume and the liquid mean and fluctuating velocities. In this setup, there are no measurements regarding bubble size distribution. However, the penetration depth of bubbles is usually a good indicator of their size. In the original publications, other scenarios are explored, we only focus on the one described above. The numerical simulations are carried out on a geometry shown in figure 4.11 matching the experimental setups.

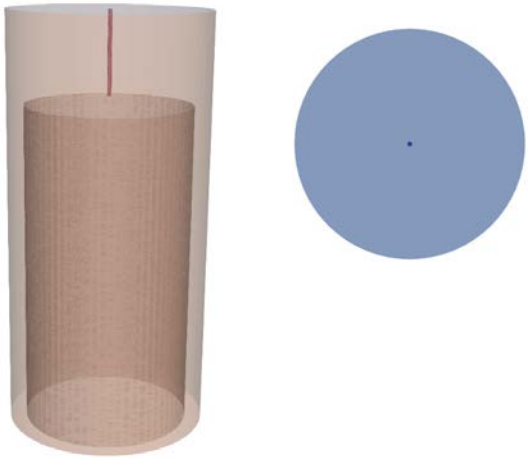

Figure 4.11: Numerical geometry and boundary conditions for simulation of the smooth water jet. Jet inlet condition in the centre (dark blue), top outlet condition (blue), tank walls (orange) and inlet tube (red).

Three 3D meshes have been generated without additional refinement near the walls with 251 775, 1 521 192 and 4 611 756 cells. Boundary conditions are defined in table 4.1. Water and air are supposed to be at atmospheric conditions, water density is $\rho_w = 1000\,\mathrm{kg\,m^{-3}}$, its viscosity is $\mu_w = 0.001\,\mathrm{Pa\,s}$; Air density is $\rho_a = 1.2\,\mathrm{kg\,m^{-3}}$, its viscosity is $\mu_a = 1.8 \times 10^{-5}\,\mathrm{Pa\,s}$. The time step is adaptive and ensures the condition CFL < 1, the turbulence model is a linear production k-ϵ model for water and no model for air. The generalised large interface method is selected. Initially, the receiving bath is filled with water, the rest of the domain is filled with air. Water is injected from the jet inlet. When the simulation reaches a steady-state, physical quantities are averaged for 20 s.

Boundary condition	Color in figure 4.11	Properties
Jet inlet tube	red	-
Walls	orange	-
Jet inlet	dark blue	Flux inlet $Q_w = 0.05\,\mathrm{kg\,s^{-1}}$
		Water volume fraction $\alpha_w = 1$
Top outlet	blue	Pressure outlet $P = 101\,325\,\mathrm{Pa}$
		Water volume fraction $\alpha_w = 0$

Table 4.1: Boundary condition definition for the numerical simulation of the smooth jet case.

Simulations are first carried out without inclusion model (the entrained bubble diameter is set at the beginning of the simulation) on the three meshes to ensure spatial convergence. The diameter is fixed to $d_b = 1\,\text{mm}$ for bubbles entrained at the point of impact of the jet. It is the size qualitatively observed experimentally near the impact point (Iguchi et al., 1998). Results plotted include the mean axial liquid velocity and mean turbulent kinetic energy as well as gas volume fraction on the vertical line centered on the jet and the dimensionless axial mean velocity on three horizontal profiles at depth 100 mm, 200 mm and 300 mm in the reference mesh (intermediate refinement). Instantaneous snapshots on a plane containing the jet centre line are shown in figure 4.12. The air volume fraction plot illustrates the ability of the framework to consider multiple regimes at once. There is the resolved air-water interface (in dark blue in the figure) and there are dispersed inclusions represented by a non-zero air volume fraction below the free-surface. The transition between the two at the jet impact point is the explored phenomenon. The turbulent quantities near the jet impact point are similar to those in a single-phase jet. High intensity on the jet surface in the mixing layer and low on the jet centre line. When sufficiently deep, the mixing has homogenised the turbulent quantities.

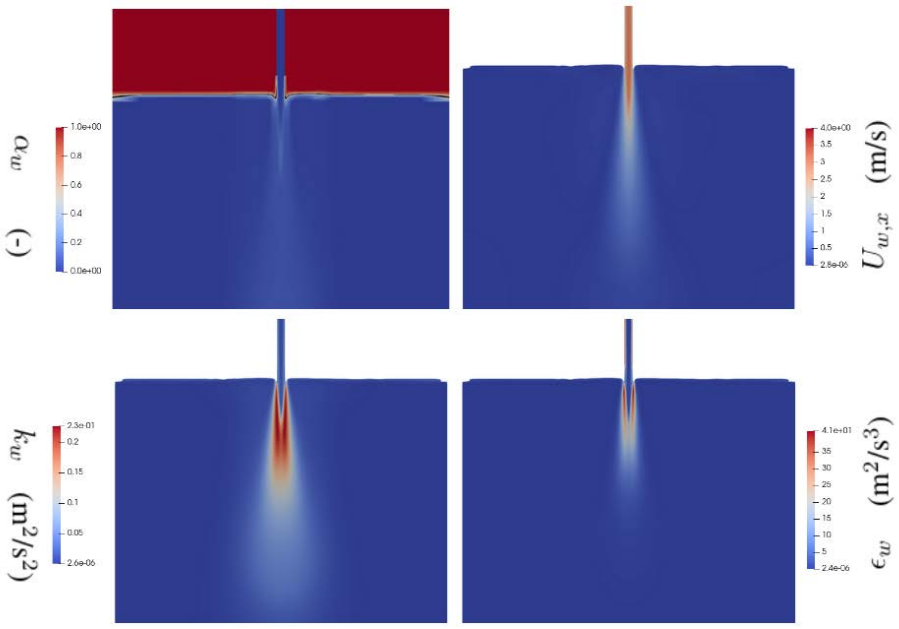

Figure 4.12: From top left to bottom right: snapshot of the free-surface and air volume fraction (α_g), liquid velocity magnitude ($\|\mathbf{U_w}\|$ in $\text{m}\,\text{s}^{-1}$), liquid turbulent kinetic energy (k_w in $\text{m}^2\,\text{s}^{-2}$) and liquid turbulent kinetic energy dissipation (ϵ_w in $\text{m}^2\,\text{s}^{-3}$).

Figure 4.13 shows correct convergence behaviour even though axial mean and turbulent velocities are not sufficiently close to experimental measurements. Moreover, it also highlights the inaccurate prediction of the bubble penetration depth. Demonstrating the need for an entrained bubble diameter model which may improve the results altogether.

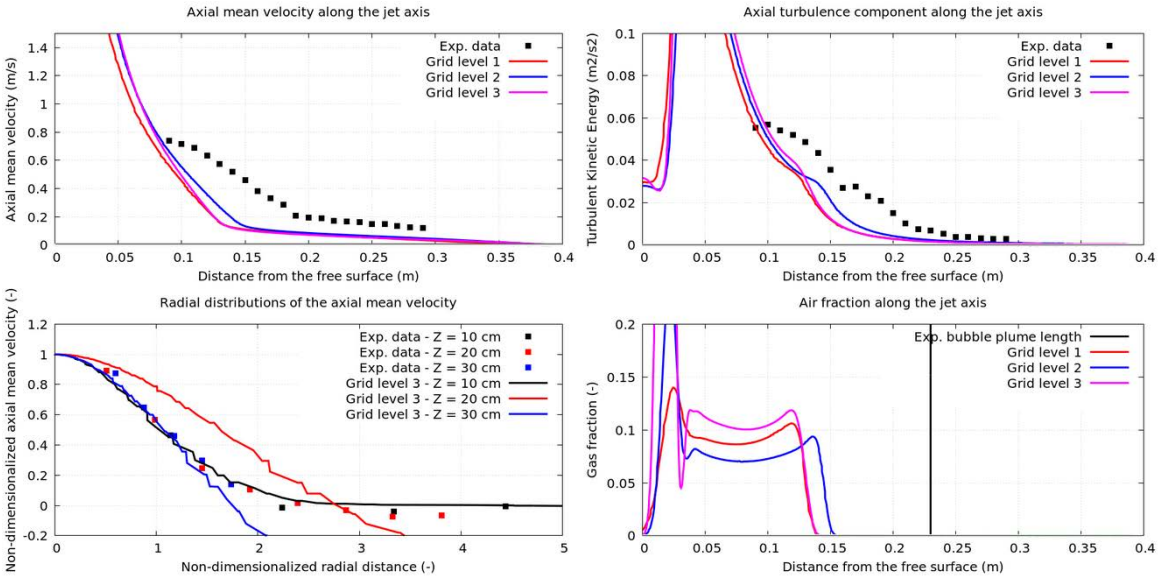

Figure 4.13: Simulation results for the three mesh refinements.

The simulations are now carried out with the two models based on the free-surface curvature and the Hinze scale described in section 4.4.3 on the reference mesh. These are shown in figure 4.14. The model based on the curvature is the only one to improve the mean and turbulent quantities as well as the bubble penetration depth. It still struggles to predict the exact experimental turbulent kinetic energy on the jet centre line but its results are generally much better than those obtained without entrainment model or with the model based on Hinze's scale. It also improves the horizontal profiles shown on the bottom left-hand side figure.

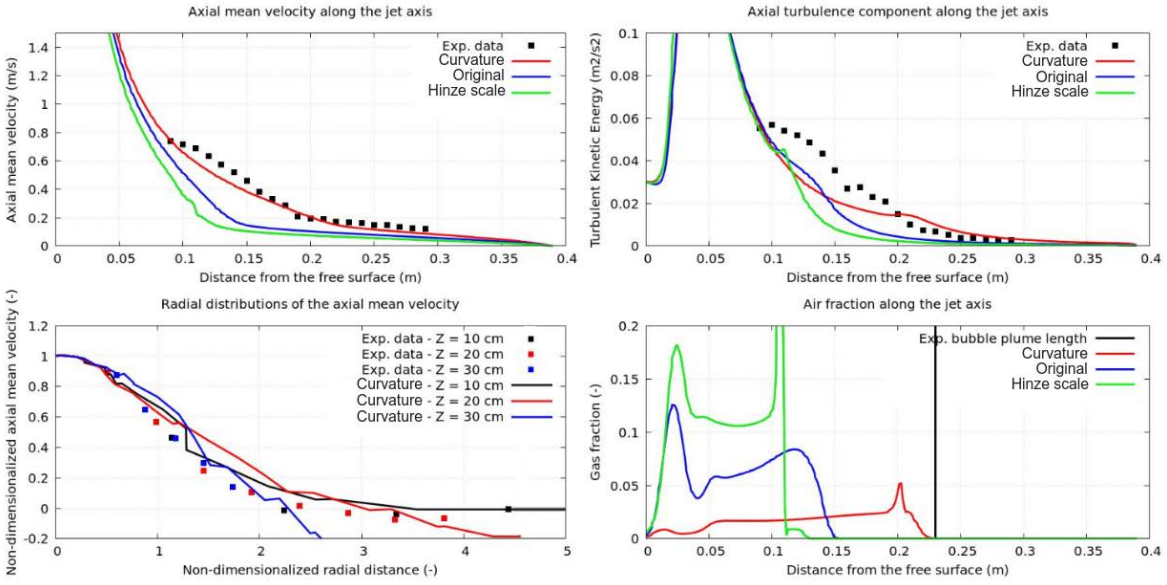

Figure 4.14: Simulation results for the three inclusion models on the reference mesh. No inclusion model (blue), inclusion model based on free-surface curvature (red) and inclusion model based on Hinze's scale (light green).

The model based on the free-surface curvature seems to give better bubble diameter prediction because the mechanism driving air entrainment in this configuration

is mostly geometric. Bubbles tend to be detached from the free-surface by growing instabilities in the cusp, creating structures of similar size to the cusp. The interface curvature is therefore a great measure of the created bubble size. On the other hand, the model based on Hinze's scale does not give satisfactory results because we think the configuration does not include the mechanisms responsible for air entrainment covered by this specific model. We would expect the model to perform better on a rougher, more turbulent jet.

4.5.2 Large scale over-flowing jet

The second air entrainment scenario explored is an experimental setup developed and exploited since 2014 (Castillo et al., 2014, 2015; Carrillo, Castillo, Marco and García, 2020; Carrillo, Marco, Castillo and García, 2020; Carrillo, Ortega, Castillo and García, 2020; Carrillo et al., 2021). The choice was motivated on the one hand by the size of this jet. The large scale means the surface of the jet is rough and the primary air entrainment mechanism taking place is the one described in figure 4.3. This gives us the opportunity to assess whether the inclusion model based on Hinze's scale, more representative of this mechanism, is more reliable. On the other hand, this case was chosen also because of its similarities with the industrial setup which motivates the thesis at EDF. The case consists in two rectangular tanks, one located above the other. When water is injected in the top tank, it overflows and creates a jet which impacts the bottom tank. At the impact point, air is entrained and transported towards the bottom tank outlet located on its right-hand side. Several scenarios have been explored during the years. Different inlet water fluxes, measurements on the receiving pool or on the jet aeration. Our goal here is to focus on bottom tank measurements in a specific scenario defined in table 4.2.

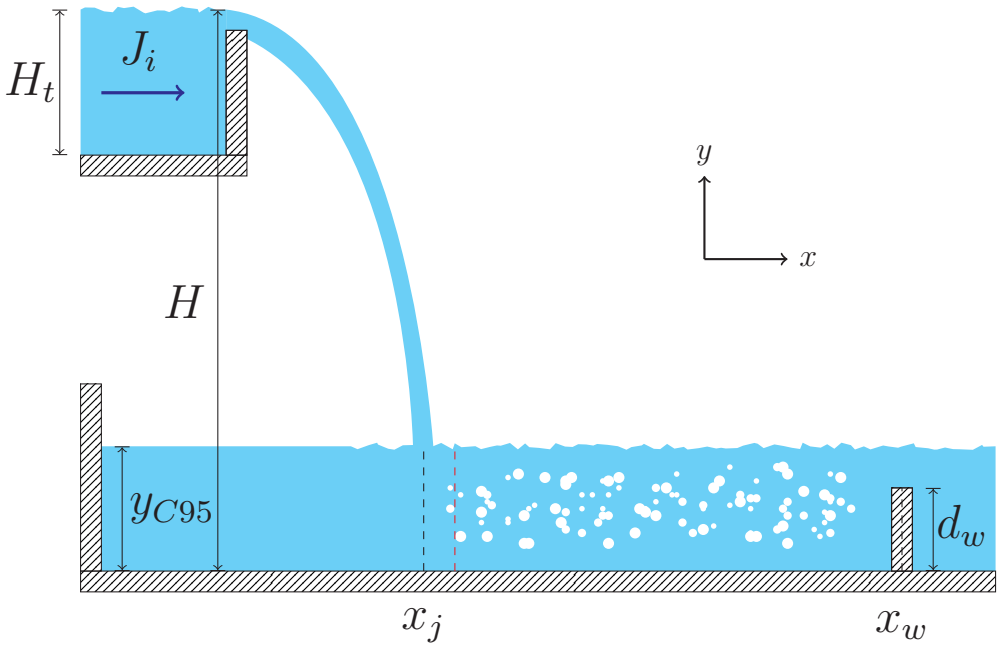

Figure 4.15: Experimental setup for the over-flowing jet (Carrillo, Castillo, Marco and García, 2020). The red dashed line represents the first measurement profile plane located 10 mm downstream the jet impact point.

Figure 4.15 represents a sketch of the experimental device. Measurements are done with an optic fiber probe and a back-flushing Pitot tube on vertical profiles in the plunge pool downstream the jet impact point. These probes give access to fluid velocity, air volume fraction, bubble detection frequency and bubble mean Sauter diameter. High speed cameras were used to measure average bubbles size and for a qualitative description of the flow. The jet impact point position and plunge pool depth are determined from these images. Measurements are also performed on air concentration profiles in the jet itself on planes perpendicular to the jet at different distances to the jet inception point.

Variable		
Top tank height	H_t	0.85 m
Jet height	H	2.2 m
Plunge pool depth (measurement)	y_{C95}	0.32 m
Weir x-coordinate	x_w	3.0 m
Weir height	d_w	0.25 m
Jet impact x-coordinate (measurement)	x_j	0.83 m
Reservoir width	H_w	1.05 m
Inlet water flux	J_i	$0.085\,\mathrm{m\,s^{-2}}$

Table 4.2: Properties definition for the experimental setup of the over-flowing jet. $x = 0$ is defined at the jet inception point.

Simulations are carried out on 3D meshes with 367 920, 733 020 and 1 491 690 cells respectively. Boundary conditions are defined in figure 4.16.

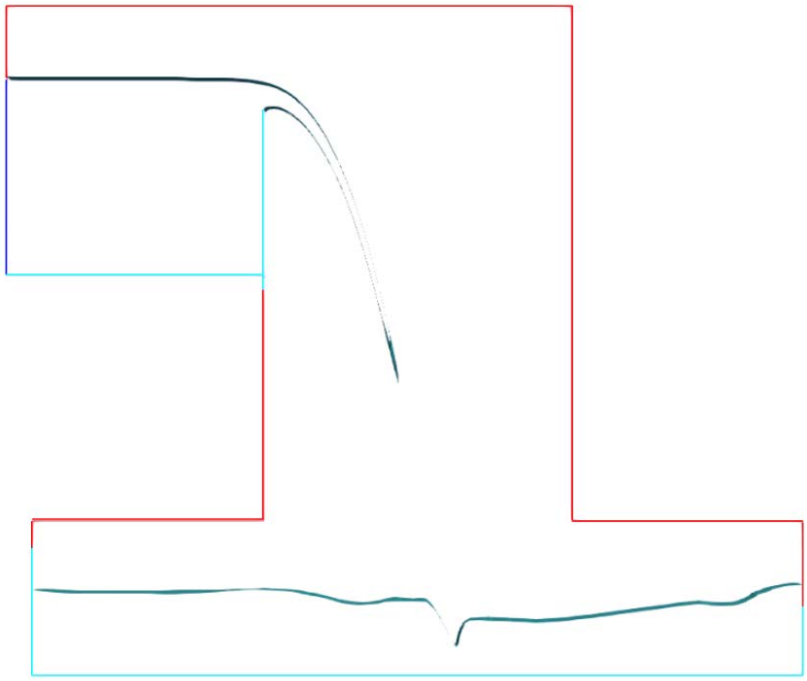

Figure 4.16: Boundary conditions for the simulation of the over-flowing jet. (red) is a pressure outlet, (light blue) is the walls and (dark blue) is the water inlet. A clipping of air volume fraction is shown: $0.45 < \alpha_g < 0.55$.

Second order Reynolds stress models are selected for continuous turbulence and the generalised large interface model is selected to describe air-water interaction. Water and air are supposed to be at atmospheric conditions, water density is $\rho_w = 998\,\mathrm{kg\,m^{-3}}$, its viscosity is $\mu_w = 0.001\,\mathrm{Pa\,s}$; Air density is $\rho_a = 1.2\,\mathrm{kg\,m^{-3}}$, its viscosity is $\mu_a = 1.85 \times 10^{-5}\,\mathrm{Pa\,s}$. The time step is adaptive and enforces the condition CFL < 1. Initially, both tanks are filled when the water is injected from the left-hand side boundary of the top reservoir. After 5 s, the simulation reaches a steady state and quantities are averaged for 20 s.

Preliminary simulations without any entrainment model give us the opportunity to assess the current performance of neptune_cfd on large scale jets as well as provide us with a reference result. Instantaneous snapshots of these simulation results are shown in figure 4.17. They illustrate the transition between the resolved interface and dispersed inclusions near the jet impact point. They also highlight the horizontal liquid jet that appears near the wall on both side of the stagnation point. A large scale vortex is also set up on the left-hand side of the receiving tank. It does not appear on the right-hand side because of the outlet condition. Overall comparison between early simulation results and experimental setups is acceptable. Table 4.3 sums up the macroscopic characteristics of the experimental setup and the simulated values. The configuration is generally well represented apart from the jet thickness. However, it is difficult to measure such a quantity on simulations due to its diffuse nature. Refining the mesh should help keep the interface solved down to the jet impact point thus giving a better estimation of its width. However, the purpose of this chapter is to introduce a model to perform industrial scale simulations of air entrainment. Trying to solve every interface is thus out of the scope of the thesis.

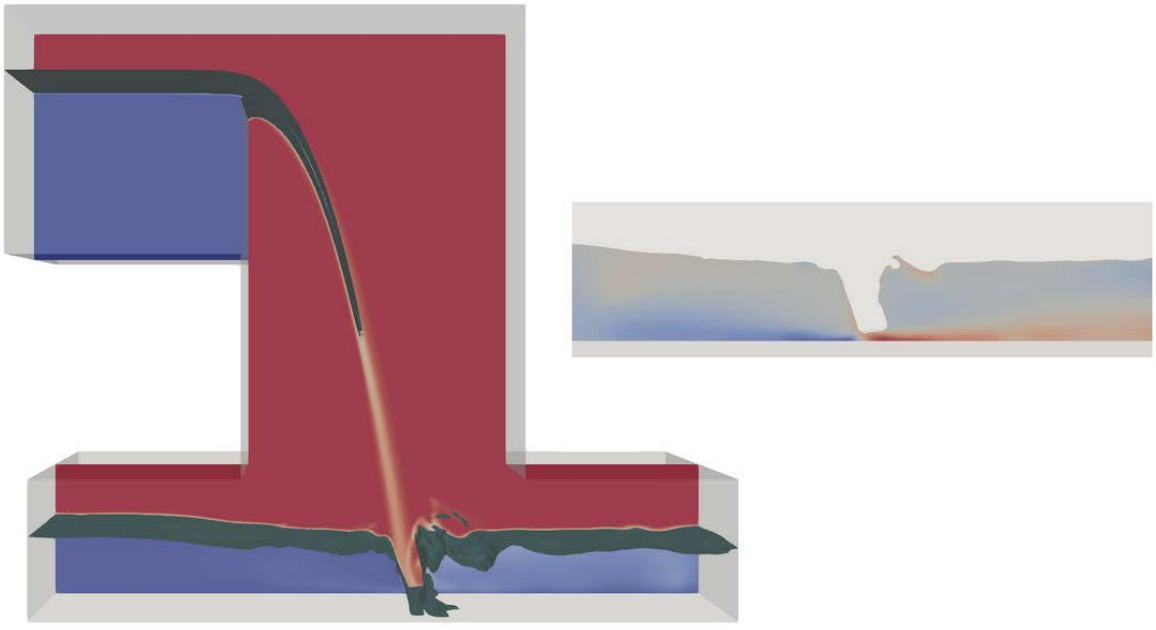

Figure 4.17: Snapshots of the simulation results with standard coalescence and fragmentation model without correction. (left) Solved air-water interface and dispersed air structures. (right) Liquid horizontal velocity in the plunge pool. The stagnation point is visible at the centre of the figure. The transition between resolved interface and dispersed inclusions happens halfway down the chute.

Variable	Carrillo et al.	neptune_cfd
Stagnation point (distance from jet inception)	0.73 m	0.75 m
Plunge pool depth	0.32 m	0.30 m
Jet velocity at the impact point	5.90 m s^{-1}	6.01 m s^{-1}
Jet thickness near the impact point	0.029 m	0.05 m

Table 4.3: Qualitative comparison between experimental and early simulation results.

Simulations to assess the solver's performance are carried out with a constant bubble diameter of 2 mm - the most present bubble diameter in the experimental results - and with a variable bubble diameter both with and without the correction of the coalescence source term. Figure 4.19 shows the bias originally introduced by the coalescence source term. Since the interfacial area decreased indefinitely in the continuous air region, when air was entrained below the free-surface it did so with a huge diameter. Results obtained with a constant diameter are consistent and provide a strong starting point for the development of entrained inclusion diameter models. Similarly, results obtained with the correction to the coalescence source term are coherent with experimental results but the predicted entrained diameter is slightly too small. The air volume fraction results illustrate the necessity to predict the correct diameter. If the prediction is too big, the air holdup tends to be increased thus degrading the results.

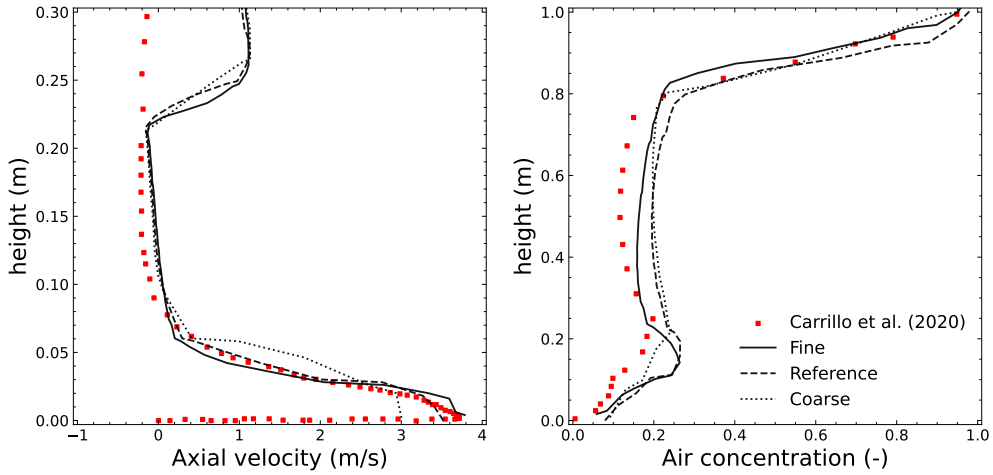

Figure 4.18: Convergence study with an entrainment model based on Hinze's scale $W_{e,c} = 5$. These profiles are located 10 mm downstream the jet stagnation point.

The simulations are then performed on the three meshes detailed above. Figure 4.18 shows the spatial convergence for the liquid velocity and air volume fraction. The three meshes give satisfying results for the air volume fraction. However, only the two finest meshes can simulate accurately the peak velocity near the wall. For future simulations, we decide to work with the finest mesh, it gives an appropriate compromise between computing time and results accuracy. In further plots, the velocity does not appear, it is always as well simulated as in the convergence study cases.

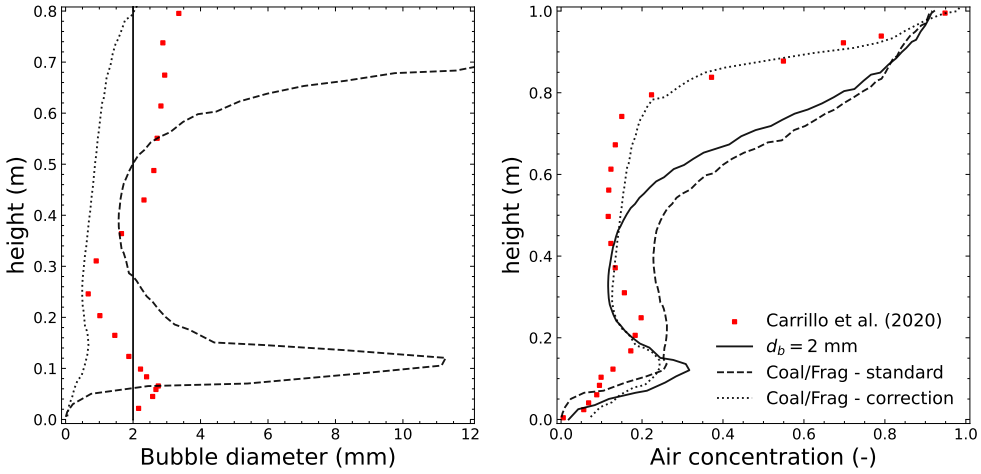

Figure 4.19: Predicted bubble diameter and air volume fraction in the plunge pool on a profile located 10 mm downstream the jet stagnation point. Correction on the coalescence source terms leads to more reasonable bubble diameters.

After mesh convergence and preliminary studies, the entrainment models are tested. Figure 4.20 illustrates the results obtained with the two entrainment models based on the free-surface curvature and Hinze's scale. It shows the bubble size prediction of the model based on Hinze's scale is more accurate mostly because of the fact that curvature is not computed precisely in the very turbulent region near the jet impact point. On the other hand, air volume fraction predictions are both satisfactory. This quantity, as long as the bubble diameters are not too big, seems to be unaffected by the inclusion size prediction. A key characteristic of the model, one of the reason it was designed in the first place, is its ability to be independent from the standard diameter set in the continuous air region. Results are not shown here for brevity but this has been thoroughly verified on all the different models and variations.

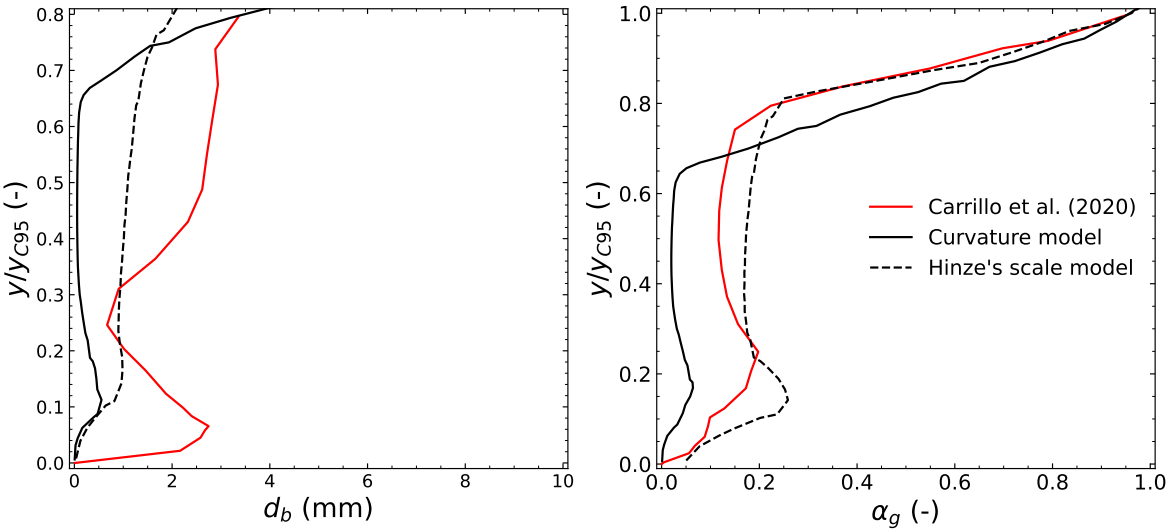

Figure 4.20: Bubble size and air volume fraction prediction depending on the entrainment model selected. The vertical profile is located 10 mm downstream the jet stagnation point.

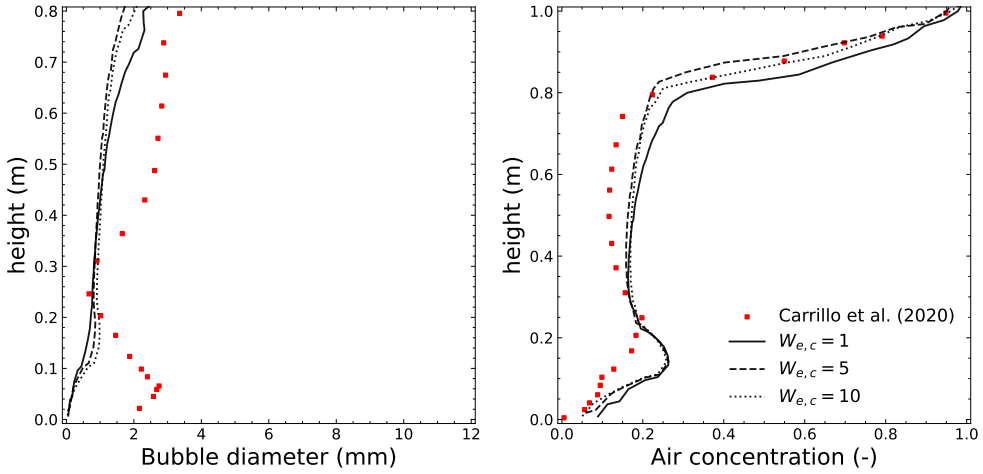

Figure 4.21: Bubble size and air volume fraction prediction depending on the critical Weber number $W_{e,c}$. The vertical profile is located 10 mm downstream the jet stagnation point.

The dependency on the critical Weber number is highlighted in figure 4.21. When it increases, the entrained bubble diameter increases as well. This is observed in bubble size prediction near the wall region even if the impact is not significant. This is consistent with the expression of Hinze's scale. In terms of air volume fraction, as noted earlier, a small change in bubble diameter prediction has little to no effect on air concentration in the plunge pool. Critical Weber number is the only parameter of the model and its impact on the results is not significant. This highlights the robustness of the entrainment model.

In all the results presented with the entrainment models, it seems that the predicted diameter is too small. Since increasing the critical Weber number did not end up in a substantial increase in predicted entrained bubble diameter, we studied the breakup model. Indeed, it is the only other term responsible for a decrease in bubble size. In neptune_cfd, the standard fragmentation model is based on the works of Prince and Blanch (1990). However, it is possible that this model overestimates the breakup rate in certain specific air-water scenarios. The breakup model from Luo and Svendsen (1996), which predicts a lower breakup efficiency, was tested. Figure 4.22 shows the results obtained without fragmentation model, with the original model from Prince and Blanch (1990) and with the model from Luo and Svendsen (1996). The results show, as expected, that bubbles tend to be larger without fragmentation model or with the one from Luo and Svendsen (1996). The simulated bubbles are closer to experimental results in size and air volume fraction profiles tend to be satisfactory as well. However, the model still cannot recreate the clear variation in bubble diameter near the wall. In the experiments, this variation fades out for profiles further away from the jet stagnation point. This makes us believe that there is probably an unsteady phenomenon happening close to the jet impact point that we are not simulating properly. All in all, results obtained with the fragmentation model from Luo and Svendsen (1996) are satisfactory with regards to bubble size and air concentration. In the end, other models could be tested such as the one from Yao and Morel (2004).

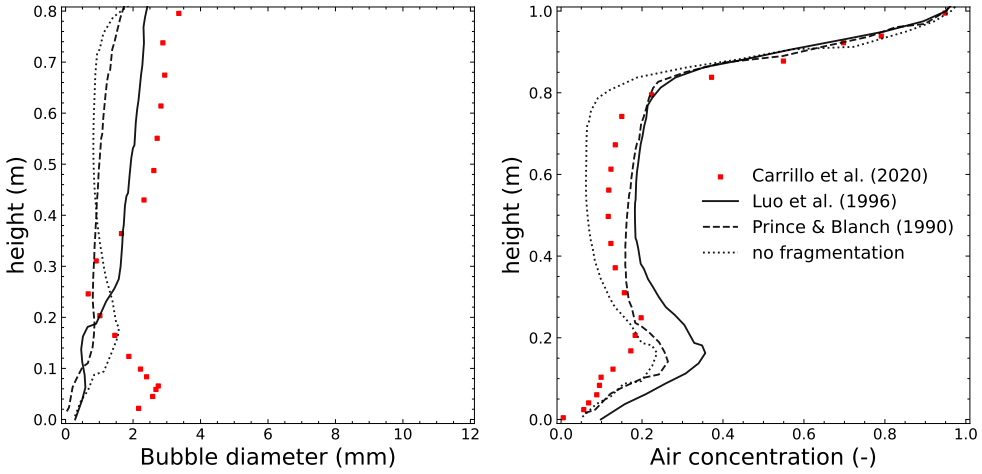

Figure 4.22: Bubble size and air volume fraction prediction depending on the fragmentation model. Results obtained with $W_{e,c} = 1$. The vertical profile is located 10 mm downstream the jet stagnation point.

Predicted bubble diameter can be underestimated compared to experimental measures for a couple of other reasons. First, in the measurements, the reconstruction of bubble diameter from probe measurement rely on several hypothesis which may not be verified in the most turbulent part of the receiving tank. Indeed, the measurements are based on the assumption that bubbles are spherical and moving at the velocity determined by CFD simulations. This might introduce a bias near the jet impact point. Further away, the flow is less turbulent and the variation in diameter is less pronounced (see figure 4.23).

Another explanation may be found in the way bubble diameters are plotted from our simulations. In fact, large resolved structures do not contribute to the average diameter in all the figures. Only dispersed structures do. In the area near the jet impact point, we can see large resolved air structures detaching from the free-surface, being transported a certain distance and then rapidly rise to the surface as shown in figure 4.24. Unfortunately these large structure tend to increase the mean air diameter measured near the bottom surface near the jet impact point in the experiment. Since we are not including these diameters in the plot, we are predicting smaller average bubble diameters. To overcome this issue, it would be necessary to create a post processing framework which first identifies the large pockets, evaluates their diameter and take it into account in the averaging process. However, this would require an entire rework of the bubble diameter post-processing routine. The fact that air volume fraction prediction further away from the jet impact point is overestimated clearly shows that the overall diameter prediction is underestimated (smaller bubbles rise more slowly to the surface than larger bubbles).

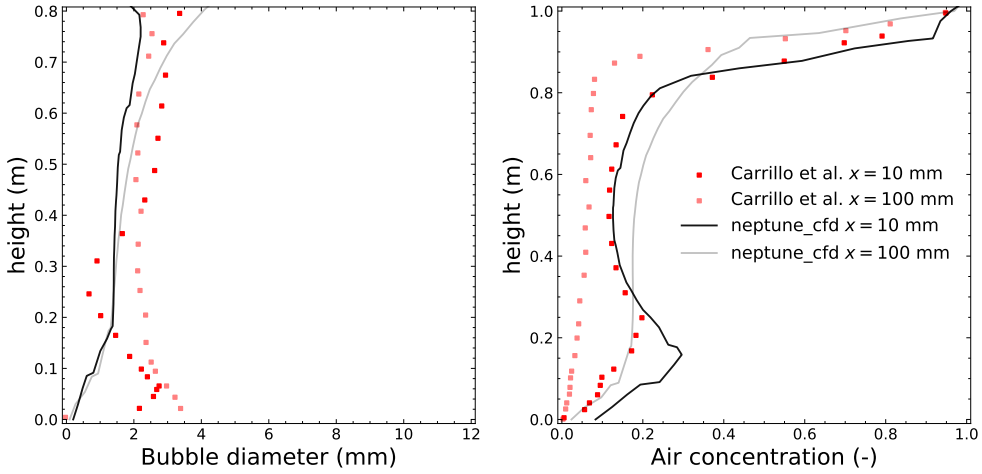

Figure 4.23: Bubble size and air volume on the nearest and farthest profiles. Simulation results (black) are obtained with $W_{e,c} = 1$, the fragmentation model from Luo and Svendsen (1996). Experimental results are shown in red.

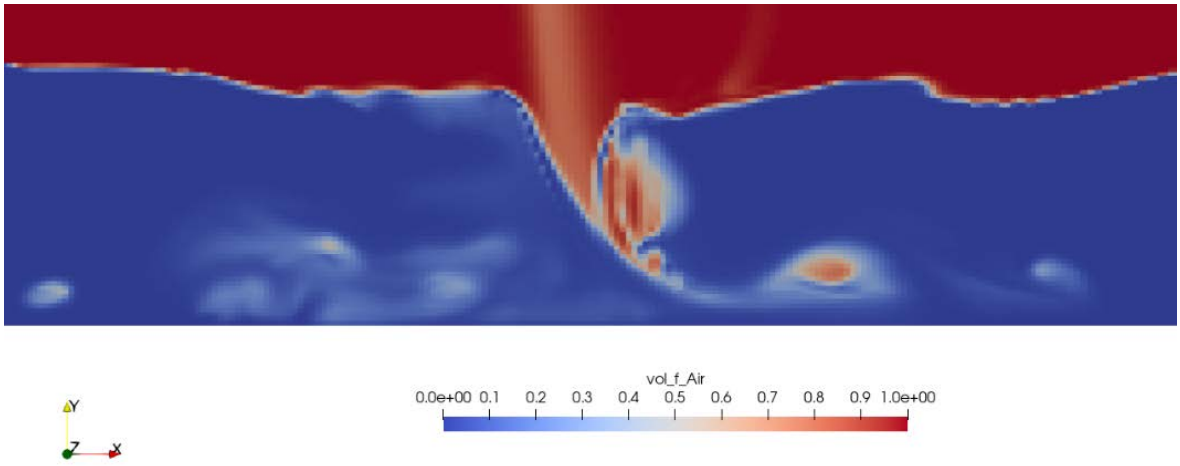

Figure 4.24: Air concentration field near the jet impact point. A large resolved air pocket is found near the bottom wall.

Experiments were also carried out to characterise air concentration within the jet (Carrillo, Ortega, Castillo and García, 2020). The setup is exactly the same as in the previous experiments but the inlet water flux is changed from $0.085\,\mathrm{m\,s^{-2}}$ to $0.072\,\mathrm{m\,s^{-2}}$. Air concentration profiles are obtained with conductivity probes on planes perpendicular to the free-falling jet. Figure 4.25 shows the simulated air volume fraction obtained without entrainment model but with the correction to the coalescence source term. Simulated aeration of the jet appears faster than it does in experimental results. This is probably due to the mesh, inadequate for these kinds of configuration. However, the final jet aeration near the impact point (green data on figure 4.25) is close to experimental results. Since this is the one driving air entrainment at the jet impact, we are happy to keep this mesh and not refine it further.

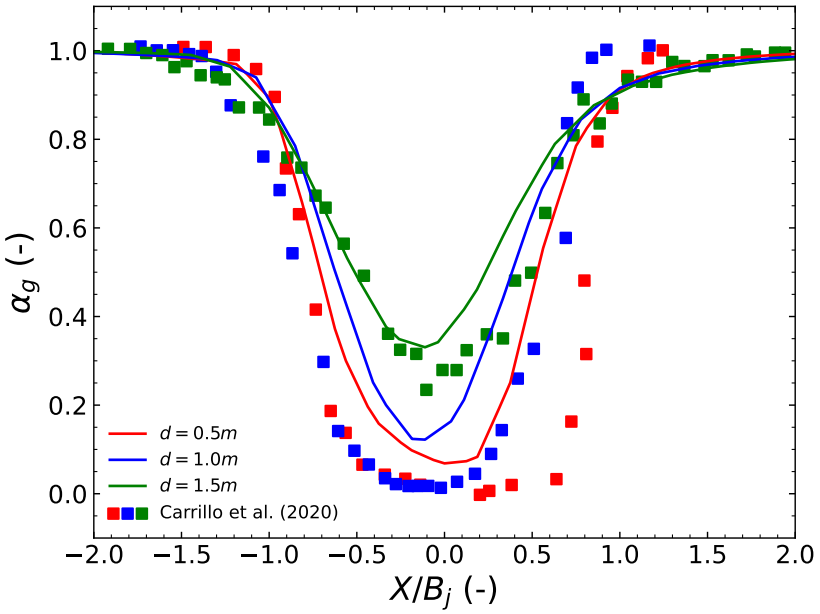

Figure 4.25: Air concentration profiles on planes perpendicular to the jet. d is the distance from the plane to the weir crest. X is the distance to the jet centre on the perpendicular plane and B_j is the jet thickness at the position of the plane.

This case has shown the inclusion model based on Hinze's scale has great potential to predict the correct bubble size for air entrained from a large scale turbulent jet. Fragmentation modelling has been identified as an important modelling choice in this configuration as well. Further studies on bubble column will arrive at the same conclusion. The model based on the free-surface curvature does not perform as well. The high turbulence generated by the jet impact seems to hinder the curvature evaluation. Moreover, air is entrained in regions where the free-surface is no longer simulated accurately. Hence the poor results obtained with such a method.

4.5.3 Hydraulic jump

This last case is supposed to illustrate another configuration where air entrainment occurs but is not related to impinging jets. It is a very good test case to check whether the model gives consistent results in another scenario. It consists in the transition from a critical flow ($F_r > 1$) to a sub-critical flow ($F_r < 1$). Where $F_r =$ is the Froude number, the ratio between kinetic energy and gravitational potential energy. In a free-surface flow, it is defined from the liquid mean velocity U, gravity g and stream depth h on a vertical plane $F_r = U/\sqrt{gh}$. This configuration generates the well-known hydraulic jump situation where turbulence induces air entrainment downstream the jump. The goal of this section is to test the air entrainment model based on Hinze's scale and to compare its results with experimental data (Murzyn et al., 2005) as well as VOF+RANS simulations from literature (Witt et al., 2015, 2018). Figure 4.26 and table 4.4 define the geometric and dynamics properties of the case.

Variable			
Channel dimension	length x width x height	$12 \times 0.3 \times 0.4$	m^3
Stream height	d	0.046	m
Weir x-coordinate	x_w	2.67	m
Weir height	d_w	0.041	m
Inlet water velocity	V_i	1.64	$m\,s^{-1}$
Froude number	F_r	2.46	-

Table 4.4: Properties definition for the experimental setup of the hydraulic jump. Distances are measured from the stream inception point.

Air and water are supposed to be at atmospheric conditions, water density is $\rho_w = 1000\,kg\,m^{-3}$, its viscosity is $\mu_w = 0.001\,Pa\,s$; Air density is $\rho_a = 1.2\,kg\,m^{-3}$, its viscosity is $\mu_a = 1.85 \times 10^{-5}\,Pa\,s$. The experiments are performed with different Froude numbers ($F_r = 2,\ 2.46,\ 3.7$ and 4.8), we only explored the case $F_r = 2.46$. Other cases must be studied in the future. The bottom panel of the channel has a roughness around 0.3 mm even if, in the simulation, this parameter is not taken into account. In experiments, control of the water flows allowed to steady the hydraulic jump position. An additional square bar was placed near the jump to make it even more steady. This obstacle is represented by the weir in the simulation which serves the same purpose. The measurements are done with an optical probe on vertical profiles downstream the hydraulic jump. These give access to air volume fraction and bubble size distribution as long as bubbles are assumed to be spherical. Published VOF+RANS simulation results from Witt et al. (2015, 2018) provide data including air volume fraction and bubble size distribution on the same planes. The size distributions are obtained from numerical counting of spherical bubbles at each time step. For more details on the published simulation work, the reader is invited to browse the referenced material.

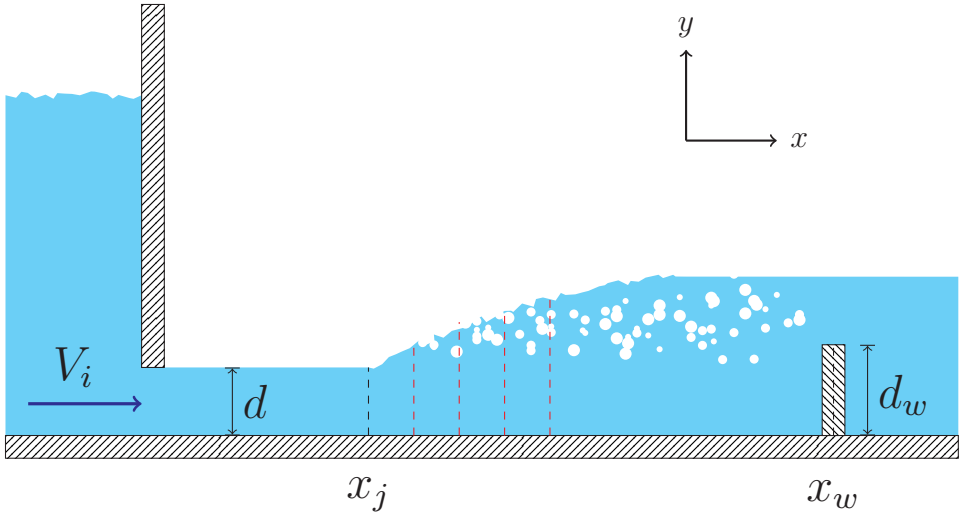

Figure 4.26: Geometric properties of the experimental setup. x_j is the position of the jump (Murzyn et al., 2005). Red dashed lines indicate the position of measurement planes.

The numerical simulation setup is illustrated in figure 4.27. Water is injected with a uniform velocity $V_l = 1.64\,m\,s^{-1}$ and the fluid domain stops at the weir. Since, for

the considered Froude number, 2D simulations seem to be sufficient (Witt et al., 2015), a 2D Cartesian mesh containing 300 000 cells is used. Second order Reynolds stress models are used for both phases and coalescence/fragmentation are taken into account for dispersed air. The entrainment model based on Hinze's scale is selected. Initially, the domain is filled with air. Water is injected and flows, without transitioning to a sub-critical Froude number flow until it reaches the obstacle. There the hydraulic jump forms and starts travelling upstream until it oscillates around an equilibrium point. Outlet water fluxes are adapted to make the jump as steady as possible.

Figure 4.27: Numerical setup of the hydraulic jump. Off plane boundaries are symmetries, on the bottom left-hand side is the inlet, red denotes a pressure outlet and light blue a wall.

Unfortunately, even by controlling the outlet water fluxes and adding the obstacles, we were unable to produce a steady jump. It keeps oscillating around its equilibrium position. Compared to one-fluid method, two-fluid formulations tend to be less stable which could explain the discrepancy with the results from Witt et al. (2015). To overcome this issue, we decided to set up a specific averaging process in the reference frame of the jump's toe. The four profiles where measurements are performed are located at 0.1 m, 0.2 m, 0.3 m and 0.4 m from x_j. The idea is to compute time averages on those profiles which change position during the simulation effectively filtering out the toe's main oscillation. By doing so, the results are less diffuse than by simply averaging on fixed profiles.

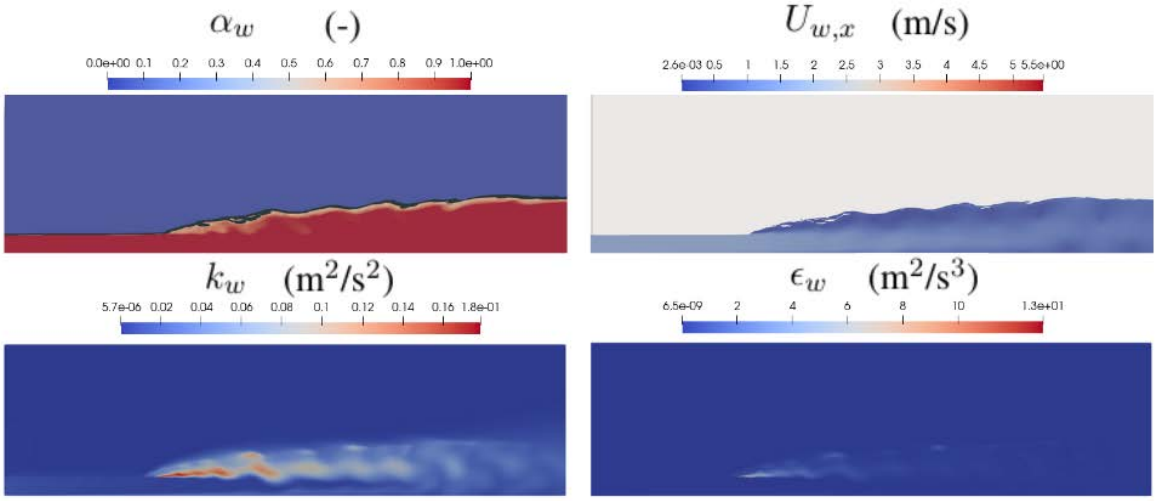

Figure 4.28: From top left to bottom right: air volume fraction and clipping showing the free surface, Water axial velocity magnitude, water turbulent kinetic energy and water turbulent kinetic energy dissipation.

Figure 4.28 contains instantaneous snapshots of the flow simulation. The air volume

fraction plot highlights once again the ability of the framework to tackle multiple regimes at once. There is the air-water resolved interface as well as some large resolved pockets and there are dispersed bubbles represented by a non-zero volume fraction below the free-surface. On the turbulent quantities plots shown below, the mixing layer is visible as well as a turbulent vortex release centered on the jump toe.

Figures 4.29 and 4.30 show the quantitative comparison to experimental and previous simulation data. y_{C95} is the vertical coordinate where averaged air volume fraction reaches 95%, C is the air concentration and d_b is the bubble mean diameter. Air volume fraction plots, especially the two most distant from the hydraulic jump toe, shows the clear increase in air entrainment at the jump's height. This is satisfactory, however, in experimental results, this increase is also visible closer to the jump. We think this is entirely related to the unsteady nature of the phenomenon. Since we did not manage to keep it in place, even though we adapted the averaging process, we think there might still be a bias which hides the increase in the first two plots. Similarly, the fact that we predict more air in the vertical profiles compared to experimental results can be explained by the unsteady nature of our jump. When no special averaging was introduced, the amount of air holdup was even larger. This overestimation of air holdup can also be explained by a poorly simulated air mass transfer from continuous to disperse. All in all, we are happy to achieve consistent results with VOF+RANS simulations which are usually more resolved than the method presented here.

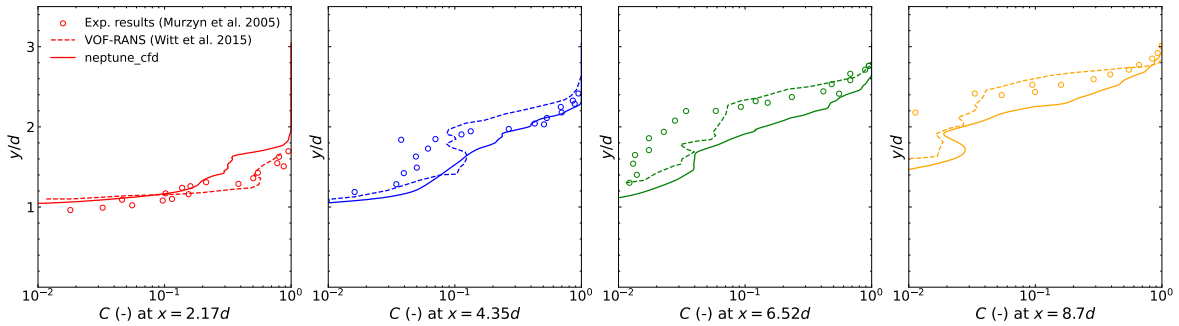

Figure 4.29: Simulated air volume fraction with the entrainment model based on Hinze's scale with $W_{e,c} = 5$. Experimental data from Murzyn et al. (2005) and RANS simulation data from Witt et al. (2015, 2018) are also included.

In terms of air bubble mean size, the results are in agreement with experimental results. In the bottom part of the vertical profile ($y/y_{C95} < 0.25$), the predicted size is large but it does not affect the results since no air volume fraction is found below that limit. In the bulk of the profile ($0.25 < y/y_{C95} < 0.75$), results match experimental as well as previous numerical simulations. In the upper part of the profile ($0.75 < y/y_{C95}$), the experimental measured bubble size increases. In the simulations with the entrainment model based on Hinze's scale, this increase is also noticeable whereas it is not in the simulation results published in Witt et al. (2015). Tests were performed without any entrainment model or with the model based on the free-surface curvature but results were not as satisfactory as those presented here. The predicted diameter was way too large and the air holdup below the free-surface way too small.

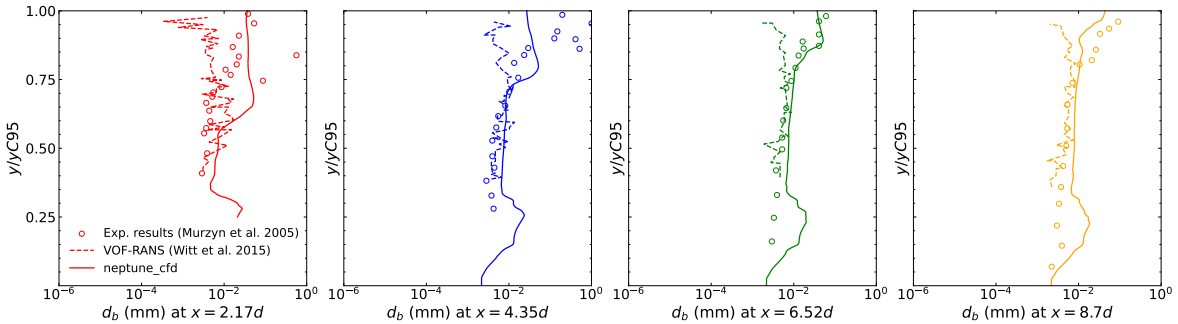

Figure 4.30: Simulated bubble diameter with the entrainment model based on Hinze's scale with $W_{e,c} = 5$. Experimental data from Murzyn et al. (2005) and RANS simulation data from Witt et al. (2015, 2018) are also included.

This case focused on the model based on Hinze's scale. It showed it is applicable to scenarios unrelated to plunging jets as well as large jet configurations. Simulation predictions are close to experimental results even though there is probably more work needed on the configuration itself to make for an easier post-processing step. Compared to other simulation models, it shows great potential for an accurate yet fast approach.

4.6 Entrained inclusion diameter modelling relevance

In this chapter, the topic of air entrainment in free-surface flows was introduced. Several options for its accounting have been explored before testing them against experimental results. The first proposition was quickly discarded due to mesh refinement inconsistencies. The options based on free-surface curvature and Hinze's scale have shown great potential in different scenarios and compared reasonably well with experimental data. It seems that mass transfer is slightly overestimated with the current method. It would be beneficial to include existing entrained air mass flux models in the framework to make it more accurate in that regard.

The model based on free-surface curvature was not kept in the end. Even though it gave encouraging results in the small jet case, the fact that it is based on curvature can be troublesome. This model is predicting the size of inclusions from the free-surface when it is no longer precisely defined. This contradiction led us to favour the last model instead. We think the previous remark is still a challenge for the last model but to a lesser degree. Finally, this work focuses on predicting the correct inclusion size. As was introduced at the beginning of the chapter, mass flux is also an important quantity describing the phenomenon. To broaden the scope of the thesis, it should be thoroughly studied as well. First, we would need to compare current mass flux with existing entrainment model and update the continuous to dispersed transfer criterion if these two quantities are not matching. This is important since, in the two cases, the air mass transfer from continuous to disperse seems to be overestimated.

5 | Analysis of liquid-gas-solid flows simulations

This last chapter is dedicated to the comparison between the liquid-gas-solid flows models developed in chapter 3 and experimental results. The main goal is to provide valuable data illustrating the capabilities and limitations of the Lagrangian stochastic and Eulerian velocity moments methods. Some cases provide in depth quantitative comparison while others, more complex, exclusively focus on a more qualitative comparison. Two particle loaded bubble columns test case are presented. In the first one, the solid loading is sufficiently low to enable Lagrangian stochastic as well as Eulerian simulations. The second case focuses on high particle loading, it is simulated with the Eulerian approach only. The other configurations consists in experiments carried out in the LNHE department at EDF R&D. They consists in several scenarios of water-particle jet. Their goal is to develop a better understanding of the particle behaviour in liquid-gas flows. Finally, the models are tested on an integral case of primary interest for the company: the liquid-gas-solid flow in a experimental representation of a reactor building during a loss of coolant accident.

5.1 Water bubble columns loaded with particles

Bubble columns and particle bubble columns are rarely found in nuclear or hydroelectric power plants. However, partners such as the IMFT are interested and it is a great opportunity to broaden the application fields of neptune_cfd. Thus reaching different communities which may not have had an interest in the software yet. It also shows that the methods are more robust since they can be applied to different configurations. These devices are often found in chemical plants and they are the ideal setup for Fischer-Tropsch synthesis reaction Basha et al. (2015) to take place. They are usually safer, easier and more efficient to run than packed bed reactors Duduković et al. (2002). They consists in a water column with an air inlet on the bottom. It can be rectangular - as it is in the two cases studied - or circular. The solid particles are already present in the water column before air is injected. They are therefore laying on the bottom which can be challenging in numerical simulations due to friction and contact forces. Air is injected most frequently through small holes at different mass flux. The flow regime depends on it. For low mass flux the regime is laminar, bubbles are uniformly dispersed; when the mass flux is increased, a transition regime sets up until the bubble coalescence regime is reached. In the latter, large air pockets appear, the water height also increases. If inlet air mass flux grows, the strong turbulence regime is reached. In this regime, there are no regularities. The flow is highly turbulent, coalescence and breakup occur at a very high pace. More details on the definition of each regime can

be found in Li et al. (2014). Inlet bubble size depends on the flow and orifice characteristics. Experimental correlations may help defining its value (Davidson, 1960). The size, density and mass loading of solid particles play a key role as well in the regime of the bubble column. Depending on their physico-chemical properties, they can enhance or inhibit bubble coalescence and breakup. Since the bubble column is highly sensitive to bubble size, this can have a noticeable impact.

5.1.1 Lightly loaded bubble column

The first scenario consists in a 3D rectangular bubble column described in Li et al. (2014); Li and Zhong (2015). The particle loading is 3% - sufficiently low to enable both Lagrangian stochastic and Eulerian simulations. The particle p and fluids characteristics are summed up in table 5.1. g represents the air phase while w represents the water phase. The global geometry and measurement setup are described in figure 5.1. In the experimental setup, pressure sensors are mounted on the side wall in four different locations shown in figure 5.1. Since there are no other measurements, this case primarily allows for a comparison between the two methods rather than a proper experimental comparison.

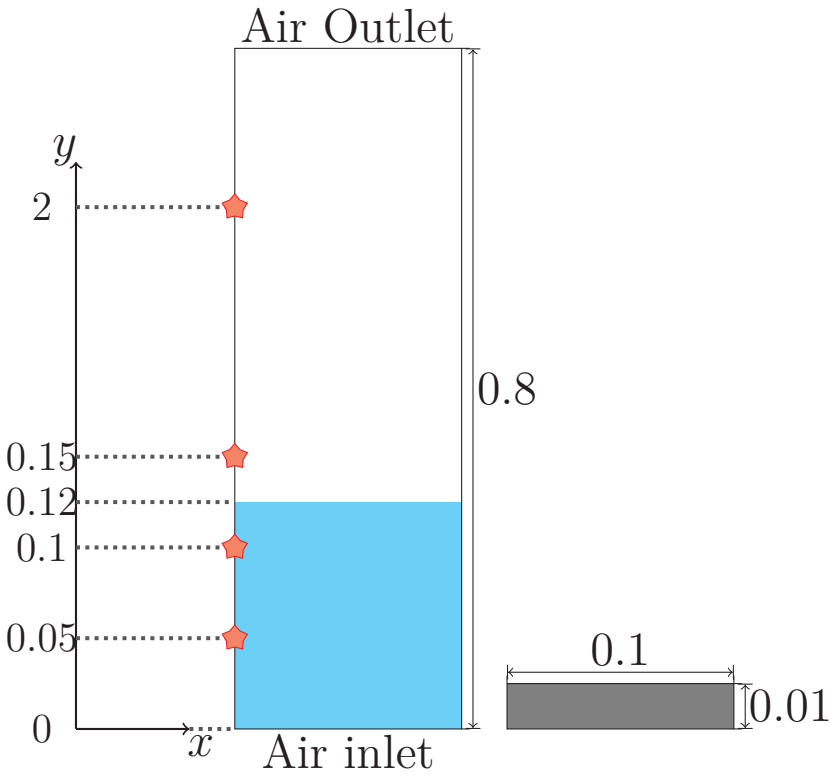

Figure 5.1: Experimental setup sketch inspired from Li et al. (2014). Red stars indicate pressure probes and the right shape represents the sintered plate for the air inlet. Distances are in meters.

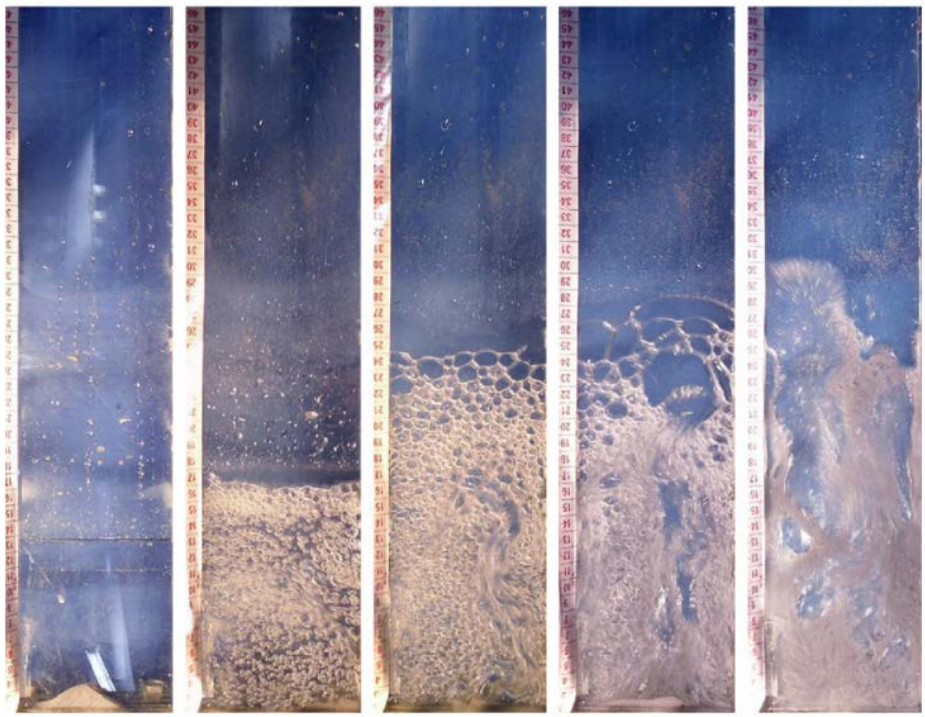

Figure 5.2: Pictures taken from the experiments carried out in (Li et al., 2014). In the initial setup the particles are stacked on the bottom. When the inlet air flux rate is increased, the flow becomes more and more chaotic (left to right). A clear curvy path for rising bubbles can be seen from the third picture on.

Particles	ρ_p kg m^{-3}	d_p µm	**Fluids**	ρ_w kg m^{-3}	ρ_g kg m^{-3}	ν_w m^2 s^{-1}	ν_g m^2 s^{-1}
(m11)	2500	150		1000	1.225	0.001	1.85×10^{-5}
Column	Height m	Width m	Depth m	Air flux m s^{-1}	Loading -	Pressure Pa	Water heigth m
(m11)	0.8	0.1	0.01	0.16	3%	101 325	0.12

Table 5.1: Characteristics for the particles, fluids and column used in the experiments of Li et al. (2014).

Simulations are carried out on the same meshes in both approaches. These contain 60 000 and 100 000 cells. The bottom boundary is an inlet. Air mass flux is $q_g = 1.94 \times 10^{-4}\,\mathrm{kg\,s^{-1}}$, its velocity is vertical, the volume fraction is $\alpha_g = 0.1$ and the associated diameter is $d_b = 3\,\mathrm{mm}$. The top boundary is a pressure outlet where $P = 101\,325\,\mathrm{Pa}$. All other boundaries are walls. Particles do not deposit on the walls, they elastically bounce off them. The column is initially filled up to the 0.12 m mark and the time advancement is adaptive. Collisions are not taken into account. In the experiment, the particles are initially at the bottom of the column. However, this is not simple to reproduce in the Lagrangian framework. Therefore, to keep things consistent between the two approaches, we decided to uniformly distribute them near the bottom wall ($y < 0.01\,\mathrm{m}$). Turbulence is second order Reynolds stress model for the two continuous

phases and dispersed inclusion diameter can vary according to the interfacial area transport equation method.

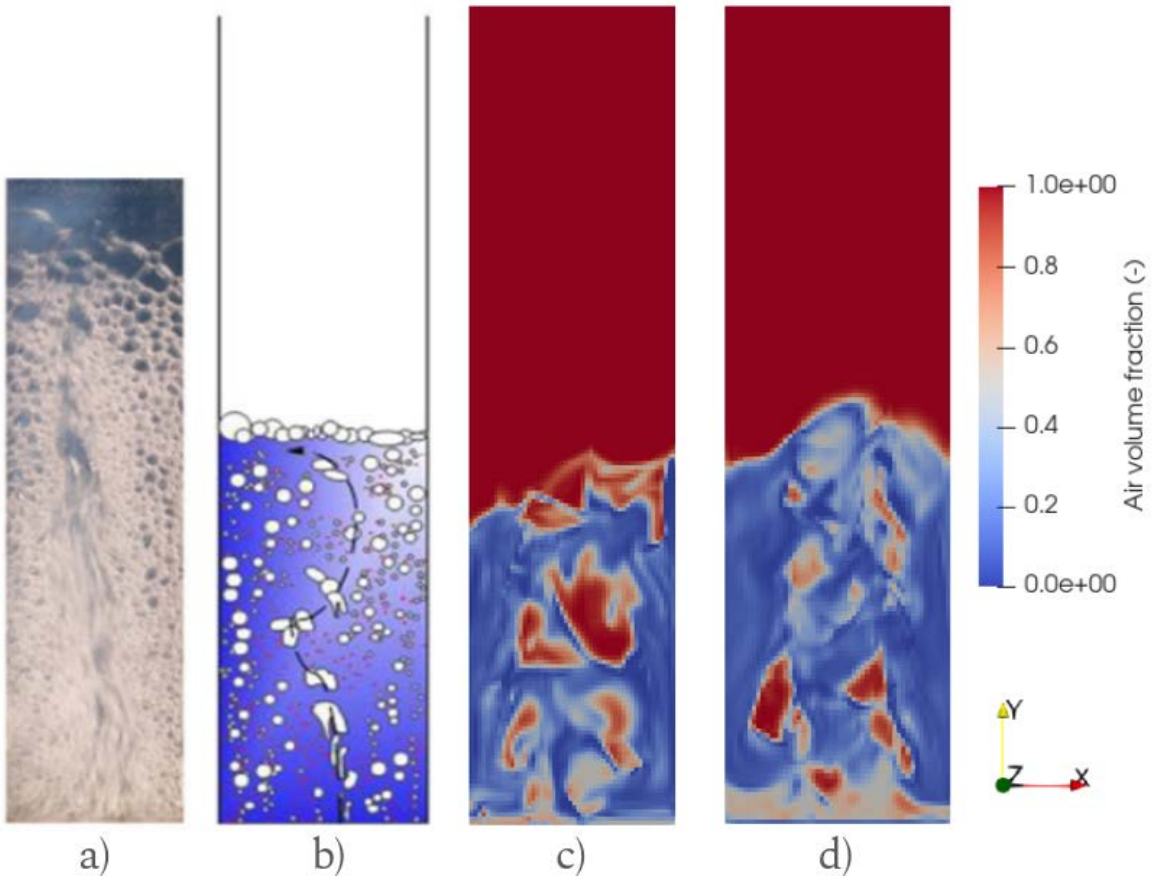

Figure 5.3: a) Photograph of the experimental setup (Li and Zhong, 2015), b) sketch of the bubble column from Li et al. (2014), air volume fraction in the Eulerian simulations with (c) and the Euler-Lagrange simulations (d) with neptune_cfd.

Figure 5.3 shows instantaneous air volume fraction obtained with the two methods developed. It also shows a photograph of the experimental setup and a sketch describing the case by the original authors. In both the simulations and the experiments, air structure tends to coalescence and rise towards the top of the column in the centre of the device. This is also observed when plotting averaged vertical air velocity. In the simulations, larger air structures are seen whereas in the experiments, the bubbles tend to be limited in size. They form a sort foam rising the water level in the column. We assume this discrepancy is related to surface tension effects of particles on the coalescence phenomenon. Since it is not taken into account in the simulations, there is no limiting factor to the size bubbles can reach. This difference also causes the simulated pressure to be higher in the column than it is in the experiments as shown in figure 5.4. The rise in water level is due to an increase in air holdup which tends to decrease the overall pressure in the apparatus.

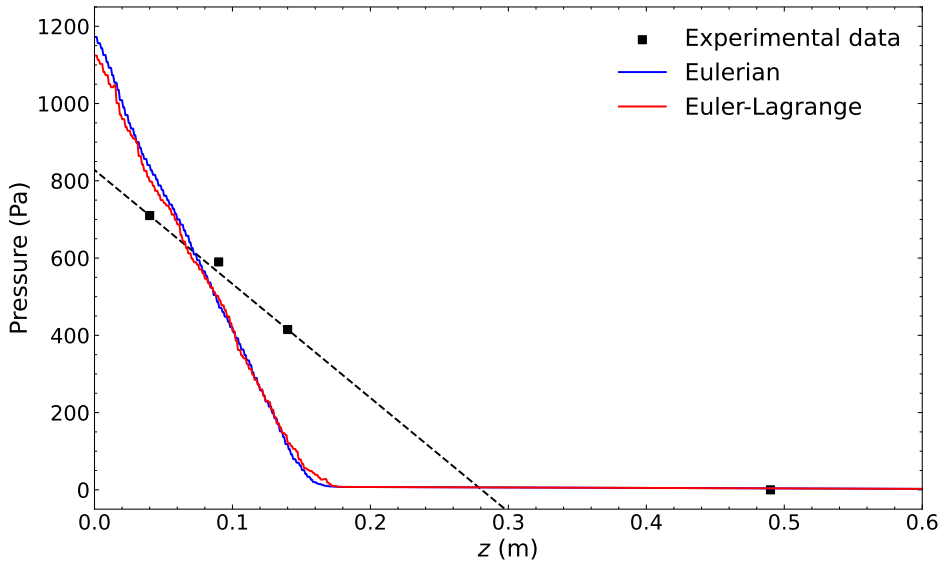

Figure 5.4: Comparison between simulated pressure and experimental data from Li and Zhong (2015).

Comparison between Lagrangian and Eulerian simulations show the effect of reverse coupling on the fluid phases is limited since the results are similar. Similarly, collisions and reverse coupling in the turbulence model has been seen to have little effect on the pressure results. This is probably because the particle loading is low ($\alpha_p < 0.03$). Finally, a sensitivity study was performed on the dispersed bubbles coalescence and fragmentation models. Simulations with constant diameters ranging from $d_b = 0.1\,\text{mm}$ to $1\,\text{mm}$ showed there was no influence of such a parameter. Simulations with different inlet diameters ranging from $d_b = 0.1\,\text{mm}$ to $3\,\text{mm}$ and activated coalescence and fragmentation models led to a similar conclusion. These can be seen in figure 5.5.

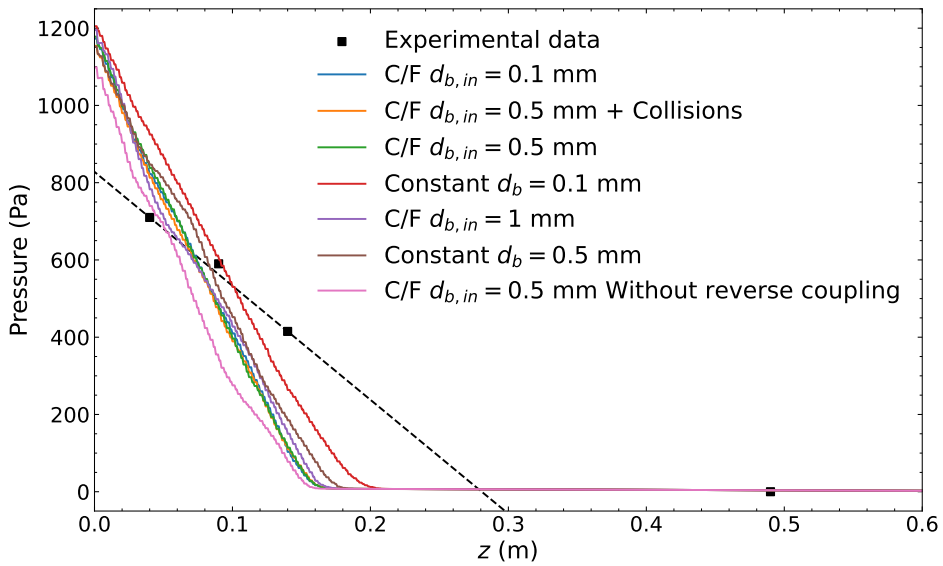

Figure 5.5: Simulated pressure sensitivity study. C/F denotes simulations with coalescence and fragmentation.

Even though this case is mostly qualitative, it still enabled a successful comparison

between the two methods and already highlighted some possible ways to improve them. In the next section, we study, with the Eulerian model, a similar bubble column with much higher solid fraction leading to a different range of conclusions regarding the parameters of interest and the behaviour of the model.

5.1.2 Heavily loaded bubble column

The second scenario also consists in a 3D bubble column with square section (Ojima et al., 2014). This time however, the original study focuses on heavy particle loading (from 0% to 40%) meaning the Lagrangian stochastic model is not applicable anymore. The notations are the same as in the previous case. The geometry and measurement setup are shown in figure 5.6, the fluid and particle characteristics are summed up in table 5.2. In the original publication, measurements include air volume fraction on profiles shown in figure 5.6 on the plane $y = 0$. The uncertainty on those measurements is between 1 and 2% - precise enough compared to the uncertainty of multiphase flow simulations. It also includes liquid velocity plots obtained from simulations with the $N + 2$ method. Finally, it provides instantaneous snapshots of the bubble column flow for three different loadings. The two quantities will provide good comparison to experimental data as well as existing numerical model supposed to be more precise. The snapshots will be helpful for qualitative understanding of the numerical results.

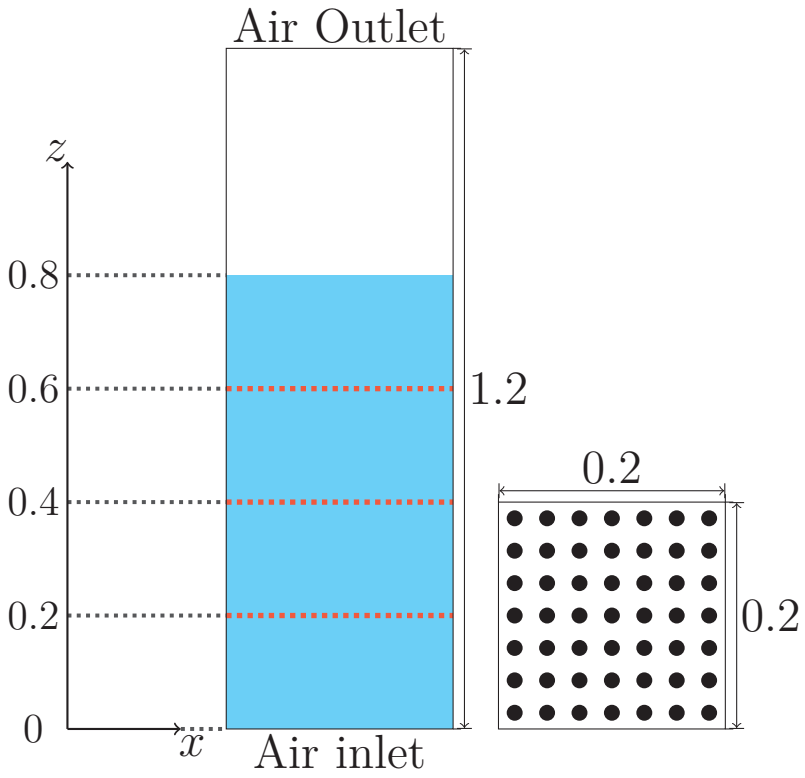

Figure 5.6: Experimental setup sketch inspired from Ojima et al. (2014). The right shape represents the sintered plate for the air inlet and the red dotted lines represent planes where measurements are made. Distances are in meters.

Particles	ρ_p kg m^{-3}	d_p µm	**Fluids**	ρ_w kg m^{-3}	ρ_g kg m^{-3}	ν_w m^2 s^{-1}	ν_g m^2 s^{-1}
	2250	100		1000	1.225	0.001	1.85×10^{-5}
Column	Height m	Width m	Depth m	Air flux m s^{-1}	Loading -	Pressure Pa	Water heigth m
	1.2	0.2	0.2	0.034	0 to 40%	101 325	0.8

Table 5.2: Characteristics for the particles, fluids and column used in the experiments of Ojima et al. (2014).

Simulations are carried out with the Eulerian velocity moments method only on three meshes with wall refinement with respectively 576 000, 770 048 and 1 109 760 cells. The bottom boundary is an inlet. Air mass flux is $q_g = 1.66 \times 10^{-3}\,\mathrm{kg\,s^{-1}}$, its velocity is vertical, the volume fraction is $\alpha_g = 1$ and the associated diameter is $d_b = 1.4\,\mathrm{mm}$. The superficial velocity J_G is defined from the inlet mass flux and surface area. Simulating each individual hole is time consuming so we chose a modelled approach instead. The top boundary is a pressure outlet where $P = 101\,325\,\mathrm{Pa}$. All other boundaries are walls. Particles rebound on all the boundaries except for the top one which they can exit from. However, they are not supposed to cross it. Initially, the column is filled with water up to $z = 0.8\,\mathrm{m}$ with the particle loading uniformly distributed in water. We assume that once the steady state is reached, the turbulent mixing is sufficiently intense to render the initial particle distribution irrelevant. This has been done to avoid having to simulate a sedimented bed of particles which can be tricky and is not in the scope of the thesis. Once the computation gets to a steady state, the results are averaged for 20 s. The first tests allowed us to highlight the major impact bubble size have on the column height. Smaller bubbles rise slowly to the surface due to reduced buoyancy while larger bubbles do it much more rapidly. The size of bubbles is related to the inlet diameter and the coalescence and breakup model. To assess its impact, several models are tested. They can be found in Prince and Blanch (1990) and Luo and Svendsen (1996). The difference between the two approaches resides in the breakup efficiency computation. In the model from Prince and Blanch (1990), the efficiency is related to the turbulent kinetic energy of the liquid eddy and the surface tension forces of the bubble to be broken down. The model from Luo and Svendsen (1996) considers the surface tension forces of child bubbles as well. This change in paradigm seems to have a sizeable effect in the configurations faced during the thesis as shown in the results.

Different fragmentation models are explored in the first place. In figure 5.7, simulation results with the original fragmentation model are compared with results obtained without the fragmentation model or with the new breakup model considered. The profiles show that for larger bubbles, the upward velocity is greater and the air volume fraction is smaller as expected.

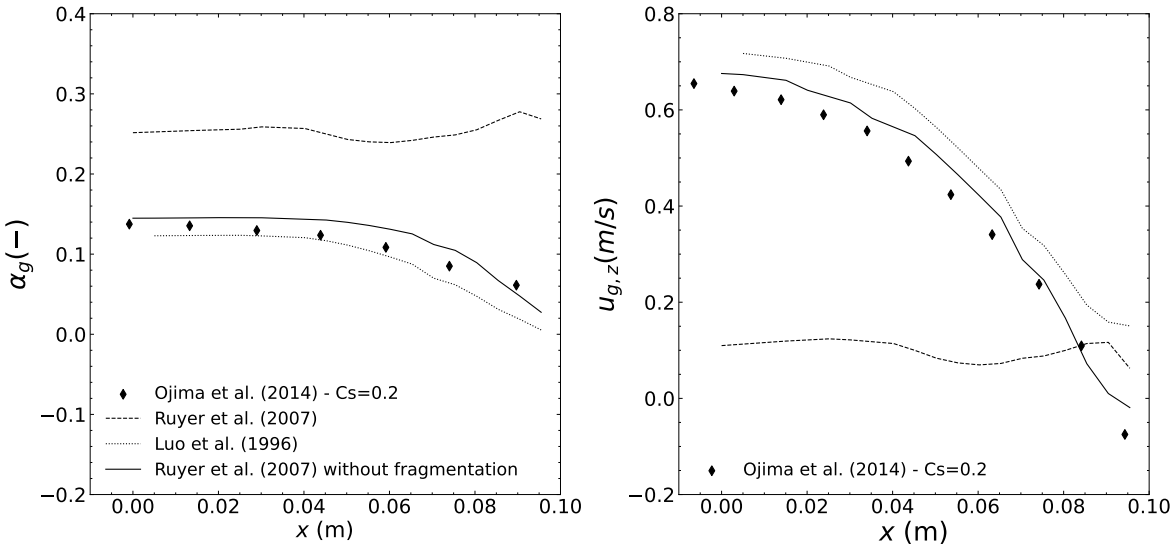

Figure 5.7: (left) Air volume fraction compared to experimental probe measurements. (right) Air upward velocity compared to simulation results with the $N + 2$ method. Data is obtained for different fragmentation models on the horizontal profile $z = 0.6\,\mathrm{m}$ for an air superficial velocity $J_G = 0.034\,\mathrm{m\,s^{-1}}$ and particle loading $C_s = 20\%$.

Simulations are then performed on three meshes to check spatial convergence. Averaged air volume fraction is shown in figure 5.8. The "reference" mesh (with 770 048 cells) seems to be sufficiently fine to capture the correct air behaviour in the column (It was also the mesh used in the previous fragmentation model study).

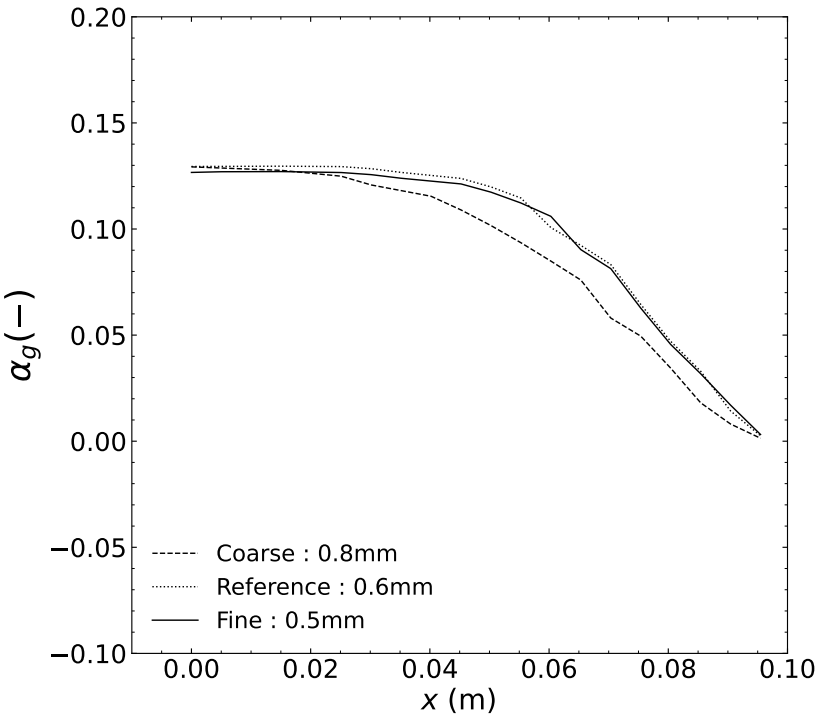

Figure 5.8: Air volume fraction compared to experimental probe measurements. Data is obtained for different meshes on the horizontal profile $z = 0.6\,\mathrm{m}$ for an air superficial velocity $J_G = 0.034\,\mathrm{m\,s^{-1}}$ and particle loading $C_s = 20\%$.

On the reference mesh, different models for the weighting coefficient have been tested. The aim is to illustrate the limitations of the standard model initially suggested and justify the use of other expressions.

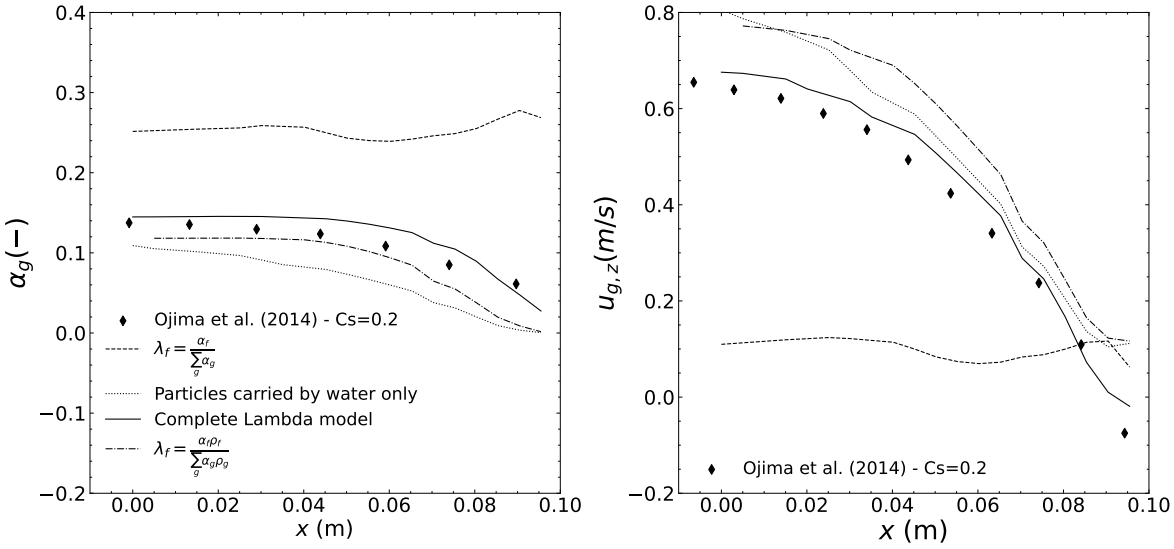

Figure 5.9: (left) Air volume fraction compared to experimental probe measurements. (right) Air upward velocity compared to simulation results with the NP2 method. Data is obtained for different weighting coefficients on the horizontal profile $z = 0.6\,\mathrm{m}$ for an air superficial velocity $J_G = 0.034\,\mathrm{m\,s^{-1}}$ and particle loading $C_s = 20\%$.

With the standard model $\lambda_f = \alpha_f / \sum_{f'} \alpha_{f'}$, the particle velocity is not correlated to the phase it is in. The predicted time each particle spends in the air is therefore too large. Thus, in the simulation, air bubbles tend to be dragged down by particles more then they are in the experiments. For other weight models, the momentum exchange between particles and bubbles is lower since particle velocity increases when they encounter air. This phenomenon is shown in figure 5.9 where a similar effect as for the different fragmentation models can be seen. When air experiences more drag because of smaller bubbles or more interaction with particles, the amount of air holdup increases and its upward velocity decreases. Finally, this figure shows the improvement obtained with the two carrier field model compared to the one carrier field approach. When water is the only phase interacting with the particles, bubbles are no longer dragged by particles which speeds their flow upwards and reduces the air content in the column.

All in all, the results shown by the velocity moments method on this specific bubble column are satisfactory. They match experimental measurements when they are available and they compare well with simulation data obtained with advanced modelling approaches. Another comparison has been performed between the Eulerian method and the $N + 2$ method for bubble size distributions. It is shown in figure 5.10.

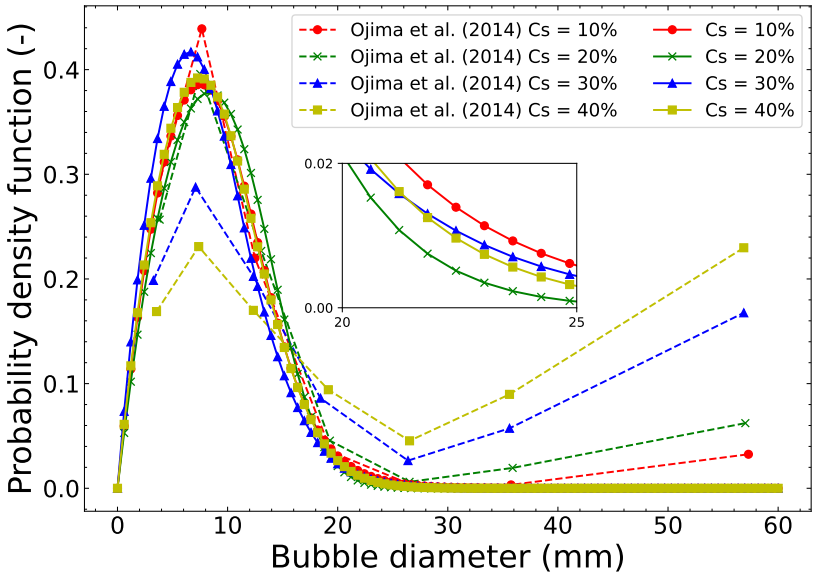

Figure 5.10: Air bubble size probability density function comparison between the published simulations (dashed lines) and the present study (solid lines). Data is obtained on the horizontal profile $z = 0.6\,\mathrm{m}$ for an air superficial velocity $J_G = 0.034\,\mathrm{m\,s^{-1}}$

The size distribution is obtained with reconstruction from the interfacial area, the air volume fraction and expression 2.90. Once the steady state is reached, all the time steps are used to compute the distribution to widen the statistical sample. There are several comments worth pointing out in this comparison. First, in the present simulations, no bubble larger than around $d_b = 20\,\mathrm{mm}$ is simulated. This is much smaller than the biggest bubble reached with the $N + 2$ method. This has to do with the way bubbles are accounted for in both methods. In the present study, the conditions lead to large bubbles being simulated rather than modelled in the dispersed approach while in the $N+2$ simulations, there is no transition to resolved interfaces until bubbles reach the column surface. They are free to grow indefinitely. Snapshots in figure 5.11 illustrate these resolved interfaces and how they are bigger and more frequent when the particle loading increases in the Eulerian model. Secondly, in the current simulations, there is no decrease in peak bubble size probability (around $d_b = 10\,\mathrm{mm}$) with increasing solid loading. This decrease is observed in the bubble size density distribution obtained with the $N + 2$ approach. However, it is exclusively caused by the accounting of larger structures in the size distribution normalisation factor. Indeed, if the distributions are truncated at $d_b = 20\,\mathrm{mm}$ (maximum size modelled in neptune_cfd) and re-normalised, the decrease in peak probability disappear. In the high loading case ($C_s = 20\%$), the size of large resolved air pockets reaches $d_b = 50\,\mathrm{mm}$.

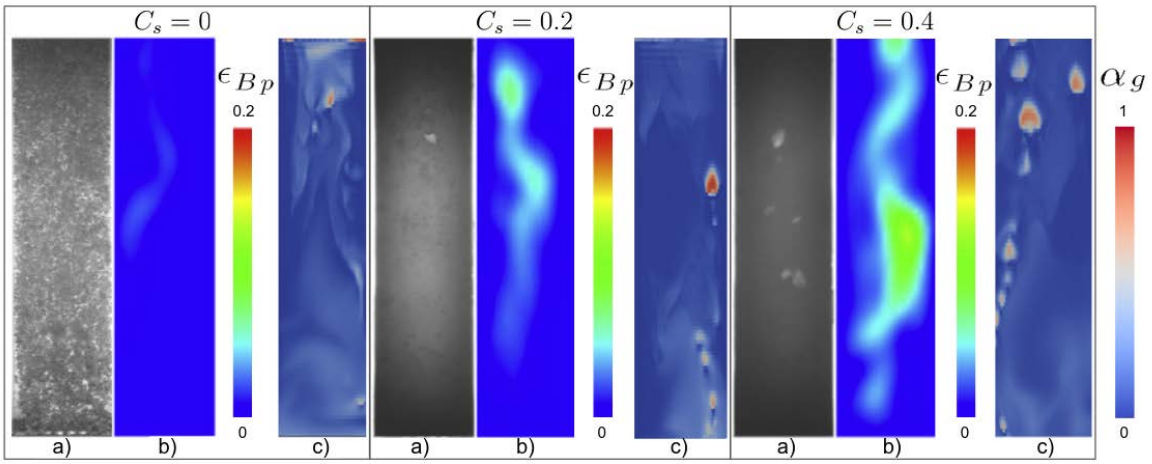

Figure 5.11: Snapshot of three different particle loadings at $J_G = 0.034\,\mathrm{m\,s^{-1}}$. a) Photographs of the experimental apparatus in the near-wall region, b) volume fraction of bubbles of diameter $d_b = 57\,\mathrm{mm}$ simulated with the NP2 method from Ojima et al. (2014). c) Present simulations air volume fraction α_g with the multi-Euler method. The scale for the Eulerian simulation is shown on the far right side.

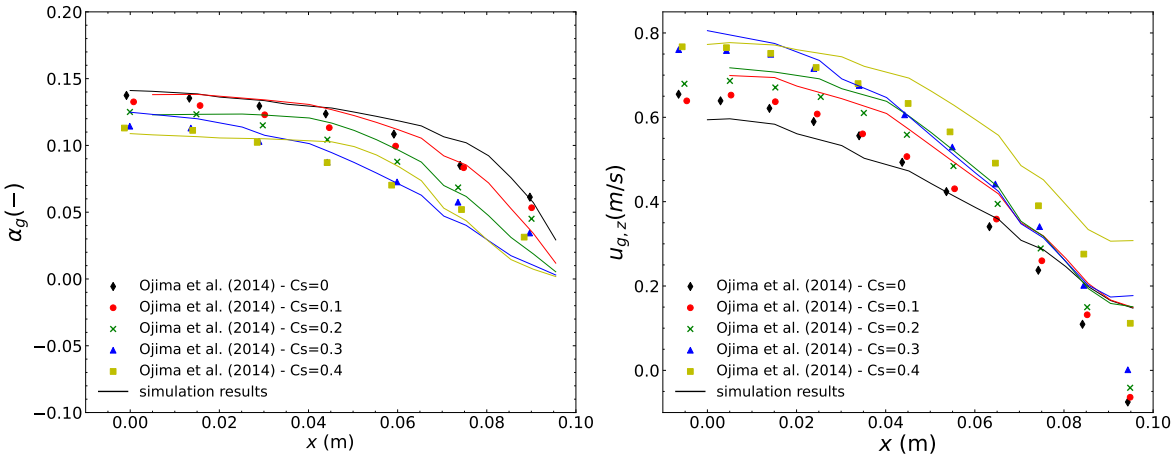

Figure 5.12: (left) Air volume fraction compared to experimental probe measurements. (right) Air upward velocity compared to simulation results with the $N + 2$ method. Data is obtained on the horizontal profile $z = 0.6\,\mathrm{m}$ for an air superficial velocity $J_G = 0.034\,\mathrm{m\,s^{-1}}$

Finally, results for all particle loadings are shown in figure 5.12. They highlight the correct behaviour of the simulation when solid concentration increases. Mainly, the fact that with more particles, air bubbles tend to flow upward more rapidly, decreasing the air holdup. This mechanism is visible in the experiments and the simulation results in the $N + 2$ framework. The correction coefficient introduced in the coalescence efficiency in the work of Ojima et al. (2014) has been tested but provided no further improvement in the results.

In the previous section, we provided simulation results for two bubble columns. The new methods developed, when applicable, showed consistent behaviour. In the case of high solid concentration, the velocity moments method performs well, its predictions

are close to experimental results as well as published numerical data. The ability to capture multiple regimes has been a key property of the framework and its predictions are consistent with experimental results. To improve the comparison and make it even more reliable, it would be useful to work on resolved large bubble identification to include them in the bubble size distribution function. It would be interesting to explore other fragmentation models since they seem to have a major influence on the simulation results. An example of such model can be found in Shi et al. (2018).

5.2 Canal with particle loaded water jet

The next three cases explored represent experimental setups developed in the LNHE department at EDF R&D. They are presented in a chronological order to illustrate the motivations behind each case. The first case, even if much simpler than the integral final case, was still too complex. There were too many interacting phenomenons which made the simulation difficult. It was therefore decided to develop a simpler case where air entrainment is no longer encountered. Instead, the interaction between bubbles and particles was studied through the use a bubbler. Thus, the diameter of bubbles is easier to estimate compared to the plunging jet case. They are all set up around a rectangle channel open at the top, of length 60 m, height 1.0 m and width 0.6 m. The channel is modular, it can be divided into smaller portions, it is filled with water up to 0.6 m and it can enforce a transverse current of $q_c = 0.1\,\mathrm{m\,s^{-1}}$. The three cases include a circular water jet of diameter $D_j = 0.08\,\mathrm{m}$. The latter can be located in different positions and can be loaded with particles depending on the case considered. The water flux in the jet is around $q_j = 10\,\mathrm{L\,s^{-1}}$ and the water supply comes from a $\Omega_T = 1000\,\mathrm{L}$ tank where particles are stirred to ensure uniformity of the solid concentration. This water flux corresponds to a mean jet velocity at the inlet point of $U_j = 2\,\mathrm{m\,s^{-1}}$. For all the cases, we consider 25 kg of solid spherical particles of density $2500\,\mathrm{kg\,m^{-3}}$ and radius 60 µm. This corresponds to 1% volume loading in the tank and jet. Thus, Lagrangian stochastic simulations are achievable. When the tank is empty, the jet stops. The detailed experimental protocol is always the same, it is described below.

1. The channel is filled with water
2. If the scenario includes a transverse current, it is activated until a steady state is reached (the bubbler, if present, is activated as well)
3. The water jet is activated for 100 s. During that time, depending on the scenario, measurements are made on the flow (solid concentration or PIV).
4. When the water jet stops, the bubbler and transverse current are stopped until there is no flow in the channel and all the particles have deposited on its bottom.
5. The channel is slowly dried out and particles are weighted in each zones. After the last step, the channel is ready to be filled with water again.

The emptying of the canal, the weighting and drying of the particles are quite labour and time consuming steps. Therefore, each experiment can take up to several days. There are several measurements available in this experimental setup. Particle image velocimetry has been used to characterise the two-phase flow before the introduction

of solid particles. This is highly valuable since it enables a thorough evaluation of the liquid flow in simulations before switching to the more complex liquid-gas-solid case. Since these studies were performed before the start of the thesis we are not presenting them here, they were used to check the correct implementation of the new models but they were not used for comparison purposes. In later configurations solid concentration sensors have been added to the setup. The output can be directly compared to simulation data which makes it a powerful comparison tool. These sensors consists in ultrasound emitters and receivers located on one side of the tank (red dots in figures 5.24 and 5.35). The wave emitted bounces off the facing wall and is received on the same side it was emitted from. They are first calibrated in a small homogeneous bath filled with increasing solid concentrations to get the characteristic response and then bonded to the side of the final channel. Since calibration is done with an homogeneous bath, no information is available on the sensor behaviour in inhomogeneous flows. Finally, the total mass deposited in each zone (regions separated by dashed lines in figure 5.13) is weighted. In the results, the total mass measured in each zone is plotted at the position of the region's centre.

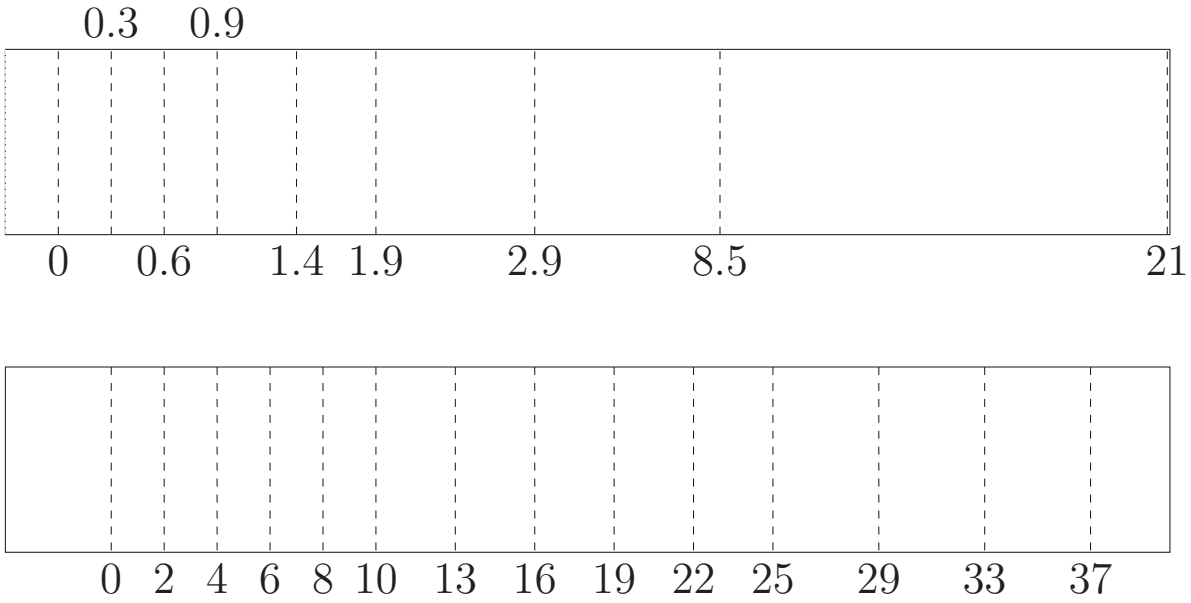

Figure 5.13: (top) Deposition regions in the impacting jet case. Only the right-hand side part is shown here, the other side is symmetric. (bottom) Deposition regions in the submerged jet case. Distances are in meters and the jet is located at the 0 marker.

5.2.1 Impacting water jet

In the first of three channel cases, the jet is located above the free-surface, it is perpendicular to it and an obstacle is diverting the jet into a cone shape. Details about the geometry of the setup and the obstacle can be found in figure 5.14. This configuration aims at representing, in a simpler manner, the situation encountered in the industrial scale scenario presented in the last section of this chapter. PIV measurements have been performed and were used to assess the accuracy of the two-phase flow simulations. Since this work had been carried out prior to my thesis it is not presented here.

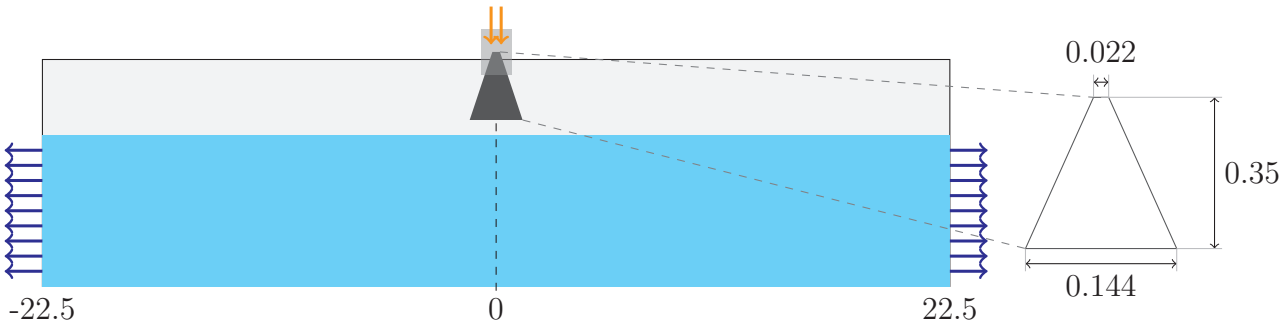

Figure 5.14: Schematic representation of the impacting water and particles jet performed at the LNHE department. Distances are in meters.

Simulations are carried out with the Lagrangian and Eulerian approaches. Details on the mesh can be seen in figure 5.15 which contains 1 034 456 hexahedron cells, second order Reynolds stress models are selected for water and air, the generalised large interface method is selected initially with constant diameter $d_b = 5\,\text{mm}$. The influence of d_b will be assessed in the Eulerian simulations. The time step is such that the CFL condition is CFL < 1. The top boundary is a pressure outlet with $P = 101\,325\,\text{Pa}$, there are two water outlets on both ends of the canal which balance the water jet inlet flux. All other boundaries except the jet inlet defined earlier are walls. The experimental protocol is followed except for the drying part, we stop the simulation once 95% of the total particle mass is deposited.

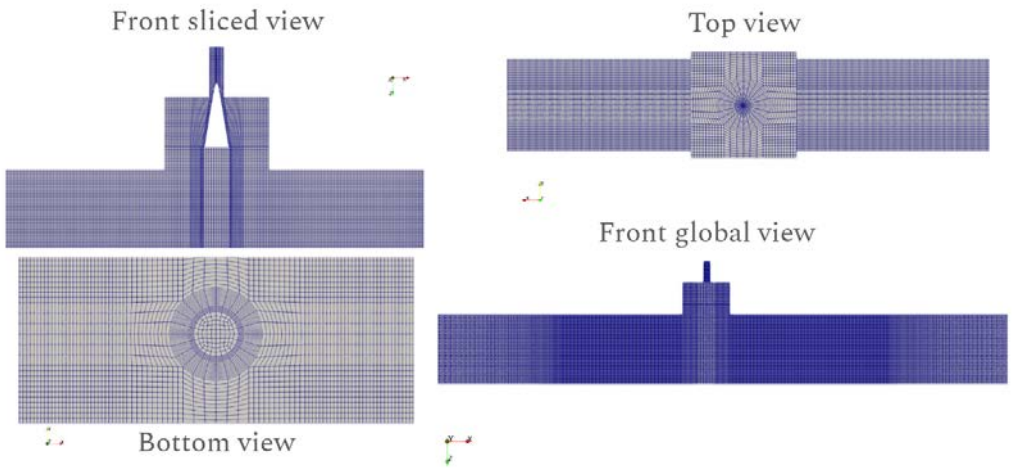

Figure 5.15: Details on the mesh used for the simulation of the impacting jet case.

Euler-Lagrange simulations

Lagrangian simulations are performed first. They are compared with experimental results as well as with previous Lagrangian simulations carried out without the multi-carrier field approach. Instantaneous snapshots of the simulation are shown in figure 5.16. They show particles are transported towards both ends of the canal near the free-surface. They also highlight the low concentration of particles below the jet at the beginning of the simulation. However, the turbulent mixing ends up homogenising the solid concentration in this region as well. Thus, this is not reflected in deposition

profiles. Figure 5.17 illustrates the results obtained with the new method. Before, most of the particles deposited right below the injection point whereas now, the particles are more dispersed. This change of behaviour is probably related to the fact that rising bubbles have an impact on particles when in the previous model their impact was only accounted through their impact on the water phase. The fluctuating motion of particles is also more consistent with water and air turbulent quantities compared to the original method. The method is still unable to predict the deposition of particles in the region further away from the jet impact point but results are still promising.

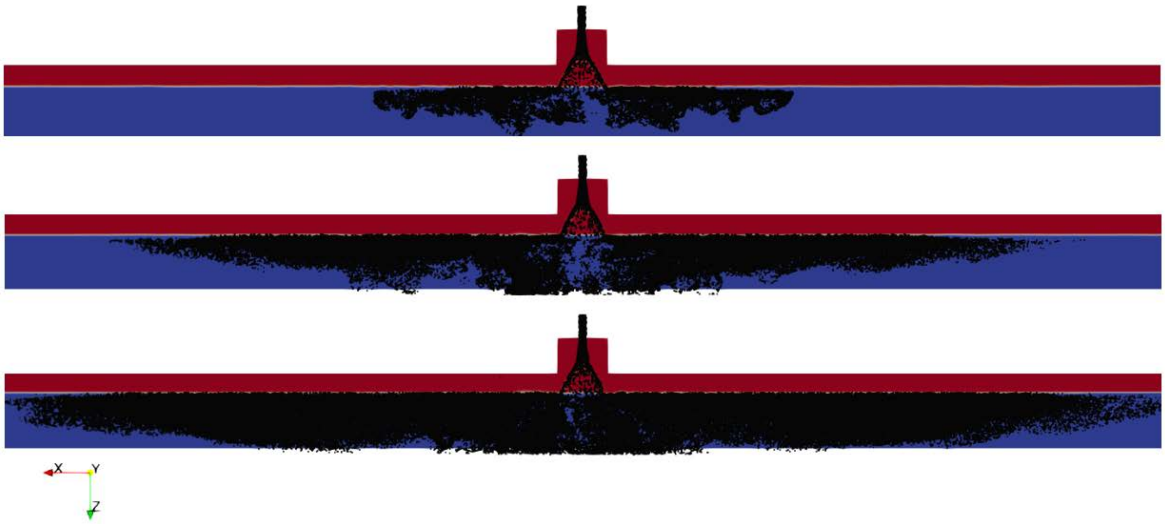

Figure 5.16: Instantaneous air volume fraction in the impacting jet case simulated with the Euler-Lagrange method. Black dots represent Lagrangian particles tracked during the simulation.

In Lagrangian methods, it is common practice to check not only the spatial and temporal convergence but also the statistical convergence with regards to the number of injected particles. Two simulations have been performed with 1 to 5 particles injected per time step. Figure 5.18 shows that increasing the number of particles does not seem to have an impact on the results. They are either statistically converged or still need more particles which computing capabilities do not allow for.

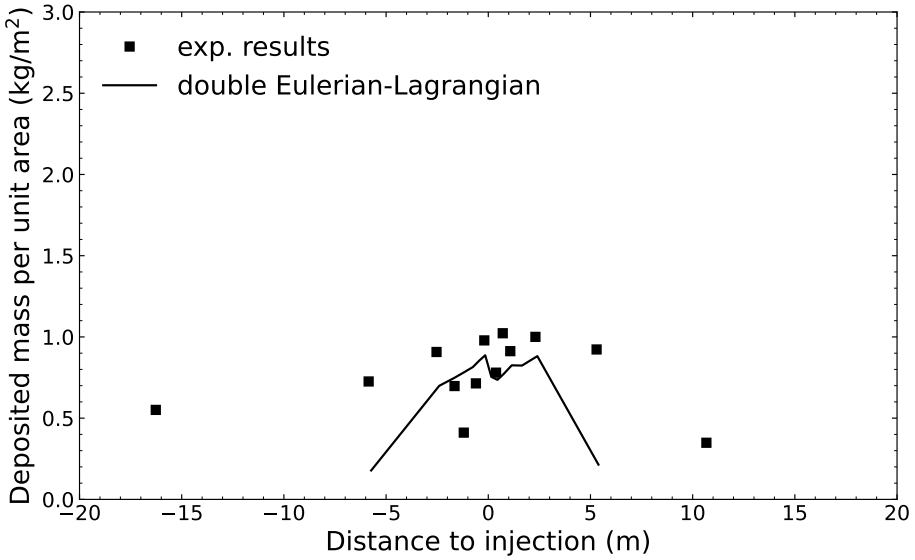

Figure 5.17: Total mass deposition at the end of the simulation in the Lagrangian simulations.

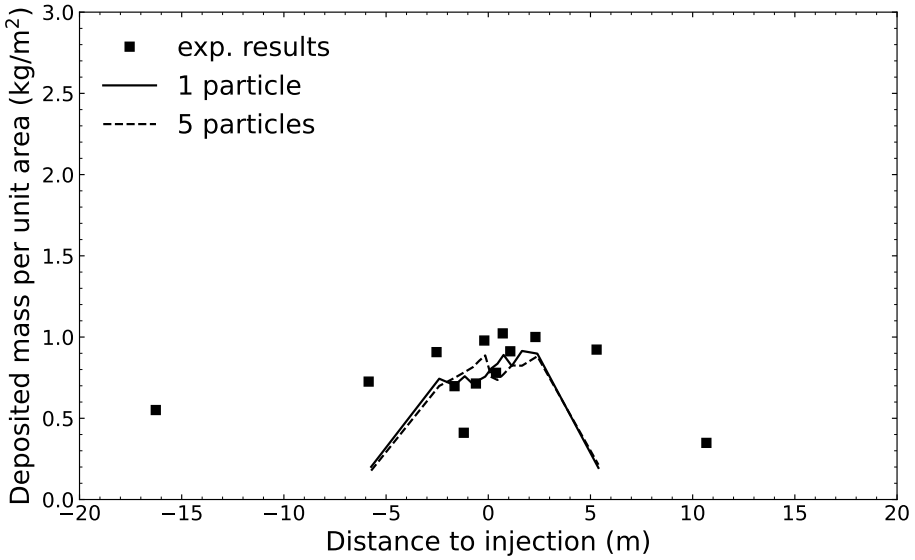

Figure 5.18: Deposited mass depending on the number of particles injected per time step.

Eulerian velocity moments simulations

Eulerian simulations are performed as well with the kinetic stress model to account for particle agitation. They are compared to experimental results and the Lagrangian approach. Figure 5.19 shows instantaneous solid concentration snapshots obtained with neptune_cfd. They illustrate that particle dispersion is qualitatively similar to that obtained with the Lagrangian method. Initially, particles tend not to accumulate

below the jet impact point. As the simulation advances, turbulent mixing transports particles even in that region but it seems to be at a lower rate than in the Lagrangian framework. Also, with the current model, it seems that more particles are transported away from the jet origin. The free-surface and jet properties seem to be unchanged, the reverse coupling has a negligible effect probably because the jet is oriented downwards.

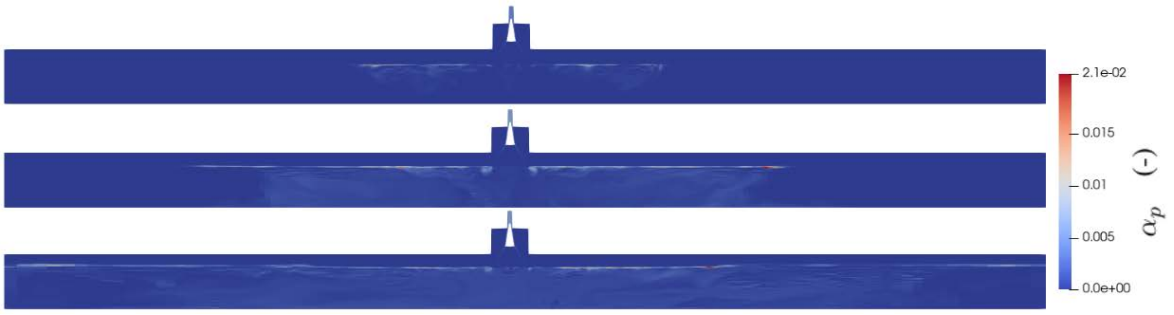

Figure 5.19: Instantaneous solid volume fraction in the impacting jet case simulated with the Eulerian method.

The first parameter we looked at is the air bubble diameter at the inception point. Since it completely changes the air content below the free-surface, it plays a key role in particle transport as shown in figure 5.20. When air bubbles are smaller, more air is entrained and its rise velocity is lower as well. This causes particles to flow downwards more slowly. They then deposit further away from the jet impact point. On the other hand, when air bubbles are larger, they rise faster to the surface and less air is held up below the free-surface. This causes particles to fall more slowly thus depositing further away from the pipe. This shows the importance of having a predictive model for the entrained inclusion diameter (see chapter 4).

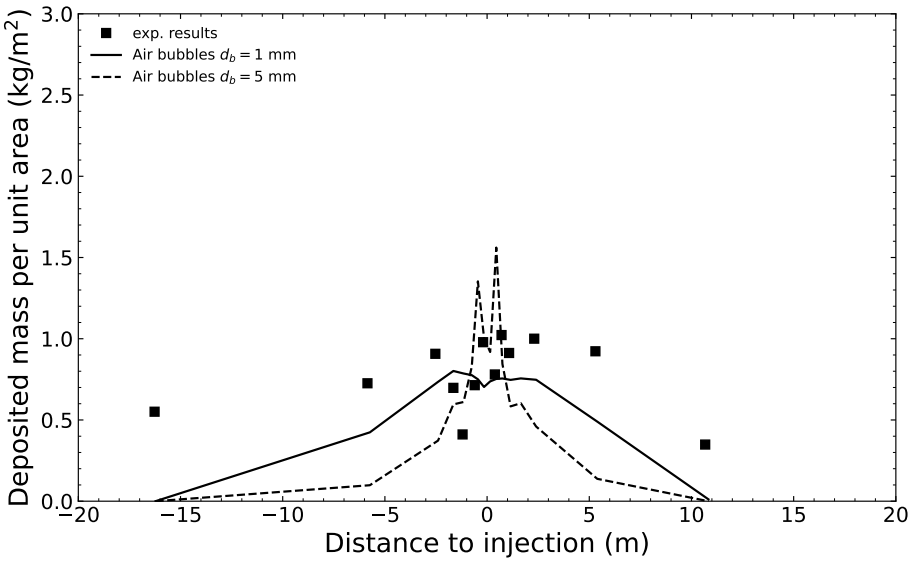

Figure 5.20: Total deposited mass for two different bubble diameters.

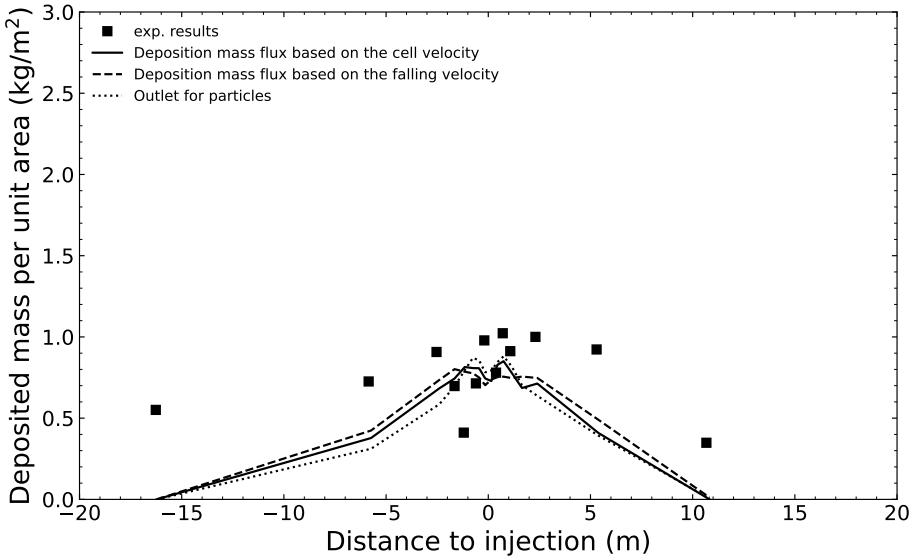

Figure 5.21: Total deposited mass for different particle deposition boundary conditions.

Another parameter of the simulation, presented in chapter 3, is the type of deposition model for the particle phase. Three boundary conditions are considered, an outlet for the particles, a deposition flux based on terminal velocity and a deposition flux based on the particle vertical velocity in the wall cell. Results in figure 5.21 show that the three models are equivalent. There are slightly more particles depositing near the centre of the channel with the outlet condition or the deposition flux based on the cell vertical velocity but, all in all, the difference is negligible.

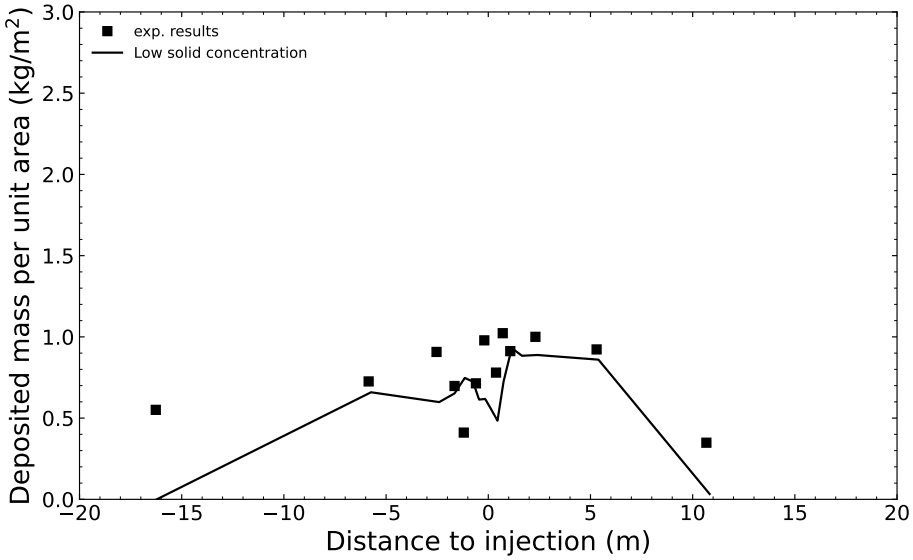

Figure 5.22: Total deposited mass for low solid concentration (re-normalised).

To assess whether particle impact on fluid quantities is important, a simulation with low solid concentration is performed and results are shown in figure 5.22. They show

that reverse coupling does not seem to play a major role in the simulation results. This is probably because the jet is oriented towards the bottom, particle slip remains small. Eulerian simulations give satisfactory results, the particle dispersion is well predicted and the parameters of the model have a predictable impact on the results.

Finally, to overcome the issue of fixing the bubble diameter at the beginning of a simulation, we included the air inclusion entrainment model presented in chapter 4. The numerical setup is the same as in the previous simulations. The main idea is to verify the results obtained with the additional model are consistent with those obtained while setting the bubble diameter beforehand. This also gives us the chance to evaluate the impacts of the initial diameter in the domain $d_{b,i}$ and that of the Weber critical number $W_{e,c}$. As seen on figure 5.23, the inclusion size model enables a consistent prediction without the need for a parameter optimisation. Also, the results demonstrate there is no sizeable effect of the initial diameter imposed for the air phase.

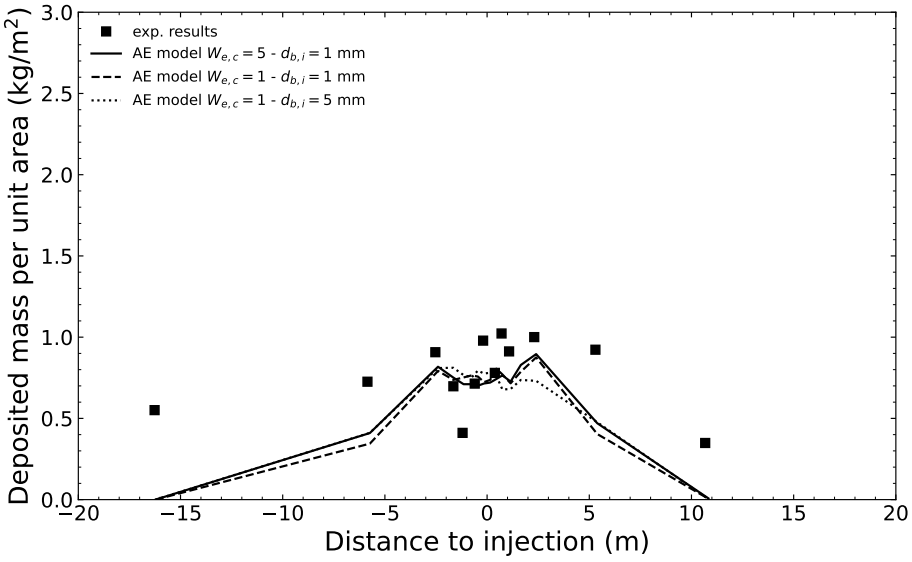

Figure 5.23: Total deposited mass with the air entrainment model for different critical Weber numbers and different standard diameters.

5.2.2 Immersed water jet

It was shown in the impacting jet case that air bubbles played a key role in the global behaviour of the experimental setup. Unfortunately, it is also a complex quantity to predict in neptune_cfd, especially in those transition regimes. Additionally, the lack of experimental measurements regarding air mass transfer and air bubble size distribution did not allow to overcome the software limitation. Thus, it was decided to design a new experimental setup to reduce the uncertainty related with air entrainment and provide data more easily comparable with CFD simulations. As illustrated in figure 5.24, the water-particle jet is now positioned below the free-surface in order to avoid air entrainment. Particles are now exclusively transported by water but the free surface is still simulated thus justifying the use of the developed liquid-gas-solid models. Furthermore, this case constitutes a foundation for the next one where a bubbler is added in the channel to introduce an interaction between bubbles and particles. Thus,

assessing the precise prediction of the models in this case is a necessity before switching to the case with the bubbles.

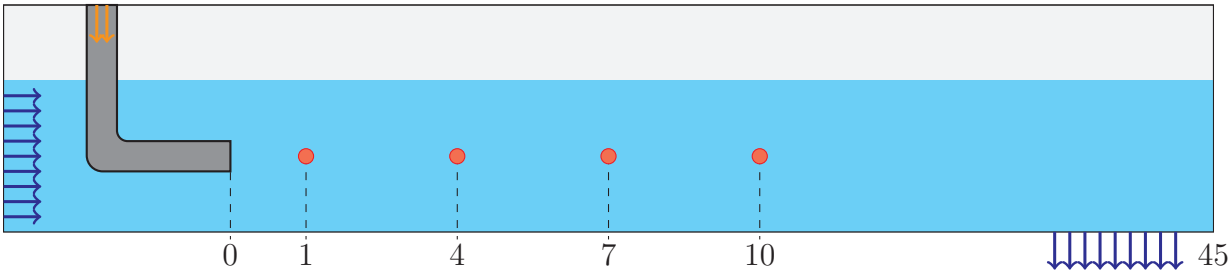

Figure 5.24: Schematic representation of the submerged water and particles jet performed at the LNHE department. Distances are in meters. The red dots represent the positions of the solid concentration sensors.

Simulations are performed on a mesh representing the complete experimental channel to avoid issues related to boundary conditions. The mesh is composed of 1 502 544 conforming hexahedron cells, there is a refinement near the jet inlet tube wall to better model turbulence. Details of it can be seen on figure 5.25. The mesh includes the entire canal and the elbow in the inlet pipe. A boundary layer is used in the pipe in order to reach acceptable y^+ values at the wall. Initially, in the tank and pipe, the water height is 0.6 m. This means air is trapped in the pipe between the free-surface and the valve located outside the channel causing an initial burst in air bubbles when the jet is activated. The kinetic stress model is used to account for particle agitation in Eulerian simulations.

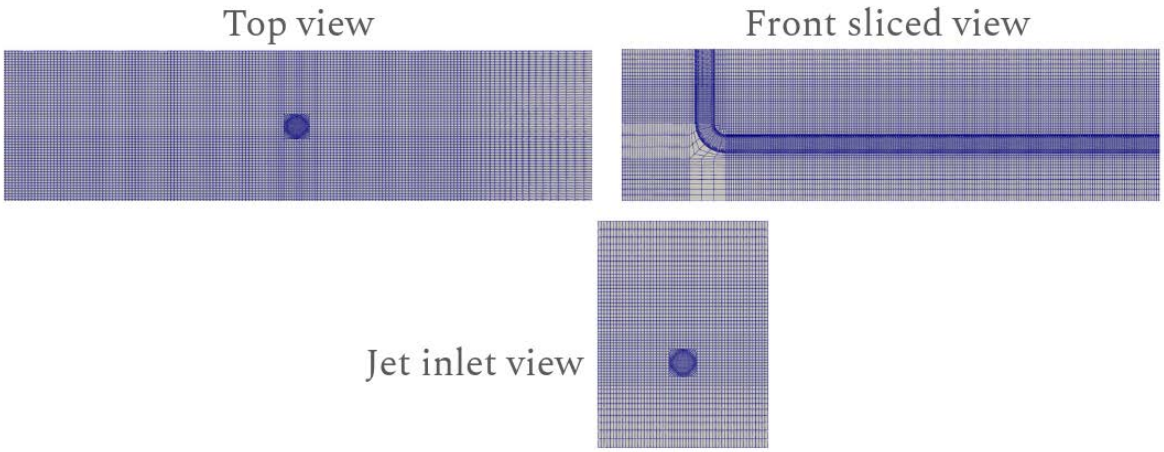

Figure 5.25: Details on the mesh used for the simulation of the immersed jet case.

Different meshes are first tested to check whether they are refined enough to capture the turbulence generated by the water jet. Figure 5.26 shows the results are consistent when the mesh is refined. There is an oscillation which is not captured on the coarser mesh, thus, the "Reference" mesh is selected for further studies. It captures the main features of the flow while also being computationally viable. Noticeably, the jet is not symmetric because of the elbow in the jet inlet pipe. Taking it into account is therefore important to capture the correct behaviour. Moreover, the effect of the pipe on the channel current - when it is activated - can be simulated only if the pipe is part of the

modelling process. The fourth plot highlights the effect of particles on the global jet direction towards the bottom.

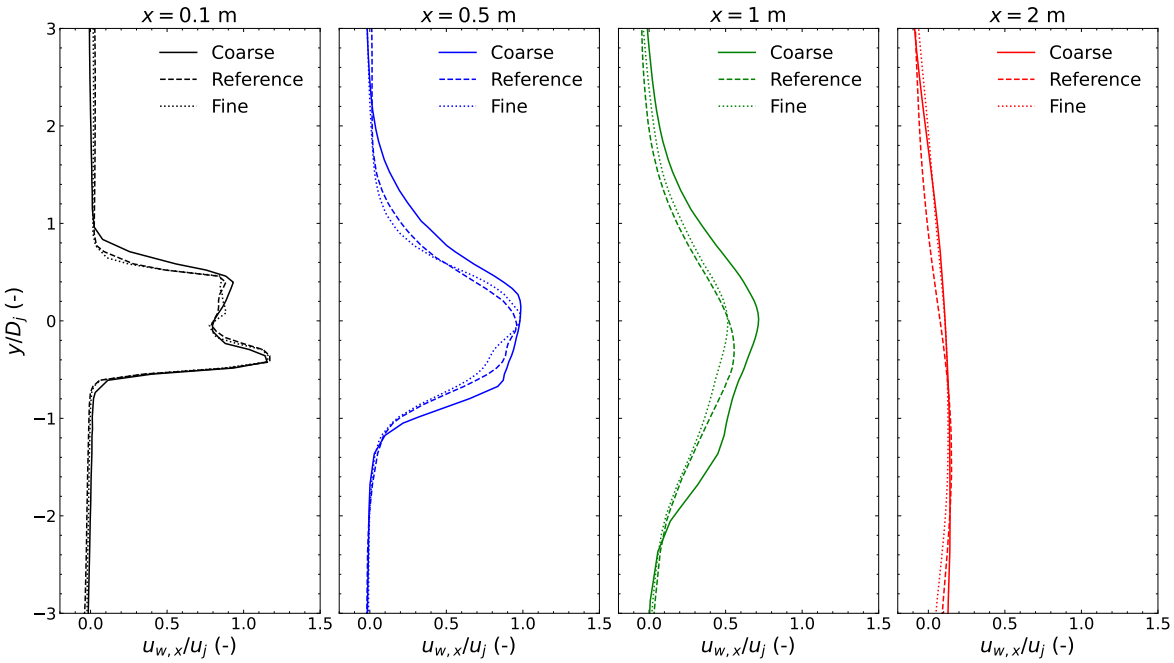

Figure 5.26: Mesh convergence study carried out with the addition of particles without current. Axial liquid jet velocity on vertical profiles downstream the jet inlet point.

Jet shape: turbulence, air pocket and reverse coupling effects

Before tackling the liquid-gas-solid configuration, air-water simulations are performed without the inclusion of particles. This aims at understanding the behaviour of the liquid jet and choosing the correct modelling parameters. Two simulations are carried out with the k-ϵ and R_{ij}-ϵ turbulence models to justify the use, computationally more expensive, of the second one. Figures 5.27 and 5.28 show axial liquid velocity instantaneous snapshots during the water inlet start.

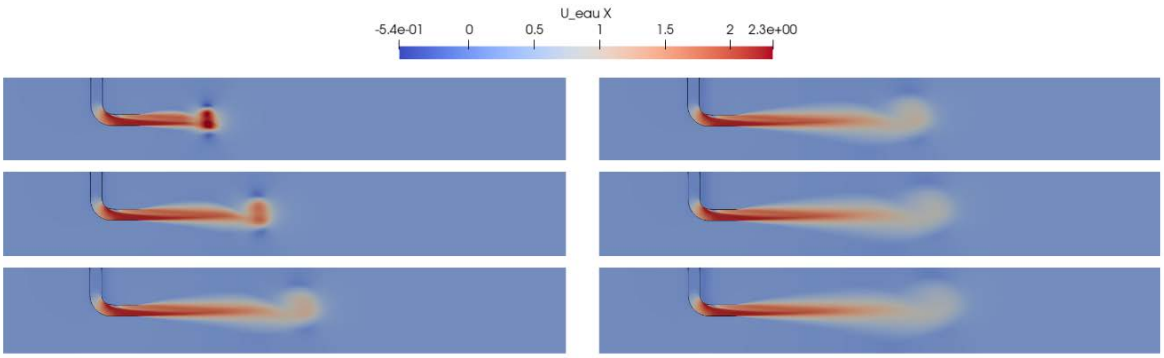

Figure 5.27: Effect of the turbulence model on the jet shape without particles with the k-ϵ turbulence model.

These results, obtained on the same mesh, show, as expected, that the second order model is able to reproduce finer velocity fluctuations. The k-ϵ, more diffusive, tends to predict a mean flow without any fluctuations. It is also unable to reproduce the initial

vortex generated by the jet inlet clearly simulated with the second order model. This vortex can accumulate particles or air bubbles which may change the initial behaviour of the setup.

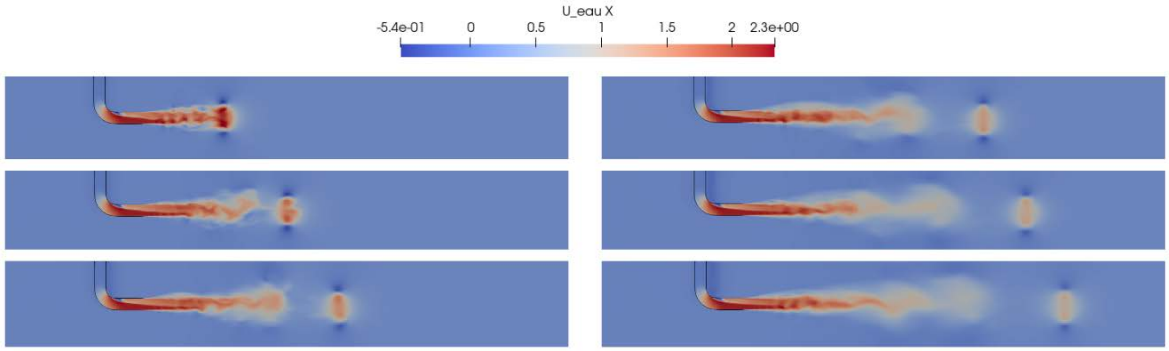

Figure 5.28: Effect of the turbulence model on the jet shape without particles with the R_{ij}-ϵ turbulence model.

In the experimental process, air is present in the upper part of the inlet pipe, the part that is above the water level. This is highlighted in the videos from the experience where, when the jet is activated, a large air structure is ejected from the pipe. Thus highlighting the presence of the large vortex obtained in the simulations. However, since particles are not present in the pipe, this vortex does not have any influence on their behaviour. It was assessed that both configurations - with and without an air pocket - led to the same behaviour once the jet reached a steady state. Hence, simulations are carried out with an inlet pipe initially fully loaded with water. Figure 5.29 shows the initial burst in the experimental setup. It is impossible to compare the experimental advancing speed of the burst with that in the simulations since the scale is undefined in the videos. This initial burst cannot explain the initial increase in concentration in the experiments.

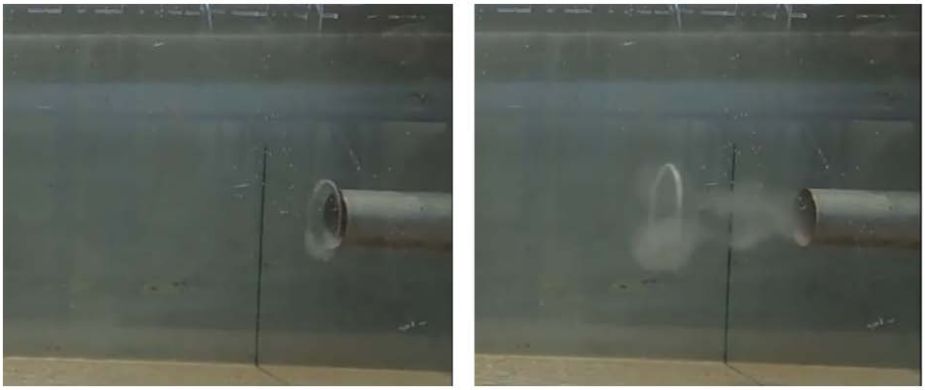

Figure 5.29: Frames of the video of the submerged water jet experiment showing the initial air pocket bursting out of the jet pipe.

Finally, particles are injected in the domain and their effect on the macroscopic jet characteristics are evaluated. The major difference between the Lagrangian and Eulerian frameworks is, in our case, the lack of reverse coupling in the first approach. The fluids are not impacted by the particle presence while, by design, it is the case in

the second approach. Unfortunately, since the loading is not negligible - around 1%, this has an impact on the jet orientation as shown in figure 5.30. In the Eulerian case, the particles make the jet heavier than the surrounding flow. This causes it to flow downwards. It was checked that, when the particle concentration is artificially reduced in the Eulerian framework, the simulations become equivalent to those performed with the Lagrangian method. Confirming the difference is caused by the reverse coupling phenomenon.

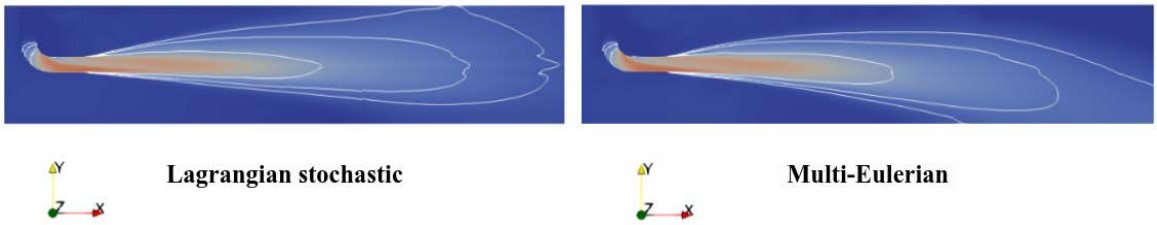

Figure 5.30: Mean liquid axial velocity with iso-surfaces shown in white. In the Eulerian case the liquid jet is clearly oriented towards the bottom.

Particle behaviour patterns without bubble plume

As expected from the preliminary studies, results shown in figure 5.31 illustrate the major difference between the Lagrangian and Eulerian frameworks.

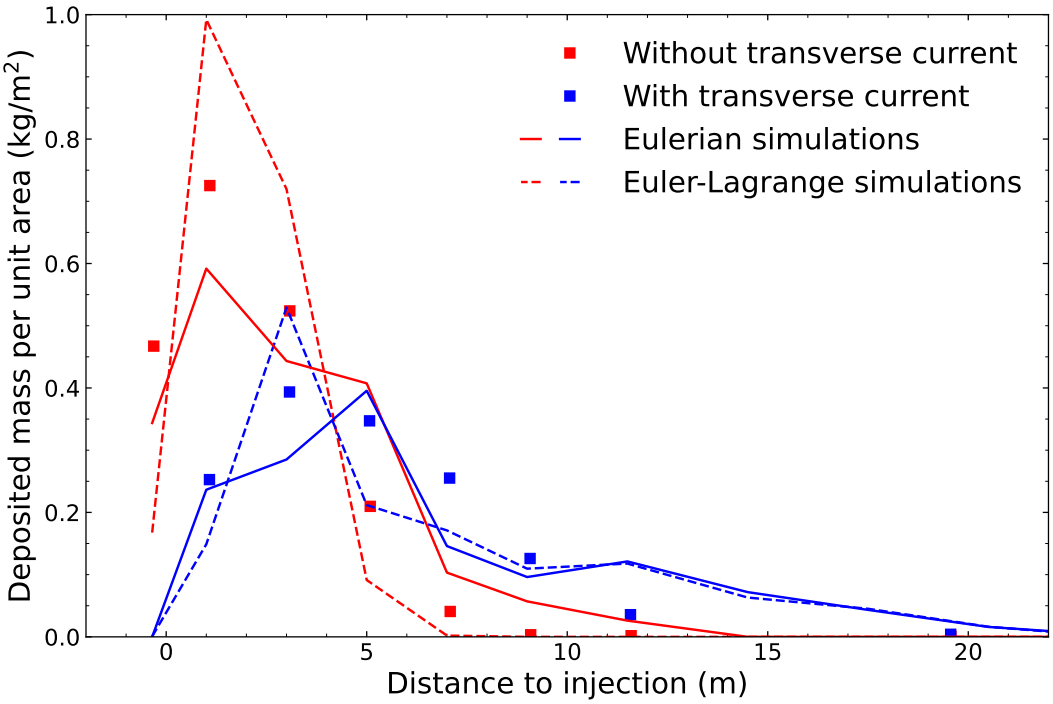

Figure 5.31: Total deposited mass at the end of the simulation with both methods and both with and without current. Squares denote experimental measurements.

In the Lagrangian simulations (dashed lines), particles deposit closer to the injection because they slip towards the bottom of the channel due to gravity without entraining the water jet with them. In the Eulerian simulations (solid lines), since reverse coupling is taken into account, this slip is slightly slower. Particles are thus transported

further down the channel. The plot shows, naturally, that in the case with current, the particles deposit further away from the jet inlet point no matter the framework. It also highlights the fact that the slip phenomenon is less pronounced. This is probably due to its relative importance in both cases. In the simulations with current, it seems there is an increase in particle deposition near $x = 12\,\mathrm{m}$ which is not present in the experiment. We struggle to understand why that is the case. The most probable cause of this discrepancy is the inlet condition. We set a uniform velocity and concentration inlet but this is probably not the case in the experiment. To assess whether that is the cause or not, it would be useful to carry out a simulation with a longer inlet pipe to establish the correct injection profiles. Since it would substantially increase the computing time for relatively low benefits, we did not perform the additional computations.

In the submerged water jet case, compared to the impacting case, solid concentration sensors were added. These allow for a time evolution comparison, substantially more informative than a final quantity such as total deposited mass which may not illustrate local unsteady phenomenons. In the experiment, these sensors have an unknown spatial extent and their response to non homogeneous flows is unclear. The first task consists in trying to reduce the uncertainty on these parameters. In the Eulerian simulations, these measurements are carried out in the post-processing step. A rectangle block is defined around the sensor location. Its width matches the width of the channel and its section has been varied to assess its impact. Since we do not know the sensors response to non homogeneous flows, we output the maximum and average solid concentration on the block on figure 5.32.

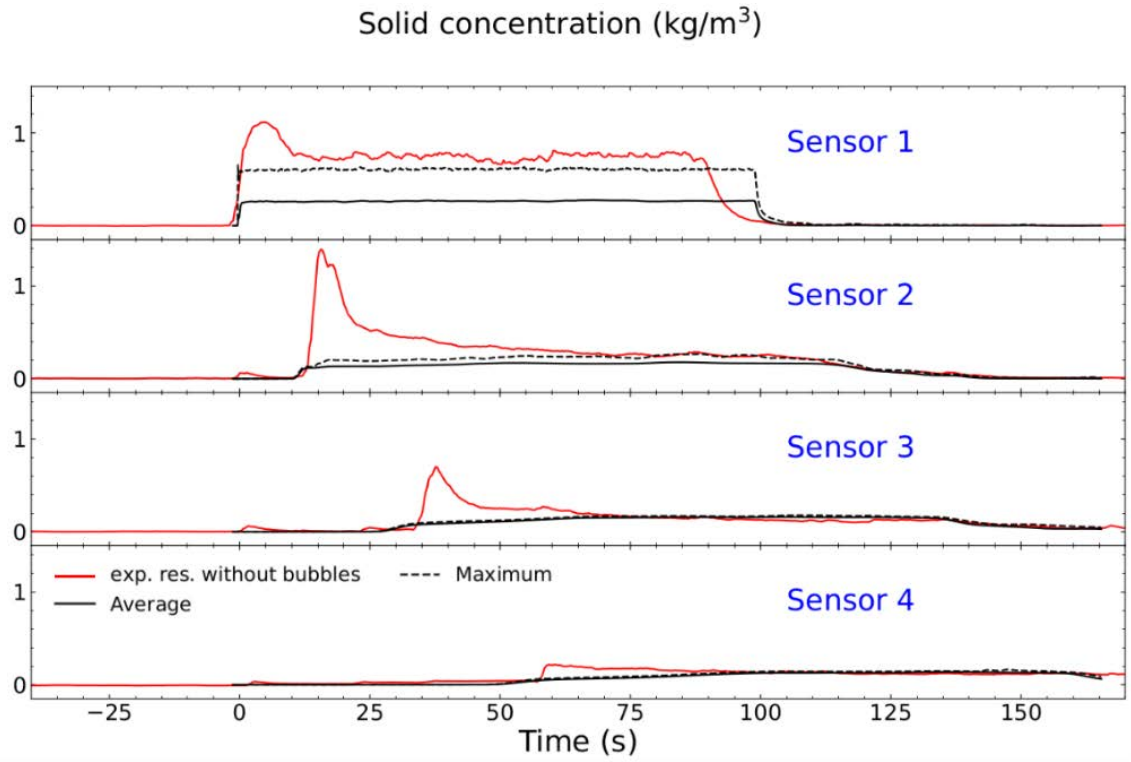

Figure 5.32: Solid concentration on the four sensors obtained with Eulerian simulations without bubbles by considering either the maximum or average concentration on the sensor block.

Figure 5.32 shows that, in the simulations, the value matching experimental results is the maximum solid volume fraction in the block. This seems to indicate the sensors are extremely non linear. Their response focuses on the maximum volume fraction in the volume. It seems that the section has little impact on the results. However, if we reduce the width of the block, the flow in it becomes more and more homogeneous and averaging or taking the maximum over the volume gives comparable results. Further away from the jet injection, due to turbulent mixing, the particle concentration is more and more uniform. At that point, taking the maximum or the average over the control volume makes no difference at all. In future simulations, the complete width of the channel is used together with a maximum solid volume fraction. This figure also illustrates that simulations suffer from a lack of axial particle dispersion. Indeed, the increase/decrease in particle concentration when the particle cloud arrives/leaves an ultrasound sensors is too steep in the simulation compared to experimental results. This difference is clear in the first sensor plot and less marked in the successive ones since particles have had the time to disperse along the jet axis.

Figure 5.32 also shows the maximum solid concentration is consistent with experimental results. The particle cloud hits the sensors at the correct time and the volume fraction is well represented if the maximum is taken over the sensor block. However, there is an initial peak in concentration that we do not predict with the solver. Experimentally, this could be related to an increase in particle concentration at the beginning of the experiment because the jet inlet pipe gets its water from the bottom of the water tank. And, even if there is a mixing device, there could, initially, be more particles at the bottom of the tank compared to its bulk. To qualitatively study this effect, the solid concentration in the inlet has been changed to match a possible experimental value. This increase can be schematically seen in figure 5.33.

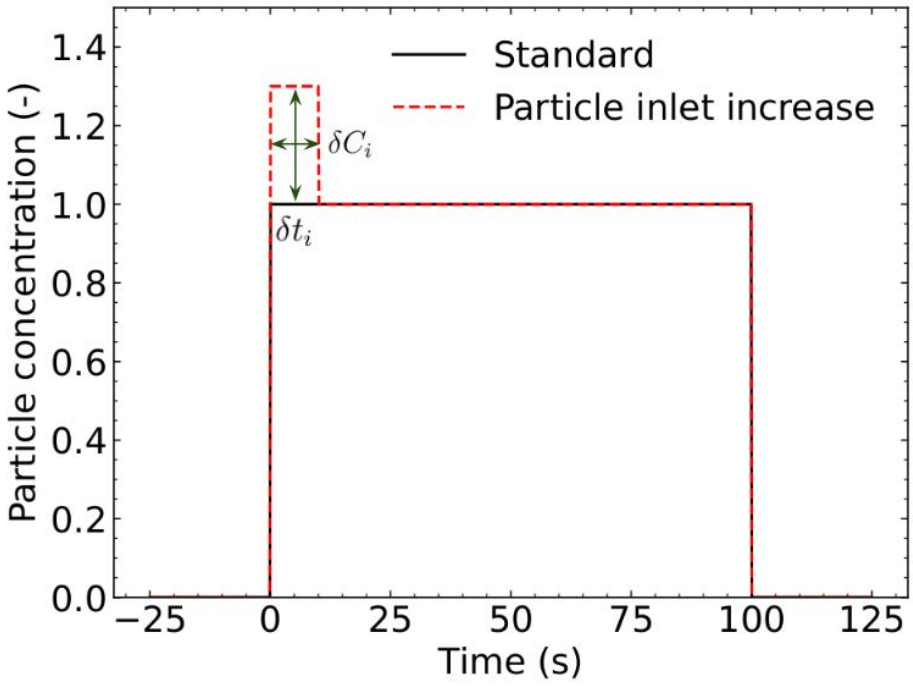

Figure 5.33: Particle concentration in the jet inlet as a function of time (normalised). δC_i and δt_i are shown with green arrows.

It is characterised by an increase in concentration δC_i and a time length δt_i. From

experimental results, it seems that the increase in particle concentration lasts around $\delta t_i = 10\,\mathrm{s}$. From experimental data, it seems that this increase in concentration is around 10%. However, we tried simulating the case with a 10% increase in initial concentration and did not achieve a noticeable improvement in the results further down the canal. Thus, we try different values for δC_i to see whether a larger increase can explain the peak observed in experimental results. These results are shown in figure 5.34 for simulations where the jet is not stopped since the initial peak is the main focus. The only way to get the increase in particle concentration observed experimentally down the channel is to massively increase the initial concentration (ten times more particles initially). This does not match with results from the first sensor and cannot be explained by a surplus in particles due to inconsistent mixing in the tank. Moreover, when the particle concentration is increased, its behaviour downstream is also impacted in the simulations. On the other hand, it has to be noted that sensors were calibrated between $0\,\mathrm{kg\,m^{-3}}$ and $1\,\mathrm{kg\,m^{-3}}$. This means that confidence in measurements from it is low when solid concentration is higher than $1\,\mathrm{kg\,m^{-3}}$ - which is the case in the first sensor. In the videos from the experiment, there is no noticeable change in particle density at the beginning. All in all, we are not able to reproduce the first peak in concentration observed experimentally. We also struggle to explain it from a physical point of view. A probable cause of the difference between the simulation and the experimental results may stem from the use of the concentration sensors. They are at the edge of their calibration range which could induce a bias but, more importantly, we do not know how the unsteady phenomenons near the jet injection interact with the measurements.

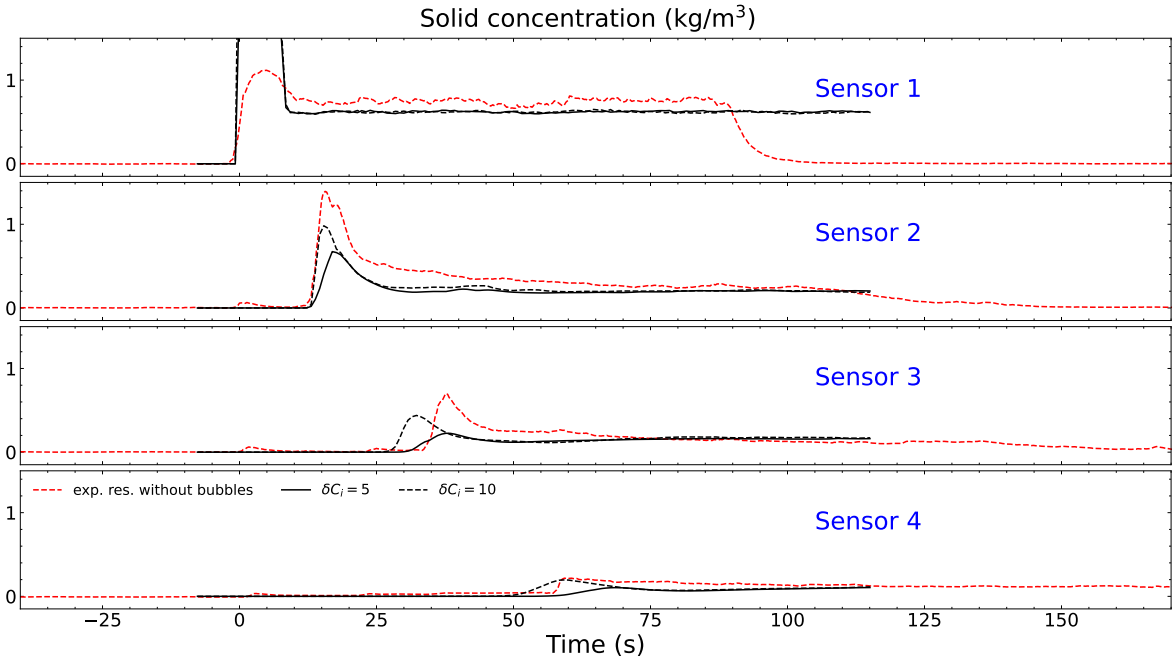

Figure 5.34: Solid concentration on the four sensors with different local increase in particle volume fraction.

Even considering this issue, results are still encouraging, the liquid-gas-solid models developed are able to predict the correct deposition pattern and the main features of solid concentration during the injection. Here, even if the particles do not directly interact with air, the presence of a free-surface justifies the use of three-phase solvers.

Simulations were performed without the free-surface and they could not achieve results as satisfying as these shown here. This is mostly due to the difficulties that arise when trying to set a boundary condition mimicking a free-surface in a single-phase computation.

5.2.3 Immersed water jet with bubble column

In this scenario, a bubbler is added on the bottom of the channel near the jet inlet. The goal is to isolate the interaction of particles and bubbles while minimising the number of unknown parameters; mainly, the entrained air bubble diameter we had to set beforehand in the impacting jet case. The added device consists in a metal tube located on the bottom wall at a distance of 2.6 m from the jet inlet. It is perpendicular to the jet stream and contains around 50 small holes of diameter 0.35 mm. This device produces uniformly shaped spherical bubbles with a diameter around $d_b = 5\,\text{mm}$. The total air flux in the tube is $q_b = 0.35\,\text{L}\,\text{s}^{-1}$. Otherwise, the experimental setup is unchanged and can be seen in figure 5.35. The simulation setup is also unchanged and the mesh identical.

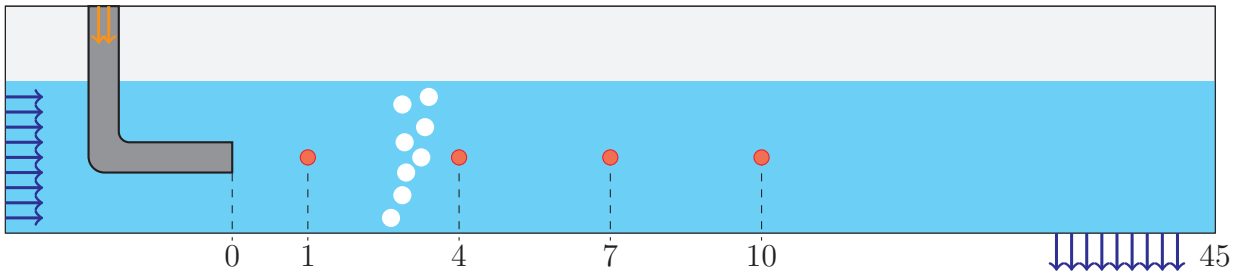

Figure 5.35: Schematic representation of the submerged water and particles jet with bubbles injection in the canal performed at the LNHE department. Distances are in meters. The red dots represent the positions of the solid concentration sensors.

Bubble injection isolated study

Before studying the whole case, a study focused on the bubbler is presented. The aim is to verify the coarse mesh is consistent with a much finer simulation of the bubble plume alone. Otherwise, the mesh would have to be locally refined near the air inlet, increasing the total computing time.

	Coarse mesh	**Fine mesh**
δx	10 mm	1 mm
δy	6 mm	0.6 mm
Air bubble inlet width	20 mm	1 mm
Air bubble inlet flux	$4.2 \times 10^{-4}\,\text{kg}\,\text{s}^{-1}$	$4.2 \times 10^{-4}\,\text{kg}\,\text{s}^{-1}$
Number cells/Air bubble	0.5	5

Table 5.3: Properties of the coarse and fine meshes for the isolated bubbler study.

This side study consists in a zoom around the bubbler. The idea is still not to model each bubble creating hole and resolve every interface but to be a lot finer nonetheless. The geometry and boundary conditions are defined on figure 5.36 and details about

the meshes are summarised in table 5.3. The water inlet on the left-hand side of the domain generates the channel current. The outlet condition on the right-hand side ensures the water level stays the same during the simulation. The channel free-surface is not accounted for, it would make the simulations longer for no extra benefit.

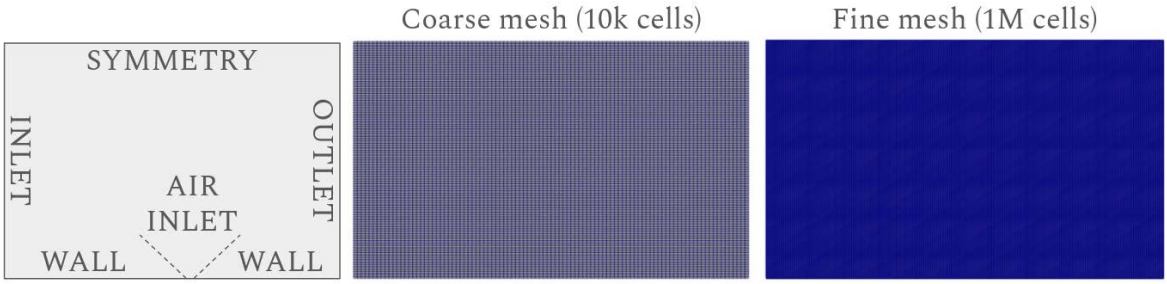

Figure 5.36: Geometry, boundary conditions, coarse and fine meshes for the isolated bubbler study.

After several seconds, the flow becomes steady. Instantaneous snapshots are presented in figure 5.37. They illustrate the difference in resolved interfaces between the two cases. In the fine mesh, there are some resolved bubbles whereas in the coarse case, the flow stays dispersed. Additionally, it seems that, in the finer case, the bubble plume is slightly thinner than in the coarse case. This is also seen in the vertical velocity plots shown in figure 5.38. This is caused by the increased numerical diffusion caused by bigger cells. The shape of the bubble plumes in both cases are shown on the right-hand side of figure 5.37. They are the contour $\alpha_g = 1 \times 10^{-3}$ and they also show the increased numerical diffusion in the coarse case. Interestingly, this diffusion is mostly generated at the inlet where air is faster. Naturally, the inlet in the coarse case being wider than in the refined case, this also leads to a larger bubble plume. With all that considered, the shape is still quite similar.

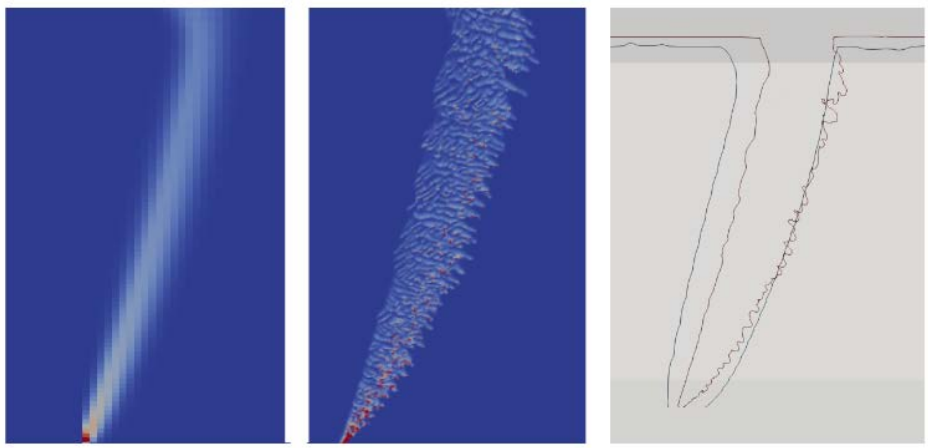

Figure 5.37: Instantaneous snapshots of the bubbler study on the coarse mesh (left - blue plume), the fine mesh (centre - red plume) and a comparison between the two bubble plumes obtained (right).

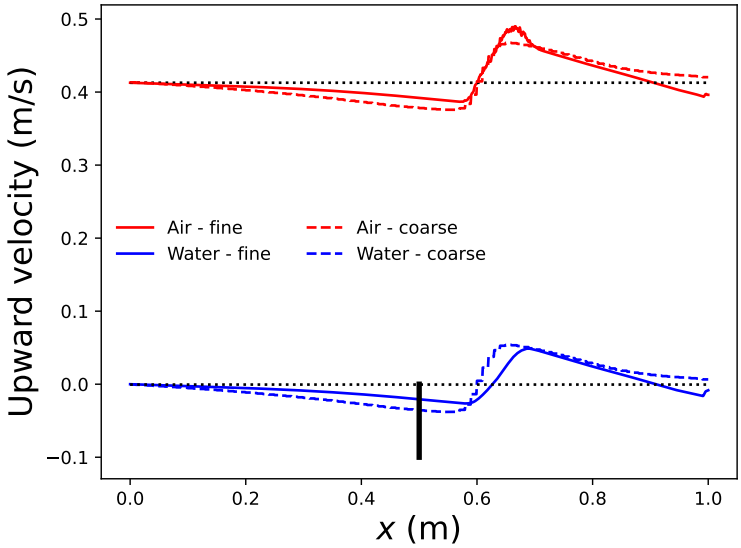

Figure 5.38: Mean vertical fluid velocity on fine (solid lines) and coarse meshes (dashed lines). The black rectangle represents the bubbler position. Dotted black lines are the mean fluid velocities without air bubbles.

Resolved interfaces shown in figure 5.37 measure around 5 mm. Since they match experimental observations, this value will be used as the inlet boundary condition in the general case. The fine mesh results are compared to a coarse mesh simulation which corresponds to the refinement in the general case. The goal is to check the momentum transfer between air and water is well represented even in the coarse mesh. In figure 5.38, the vertical velocity for each phase is plotted in both meshes. The bubbler location is pictured by a black rectangle at $x = 0.5\,\mathrm{m}$. The figure highlights its impact on the mean flow and shows that the difference between the meshes is not significant. The coarse mesh can be used to model the bubble plume correctly. To further reduce the error introduced by the mesh, the inlet air velocity obtained in the fine simulations is used to determine the boundary conditions on the coarse mesh.

Impact of bubble plume on the particle behaviour

As in the case without bubbles, the total deposited mass at the end of the simulation is compared to experimental results. An issue immediately arises from standard simulations. It seems that particles are not really affected by the presence of the bubbler in the simulations. They deposit exactly as they did in the case without bubbles whereas, in experimental results, the difference is obvious. The particle deposit uniformly throughout the channel. To try and understand that, we can compare the experimental and simulated solid concentration evolution in the two different configurations. Figure 5.39 shows this comparison and highlights that there is no noticeable difference between the two concentration time series. This means that the difference in the experimental setup occurs after the particle cloud passage or is only visible near the bottom.

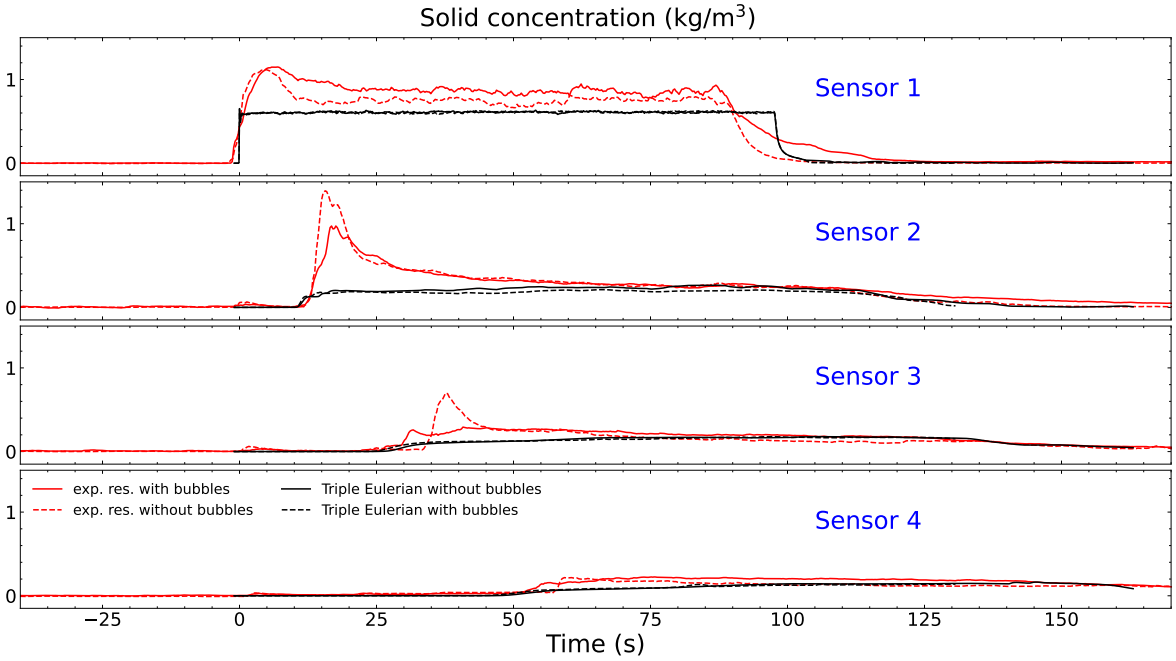

Figure 5.39: Concentration evolution in Eulerian simulations and experiments with and without additional bubbles.

Similarly, the videos show no clear impact of bubbles on the particle cloud. It is rather the opposite, the particles seem to have an impact on the bubbler. This is also what is observed in the simulations as can be seen in figure 5.40. When the cloud hits the bubble plume, it goes down with it.

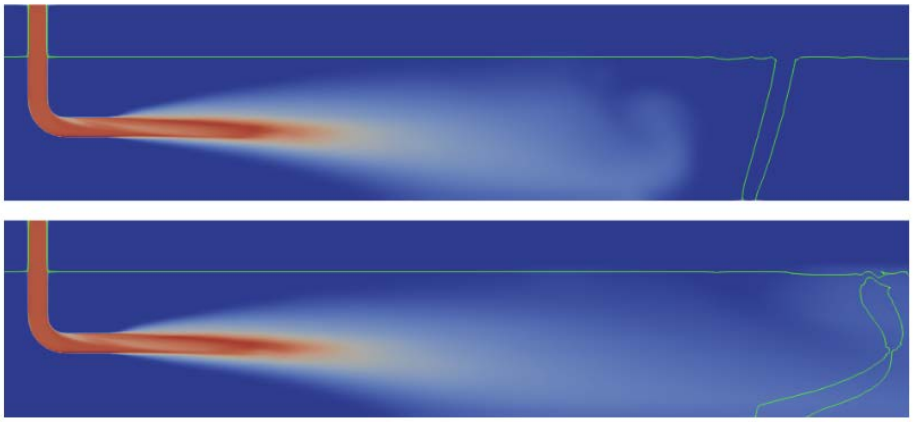

Figure 5.40: Instantaneous snapshot showing the particle volume fraction and bubble plume shape before and after the cloud hits it. The light green line indicates the iso-surface $\alpha_g = 0.1$.

Our assumption is that the bubbler causes particles on the bottom of the channel to be injected again in the flow. When this phenomenon happens, they flow down the channel due to the jet and the current. Additionally, the bubbler and current must stop at the same time as the jet does. But, due to practical latencies, there is a delay before they stop completely. Thus, the bubbler re-entrain particles in the flow which has not stopped completely and therefore transport them further downstream. These processes

are difficult to model in the simulations, especially in the Lagrangian framework, since, in practice, after particles deposit, they are no longer in the domain. In the Eulerian framework, we decided to model this re-entrainment by reducing the deposition rate ϕ_d computed at each time step in each cell. When the rate is 0, the particles no longer deposit, they accumulate on the bottom wall. When everything settles down, the total mass of particles in each zone is counted, not from the cumulative mass deposition but rather from the total volume of particles present in the water column above the region. This is illustrated in figure 5.41 where simulation results with a modified deposition rate ϕ_d seem to give better results.

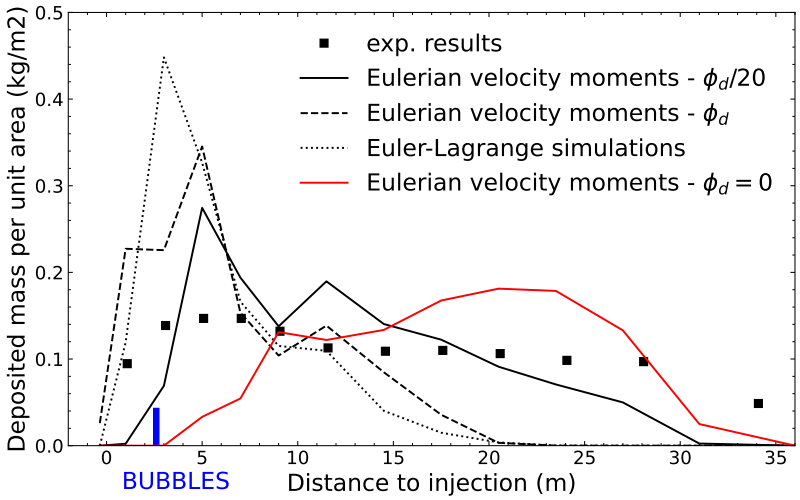

Figure 5.41: Total deposited mass in the case with bubbles depending on the deposition rates in Eulerian simulations and Euler-Lagrange simulation.

This comparison shed some light on the fact that, in both methods, the behaviour of particles accumulating on a wall needs more careful modelling to be taken into account properly. This means correctly representing the behaviour of particles in a boundary layer and being able to reproduce the re-entrainment, slip and rebound phenomenons which may take place. For now, this is a clear limitation of the two methods developed during the thesis. Limitation which was not encountered in the bubble column case since deposition was neglected. In general, the cut in computing costs introduced with the Eulerian method allows for simulation of more complex cases, since they are not limited to a number of particles.

5.3 Integral case : nuclear reactor building

The last experimental case studied during the thesis highlights the main motivation for the company to work on liquid-gas-solid flows. It consists in the simulation of a large scale experimental representation of a reactor building floor during an eventual loss of coolant accident. As presented in chapter 1, during a loss of coolant accident, the reactor building water level increases until the safety mechanism start getting their water from its bottom rather than an isolated tank. If debris accumulate on the filters located upstream the pumps, they may cause their clogging which would hinder

the safety devices, slowing down the cooling of the reactor. Predicting the particle trajectory or their final deposition location is therefore a key feature for liquid-solid-gas multiphase solver or experimental setups. This is the main focus for this section, use both methods to predict the deposition pattern in the reactor building under specific flow conditions matching the experimental setup designed by the LNHE department.

5.3.1 Experimental and numerical setup

A photograph of the setup is shown in figure 5.42 along with the geometry used in the simulations. The water flowing towards the bottom of the building is represented by five vertical pipes and five obstacles. Each set of pipe and obstacle is a scaled version of the one found in the impacting jet study presented above. There are two large, two medium and one small pipes. Similarly to that case, the jet created has a cone-like shape which can be seen in figure 5.42.

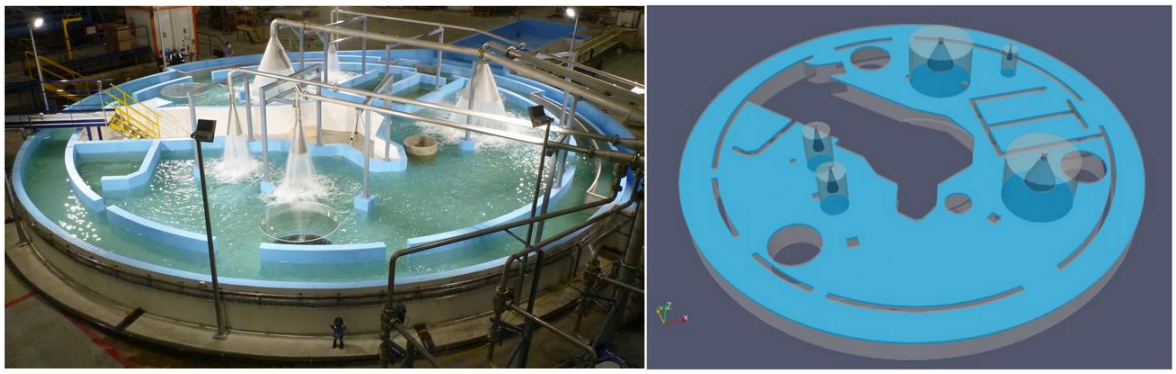

Figure 5.42: (left) Picture of the experimental setup and (right) associated geometry used in the numerical simulations.

The experimental protocol is summed up in table 5.4. Water is injected to fill the bottom pool, when it reaches a certain height, particles are also injected and outlets are activated so that the water height decreases. After all the particles have been injected, water continues to flow out of the pipes. Then, when most of the particles have been deposited, the jets are stopped, the pool is dried and the total deposited solid mass is dried and weighted in all the regions shown in figure 5.43. Particles have a density ratio of 2.5, and an equivalent diameter of 60 µm whereas air and water are considered to be at their standard atmospheric conditions. Other particles were tested in the experiments but we focus on only one type, the same used in the simpler setups presented previously.

Step	Time (s)	Water level (m)	Water flux ($\mathrm{kg\,s^{-1}}$)	Particle flux ($\mathrm{kg\,s^{-1}}$)
1	t_0 to t_1	0 to h_1	ϕ_w	0
2	t_1 to t_2	h_1 to h_0	ϕ_w	ϕ_p
3	t_2 to t_3	h_0	ϕ_w	0

Table 5.4: Steps in the experimental protocol.

The first and third steps being irrelevant in numerical simulations, these are started at the end of step 1, when the water level is nearly at 0.135 m. They are stopped

when most of the injected particles have deposited. The generalised large interface method is used in order to account for both free-surfaces and dispersed inclusions in the simulations. This is slightly more expensive but more accurate. The solid particles are either tracked with the Lagrangian stochastic method or with the Eulerian velocity moments method. Turbulence is second order R_{ij}-ϵ for air and water while the particles turbulence is accounted for with the models described in chapter 3. A pressure outlet ($P = 101\,325\,\mathrm{Pa}$) is defined at the top of the domain, the pipes are inlet where water volume fraction is $\alpha_w = 1$ in Lagrangian simulations and $\alpha_w = 1 - \alpha_p$ in Eulerian simulations and the imposed flux depends on the pipe size according to table 5.5. The particle inlet flux, when there is one, does not depend on the inlet pipe. The same amount of solid (25 kg) is injected from each pipe. The kinetic stress model is used to account for particle agitation in Eulerian simulations.

Size	Water mass flux ($\mathrm{kg\,s^{-1}}$)	Solid mass flux ($\mathrm{kg\,s^{-1}}$)
Large	112.8	0.05
Medium	28.2	0.05
Small	18	0
Total	300	0.20

Table 5.5: Inlet water and solid mass fluxes depending on the inlet pipe size.

The bottom of the pool is a rough wall where particles can deposit whereas side panels, pipes and obstacles are walls where particles bounce off. Water outlet are also activated during the second step to work at constant water height.

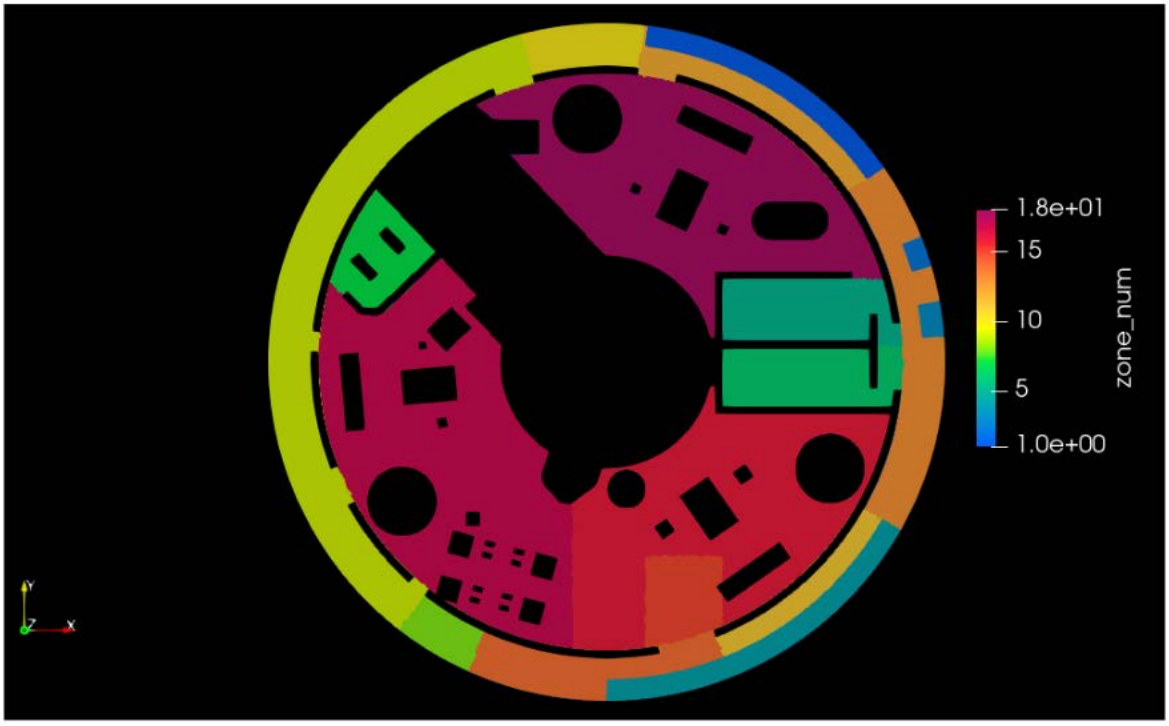

Figure 5.43: Regions where total deposited mass is weighted.

The mesh used contains 1 144 925 hexahedron cells ensuring the condition $y^+ < 180$ at the wall, it is shown in figure 5.44. The time step is constant $\delta t = 5 \times 10^{-3}\,\mathrm{s}$ ensuring

the condition CFL < 5. Initially, the size of air transitioning from continuous to dispersed inclusions is set between $d_b = 1\,\text{mm}$ and $d_b = 5\,\text{mm}$. In the last computations, the air bubble inclusion size will be determined by the model described in chapter 4.

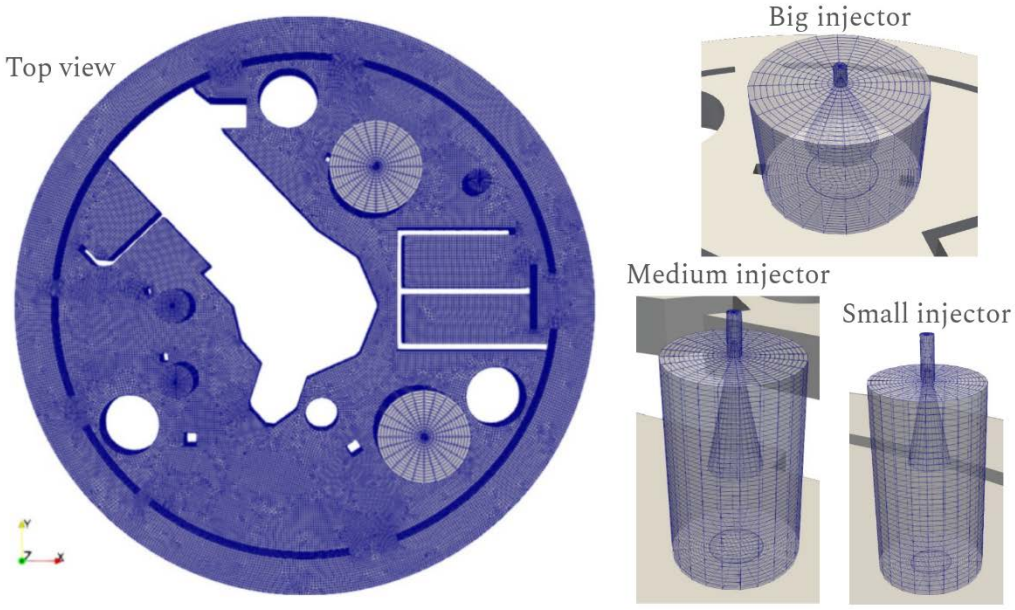

Figure 5.44: Top general view of the mesh and detailed view of each injector mesh used in the simulations.

5.3.2 Preliminary verifications

In earlier studies, LSPIV were performed on the setup without the addition of particles. The aim was to qualitatively check if the flow prediction was accurate without the addition of a third phase. Since the comparison was carried out before the start of my thesis by another researcher, it is not presented here.

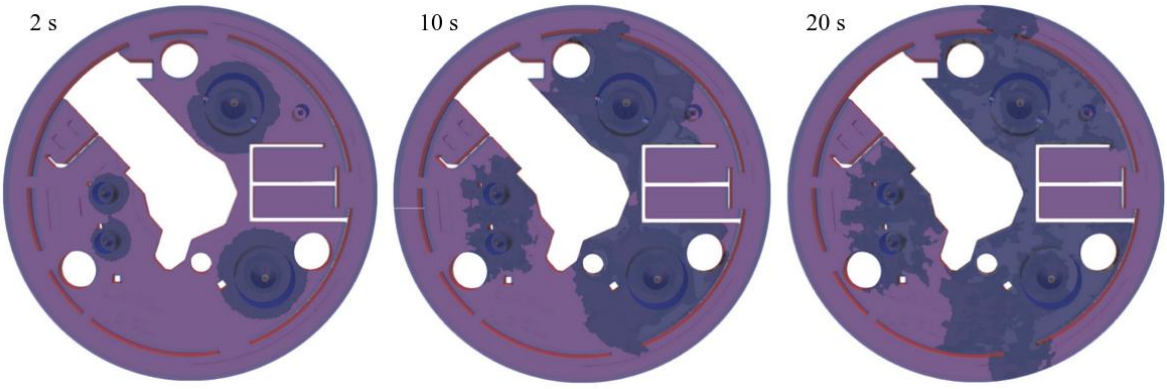

Figure 5.45: Clipping at $\alpha_p = 0.1\%$ of the instantaneous solid volume fraction 2, 10 and 20 seconds after the injection start.

The particle dispersion obtained with the Eulerian method is qualitatively shown in figure 5.45. At first, particles are found just below the injectors. Then, as time advances, particles are transported further away. Some reach the outer regions of the domain and the outlet conditions representing the re-circulation pump channel inlet.

At the end of the simulation, particles can be found all around the domain as illustrated in the next section in deposition distribution plots.

5.3.3 Particle deposition distribution study

As in the canal experiments, we compare the total deposited mass in each region with the experimental measurements. In an early study, with the original Lagrangian tracking model, particles were mostly falling right below the injector even though that is not the case in the experiments. The goal is to determine if the new models predict a more disperse deposition distribution compared to the standard simulations. Figure 5.46 shows a comparison between a Eulerian simulation with air bubble diameter $d_b = 5\,\text{mm}$ and previous Lagrangian results obtained without the multi-carrier field approach. From the figure, it can be seen that the new method predicts a much more disperse deposition distribution. However, it seems that it also underestimates the quantity of particles depositing below the jet. Since this phenomenon was already observed in the impacting jet case, the entrained air bubble diameter was changed to assess its influence on the global results. Figure 5.47 shows two different results obtained with the Eulerian approach. It shows that the entrained air bubble diameter has an impact but it does not give a better prediction for solid deposition below the jet as it did in the channel case. We think this is related to the change in experimental setup. Indeed, in the reactor building case, the water jet is still active after the particle flux is stopped. This contributes to changing the way particles are transported altogether.

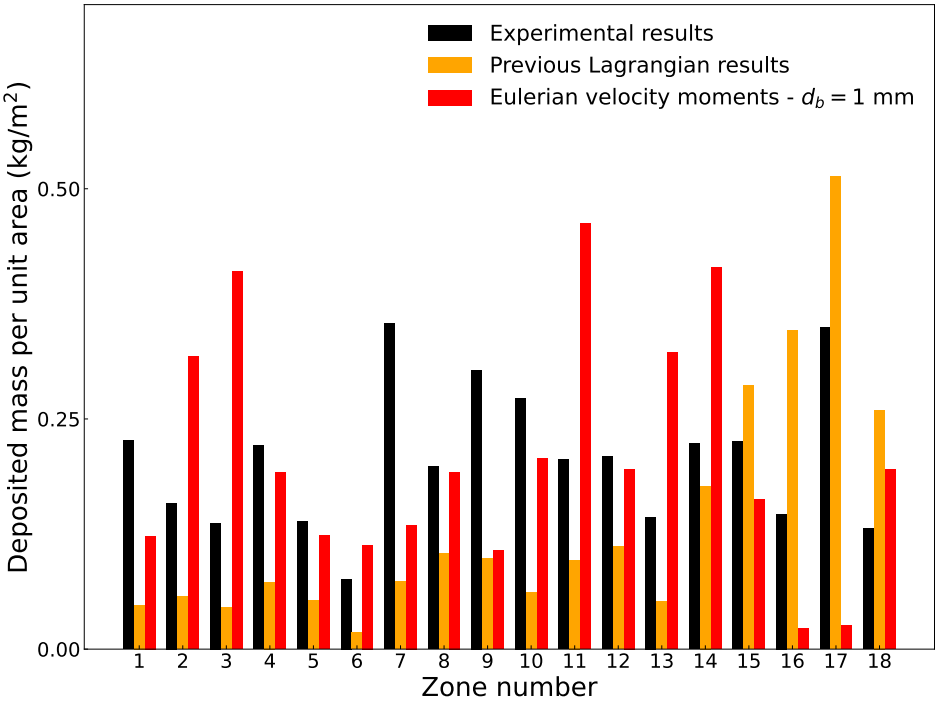

Figure 5.46: Total deposited mass at the end of Eulerian simulation with $d_b = 5\,\text{mm}$.

In the Eulerian simulations, more particles tend to be transported towards the outer parts of the reactor building floor compared to earlier Lagrangian simulations. It provides a worst case scenario answer to the clogging of the safety device filters. Results with the new Lagrangian model did not improve compare with original simulations. We

think this is related to the complexity of the case. We are not able to reach convergence, thus, results are still as bad as before. To improve them, we would need to increase the computing power, increase the number of particles and rework the mesh. Similarly, results with the air entrainment model could not be obtained. The additional model and the resolution of the interfacial area transport equation is too demanding, it cannot be afforded in this complex scenario.

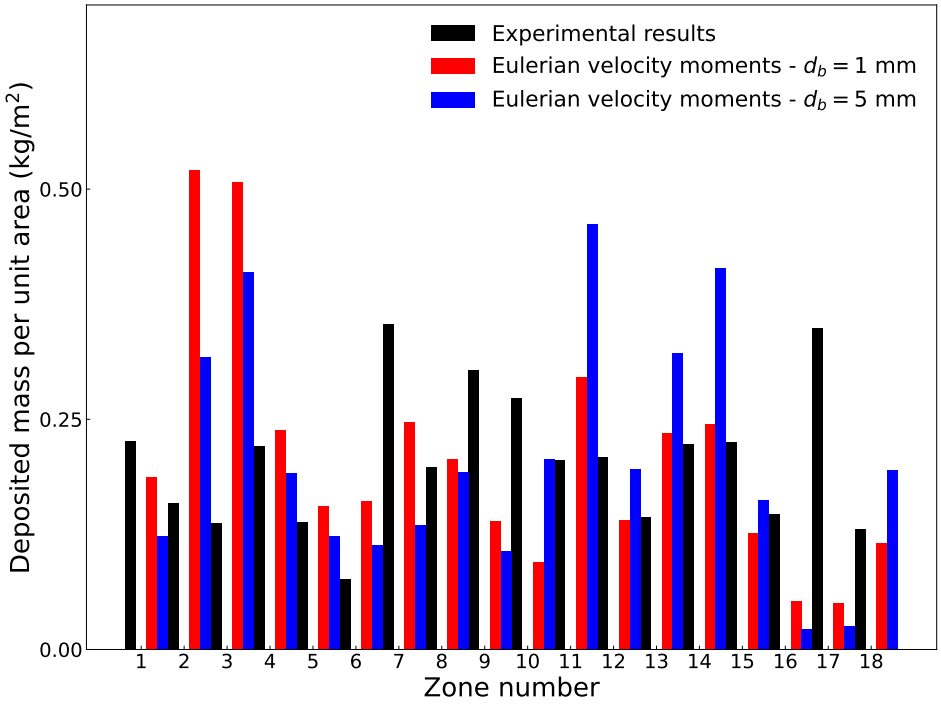

Figure 5.47: Total deposited mass at the end of Eulerian simulations with $d_b = 1\,\text{mm}$ and $d_b = 5\,\text{mm}$.

All in all, the new models provided valuable insights on the behaviour of particles in the LNHE experiments. In the channel case, the results as well as the differences between the two methods are well understood and consistent with experimental measurements. In the more complex reactor build setup, the results are less precise.

6 | Conclusion and perspectives

6.1 Summary of the manuscript

After a brief introduction to liquid-gas-solid flows, the challenges this field of study faces and the numerical methods already available, we proposed a detailed presentation of the two-phase flow models over which we based our new modelling approaches (chapter 2). This preliminary chapter gave us the opportunity to review the Lagrangian stochastic and Eulerian models that exist in the literature. In that chapter, we also introduced a new stochastic model for the fluid velocity seen at the position of the particle and tested in on several analytic or verification cases. This new model was driven by the inconsistency of existing models in the large inertia case of particles in an established turbulent channel. Finally, the framework of netpune_cfd is presented at the end of the chapter.

Chapter 3 focuses on presenting the two new methods for liquid-gas-solid flows developed during the thesis. The Euler-Lagrange approach is based on the classic Lagrangian stochastic model. It considers as many fluid velocities seen by the particle and stochastic equations as there are continuous fluids susceptible to carry each solid particle. The influence each phase has on the particle is represented with the weight coefficient λ_f for which we proposed several closures. A first order numerical scheme solving the stochastic system is then suggested. Two simple verification cases are presented. One analytical, where particles fall through an air-water interface and we ensure the correct behaviour of the solver; the second is similar but with experimental measurements. From this new Lagrangian model, we derive a multi-Eulerian framework according to common practice in two-phase flows. A thorough verification is performed to establish the consistency of the interfacial transfer term between the mean equations obtained for the continuous phases and the dispersed phases. Then, the Lagrangian model is used to close the system and obtain evolution equations for the particle phase mean quantities and its turbulence. Reverse coupling and collisions are rapidly explored before introducing the turbulence and gravity deposition models used during the thesis. In this last section we also explore verification test cases with the Lagrangian stochastic model for particle depositing in a turbulent channel. We suggest using interpolation or an existing probabilistic model to enhance the results.

In the following chapter 4, air entrainment phenomenon is explored. It constitutes a sizeable challenge encountered in the experimental cases we tried to reproduce, hence our interest in it. After a literature review of the mechanism driving air entrainment and the numerical methods which account for this phenomenon, we propose a model of our own, embedded in neptune_cfd. This new model's prediction are then compared against experimental data for a small size laminar jet, a large over-flowing turbulent jet and an hydraulic jump. Depending on the case, satisfactory results were obtained with

different model closures. In the case where air entrainment is driven by small scale surface instabilities, the model based on the free-surface curvature is more effective whereas in the case where large turbulent eddies seem to be the cause of aeration, the model based on Hinze's scale performs better.

The last chapter compiles the different liquid-gas-solid configurations used to evaluate the performance of the methods developed during the thesis. First, we considered two bubble columns loaded with particles. The main motivation for the subject was to provide an outlook on other topics which might not be the core interest for EDF but that still constitute valuable configurations from an academic or industrial standpoint. Lagrangian and Eulerian simulations could not be performed in both studies which highlighted the necessity, in some scenarios, for collision and two-way coupling models. These illustrated the key role played by coalescence, fragmentation models in air-water bubbly flows. They also highlighted the need for careful weight coefficient closures. The second series of test cases were based on experiments carried out in the LNHE department of EDF R&D. These were designed to evaluate the accuracy of numerical simulation predictions for three-phase flows in order to increase the confidence on the model's prediction for an industrial scale experiment presented at the end. Again, these cases gave us the opportunity to highlight the importance of the air entrainment phenomenon and the necessity to model it precisely. They also illustrated the difference between the Lagrangian and Eulerian approaches, specifically in terms of two-way coupling. Finally, these cases stressed the need in more precise deposition models. A simple one was introduced and its limitations were clearly visible in the submerged water jet case.

All in all, both methods were successfully used in different scenarios at different scales. These put forward their advantages as well as their limitations. The main quality of the Eulerian approach, at least in the framework we have, is its ability to naturally take into account the impact of the solid phase on the continuous fields. It is also quite fast compared to Lagrangian simulations. It requires more equations to be solved but the time step is not as restricted as in the Lagrangian case and, moreover, for scenarios with many particles, the time spent solving the stochastic system can be vastly superior to that spent for the Eulerian equations resolutions. This also enables simulations with high solid concentration to be carried out. Simulations which would be impossible with the current Lagrangian approach due to the enormous amount of particles needed to describe the solid phase. All these comparisons highlighted the difficulties that arise when experiments are numerically recreated. No matter how careful the work, there will always be some indefinite experimental parameter which has an important impact on the numerical results. In our case, several such parameters have been observed, some are indefinite due to the nature of the measurement device and some are indefinite due to an inability to extract them from the setup.

6.2 Enhancements of the developed models

The two methods developed during the thesis constitute valuable tools for the numerical simulation of liquid-gas-solid flows in an industrial context. However, there are a number of areas where improvements are needed. These were not explored during the thesis but were identified as key perspectives to improve the framework. Hereafter is a description of these perspectives.

The most accessible area involves particle deposition modelling. Studies have shown the limitations of the current approach, working on it would most certainly lead to better, more robust results. In the Lagrangian stochastic approach, this is considered as a major challenge since the current approach lacks consistency for particles near a boundary layer. Tackling the deposition problem correctly implies, either to rework the stochastic model and include a more sophisticated approach or, as was hinted at in chapter 3 to consider a probabilistic approach where particles are not transported to the boundary face. In the second option, as in deposition/rebound, a probability could be used to account for particle re-entrainment or slip. If a more sophisticated stochastic model is chosen, a special focus should be made on particle behaviour when it hits a boundary face in order to make sure all the possible scenarios are represented. In Eulerian simulations, the solid mass flux near the wall, which actually represents particle deposition, could also be used to account for particle slip or re-entrainment. The model suggested in chapter 5 is very basic and naive, a more consistent model should be developed instead. Also, in both methods, we could imagine coupling the deposition model to an immersed boundary method to account for the obstruction generated by sedimented particles. With an Exner type equation (Paola and Voller, 2005), it could be possible to determine the evolution of the immersed boundary conditions due to deposition, re-entrainment (or erosion) and slip. Numerical results from Eulerian simulations of solid beds could also help determine the behaviour of such granular boundary.

Another topic which may benefit from more investigation is turbulence modulation. As soon as particles are transported in a continuous structure, they impact its turbulence. Either production or damping, their effect depends on the flow characteristics. In this thesis we only addressed the topic once in chapter 3. This should drive more interest in the matter. Additionally, there is a serious challenge regarding turbulence models and the multi-regime modelling approach used in neptune_cfd. Indeed, continuous turbulence models are applied when a continuous phase is transferred into a dispersed one. Some terms are added to account for the change in scenario but more work is necessary to make them more consistent. Additionally, it should be kept in mind that we assumed, in the Eulerian and Lagrangian frameworks, that there was no correlation between the velocity fluctuations of two different fluids carrying a particle. As long as all the fluids are continuous, this is not an issue. However, this is not the case near a resolved interface and in the multi-regime model in neptune_cfd. In these cases, the velocity fluctuations of the two fluids are correlated. Thus, additional terms are required in the Langevin equations to account for this coupling. Also, particles may have an impact on other dispersed structure turbulence. This is unaccounted for at the moment but it would be interesting to see its impact and what are the scales where this phenomenon might be predominant. Not to mention that turbulence modulation models for two-phase flows are still under development. Lastly, the impact of particles is not accounted for in the bubble coalescence and fragmentation models. A simple model was tested in chapter 5 but no clear improvement could be noted. However, particles may induce breakup when they collide with bubbles or increase coalescence by promoting film drainage. Thus, an in depth exploration of the topic might lead to better modelling approaches.

A serious limitation, caused by the current framework we are working on, is the lack of reverse coupling and collision modelling in the Lagrangian approach. As we

have seen, this introduces, in many configurations, errors which would be avoided otherwise. However taking these matters into account is far from easy. As hinted at in chapter 2, reverse coupling terms might render the fluctuation formulation a lot more difficult to implement. To take it into account, source terms should be added in the continuous evolution equations and, in turn, they should be added as well in the stochastic equations. There are models that already exist for two-phase flows, they could be adapted to make them compatible with the multi-carrier formulation presented in chapter 3. Similarly, collisions are not easily accounted for in Lagrangian frameworks. Even though this phenomenon appears only for high solid volume fraction hardly accessible with particle tracking methods, being able to take collisions into account could make the model more accurate. This would not be necessary for the cases studied during the thesis but it might be in other situations.

One last effect related to particles, not taken into account in this manuscript because negligible in our case, is the effect particles have on free-surface. Since they carry air in their wake when crossing a water interface, if many particles are doing it at the same time, this can have a sizeable effect which requires modelling.

On the topic of air entrainment, there are many possible ways of boosting the model performance and accuracy. The first modelling aspect which needs more research is the mass transfer modelling between continuous air and dispersed bubbles. For now, this transfer is the output of the simulation and it might be overestimated compared to experimental results. Depending on the flow quantities, a certain fraction of air is considered continuous while the other is considered dispersed. It would be useful to be able to introduce a forcing term which defines the mass transfer between the two structures (continuous and dispersed). This could also be performed with a three field formulation. Similarly to what is done in GENTOP, by defining the dispersed inclusions and the continuous structures as separated entities, it is easier to control the mass transfer between the two. It is also easier to set the inclusion sizes when mass is transferred. This model might also make it easier to ensure the conservation of quantities involved in the process. Unfortunately, these assets are balanced out by the increase in computational cost. Since in industrial applications it is a recurrent challenge, maybe more efforts are needed in the two field formulation to make them capture these transition effects rather than switching to a three field formulation directly. If we choose to keep the interfacial area method to track bubble diameters, further verification will be needed to assess whether the assumed PDF in the model is compatible with experimental distribution of entrained bubbles. The models we introduced for the inclusion diameter might also be subject to enhancements. The main challenge is that we are trying to determine an inclusion size from free-surface quantities in the specific situation where the free-surface is not resolved anymore. Therefore, more investigation is needed to make this method more consistent. Eventually, coalescence and fragmentation model might also need to be adapted because of the presence of a free-surface. For now, they are used as if the bubbles were located in a single phase domain. Unfortunately, the expression of these terms might be impacted by the presence of an interface. This has not been investigated yet and might be an important addition to the interfacial area framework. Especially since their treatment with entrained inclusion modelling is not straightforward. Finally, another topic which would require further exploration is the entrained bubble turbulence. The flow characteristics at the inception point are difficult to determine but might play a major role in the overall

behaviour of a system.

Finally, another topic which might need further investigation is the modelling of non-spherical particles. In industrial applications, solid objects are rarely spherical. Most frequently they are natural compounds which tend to have fibrous geometries instead. Since the approaches explored during the thesis are limited to spherical particles, more work is needed to extend the capabilities towards fibrous solid inclusions. It could be possible, in the Lagrangian framework to consider several point particles for each fiber and to include a new interaction force between them. This has not been done and would require extensive modelling and validation.

From a long-term point of view, it seems that particle resolved direct numerical simulations will overcome all of the challenges faced during the thesis. The transition from resolved to unresolved interfaces does not exist since all relevant structures are resolved and every particle and the flow around it is simulated removing the need for specific modelling. Unfortunately, even if available computing capabilities increases to the point where such simulations are possible, the power needed to run such simulations at an industrial scale will be enormous. Therefore, developing models to increase the scope of current simulation frameworks and reduce their computing time will always be necessary. Specifically for industrial applications.

Bibliography

[1] Aguinaga, S., Simonin, O., Borée, J. and Herbert, V. (2009), A lagrangian stochastic model for droplet deposition simulations in connection with wall function approaches, *in* 'Proceedings of the ASME Fluids Engineering Division Summer Conference 2009, FEDSM2009', Vol. 1, pp. 795–805.

[2] Arcen, B. and Tanière, A. (2009), 'Simulation of a particle-laden turbulent channel flow using an improved stochastic lagrangian model', *Physics of Fluids* **21**.

[3] Ashgriz, N. (2011), *Handbook of atomization and sprays: theory and applications*, Springer Science & Business Media.

[4] Bahlali, M. L., Henry, C. and Carissimo, B. (2020), 'On the well-mixed condition and consistency issues in hybrid eulerian/lagrangian stochastic models of dispersion', *Boundary-Layer Meteorology* **174**, 275–296.

[5] Balachandar, S. and Eaton, J. K. (2010), 'Turbulent dispersed multiphase flow'.

[6] Baltussen, M., Kuipers, J. and Deen, N. (2017), 'Direct numerical simulation of effective drag in dense gas–liquid–solid three-phase flows', *Chemical Engineering Science* **158**, 561–568.

[7] Basha, O. M., Sehabiague, L., Abdel-Wahab, A. and Morsi, B. I. (2015), 'Fischer–tropsch synthesis in slurry bubble column reactors: experimental investigations and modeling–a review', *International Journal of Chemical Reactor Engineering* **13**(3), 201–288.

[8] Batchelor, G. K. (2000), *An Introduction to Fluid Dynamics*, Cambridge Mathematical Library, Cambridge University Press.

[9] Baumgarten, C. (2006), *Mixture formation in internal combustion engines*, Springer Science & Business Media.

[10] Belden, J., Ravela, S., Truscott, T. T. and Techet, A. H. (2012), 'Three-dimensional bubble field resolution using synthetic aperture imaging: Application to a plunging jet', *Experiments in Fluids* **53**, 839–861.

[11] Bertola, N., Wang, H. and Chanson, H. (2018), 'A physical study of air–water flow in planar plunging water jet with large inflow distance', *International Journal of Multiphase Flow* **100**, 155–171.

[12] Bin, A. K. (1993), 'Gas entrainment by plunging liquid jets', *Chemical Engineering Science* **48**, 3585–3630.

[13] Blenkinsopp, C. and Chaplin, J. (2007), 'Void fraction measurements in breaking waves', *Proceedings of the Royal Society A: Mathematical, Physical and Engineering Sciences* **463**(2088), 3151–3170.

[14] Bocksell, T. L. and Loth, E. (2006), 'Stochastic modeling of particle diffusion in a turbulent boundary layer', *International Journal of Multiphase Flow* **32**, 1234–1253.

[15] Boualouache, A., Kendil, F. Z. and Mataoui, A. (2017), 'Numerical assessment of two phase flow modeling using plunging jet configurations', *Chemical Engineering Research and Design* **128**, 248–256.

[16] Boutsikakis, A., Fede, P. and Simonin, O. (2022), 'Effect of electrostatic forces on the dispersion of like-charged solid particles transported by homogeneous isotropic turbulence', *Journal of Fluid Mechanics* **938**.

[17] Brocchini, M. and Peregrine, D. H. (2001*a*), 'The dynamics of strong turbulence at free surfaces. part 1. description', *Journal of Fluid Mechanics* **449**, 225–254.

[18] Brocchini, M. and Peregrine, D. H. (2001*b*), 'The dynamics of strong turbulence at free surfaces. part 2. free-surface boundary conditions', *Journal of Fluid Mechanics* **449**, 255–290.

[19] Capecelatro, J. and Desjardins, O. (2013), 'An euler–lagrange strategy for simulating particle-laden flows', *Journal of Computational Physics* **238**, 1–31.

[20] Carrica, P., Drew, D., Bonetto, F. and Lahey, R. (1999), 'A polydisperse model for bubbly two-phase flow around a surface ship', *International Journal of Multiphase Flow* **25**(2), 257–305.

[21] Carrillo, J. M., Castillo, L. G., Marco, F. and García, J. T. (2020), 'Experimental and numerical analysis of two-phase flows in plunge pools', *Journal of Hydraulic Engineering* **146**, 04020044.

[22] Carrillo, J. M., Marco, F., Castillo, L. G. and García, J. T. (2020), Analysis of two-phase flows in plunge pools of nappe jets, *in* 'Proceedings of the 8th IAHR International Symposium on Hydraulic Structures, ISHS 2020', University of Queensland.

[23] Carrillo, J. M., Marco, F., Castillo, L. G. and García, J. T. (2021), 'Experimental study of submerged hydraulic jumps generated downstream of rectangular plunging jets', *International Journal of Multiphase Flow* p. 103579.

[24] Carrillo, J. M., Ortega, P. R., Castillo, L. G. and García, J. T. (2020), 'Experimental characterization of air entrainment in rectangular free falling jets', *Water (Switzerland)* **12**.

[25] Cartellier, A. and Achard, J. (1991), 'Local phase detection probes in fluid/fluid two-phase flows', *Review of Scientific Instruments* **62**(2), 279–303.

[26] Castillo, L. G., Carrillo, J. M. and Blázquez, A. (2015), 'Plunge pool dynamic pressures: A temporal analysis in the nappe flow case', *Journal of Hydraulic Research* **53**, 101–118.

[27] Castillo, L. G., Carrillo, J. M. and Álvaro Sordo-Ward (2014), 'Simulation of overflow nappe impingement jets', *Journal of Hydroinformatics* **16**, 922–940.

[28] Castro, A. M., Li, J. and Carrica, P. M. (2016), 'A mechanistic model of bubble entrainment in turbulent free surface flows', *International Journal of Multiphase Flow* **86**, 35–55.

[29] Cazarez, O., Montoya, D., Vital, A. and Bannwart, A. (2010), 'Modeling of three-phase heavy oil–water–gas bubbly flow in upward vertical pipes', *International Journal of Multiphase Flow* **36**(6), 439–448.

[30] Champagne, F., Pao, Y. and Wygnanski, I. (1976), 'On the two-dimensional mixing region', *Journal of Fluid Mechanics* **74**, 209–250.

[31] Chan, T. T. K., Ng, C. S. and Krug, D. (2022), 'Bubble-particle collisions in turbulence: insights from point-particle simulations', *arXiv* .

[32] Chanson, H. (2009), 'Turbulent air-water flows in hydraulic structures: Dynamic similarity and scale effects', *Environmental Fluid Mechanics* **9**, 125–142.

[33] Chanson, H. and Cummings, P. (1992), 'Aeration of the ocean due to plunging breaking waves'.

[34] Chieng, C.-C. and Launder, B. E. (1980), 'On the calculation of turbulent heat transport downstream from an abrupt pipe expansion', *Numerical Heat Transfer Part A-applications* **3**, 189–207.

[35] Clanet, C. and Lasheras, J. C. (1997), 'Depth of penetration of bubbles entrained by a plunging water jet', *Physics of Fluids* **9**, 1864–1866.

[36] Coste, P. (2013), 'A large interface model for two-phase cfd', *Nuclear Engineering and Design* **255**, 38–50.

[37] Coste, P. and Laviéville, J. (2015), 'A turbulence model for large interfaces in high reynolds two-phase cfd', *Nuclear Engineering and Design* **284**, 162–175.

[38] Couturier, J. (2004), *État des recherches dans le domaine de la sûreté des réacteurs à eau sous pression*, IRSN, chapter 5.

[39] Csanady, G. (1963), 'Turbulent diffusion of heavy particles in the atmosphere', *Journal of Atmospheric Sciences* **20**(3), 201–208.

[40] Dai, Z., Fornasiero, D. and Ralston, J. (2000), 'Particle bubble collision models a review', *Advaces in colloid and interface science* **85**, 231–256.

[41] Dalrymple, R. A. and Rogers, B. D. (2006), 'Numerical modeling of water waves with the sph method', *Coastal engineering* **53**(2-3), 141–147.

[42] Daly, B. J. and Harlow, F. H. (1970), 'Transport equations in turbulence', *The physics of fluids* **13**(11), 2634–2649.

[43] Davidson, J. (1960), 'Bubble formation at an orifice in an inviscid liquid', *Trans. Inst. Chem. Eng.* **38**, 335–342.

[44] Davoust, L., Achard, J.-L., Hammoumi, M. E., El, M., Davoust, L. and Achard, J. L. (2002), 'Air entrainment by a plunging jet: the dynamical roughness concept and its estimation by a light absorption technique', *International Journal of Multiphase Flow* .

[45] De Padova, D., Mossa, M., Sibilla, S. and Torti, E. (2013), '3d sph modelling of hydraulic jump in a very large channel', *Journal of Hydraulic Research* **51**(2), 158–173.

[46] De Santis, A., Colombo, M., Hanson, B. and Fairweather, M. (2021), 'A generalized multiphase modelling approach for multiscale flows', *Journal of Computational Physics* **436**, 110321.

[47] De Santis, A., Hanson, B. and Fairweather, M. (2021), 'Hydrodynamics of annular centrifugal contactors: A cfd analysis using a novel multiphase flow modelling approach', *Chemical Engineering Science* **242**, 116729.

[48] Deane, G. B. and Stokes, M. D. (2002), 'Scale dependence of bubble creation mechanisms in breaking waves', *nature* **418**.

[49] Dehbi, A. (2008), 'Turbulent particle dispersion in arbitrary wall-bounded geometries: A coupled cfd-langevin-equation based approach', *International Journal of Multiphase Flow* **34**, 819–828.

[50] Deike, L., Melville, W. K. and Popinet, S. (2016), 'Air entrainment and bubble statistics in breaking waves', *Journal of Fluid Mechanics* **801**, 91–129.

[51] Delhaye, J. (1974), 'Jump conditions and entropy sources in two-phase systems. local instant formulation', *International Journal of Multiphase Flow* **1**(3), 395–409.

[52] Derakhti, M. and Kirby, J. T. (2014), 'Bubble entrainment and liquid–bubble interaction under unsteady breaking waves', *Journal of fluid mechanics* **761**, 464–506.

[53] Desjonqueres, P., Gouesbet, G., Berlemont, A. and Picart, A. (1986), 'Dispersion of discrete particles by continuous turbulent motions: new results and discussions.', *Physics of Fluids* **29**(7 , Jul. 1986), 2147–2151.

[54] Donk, J. A. C. V. D. (1981), *Water aeration with plunging jets*, Dutch Efficiency Bureau.

[55] Duduković, M. P., Larachi, F. and Mills, P. L. (2002), 'Multiphase catalytic reactors: a perspective on current knowledge and future trends', *Catalysis reviews* **44**(1), 123–246.

[56] Dukhin, S., Kretzschmar, G. and Miller, R. (1995), *Dynamics of adsorption at liquid interfaces*, Elsevier.

[57] Eaton, J. K. (2009), 'Two-way coupled turbulence simulations of gas-particle flows using point-particle tracking', *International Journal of Multiphase Flow* **35**(9), 792–800.

[58] Elghobashi, S. (1994), 'Elghobashi, s.: On predicting particle-laden turbulent flows. applied scientific research 52, 309-329', *Applied Scientific Research* **52**, 309–329.

[59] Enright, D., Fedkiw, R., Ferziger, J. and Mitchell, I. (2002), 'A hybrid particle level set method for improved interface capturing', *Journal of Computational Physics* **183**(1), 83–116.

[60] Ergun, S. (1952), 'Fluid flow through packed columns', *Chemical Engineering Progesses* **2**, 89–94.

[61] Essadki, M., Drui, F., Chaisemartin, S. D., Larat, A., Ménard, T., Massot, M., Mohamed, E., Florence, D., Stéphane, C., Adam, L., Thibault, M. and Marc, M. (2019), 'Statistical modeling of the gas-liquid interface using geometrical variables: toward a unified description of the disperse and separated phase flows'.

[62] Evans, G. M., Jameson, G. J. and Atkinson, B. W. (1992), 'Prediction of the bubble size generated by a plunging liquid jet bubble column', *Chemical Engineering Science* **47**, 3265–3272.

[63] Fonty, T. (2019), 'Modélisation de l'entraînement d'air dans l'eau avec la méthode sph'.

[64] Fuster, D., Agbaglah, G., Josserand, C., Popinet, S. and Zaleski, S. (2009), 'Numerical simulation of droplets, bubbles and waves: state of the art', *Fluid dynamics research* **41**(6), 065001.

[65] Gai, G., Hadjadj, A., Kudriakov, S. and Thomine, O. (2020), 'Particles-induced turbulence: A critical review of physical concepts, numerical modelings and experimental investigations', *Theoretical and Applied Mechanics Letters* **10**, 241–248.

[66] Gandhi, B., Prakash, A. and Bergougnou, M. A. (1999), 'Hydrodynamic behavior of slurry bubble column at high solids concentrations'.

[67] Garrett, C., Li, M. and Farmer, D. (2000), 'The connection between bubble size spectra and energy dissipation rates in the upper ocean', *Journal of Physical Oceanography* **30**, 2163–2171.

[68] Gatignol, R. (1983), 'The faxén formulae for a rigid particle in an unsteady non-uniform stokes flow', *Journal de Mécanique Théorique Appliquée* **1**, 143–160.

[69] Gidaspow, D. (1994), *Multiphase flow fluidization*, Elsevier, Academic Press, New York.

[70] Gidaspow, D., Bezburuah, R. and Ding, J. (1991), Hydrodynamics of circulating fluidized beds: Kinetic theory approach, *in* '7th international conference on fluidization', Goald Coast (Australia).

[71] Gonzalez, C. A. and Chanson, H. (2007), 'Hydraulic design of stepped spillways and downstream energy dissipators for embankment dams', *Dam Engineering* **17**(4), 223–244.

[72] Gosman, A. D. and loannides, E. (1983), 'Aspects of computer simulation of liquid-fueled combustors', *Journal of Energy* **7**(6), 482–490.

[73] Gourdel, C., Simonin, O. and Brunier, E. (2000), 'Two-maxwellian equilibrium distribution function for the modelling of a binary mixture of particles'.

[74] Grad, H. (1949), 'On the kinetic theory of rarefied gases', *Communications on Pure and Applied Mathematics* **2**(4), 331–407.

[75] Guimet, V. and Laurence, D. (2002), A linearised turbulent production in the k-ϵ model for engineering applications, *in* W. Rodi and N. Fueyo, eds, 'Engineering Turbulence Modelling and Experiments 5', Elsevier Science Ltd, Oxford, pp. 157–166.

[76] Guingo, M. and Minier, J. P. (2008), 'A stochastic model of coherent structures for particle deposition in turbulent flows', *Physics of Fluids* **20**.

[77] Guo, B., Xiao, Y., Rai, A. K., Liang, Q. and Liu, J. (2021), 'Analysis of the air-water-sediment flow behavior in pelton buckets using a eulerian-lagrangian approach', *Energy* **218**.

[78] Guyot, G., Rodriguez, M., Pfister, M., Matas, J.-P. and Cartellier, A. H. (2020), 'Experimental study of large scale plunging jets', *PhD* .

[79] Hanjalić, K. and Launder, B. E. (1972), 'A reynolds stress model of turbulence and its application to thin shear flows', *Journal of Fluid Mechanics* **52**(4), 609–638.

[80] Hardy, B., Simonin, O., Wilde, J. D. and Winckelmans, G. (2022), 'Simulation of the flow past random arrays of spherical particles: Microstructure-based tensor quantities as a tool to predict fluid–particle forces', *International Journal of Multiphase Flow* **149**.

[81] Harlow, F. H. and Welch, J. E. (1965), 'Numerical Calculation of Time-Dependent Viscous Incompressible Flow of Fluid with Free Surface', *Physics of Fluids* **8**(12), 2182–2189.

[82] Haworth, D. C. and Pope, S. B. (1986), 'A generalized langevin model for turbulent flows.', *Physics of Fluids* **29**, 387–405.

[83] Hinze, J. O. (1955), 'Fundamentals of the hydrodynamic mechanism of splitting in dispersion processes', *AIChE journal* **1**(3), 289–295.

[84] Hinze, J. O. (1959), *Turbulence: An introduction to its mechanism and theory*, McGraw Hill, New York.

[85] Hirt, C. and Nichols, B. (1981), 'Volume of fluid (vof) method for the dynamics of free boundaries', *Journal of Computational Physics* **39**(1), 201–225.

[86] Hoomans, B. P. B., Kuipers, J. A. M., Briels, W. J. and van Swaaij, W. P. M. (1996), 'Discrete particle simulation of bubble and slug formation in a two-dimensional gas-fluidised bed: A hard-sphere approach', *Chemical Engineering Science* **51**(1), 99–118.

[87] Horne, W. J. and Mahesh, K. (2019), 'A massively-parallel, unstructured overset method for mesh connectivity', *J. Comput. Phys.* **376**, 585–596.

[88] Hu, H. H., Patankar, N. and Zhu, M. (2001), 'Direct numerical simulations of fluid–solid systems using the arbitrary lagrangian–eulerian technique', *Journal of Computational Physics* **169**(2), 427–462.

[89] Hänsch, S., Lucas, D., Krepper, E. and Höhne, T. (2012), 'A multi-field two-fluid concept for transitions between different scales of interfacial structures', *International Journal of Multiphase Flow* **47**, 171–182.

[90] Iguchi, M., Okita, K. and Yamamoto, F. (1998), 'Mean velocity and turbulence characteristics of water flow in the bubble dispersion region induced by plunging water jet'.

[91] Iliopoulos, I., Mito, Y. and Hanratty, T. J. (2003), 'A stochastic model for solid particle dispersion in a nonhomogeneous turbulent field', *International Journal of Multiphase Flow* **29**(3), 375–394.

[92] Ishii, M. and Hibiki, T. (2011), *Thermo-fluid dynamics of two-phase flow (Second edition)*, Springer New York.

[93] Ishii, M. and Zuber, N. (1979), 'Drag coefficient and relative velocity in bubbly, droplet or particulate flows', *AIChE Journal* **25**(5), 843–855.

[94] Jackson, R. (2000), *The dynamics of fluidized particles*, Cambridge University Press.

[95] Jianping Wen, P. L. and Huang, L. (2005), 'Modeling and simulation of gas-liquid-solid three-phase fluidization', *Chemical Engineering Communications* **192**(7), 941–955.

[96] Johnson, C. A., Solomon, E., Rubin, L. C., Gerster, J. A., Colburn, A. P., Wohl, K., l Wang, Y., Eng, Z., Wen, C. Y. and Yu, Y. H. (1953), 'A generalized method for predicting the minimum fluidization velocity', *Wohl, K., Trans. Am. Inst. Chem. Eng* **47**, 271–272.

[97] Kara, S., Kelkar, B. G., Shah, Y. T. and Carr, N. L. (1982), 'Hydrodynamics and axial mixing in a three-phase bubble column', *Industrial & Engineering Chemistry Process Design and Development* **21**(4), 584–594.

[98] Kasper, R., Turnow, J. and Kornev, N. (2019), 'Multiphase eulerian–lagrangian les of particulate fouling on structured heat transfer surfaces', *International Journal of Heat and Fluid Flow* **79**.

[99] Kataoka, I. (1985), 'Local instant formulation of two-phase flow', *International journal of multiphase flows* **12**, 745–758.

[100] Kendil, F. Z., Danciu, D. V., Schmidtke, M., Salah, A. B., Lucas, D., Krepper, E. and Mataoui, A. (2012), 'Flow field assessment under a plunging liquid jet', *Progress in Nuclear Energy* **56**, 100–110.

[101] Khezzar, L., Kharoua, N. and Kiger, K. T. (2015), 'Large eddy simulation of rough and smooth liquid plunging jet processes', *Progress in Nuclear Energy* **85**, 140–155.

[102] Kiger, K. T. and Duncan, J. H. (2011), 'Air-entrainment mechanisms in plunging jets and breaking waves', *Annual Review of Fluid Mechanics* **44**, 563–596.

[103] Kihara, K. and Okada, N. (2023), 'Numerical simulation model of gas–liquid–solid flows with gas–liquid free surface and solid-particle flows', *Chemical Engineering Science* **270**.

[104] Kim, S. H. and Pitsch, D. H. (2009), 'On the lattice boltzmann method for multiphase flows', *Annual research briefs* pp. 377–388.

[105] Kim, S., Ishii, M., Kong, R. and Wang, G. (2021), 'Progress in two-phase flow modeling: Interfacial area transport', *Nuclear Engineering and Design* **373**, 111019.

[106] King, J., Lind, S., Rogers, B., Stansby, P. and Vacondio, R. (2023), 'Large eddy simulations of bubbly flows and breaking waves with smoothed particle hydrodynamics', *Journal of Fluid Mechanics* **972**.

[107] Kolmogorov, A. (1949), On the breakage of drops in a turbulent flow, *in* 'Dokl. Akad. Navk. SSSR', Vol. 66, pp. 825–828.

[108] Kramer, M., Wieprecht, S. and Terheiden, K. (2016), 'Penetration depth of plunging liquid jets - a data driven modelling approach', *Experimental Thermal and Fluid Science* **76**, 109–117.

[109] Kuang, S., Chu, K., Yu, A. and Vince, A. (2012), 'Numerical study of liquid–gas–solid flow in classifying hydrocyclones: Effect of feed solids concentration', *Minerals Engineering* **31**, 17–31.

[110] Kuczaj, A. K. and Geurts, B. J. (2006), 'Mixing in manipulated turbulence', *Journal of Turbulence* .

[111] Kuerten, J. G. M. (2016), 'Point-particle dns and les of particle-laden turbulent flow - a state-of-the-art review', *Flow, Turbulence and Combustion* **97**, 689 – 713.

[112] Lahey Jr, R. T. (2009), 'On the direct numerical simulation of two-phase flows', *Nuclear engineering and design* **239**(5), 867–879.

[113] Lahey, R. T. (1991), 'An experimental study of plunging liquid jet induced air carryunder and dispersion'.

[114] Lang, S. (2002), *Algebra*, Springer.

[115] Langmuir, I. and Blodgett, K. (1946), *A mathematical investigation of water droplet trajectories*, Army Air Forces Headquarters, Air Technical Service Command.

[116] Launder, B. E. and Spalding, D. B. (1974), 'The numerical computation of turbulent flows', *Computer Methods in Applied Mechanics and Engineering* **3**, 269–289.

[117] Lavieville, J., Simonin, O., Berlemont, A. and Chang, Z. (1997), Validation of inter-particle collision models based on large eddy simulation in gas-solid turbulent homogeneous shear flow, *in* 'ASME Fluids engineering division summer meeting'.

[118] Laviéville, J., Mérigoux, N., Guingo, M., Baudry, C. and Mimouni, S. (2017), 'A generalized turbulent dispersion model for bubbly flow numerical simulation in neptune_cfd', *Nuclear Engineering and Design* **312**, 284–293.

[119] Lee, C.-H., Huang, Z. and Chiew, Y.-M. (2015), 'A three-dimensional continuum model incorporating static and kinetic effects for granular flows with applications to collapse of a two-dimensional granular column', *Physics of Fluids* **27**(11).

[120] Li, W. and Zhong, W. (2015), 'CFD simulation of hydrodynamics of gas-liquid-solid three-phase bubble column', *Powder Technology* **286**, 766–788.

[121] Li, W., Zhong, W., Jin, B., Lu, Y. and He, T. (2014), 'Flow patterns and transitions in a rectangular three-phase bubble column', *Powder Technology* **260**, 27–35.

[122] Li, Y., Zhang, J. and Fan, L.-S. (1999), 'Numerical simulation of gas–liquid–solid fluidization systems using a combined cfd-vof-dpm method: bubble wake behavior', *Chemical Engineering Science* **54**(21), 5101–5107.

[123] Liu, X. and Duncan, J. H. (2003), 'The effects of surfactants on spilling breaking waves', *Nature* **421**(6922), 520–523.

[124] Liu, Y., Jiang, L. and Zhang, Y. (2021), 'Hydrodynamic modeling of turbulence modulation by particles in a swirling gas-particle two-phase flow', *ACS Omega* **6**, 10106–10118.

[125] Loudet, J. C., Qiu, M., Hemauer, J. and Feng, J. (2020), 'Drag force on a particle straddling a fluid interface: Influence of interfacial deformations', *European Physical Journal E: Soft matter and biological physics* **43**(2).

[126] Luo, H. and Svendsen, H. F. (1996), 'Theoretical model for drop and bubble breakup in turbulent dispersions', *AIChE Journal* **42**(5), 1225–1233.

[127] Ma, J., Oberai, A. A., Drew, D. A., Lahey, R. T. and Hyman, M. C. (2011), 'A comprehensive sub-grid air entrainment model for rans modeling of free-surface bubbly flows', *Journal of Computational Multiphase Flows* **3**, 41–56.

[128] Ma, J., Oberai, A. A., Drew, D. A., Lahey, R. T. and Moraga, F. J. (2010), 'A quantitative sub-grid air entrainment model for bubbly flows - plunging jets', *Computers and Fluids* **39**, 77–86.

[129] Magnaudet, J., Mercier, M. and Mercier, M. J. (2020), 'Particles, drops, and bubbles moving across sharp interfaces and stratified layers', *Annual Review of Fluid Mechanics* **52**, 61–91.

[130] Malgarinos, I., Nikolopoulos, N. and Gavaises, M. (2016), 'A numerical study on droplet-particle collision dynamics', *International Journal of Heat and Fluid Flow* **61**, 499–509.

[131] Manceau, R. and Hanjalic, K. (2002), 'Elliptic blending model: A new near-wall reynolds-stress turbulence closure', *Physics of Fluids* **14**, 744–754.

[132] Manga, M. and Stone, H. A. (1995), 'Low reynolds number motion of bubbles, drops and rigid spheres through fluid–fluid interfaces', *Journal of Fluid Mechanics* **287**, 279–298.

[133] Marchioli, C. and Soldati, A. (2002), 'Mechanisms for particle transfer and segregation in a turbulent boundary layer', *Journal of Fluid Mechanics* **468**, 283–315.

[134] Mathur, A., Dovizio, D., Frederix, E. M. and Komen, E. M. (2019), 'A hybrid dispersed-large interface solver for multi-scale two-phase flow modelling', *Nuclear Engineering and Design* **344**, 69–82.

[135] Maxey, M. R. and Riley, J. J. (1983), 'Equation of motion for a small rigid sphere in a nonuniform flow', *The Physics of Fluids* **26**(4), 883–889.

[136] Mimouni, S., Laviéville, J., Seiler, N. and Ruyer, P. (2011), 'Combined evaluation of second order turbulence model and polydispersion model for two-phase boiling flow and application to fuel assembly analysis', *Nuclear Engineering Design* .

[137] Minier, J. P., Chibbaro, S. and Pope, S. B. (2014), 'Guidelines for the formulation of lagrangian stochastic models for particle simulations of single-phase and dispersed two-phase turbulent flows', *Physics of Fluids* **26**.

[138] Minier, J.-P. and Peirano, E. (2001), 'The pdf approach to turbulent polydispersed two-phase flows'.

[139] Miwa, S., Moribe, T., Tsutstumi, K. and Hibiki, T. (2018), 'Experimental investigation of air entrainment by vertical plunging liquid jet', *Chemical Engineering Science* **181**, 251–263.

[140] Monaghan, J. J. and Kocharyan, A. (1995), 'Sph simulation of multi-phase flow', *Computer Physics Communications* **87**, 225–235.

[141] Monin, A. S. and Yaglom, A. M. (1971), *Statistical Fluid Mechanics: The Mechanics of Turbulence*, Vol. 1, M.I.T. Press.

[142] Montoya, G., Lucas, D., Krepper, E., Hänsch, S. and Baglietto, E. (2014), 'Analysis and applications of a generalized multi-field two-fluid approach for treatment of multi-scale interfacial structures in high void-fraction regimes'.

[143] Moraga, F. J., Carrica, P. M., Drew, D. A. and Lahey, R. T. (2008), 'A sub-grid air entrainment model for breaking bow waves and naval surface ships', *Computers and Fluids* **37**, 281–298.

[144] Morel, C., Ruyer, P., Seiler, N. and Laviéville, J. M. (2010), 'Comparison of several models for multi-size bubbly flows on an adiabatic experiment', *International Journal of Multiphase Flow* **36**, 25–39.

[145] Mostert, W., Popinet, S. and Deike, L. (2022), 'High-resolution direct simulation of deep water breaking waves: Transition to turbulence, bubbles and droplets production', *Journal of Fluid Mechanics* **942**.

[146] Mou, T. (1947), 'Mean value and correlation problems connected with the motion of small particles suspended in a turbulent fluid'.

[147] Muroyama, K. and Fan, L.-S. (1985), 'Fundamentals of gas-liquid-solid fluidization', *AIChE Journal* **31**(1), 1–34.

[148] Murzyn, F., Mouaze, D. and Chaplin, J. R. (2005), 'Optical fibre probe measurements of bubbly flow in hydraulic jumps', *International Journal of Multiphase Flow* **31**, 141–154.

[149] Mérigoux, N. (2022), 'Multiphase eulerian-eulerian cfd supporting the nuclear safety demonstration', *Nuclear Engineering and Design* **397**.

[150] Nerisson, P. (2009), 'Modélisation du transfert des aérosols dans un local ventilé'.

[151] Nones, M. (2019), 'Dealing with sediment transport in flood risk management', *Acta Geophysica* **67**, 677–685.

[152] Obukhov, A. M. (1959), 'Description of turbulence in terms of lagrangian variables', *Advances in Geophysics* **6**, 113–116.

[153] Ohl, C. D., uz, H. N. O. and Prosperetti, A. (2000), 'Mechanism of air entrainment by a disturbed liquid jet', *Physics of Fluids* **12**, 1710–1714.

[154] Ojima, S., Hayashi, K. and Tomiyama, A. (2014), 'Effects of hydrophilic particles on bubbly flow in slurry bubble column', *International Journal of Multiphase Flow* **58**, 154–167.

[155] Pan, H., Chen, X. Z., Liang, X. F., Zhu, L. T. and Luo, Z. H. (2016), 'Cfd simulations of gas-liquid-solid flow in fluidized bed reactors - a review'.

[156] Panneerselvam, R., Savithri, S. and Surender, G. D. (2009), 'Cfd simulation of hydrodynamics of gas-liquid-solid fluidised bed reactor', *Chemical Engineering Science* **64**, 1119–1135.

[157] Paola, C. and Voller, V. R. (2005), 'A generalized exner equation for sediment mass balance', *Journal of Geophysical Research: Earth Surface* **110**(F4).

[158] Picano, F., Breugem, W.-P. and Brandt, L. (2015), 'Turbulent channel flow of dense suspensions of neutrally buoyant spheres', *Journal of Fluid Mechanics* **764**, 463–487.

[159] Pierson, J. L. and Magnaudet, J. (2018*a*), 'Inertial settling of a sphere through an interface. part 1. from sphere flotation to wake fragmentation', *Journal of Fluid Mechanics* **835**, 762–807.

[160] Pierson, J. L. and Magnaudet, J. (2018*b*), 'Inertial settling of a sphere through an interface. part 2. sphere and tail dynamics', *Journal of Fluid Mechanics* **835**, 808–851.

[161] Pope, S. B. (2000), *Turbulent flows*, Cambridge University Press.

[162] Popinet, S. (2015), 'A quadtree-adaptive multigrid solver for the serre–green–naghdi equations', *Journal of Computational Physics* **302**, 336–358.

[163] Prince, M. J. and Blanch, H. W. (1990), 'Bubble coalescence and break-up in air-sparged bubble columns', *AIChE Journal* **36**(10), 1485–1499.

[164] Qu, X. L., Khezzar, L., Danciu, D., Labois, M. and Lakehal, D. (2011), 'Characterization of plunging liquid jets: A combined experimental and numerical investigation', *International Journal of Multiphase Flow* **37**, 722–731.

[165] Reeks, M. W. (1991), 'On a kinetic equation for the transport of particles in turbulent flows', *Physics of Fluids A* **3**, 446–456.

[166] Reynolds, A. M. (1999), 'A second-order lagrangian stochastic model for particle trajectories in inhomogeneous turbulence', *Quarterly Journal of the Royal Meteorological Society* **125**(557), 1735–1746.

[167] Reynolds, A. M. and Cohen, J. E. (2002), 'Stochastic simulation of heavy-particle trajectories in turbulent flows', *Physics of Fluids* **14**, 342–351.

[168] Riou, X. (2002), 'Contribution à la modélisation de l'aire interfaciale en écoulement gaz-liquide en conduite'.

[169] Risso, F. and Fabre, J. (1998), 'Oscillations and breakup of a bubble immersed in a turbulent field', *Journal of Fluid Mechanics* **372**, 323–355.

[170] Roy, A. K., Maiti, B. and Das, P. K. (2013), Visualisation of air entrainment by a plunging jet, *in* '5th BSME International Conference on Thermal Engineering', Vol. 56, Elsevier Ltd, pp. 468–473.

[171] Ruyer, P. (2007), A bubble size distribution model for the numerical simulation of bubbly flows, *in* 'Proceedings of the 6th International Conference on Multiphase Flows', Elsevier, Leipzig (Germany).

[172] Sato, Y., Sadatomi, M. and Sekoguchi, K. (1981), 'Momentum and heat transfer in two-phase bubble flow—i. theory', *International Journal of Multiphase Flow* **7**(2), 167–177.

[173] Schulze, H. (1989), 'Hydrodynamics of bubble-mineral particle collisions', *Min. Process. Extractive Metall. Rev.* **5**, 43–76.

[174] Schwartz, L. and Huet, D. (1961), *Méthodes mathématiques pour les sciences physiques: avec le concours de Denise Huet*, Collection enseignement des sciences, Paris.

[175] Sene, K. J. (1988), 'Air entrainment by plunging jets', *Chemical engineering science* **43**, 2615–2623.

[176] Shahbazi, B., Rezai, B. and Koleini, S. M. J. (2010), 'Bubble-particle collision and attachment probability on fine particles flotation', *Chemical Engineering and Processing: Process Intensification* **49**, 622–627.

[177] Shi, W., Yang, J., Li, G., Yang, X., Zong, Y. and Cai, X. (2018), 'Modelling of breakage rate and bubble size distribution in bubble columns accounting for bubble shape variations', *Chemical Engineering Science* **187**, 391–405.

[178] Shotorban, B. and Mashayek, F. (2005), 'Modeling subgrid-scale effects on particles by approximate deconvolution', *Physics of Fluids* **17**(8).

[179] Sikovsky, D. P. (2015), 'Stochastic lagrangian simulation of particle deposition in turbulent channel flows', *Flow, Turbulence and Combustion* **95**, 561–582.

[180] Sikovsky, D. P. (2016), Tensorially invariant normalized langevin model for particle dispersion and deposition in turbulent flows, *in* '9th International Conference on Multiphase Flow', Firenze (Italy).

[181] Simonin, O. (1996), Continuum modeling of dispersed two-phase flows, *in* 'Combustion and turbulence in two-phase flows', von Karman Institue for fluid dynamics, Rhode Saint Genère (Belgium).

[182] Simonin, O. (2000), Statistical and continuum modelling of turbulent reactive particulate flows. part 1: Theoretical derivation of dispersed Eulerian modeling from probability density function kinetic equation, *in* 'Theoretical and experimental modeling of particulate flows', von Karman Institue for fluid dynamics, Rhode Saint Genère (Belgium).

[183] Simonin, O. (2008), 'Développement de conditions aux limites sur la concentration pour la prise en compte du dépôt de particules en écoulement turbulent', IMFT Internal Report.

[184] Simonin, O., Deutsch, E. and Minier, J. R. (1993), 'Eulerian prediction of the fluid/particle correlated motion in turbulent two-phase flows', *Applied Scientific Research* **51**, 275–283.

[185] Sommerfeld, M. (2017), *Numerical Methods for Dispersed Multiphase Flows*, Springer.

[186] Speziale, C. G., Sarkar, S. and Gatski, T. B. (1991), 'Modelling the pressure-strain correlation of turbulence: an invariant dynamical systems approach', *J. Fluid Mech* pp. 245–272.

[187] Sun, L., Masi, E., Simonin, O., Øyvind Langørgen, Saanum, I. and Haugen, N. E. L. (2022), 'Three-dimensional unsteady numerical simulation of a 150 kwth full-loop chemical looping combustion pilot with biomass as fuel: A hydrodynamic investigation', *Chemical Engineering Science* **260**, 117835.

[188] Sun, X. and Sakai, M. (2015), 'Three-dimensional simulation of gas–solid–liquid flows using the dem–vof method', *Chemical Engineering Science* **134**, 531–548.

[189] Sun, X. and Sakai, M. (2016), 'Direct numerical simulation of gas-solid-liquid flows with capillary effects: An application to liquid bridge forces between spherical particles', *Phys. Rev. E* **94**.

[190] Sutherland, K. L. (1948), 'Physical chemistry of flotation. xi. kinetics of the flotation process', *The Journal of Physical and Colloid Chemistry* **52**(2), 394–425.

[191] Swailes, D. C., Sergeev, Y. A. and Parker, A. (1998), 'Chapman-enskog closure approximation in the kinetic theory of dilute turbulent gas-particulate suspensions'.

[192] Tang, Y., Peters, F., Kuipers, H., Kriebitzsch, S. and van der Hoef, M. (2015), 'A new drag correlation from fully resolved simulations of flow past monodisperse static arrays of spheres', *AIChE Journal* **61**(2), 688–698.

[193] Tanière, A., Arcen, B., Oesterlé, B. and Pozorski, J. (2010), 'Study on langevin model parameters of velocity in turbulent shear flows', *Physics of Fluids* **22**.

[194] Tanière, A. and Arcen, B. (2016), 'Overview of existing langevin models formalism for heavy particle dispersion in a turbulent channel flow', *International Journal of Multiphase Flow* **82**, 106–118.

[195] Tenneti, S., Garg, R. and Subramaniam, S. (2011), 'Drag law for monodisperse gas–solid systems using particle-resolved direct numerical simulation of flow past fixed assemblies of spheres', *International Journal of Multiphase Flow* **37**(9), 1072–1092.

[196] Thomson, D. J. (1987), 'Criteria for the selection of stochastic models of particle trajectories in turbulent flows', *J. Fluid Mech* **180**, 529–556.

[197] Tomiyama, A., Kataoka, I., Zun, I. and Sakaguchi, T. (1998), 'Drag coefficients of single bubbles under normal and micro gravity conditions', *JSME International Journal Series B* **41**(2), 472–479.

[198] Tomiyama, A., Sakoda, K., Hayashi, K., Sou, A., Shimada, N. and Hosokawa, S. (2006), 'Modeling and hybrid simulation of bubbly flow', *Multiphase Science and Technology* **18**, 73–110.

[199] Tomiyama, A. and Shimada, N. (2001), 'A numerical method for bubbly flow simulation based on a multi-fluid model', *J. Pressure Vessel Technol.* **123**(4), 510–516.

[200] Tryggvason, G., Bunner, B., Esmaeeli, A., Juric, D., Al-Rawahi, N., Tauber, W., Han, J., Nas, S. and Jan, Y.-J. (2001), 'A front-tracking method for the computations of multiphase flow', *Journal of Computational Physics* **169**(2), 708–759.

[201] Tryggvason, G., Scardovelli, R. and Zaleski, S. (2011), *Direct Numerical Simulations of Gas–Liquid Multiphase Flows*, Cambridge University Press.

[202] Uhlmann, M. (2005), 'An immersed boundary method with direct forcing for the simulation of particulate flows', *Journal of Computational Physics* **209**(2), 448–476.

[203] Unverdi, S. O. and Tryggvason, G. (1992), 'A front-tracking method for viscous, incompressible, multi-fluid flows', *Journal of Computational Physics* **100**(1), 25–37.

[204] Valero, D. and García-Bartual, R. (2016), *Calibration of an Air Entrainment Model for CFD Spillway Applications*, Springer Nature, pp. 571–582.

[205] Valero, D., Viti, N. and Gualtieri, C. (2018), 'Numerical simulation of hydraulic jumps. part 1: Experimental data for modelling performance assessment'.

[206] Van Driest, E. R. (1956), 'On turbulent flow near a wall', *Journal of the Aeronautical Sciences* **23**(11), 1007–1011.

[207] van Sint Annaland, M., Deen, N. and Kuipers, J. (2005), 'Numerical simulation of gas–liquid–solid flows using a combined front tracking and discrete particle method', *Chemical Engineering Science* **60**(22), 6188–6198.

[208] Vella, D. (2015), 'Floating versus sinking', *Annual Review of Fluid Mechanics* **47**, 115–135.

[209] Vermorel, O., Bédat, B., Simonin, O. and Poinsot, T. (2003), 'Numerical study and modelling of turbulence modulation in a particle laden slab flow', *Journal of Turbulence* **4**(1), 025.

[210] Verso, L., van Reeuwijk, M. and Liberzon, A. (2019), 'Transient stratification force on particles crossing a density interface', *International Journal of Multiphase Flow* **121**.

[211] Vilela, V. and de Souza, F. J. (2020), 'A numerical study on droplet-particle collision: Lamella characterization', *Flow, Turbulence and Combustion* **105**, 965–987.

[212] Viti, N., Valero, D. and Gualtieri, C. (2018).

[213] Vreman, A. W. (2016), 'Particle-resolved direct numerical simulation of homogeneous isotropic turbulence modified by small fixed spheres', *Journal of Fluid Mechanics* **796**, 40–85.

[214] Wallis, G. B. (2020), *One-dimensional two-phase flow*, Courier Dover Publications.

[215] Wang, Q. and Squires, K. (1996*a*), 'Large eddy simulation of particle deposition in a vertical turbulent channel flow', *International Journal of Multiphase Flow* **22**(4), 667–683.

[216] Wang, Q. and Squires, K. D. (1996*b*), 'Large eddy simulation of particle-laden turbulent channel flow', *Physics of Fluids* **8**, 1207.

[217] Weber, A., Wolf, S., Becker, N., Märker-Neuhaus, L., Bellanova, P., Brüll, C., Hollert, H., Klopries, E. M., Schüttrumpf, H. and Lehmkuhl, F. (2023), 'The risk may not be limited to flooding: polluted flood sediments pose a human health threat to the unaware public', *Environmental Sciences Europe* **35**.

[218] Wen, C. Y. and Yu, Y. H. (1966), 'A generalized method for predicting the minimum fluidization velocity', *Chemical engineering journal* **12**, 610–612.

[219] Witt, A., Gulliver, J. S. and Shen, L. (2018), 'Numerical investigation of vorticity and bubble clustering in an air entraining hydraulic jump', *Computers and Fluids* **172**, 162–180.

[220] Witt, A., Gulliver, J. and Shen, L. (2015), 'Simulating air entrainment and vortex dynamics in a hydraulic jump', *International Journal of Multiphase Flow* **72**, 165–180.

[221] Xiao, Y., Guo, B., Ahn, S.-H., Luo, Y., Wang, Z., Shi, G. and Li, Y. (2019), 'Slurry flow and erosion prediction in a centrifugal pump after long-term operation', *Energies* **12**(8).

[222] Yang, S.-M., Han, S. P. and Hong, J. J. (1995), 'Capture of Small Particles on a Bubble Collector by Brownian Diffusion and Interception', *Journal of Colloid and Interface Science* **169**(1), 125–134.

[223] Yao, W. and Morel, C. (2004), 'Volumetric interfacial area prediction in upward bubbly two-phase flow', *International Journal of Heat and Mass Transfer* **47**(2), 307–328.

[224] Yeung, P. and Pope, S. (1988), 'An algorithm for tracking fluid particles in numerical simulations of homogeneous turbulence', *Journal of Computational Physics* **79**(2), 373–416.

[225] Young, J. and Leeming, A. (1997), 'A theory of particle deposition in turbulent pipe flow', *J. Fluid Mech* **340**, 129–159.

[226] Zahtila, T., Chan, L., Ooi, A. and Philip, J. (2023), 'Particle transport in a turbulent pipe flow: direct numerical simulations, phenomenological modelling and physical mechanisms', *Journal of Fluid Mechanics* **957**, A1.

[227] Zaichik, L. I. (1999), 'A statistical model of particle transport and heat transfer in turbulent shear flows', *Physics of Fluids* **11**(6), 1521–1534.

[228] Zeren, Z., Bédat, B. and Simonin, O. (2010), 'Lagrangian stochastic modeling of turbulent gas-solid flows with two-way coupling in homogeneous isotropic turbulence lagrangian stochastic modeling of gas-solid flows with two-way coupling', *7th international conference on multiphase flow* .

[229] Zhang, D. Z. and Prosperetti, A. (1994), 'Averaged equations for inviscid disperse two-phase flow', *Journal of Fluid Mechanics* **267**, 185–219.

[230] Zhang, G., Wang, H. and Chanson, H. (2013), 'Turbulence and aeration in hydraulic jumps: Free-surface fluctuation and integral turbulent scale measurements', *Environmental Fluid Mechanics* **13**, 189–204.

[231] Zhang, H., Yin, Z., Chi, W. and Zhang, W. (2023), 'A new eulerian-eulerian-lagrangian solver in openfoam and its application in a three-phase bubble column', *Powder Technology* **426**, 118661.

[232] Zhang, X. and Ahmadi, G. (2005), 'Eulerian–lagrangian simulations of liquid–gas–solid flows in three-phase slurry reactors', *Chemical Engineering Science* **60**(18), 5089–5104.

[233] Zuber, N. (1964), 'On the dispersed two-phase flow in the laminar flow regime.', *Chemical Engineering Science* **19**, 897–917.

A | Variance and covariance equations

In this appendix, we would like to detail a little further how the evolution equations are obtained for the fluid velocity seen and particle velocity variance and fluid-particle covariance. The main goal is to give the reader enough material to be able to reproduce the demonstrations without having to overburden the chapters. Notations are the same as in the chapter 2 and 3. $\mathbf{u_p}$, $\mathbf{u_{f@p}}$ and $\mathbf{u_f}$ are the particle velocity, the fluid velocity seen by the particle and the fluid velocities. From these, the usual fluctuations are defined alongside an averaging operator such that $x = \langle x \rangle + x'' = X + x''$. ψ_p is a moment of the particle density probability function and $\mathbb{C}$ accounts for the effect of collisions, friction and solid pressure. f and g are fluids while p represents the particle phase and $\tau_{p,f}$ is the particle relaxation time if it evolves in phase f. In all the following sections, the increment $x \mapsto \mathrm{d}x$ is computed along the trajectory of a particle. The starting equation is always the same. It is reminded hereafter:

$$\begin{aligned}\frac{\partial}{\partial t}(n_p m_p \langle \psi_p \rangle) + \frac{\partial}{\partial x_j}(n_p m_p \langle u_{p,j} \psi_p \rangle) + n_p m_p \left\langle \langle \frac{\mathrm{d}u_{p,i}}{\mathrm{d}t} | \mathbf{c_p}, \mathbf{c_f} \rangle \frac{\partial \psi_p}{\partial c_{p,j}} \right\rangle \\ + \sum_f n_p m_p \left\langle \langle \frac{\mathrm{d}u_{f@p,i}}{\mathrm{d}t} | \mathbf{c_p}, \mathbf{c_f} \rangle \frac{\partial \psi_p}{\partial c_{f,j}} \right\rangle + n_p \mathbb{C}(m_p u_{p,i}) = 0\end{aligned} \tag{A.1}$$

A.1 Fluid velocity seen variance

As hinted at in chapter 2, to obtain the evolution equation for the fluid velocity seen variance $R_{f@p,ij}$, we need to replace ψ_p by $c_{f,i}c_{f,j}$ in the general moment equation above. By carefully computing the terms on the right-hand side of the equation, this leads to:

$$\begin{aligned}\frac{\partial}{\partial t}(n_p m_p \langle u_{f@p,i} u_{f@p,j} \rangle) + \frac{\partial}{\partial x_k}(n_p m_p \langle u_{f@p,i} u_{f@p,j} u_{p,k} \rangle) = n_p m_p \langle \frac{\mathrm{d}u_{f@p,i}}{\mathrm{d}t} u_{f@p,j} \rangle \\ + n_p m_p \langle \frac{\mathrm{d}u_{f@p,j}}{\mathrm{d}t} u_{f@p,i} \rangle\end{aligned} \tag{A.2}$$

By using the relation $u_{p,k} = U_{p,k} + u''_{p,k}$ in the second term on the left-hand side of the previous equation:

$$\begin{aligned}\frac{\partial}{\partial t}(n_p m_p \langle u_{f@p,i} u_{f@p,j}\rangle) + \frac{\partial}{\partial x_k}(n_p m_p \langle u_{f@p,i} u_{f@p,j}\rangle U_{p,k}) \\ + \frac{\partial}{\partial x_k}(n_p m_p \langle u_{f@p,i} u_{f@p,j} u'_{p,k}\rangle) \\ = n_p m_p \langle \frac{\mathrm{d}u_{f@p,i}}{\mathrm{d}t} u_{f@p,j}\rangle + n_p m_p \langle \frac{\mathrm{d}u_{f@p,j}}{\mathrm{d}t} u_{f@p,i}\rangle\end{aligned} \tag{A.3}$$

By using the relation $u_{f@p,i} = U_{f@p,i} + u''_{f@p,i}$ and the fact that $\langle u''_{f@p,i}\rangle = 0$, the previous equation becomes:

$$\begin{aligned}&\frac{\partial}{\partial t}(n_p m_p R_{f@p,ij}) + \frac{\partial}{\partial x_k}(n_p m_p R_{f@p,ij} U_{p,k}) \\ &+ \frac{\partial}{\partial t}(n_p m_p U_{f@p,i} U_{f@p,j}) + \frac{\partial}{\partial x_k}(n_p m_p U_{f@p,i} U_{f@p,j} U_{p,k}) \\ &+ \frac{\partial}{\partial x_k}(n_p m_p \langle u''_{f@p,i} u''_{f@p,j} u'_{p,k}\rangle) + \frac{\partial}{\partial x_k}(n_p m_p U_{f@p,i} R_{fp,jk}) + \frac{\partial}{\partial x_k}(n_p m_p U_{f@p,j} R_{fp,ik}) \\ &= n_p m_p \left[\langle \frac{\mathrm{d}u_{f@p,i}}{\mathrm{d}t}\rangle U_{f@p,j} + \langle \frac{\mathrm{d}u_{f@p,j}}{\mathrm{d}t}\rangle U_{f@p,i} + \langle \frac{\mathrm{d}u_{f@p,i}}{\mathrm{d}t} u''_{f@p,j}\rangle + \langle \frac{\mathrm{d}u_{f@p,j}}{\mathrm{d}t} u''_{f@p,i}\rangle\right]\end{aligned} \tag{A.4}$$

By expanding the partial derivatives and grouping the terms together, we end up with:

$$\begin{aligned}&\frac{\partial}{\partial t}(n_p m_p R_{f@p,ij}) + \frac{\partial}{\partial x_k}(n_p m_p R_{f@p,ij} U_{p,k}) \\ &+ \frac{\partial}{\partial t}(n_p m_p U_{f@p,i} U_{f@p,j}) + \frac{\partial}{\partial x_k}(n_p m_p U_{f@p,i} U_{f@p,j} U_{p,k}) \\ &= -\frac{\partial}{\partial x_k}(n_p m_p \langle u''_{f@p,i} u''_{f@p,j} u'_{p,k}\rangle) - n_p m_p R_{fp,jk} \frac{\partial U_{f@p,i}}{\partial x_k} - n_p m_p R_{fp,ik} \frac{\partial U_{f@p,j}}{\partial x_k} \\ &+ n_p m_p \langle \frac{\mathrm{d}u_{f@p,i}}{\mathrm{d}t} u''_{f@p,j}\rangle + n_p m_p \langle \frac{\mathrm{d}u_{f@p,j}}{\mathrm{d}t} u''_{f@p,i}\rangle \\ &+ n_p m_p \left[\langle \frac{\mathrm{d}u_{f@p,i}}{\mathrm{d}t}\rangle U_{f@p,j} + \langle \frac{\mathrm{d}u_{f@p,j}}{\mathrm{d}t}\rangle U_{f@p,i}\right] - U_{f@p,i} \frac{\partial n_p m_p R_{fp,jk}}{\partial x_k} - U_{f@p,j} \frac{\partial n_p m_p R_{fp,ik}}{\partial x_k}\end{aligned} \tag{A.5}$$

The terms in red from both side of the previous equation cancel out. This can be shown by writing down the evolution equation for the fluid velocity seen and the particle number. The computation is the same in the two next demonstration so we detail it here:

$$
\begin{aligned}
&n_p m_p \langle \frac{\mathrm{d}u_{f@p,i}}{\mathrm{d}t} U_{f@p,j} \rangle + n_p m_p \langle \frac{\mathrm{d}u_{f@p,j}}{\mathrm{d}t} U_{f@p,i} \rangle = \\
&n_p m_p U_{f@p,i} \frac{\partial U_{f@p,j}}{\partial t} + n_p m_p U_{f@p,i} U_{p,k} \frac{\partial U_{f@p,j}}{\partial x_k} + U_{f@p,i} \frac{\partial n_p m_p R_{fp,jk}}{\partial x_k} \\
&\qquad + \\
&n_p m_p U_{f@p,j} \frac{\partial U_{f@p,i}}{\partial t} + n_p m_p U_{f@p,j} U_{p,k} \frac{\partial U_{f@p,i}}{\partial x_k} + U_{f@p,j} \frac{\partial n_p m_p R_{fp,ik}}{\partial x_k} \\
&\qquad = \\
&\frac{\partial}{\partial t}(n_p m_p U_{f@p,i} U_{f@p,j} \rangle) + \frac{\partial}{\partial x_k}(n_p m_p U_{f@p,i} U_{f@p,j} U_{p,k}) \\
&+ U_{f@p,i} \frac{\partial n_p m_p R_{fp,jk}}{\partial x_k} + U_{f@p,j} \frac{\partial n_p m_p R_{fp,ik}}{\partial x_k}
\end{aligned}
\tag{A.6}
$$

Therefore:

$$
\begin{aligned}
&\frac{\partial}{\partial t}(n_p m_p R_{f@p,ij}) + \frac{\partial}{\partial x_k}(n_p m_p R_{f@p,ij} U_{p,k}) \\
&= -\frac{\partial}{\partial x_k}(n_p m_p \langle u''_{f@p,i} u''_{f@p,j} u'_{p,k} \rangle) - n_p m_p R_{fp,jk} \frac{\partial U_{f@p,i}}{\partial x_k} - n_p m_p R_{fp,ik} \frac{\partial U_{f@p,j}}{\partial x_k} \\
&+ n_p m_p \langle \frac{\mathrm{d}u_{f@p,i}}{\mathrm{d}t} u''_{f@p,j} \rangle + n_p m_p \langle \frac{\mathrm{d}u_{f@p,j}}{\mathrm{d}t} u''_{f@p,i} \rangle
\end{aligned}
\tag{A.7}
$$

Now we can simplify the two last term on the right-hand side of the previous equation with the Langevin type stochastic equation:

$$
\begin{aligned}
n_p m_p \langle \frac{\mathrm{d}u_{f@p,i}}{\mathrm{d}t} u''_{f@p,j} \rangle = {} & n_p m_p R_{fp,ik} \frac{\partial U_{f,j}}{\partial x_k} + n_p m_p R_{fp,jk} \frac{\partial U_{f,i}}{\partial x_k} \\
& + n_p m_p G_{fp,ik} R_{f@p,kj} + n_p m_p G_{fp,jk} R_{f@p,ki} + n_p m_p B_{fp,ik} B_{fp,jk}
\end{aligned}
\tag{A.8}
$$

Notice that the additional parameter H_i introduced in chapter 2 does not appear in the variance evolution equation (also the case in the covariance evolution equations). Its impact is only noticeable in the drift velocity evolution equation. This leads to the final equation:

$$
\begin{aligned}
&\frac{\partial}{\partial t}(n_p m_p R_{f@p,ij}) + \frac{\partial}{\partial x_k}(n_p m_p R_{f@p,ij} U_{p,k}) = -\frac{\partial}{\partial x_k}(n_p m_p \langle u''_{f@p,i} u''_{f@p,j} u'_{p,k} \rangle) \\
&- n_p m_p R_{fp,jk} \frac{\partial V_{f,i}}{\partial x_k} - n_p m_p R_{fp,ik} \frac{\partial V_{f,j}}{\partial x_k} + n_p m_p G_{fp,ik} R_{f@p,kj} + n_p m_p G_{fp,jk} R_{f@p,ki} \\
&+ n_p m_p B_{fp,ik} B_{fp,jk}
\end{aligned}
\tag{A.9}
$$

A.2 Particle velocity variance

To get the evolution equation for the particle velocity variance, we need to replace ψ_p by $c_{p,i} c_{p,j}$ in equation A.1.

$$\frac{\partial}{\partial t}(n_p m_p \langle u_{p,i} u_{p,j} \rangle) + \frac{\partial}{\partial x_k}(n_p m_p \langle u_{p,i} u_{p,j} u_{p,k} \rangle) = n_p m_p \langle \frac{\mathrm{d}u_{p,i}}{\mathrm{d}t} u_{p,j} \rangle + n_p m_p \langle \frac{\mathrm{d}u_{p,j}}{\mathrm{d}t} u_{p,i} \rangle \tag{A.10}$$

By using the relation $u_{p,i} = U_{p,i} + u''_{p,i}$, the previous equation becomes:

$$\begin{aligned} &\frac{\partial}{\partial t}(n_p m_p R_{p,ij}) + \frac{\partial}{\partial x_k}(n_p m_p R_{p,ij} U_{p,k}) + \frac{\partial}{\partial x_k}(n_p m_p \langle u''_{p,i} u''_{p,j} u''_{p,k} \rangle) \\ &+ \frac{\partial}{\partial x_k}(n_p m_p U_{p,i} R_{p,jk}) + \frac{\partial}{\partial x_k}(n_p m_p U_{p,j} R_{p,ik}) \\ &+ \frac{\partial}{\partial t}(n_p m_p U_{p,i} U_{p,j}) + \frac{\partial}{\partial x_k}(n_p m_p U_{p,i} U_{p,j} U_{p,k}) \\ &= n_p m_p \langle \frac{\mathrm{d}u_{p,i}}{\mathrm{d}t} u''_{p,j} \rangle + n_p m_p \langle \frac{\mathrm{d}u_{p,j}}{\mathrm{d}t} u''_{p,i} \rangle \\ &n_p m_p \langle \frac{\mathrm{d}u_{p,i}}{\mathrm{d}t} \rangle U_{p,j} + n_p m_p \langle \frac{\mathrm{d}u_{p,j}}{\mathrm{d}t} \rangle U_{p,i} \end{aligned} \tag{A.11}$$

Again, by developing the derivatives on the second line of the previous equation and transferring them on the right-hand side along with the triple correlation term, we get:

$$\begin{aligned} &\frac{\partial}{\partial t}(n_p m_p R_{p,ij}) + \frac{\partial}{\partial x_k}(n_p m_p R_{p,ij} U_{p,k}) \\ &+ \frac{\partial}{\partial t}(n_p m_p U_{p,i} U_{p,j}) + \frac{\partial}{\partial x_k}(n_p m_p U_{p,i} U_{p,j} U_{p,k}) \\ &= -\frac{\partial}{\partial x_k}(n_p m_p \langle u''_{p,i} u''_{p,j} u''_{p,k} \rangle) - n_p m_p R_{p,jk} \frac{\partial U_{p,i}}{\partial x_k} - n_p m_p R_{p,ik} \frac{\partial U_{p,j}}{\partial x_k} \\ &n_p m_p \langle \frac{\mathrm{d}u_{p,i}}{\mathrm{d}t} u''_{p,j} \rangle + n_p m_p \langle \frac{\mathrm{d}u_{p,j}}{\mathrm{d}t} u''_{p,i} \rangle \\ &n_p m_p \left[\langle \frac{\mathrm{d}u_{p,i}}{\mathrm{d}t} \rangle U_{p,j} + \langle \frac{\mathrm{d}u_{p,j}}{\mathrm{d}t} \rangle U_{p,i} \right] - U_{p,i} \frac{\partial n_p m_p R_{p,jk}}{\partial x_k} - U_{p,j} \frac{\partial n_p m_p R_{p,ik}}{\partial x_k} \end{aligned} \tag{A.12}$$

Then, as in the previous case, the terms in red cancel out. We are left with:

$$\begin{aligned} &\frac{\partial}{\partial t}(n_p m_p R_{p,ij}) + \frac{\partial}{\partial x_k}(n_p m_p R_{p,ij} U_{p,k}) \\ &= -\frac{\partial}{\partial x_k}(n_p m_p \langle u''_{p,i} u''_{p,j} u''_{p,k} \rangle) - n_p m_p R_{p,jk} \frac{\partial U_{p,i}}{\partial x_k} - n_p m_p R_{p,ik} \frac{\partial U_{p,j}}{\partial x_k} \\ &n_p m_p \langle \frac{\mathrm{d}u_{p,i}}{\mathrm{d}t} u''_{p,j} \rangle + n_p m_p \langle \frac{\mathrm{d}u_{p,j}}{\mathrm{d}t} u''_{p,i} \rangle \end{aligned} \tag{A.13}$$

Now we need to compute the two last terms on the right-hand side of this equation. This can be done by considering the particle velocity evolution equation.

$$
\begin{aligned}
n_p m_p \langle \frac{\mathrm{d}u_{p,i}}{\mathrm{d}t} u''_{p,j} \rangle &= n_p m_p \sum_f \frac{\lambda_f}{\tau_{p,f}} \left(R_{fp,ij} - R_{p,ij} \right) \\
&= n_p m_p \left[\left(\sum_f \frac{\lambda_f}{\tau_{p,f}} R_{fp,ij} \right) - \left(\sum_f \frac{\lambda_f}{\tau_{p,f}} \right) R_{p,ij} \right]
\end{aligned}
\tag{A.14}
$$

Thus ending up in the following equation:

$$
\begin{aligned}
&\frac{\partial}{\partial t}(n_p m_p R_{p,ij}) + \frac{\partial}{\partial x_k}(n_p m_p R_{p,ij} U_{p,k}) \\
&= -\frac{\partial}{\partial x_k}(n_p m_p \langle u''_{p,i} u''_{p,j} u''_{p,k} \rangle) - n_p m_p R_{p,jk} \frac{\partial U_{p,i}}{\partial x_k} - n_p m_p R_{p,ik} \frac{\partial U_{p,j}}{\partial x_k} \\
&+ n_p m_p \left[\left(\sum_f \frac{\lambda_f}{\tau_{p,f}} (R_{fp,ij} + R_{fp,ji}) \right) - 2 \left(\sum_f \frac{\lambda_f}{\tau_{p,f}} \right) R_{p,ij} \right]
\end{aligned}
\tag{A.15}
$$

A.3 Fluid seen-particle velocity covariance

Finally, the process is similar with the fluid velocity seen-particle velocity covariance tensor evolution equation. We need to replace ψ_p in equation A.1 by $c_{f,i} c_{p,j}$. This leads to the following relation:

$$
\begin{aligned}
\frac{\partial}{\partial t}(n_p m_p \langle u_{f@p,i} u_{p,j} \rangle) + \frac{\partial}{\partial x_k}(n_p m_p \langle u_{f@p,i} u_{p,j} u_{p,k} \rangle) &= n_p m_p \langle \frac{\mathrm{d}u_{f@p,i}}{\mathrm{d}t} u_{p,j} \rangle \\
&+ n_p m_p \langle \frac{\mathrm{d}u_{p,j}}{\mathrm{d}t} u_{f@p,i} \rangle
\end{aligned}
\tag{A.16}
$$

Then, as in the previous cases, we can use the two relations $u_{f@p,i} = U_{f@p,i} + u''_{f@p,i}$ and $u_{p,i} = U_{p,i} + u''_{p,i}$ to get the following moment equation:

$$
\begin{aligned}
&\frac{\partial}{\partial t}(n_p m_p R_{fp,ij}) + \frac{\partial}{\partial x_k}(n_p m_p R_{fp,ij} U_{p,k}) + \frac{\partial}{\partial x_k}(n_p m_p \langle u''_{f@p,i} u''_{p,j} u''_{p,k} \rangle) \\
&+ \frac{\partial}{\partial x_k}(n_p m_p U_{f@p,i} R_{p,jk}) + \frac{\partial}{\partial x_k}(n_p m_p U_{p,j} R_{fp,ik}) \\
&+ \frac{\partial}{\partial t}(n_p m_p U_{f@p,i} U_{p,j}) + \frac{\partial}{\partial x_k}(n_p m_p U_{f@p,i} U_{p,j} U_{p,k}) \\
&= n_p m_p \langle \frac{\mathrm{d}u_{f@p,i}}{\mathrm{d}t} u''_{p,j} \rangle + n_p m_p \langle \frac{\mathrm{d}u_{p,j}}{\mathrm{d}t} u''_{f@p,i} \rangle \\
&+ n_p m_p \langle \frac{\mathrm{d}u_{f@p,i}}{\mathrm{d}t} \rangle U_{p,j} + n_p m_p \langle \frac{\mathrm{d}u_{p,j}}{\mathrm{d}t} \rangle U_{f@p,i}
\end{aligned}
\tag{A.17}
$$

Then, by developing the derivatives in the two terms on the second line of the previous equation and transferring them on the right-hand side along with the triple correlation term, we get:

$$
\begin{aligned}
&\frac{\partial}{\partial t}(n_p m_p R_{fp,ij}) + \frac{\partial}{\partial x_k}(n_p m_p R_{fp,ij} U_{p,k}) \\
&+\frac{\partial}{\partial t}(n_p m_p U_{f@p,i} U_{p,j}) + \frac{\partial}{\partial x_k}(n_p m_p U_{f@p,i} U_{p,j} U_{p,k}) \\
&= -\frac{\partial}{\partial x_k}(n_p m_p \langle u''_{f@p,i} u''_{p,j} u''_{p,k} \rangle) - n_p m_p R_{p,jk} \frac{\partial U_{f@p,i}}{\partial x_k} - n_p m_p R_{fp,ik} \frac{\partial U_{p,j}}{\partial x_k} \\
&+n_p m_p \langle \frac{\mathrm{d}u_{f@p,i}}{\mathrm{d}t} u''_{p,j} \rangle + n_p m_p \langle \frac{\mathrm{d}u_{p,j}}{\mathrm{d}t} u''_{f@p,i} \rangle \\
&+n_p m_p \left[\langle \frac{\mathrm{d}u_{f@p,i}}{\mathrm{d}t} \rangle U_{p,j} + \langle \frac{\mathrm{d}u_{p,j}}{\mathrm{d}t} \rangle U_{f@p,i} \right] - U_{f@p,i} \frac{\partial n_p m_p R_{p,jk}}{\partial x_k} - U_{p,j} \frac{\partial n_p m_p R_{fp,ik}}{\partial x_k}
\end{aligned}
\tag{A.18}
$$

As in the two previous cases, the terms in red cancel out and we are left with:

$$
\begin{aligned}
&\frac{\partial}{\partial t}(n_p m_p R_{fp,ij}) + \frac{\partial}{\partial x_k}(n_p m_p R_{fp,ij} U_{p,k}) \\
&= -\frac{\partial}{\partial x_k}(n_p m_p \langle u''_{f@p,i} u''_{p,j} u''_{p,k} \rangle) - n_p m_p R_{p,jk} \frac{\partial U_{f@p,i}}{\partial x_k} - n_p m_p R_{fp,ik} \frac{\partial U_{p,j}}{\partial x_k} \\
&+ n_p m_p \langle \frac{\mathrm{d}u_{f@p,i}}{\mathrm{d}t} u''_{p,j} \rangle + n_p m_p \langle \frac{\mathrm{d}u_{p,j}}{\mathrm{d}t} u''_{f@p,i} \rangle
\end{aligned}
\tag{A.19}
$$

By using the evolution equation for the particle and fluid see velocities, we can simplify the last two terms on the right-hand side. During the development, the velocity covariance between two fluid velocity seen by the particle appears ($R_{ff',ij} = \langle u_{f@p,i} u_{f'@p,j} \rangle$). To make it consistent with the stochastic modelling, we neglect these for $f' \neq f$.

$$
\begin{aligned}
n_p m_p \langle \frac{\mathrm{d}u_{f@p,i}}{\mathrm{d}t} u''_{p,j} \rangle &= n_p m_p R_{p,jk} \frac{\partial U_{f,i}}{\partial x_k} + n_p m_p G_{fp,jk} R_{f@p,ki} \\
n_p m_p \langle \frac{\mathrm{d}u_{p,j}}{\mathrm{d}t} u''_{f@p,i} \rangle &= n_p m_p \sum_{f'} \frac{\lambda_{f'}}{\tau_{p,f'}} \left(R_{f'f,ij} - R_{fp,ij} \right) \\
&= n_p m_p \left[\frac{\lambda_f}{\tau_{p,f}} R_{f@p,ij} - \left(\sum_{f'} \frac{\lambda_{f'}}{\tau_{p,f'}} \right) R_{fp,ij} \right]
\end{aligned}
\tag{A.20}
$$

Which leads to the final formulation:

$$
\begin{aligned}
&\frac{\partial}{\partial t}(n_p m_p R_{fp,ij}) + \frac{\partial}{\partial x_k}(n_p m_p R_{fp,ij} U_{p,k}) \\
&= -\frac{\partial}{\partial x_k}(n_p m_p \langle u''_{f@p,i} u''_{p,j} u''_{p,k} \rangle) - n_p m_p R_{p,jk} \frac{\partial V_{f,i}}{\partial x_k} - n_p m_p R_{fp,ik} \frac{\partial U_{p,j}}{\partial x_k} \\
&+ n_p m_p G_{fp,jk} R_{f@p,ki} + n_p m_p \left[\frac{\lambda_f}{\tau_{p,f}} R_{f@p,ij} - \left(\sum_{f'} \frac{\lambda_{f'}}{\tau_{p,f'}} \right) R_{fp,ij} \right]
\end{aligned}
\tag{A.21}
$$

B | Turbulence modulation in the GLIM approach

In this appendix, we detail the different models used in the GLIM approach to account for turbulence modulation in multiphase flows. In this approach, the two fluid phases simulated can either be continuous or dispersed depending on the flow characteristics. When the two phases are continuous, they are separated by a large interface, when the volume fraction of one of them becomes too low, it is considered dispersed. In both cases, if it is taken into account, the turbulence model for each fluid is altered. The purpose of this appendix is to detail the nature of this alteration.

B.1 Turbulence modulation near a large interface

Near a free-surface, the production terms are modified as if the large interface operates on the flow exactly like a wall boundary condition would. This allows to progressively dampen the turbulence near the interface which shows better results than without treatment in standard stratified flows. It is important to note this modification is purely numerical and does not reflect a specific theoric development.

B.2 Continuous turbulence modulation in the presence of inclusions

When the volume fraction of a fluid becomes too small in a GLIM simulation, it is considered as dispersed. In that case, the interfacial momentum transfer term is changed accordingly and the turbulence model of the carrier field undergoes some minor changes to account for the presence of bubbles or droplets. This turbulence modulation is valid only for small inclusions compared to large turbulence length scales and is modelled with a supplementary source term $M_{c,ij}$ in the evolution equation of the turbulent kinetic stress $R_{f,ij}$.

$$\rho_f \frac{\partial R_{f,ij}}{\partial t} + \frac{\partial}{\partial x_k}(\rho_f u_{f,k} R_{f,ij}) - \frac{\partial}{\partial x_k}\left(\mu_f \frac{\partial}{\partial x_k} R_{f,ij}\right) = \frac{\partial}{\partial x_k}(S_{f,ijk}) + P_{f,ij} + g_{f,ij} + \Phi_{f,ij} - \rho_f \epsilon_{f,ij} + \rho_f M_{c,ij} \tag{B.1}$$

Where, if the dispersed phase is named g, the coupling term reads:

$$M_{c,ij} = \beta \alpha_g C_D (\frac{2}{3} \|\mathbf{U_r}^2\| \delta_{ij} + U_{r,i} U_{r,j}) \tag{B.2}$$

Where C_D is the drag coefficient, $\mathbf{U_r}$ is the relative velocity between the two phases and δ_{ij} is the unit second-order tensor. This term then undergoes the same weighting operation as interfacial transfer term to make sure they are taken into account only where there are dispersed inclusions. A similar term is added when using the k-ϵ turbulence model.

C | Interfacial area theta-scheme

In order to avoid truncation errors, it has been thought of developing a θ-scheme for the resolution of the interfacial area transport equation. However, since practical benefits from it have not been highlighted in experimental comparison, the scheme was dropped. It is described here for further works. The starting point equation reads:

$$\frac{\alpha_I \rho_I \Omega_I}{\delta t}\left(X_I^{n+1} - X_I^n\right) - X_I^{n+1}\sum_{J\in V_I}\phi_{IJ}\alpha_{IJ} + \sum_{J\in V_I}\phi_{IJ}\alpha_{IJ}X_{\theta,IJ}^{n+1} = 0 \tag{C.1}$$

Where Ω_I is the cell volume, ρ_I is the fluid density, δt is the time increment, α_I is the fluid volume fraction in cell I, $J \in V_I$ are the neighbours of I and $\phi_{IJ}\alpha_{IJ}$ defines the mass flux between cells I and J. The main idea is to make sure the imposed flux value does not cause negative values for X. Otherwise, the value would be truncated and the conservation of x would not be verified. Following common practice, we define a field θ such that the imposed flux is:

$$X_{\theta,IJ}^{n+1} = \theta((1-\gamma)X_{fs,IJ} + \gamma X_{IJ}^{n+1}) + (1-\theta)X_{IJ}^{n+1} \tag{C.2}$$

Rather than:

$$X_{m,IJ}^{n+1} = (1-\gamma)X_{fs,IJ} + \gamma X_{IJ}^{n+1} \tag{C.3}$$

With an upwind formulation, if the implicit part does not depend on θ, the evolution equation can be written:

$$\begin{aligned}\left(\frac{\alpha_I \rho_I \Omega_I}{\delta t} - \sum_{J\in V_I}\phi_{IJ}\alpha_{IJ}\right)X_I^{n+1} &= \frac{\alpha\rho_I\Omega_I}{\delta t}X_I^n \\ &\quad - \left(\sum_{\phi>0}\phi_{IJ}\alpha_{IJ}((1-\theta)X_{I,fs}^n + \theta X_I^n + \delta X_I)\right. \\ &\quad \left. + \sum_{\phi<0}\phi_{IJ}\alpha_{IJ}((1-\theta)X_{J,fs}^n + \theta X_J^n + \delta X_J)\right)\end{aligned} \tag{C.4}$$

Which leads to, by developing and passing the implicit part on the left-hand side of the equation:

$$\left(\frac{\alpha_I\rho_I\Omega_I}{\delta t} - \sum_{\phi<0}\phi_{IJ}\alpha_{IJ}\right)X_I^{n+1} = \frac{\alpha_I\rho_I\Omega_I}{\delta t}X_I^n \\ - \left(\sum_{\phi>0}\phi_{IJ}\alpha_{IJ}(1-\theta)(X_{I,fs}^n - X_I^n) + \sum_{\phi<0}\phi_{IJ}\alpha_{IJ}(1-\theta)(X_{J,fs}^n - X_J^n) + X_J^{n+1})\right) \tag{C.5}$$

Eventually, the previous equation can be transposed in a condition on θ for X_I^{n+1} to be positive:

$$\frac{\alpha_I\rho_I\Omega_I}{\delta t}X_I^n + \theta\left(\sum_{\phi>0}\phi_{IJ}\alpha_{IJ}(X_I^n - X_{I,fs}^n) + \sum_{\phi<0}\phi_{IJ}\alpha_{IJ}(X_J^n - X_{J,fs}^n)\right) > 0 \tag{C.6}$$

The correction was implemented in the numerical method but no clear improvement could be noted.

RÉPUBLIQUE FRANÇAISE
Liberté Égalité Fraternité

Université de Toulouse

Titre : Développement d'un modèle triphasique Euler/Euler/Lagrange pour la simulation numérique des écoulements liquide-gaz chargés en particules.

Mots clés : Triphasique, Euler/Lagrange, Surface libre, particules, turbulence, Jet plongeant

Résumé : Ce manuscrit retranscris un travail effectué au cours d'une thèse au département MFEE d'EDF R&D sur les écoulements liquid-gaz chargés en particules dispersées sous la direction d'Olivier Simonin (IMFT), de Jérôme Laviéville (EDF) et de Nicolas Mérigoux (EDF). Le but de la thèse est de fournir un environnement de travail pour la simulation numérique d'écoulement eau-air à bulles, à phases séparés ou en régime mixte, chargé en particules qui peuvent interagir avec les fluides présents sous leur forme continue ou dispersée. Ces écoulements peuvent se retrouver aussi bien dans des situations industrielles comme des réacteurs chimiques, des centrales de production d'électricité ou des usines de traitement des eaux usées que dans des situations naturelles comme durant la crue d'un fleuve. L'outil développé permet de faire des prédictions sur les performances de ces dispositifs industriels ou sur les dégâts causés par des évènements naturels exceptionnels. Les développements sont inclus dans la version la plus à jour du code de calcul neptune_cfd, un solveur N-fluides développé par EDF, le CEA, l'IRSN et Framatome, basé sur la méthode multi-fluide standard qui permet la simulation d'écoulement à plusieurs phases indépendamment de leur typologie. Les méthodes misent en place sont basées sur des approches diphasiques bien connues. La méthode Lagrangienne stochastique de suivi de particules est adaptées pour que chaque particule puisse interagir avec toutes les champs fluides présents. Des fermetures sont proposées pour déterminer l'impact de chacune des phases sur le comportement des particules. Afin de vérifier certaines hypothèses, une nouvelle fermeture pour l'équation de Langevin sur la vitesse de fluide vue par la particule est proposée. Son comportement est comparée aux modèles standards et de la littérature sur des cas de vérification simples de turbulence homogène isotrope et des cas inhomogènes. Les équations Lagrangiennes obtenues sont utilisées pour fermer un modèle Eulerien basé sur l'approche fonction densité de probabilité. Les performances des deux modèles triphasiques développés sont établies en matière de déposition de particules pilotée par la turbulence et la gravité. Un pan entier de la thèse se concentre sur une problématique apparue durant des vérifications préliminaires: le phénomène d'entraînement d'air dans les jets plongeants. En effet, à partir d'une structure résolue, en fonction des conditions d'écoulements, des bulles ou gouttelettes dispersées peuvent apparaître. La quantité de ces structures transférées ainsi que leur taille caractéristique étant des grandeurs primordiales, il a fallu mettre en place un nouveau modèle. Le transfert de masse entre structures continues et inclusions dispersées est assuré par le modèle qui décrit l'évolution des interfaces résolues. Nous ne l'avons pas modifié. Celui qui concerne la taille des bulles/gouttelettes créées s'intègre dans l'équation d'évolution de l'aire interfaciale, grandeur qui permet de suivre le diamètre des inclusions. Tous les modèles développés sont comparés à des mesures expérimentales. Le modèle d'entraînement d'air est d'abord testé sans la présence des particules sur des cas divers. Un cas de ressaut hydraulique est aussi envisagé pour établir la généralité du modèle mis en place. Les modèles triphasiques sont testés sur des configurations variées, d'abord sans entraînement d'air pour isoler le comportement des particules puis avec tous les phénomènes. Les différents cas ont permis de mettre en valeur l'importance de certains modèles ainsi que les différences entre les méthodes Lagrangienne stochastique et Eulerienne.

Title: Euler/Euler/Lagrange model development for the numerical simulation of multiphase flows loaded with particles

Key words: free surface flows, Multi-phase, particles, Euler/Lagrange, dispersion, turbulence

Abstract: This manuscript sums up work carried out during a thesis at the MFEE department of EDF R&D on liquid-gas flows laden with dispersed particles under the supervision of Olivier Simonin (IMFT), Jérôme Laviéville (EDF), and Nicolas Mérigoux (EDF). The thesis aims at providing a working environment for the numerical simulation of two-phase bubbly flows, free-surface flows or in a mixed regime, loaded with particles that can interact with the fluids present in their continuous or dispersed form. These flows can be found in industrial situations such as chemical reactors, power plants, or wastewater treatment plants, as well as in natural situations such as during a flood. The developed tool allows predictions to be made about the performance of these industrial devices or the damage caused by exceptional natural events. The developments are included in the most up-to-date version of neptune_cfd, a multi-fluid solver developed by EDF, CEA, IRSN, and Framatome, based on the standard multi-fluid method that allows the simulation of multiphase flow independently of their typology. The methods implemented are based on well-known two-phase approaches. The stochastic Lagrangian particle tracking method is adapted so that each particle can interact with all the fluids. Closures are proposed to determine the impact of each phase on the behavior of the particles. To verify certain assumptions, a new closure for the Langevin equation on the fluid velocity seen by the particle is proposed. Its behavior is compared to standard models and literature on simple verification cases of homogeneous isotropic turbulence and inhomogeneous cases. The Lagrangian equations obtained are used to close an Eulerian model based on the probability density function approach. The performance of the two developed threephase models is established in terms of particle deposition driven by turbulence or gravity. A significant part of the thesis focuses on an issue that arose during preliminary checks: the phenomenon of air entrainment in plunging jets. Indeed, due to the nature of the solver, bubbles or dispersed droplets can detach from the free-surface depending on the flow conditions. The quantity of these transferred structures and their characteristic size being crucial quantities which drives their behavior, a new model had to be developed. Mass transfer between continuous structures and dispersed inclusions is ensured by the model that describes the evolution of resolved interfaces, the latter was not modified. The one regarding the size of the created bubbles/droplets is integrated into the evolution equation of the interfacial area, a quantity that allows tracking the diameter of the inclusions. All developed models are compared to experimental measurements. The air entrainment model is first tested without the presence of particles in various cases. A hydraulic jump case is also considered to establish the generality of the model. Then, the threephase models are tested in various configurations. First, configurations without air entrainment to isolate the behavior of the particles, and then with air entrainment. The different cases highlighted the importance of certain models and the differences between stochastic Lagrangian and Eulerian methods.